SAFEGUARDS ASSESSMENT OF GAMMA-RAY DETECTION FOR PROCESS MONITORING AT NATURAL URANIUM CONVERSION FACILITIES

A Dissertation
Presented to
The Academic Faculty

by

Shaheen Azim Dewji

In Partial Fulfillment
of the Requirements for the Degree
Doctor of Philosophy in the
School of Mechanical Engineering
Nuclear and Radiological Engineering Program

Georgia Institute of Technology
May 2014

SAFEGUARDS ASSESSMENT OF GAMMA-RAY DETECTION FOR PROCESS MONITORING AT NATURAL URANIUM CONVERSION FACILITIES

Approved by:

Dr. Nolan Hertel, Advisor
School of Mechanical Engineering, Nuclear and Radiological Engineering Program
Georgia Institute of Technology

Dr. Adam Stulberg
School of International Affairs
Georgia Institute of Technology

Dr. Glenn Sjoden
School of Mechanical Engineering, Nuclear and Radiological Engineering Program
Georgia Institute of Technology

Dr. Alan Icenhour
Nuclear Security and Isotope Technology Division
Oak Ridge National Laboratory

Dr. Bernd Kahn
School of Mechanical Engineering, Nuclear and Radiological Engineering Program
Georgia Institute of Technology

Dr. Robert McElroy
Nuclear Security and Isotope Technology Division
Oak Ridge National Laboratory

Date Approved: October 11, 2013

ACKNOWLEDGEMENTS

I must first start by thanking God – everyday I am ever thankful for the opportunities I have been granted.

I would like to extend my deep gratitude to Dr. Nolan Hertel, who has been a phenomenal adviser. I feel it was providencial that I ended up with such an amazing adviser who unwaveringly encouraged my intellectual pursuits. He has instilled confidence in my abilities as an engineer, and I look forward to working with and continuing to learn from him in the future for many years to come. I would also like to thank Dr. Adam Stulberg, who has been instrumental in fostering my technology-policy interests and provided me with an invaluable skill set for approaching real-world challenges through the lens of a political scientist armed with the toolbox of an engineer.

I would also like to thank my committee – both from Georgia Tech (Dr.Sjoden and Dr. Kahn) and Oak Ridge National Laboratory (Dr. Icenhour and Dr. McElroy), for their guidance throughout the duration of my academic and research endeavors in graduate school.

None of this research would be possible without the strong support of my colleagues at ORNL. First and foremost, I would like to thank Bernie Kirk for her unwavering support. Bernie has been a truly phenomenal mentor without whom any of my doctoral work would have not been possible. Second, I would like to thank Dawn Eipeldauer for developing my initial interest in safeguards work at ORNL. I would also like to thank Jeff Chapman for his confidence, enthusiasm and perpetual

optimism, Chris Pickett for his investment in my early career development in nuclear safeguards, and Dr. Denise Lee, who has supported me though all my work at UNCLE. I would like to extend special gratitude to Dr. Stephen Croft, who spent many long hours with my dissertation and was truly instrumental in guiding the development of my work. Further thanks are due in spades to Steve Cleveland, Linda Paschal, and Cheryl Brown, who were always willing to extend a helping hand with a smile! I would finally like to thank Michael Whitaker, Joe Birdwell, Tyler Guzzardo also from ORNL, and Ram Venkataraman from Canberra, for their support in my dissertation research activities.

Further appreciation is extended to NA-241 for funding the UNCLE project and most notably to Marc Humphrey, Kevin Veal, Dunbar Lockwood and Melissa Scholz for being steadfast supporters of my work along the years. I owe a special debt of gratitude to Melissa, as I would not have been able to achieve my goals and am forever indebted to her for her support and kindness.

Finally, I would like to thank my family, whose love, support, and prayers have been the motivation and the driving factor behind my accomplishments. I would like to thank Pasquale Fulvio, for being a source of strength and balance through the final trials of completing my dissertation, and for constantly reminding me that "there is no such thing as half a Ph.D!" I would especially like to thank my mother (Parin Ph.D.!) for instilling a desire for the lifelong pursuit of knowledge from a young age and my father for unconditionally supporting all my educational endeavors. Last but not least, I am forever thankful to my sister for always being there when I needed her and for always queuing a movie on the weekend despite my mountains of homework (this is the last schoolwork, I promise!). It was with her love, encouragement, and sacrifice that made all my successes possible.

TABLE OF CONTENTS

LIST OF TABLES

LIST OF FIGURES

LIST OF ACRONYMS AND ABBREVIATIONS

ABACC	Brazilian-Argentine Agency for Accounting and Control of Nuclear
ADU	Materials
AP	Ammonium diuranate
AUC	[Model] Additional Protocol
BEGe	Ammonium uranyl carbonate
CA	Broad Energy Germanium
CANDU	Complementary Access
CNEN	CANada Deuterium Uranium
CS	Brazilian Nuclear Energy Commission
DA	Containment and Surveillance
DIV	Destructive Analysis
DOE	Design Information Verification
FWHM	U.S. Department of Energy
GCP	full-width-at-half-maximum
GDP	Gaseous Centrifuge Plant
GEB	Gaseous Diffusion Plant
HPGe	Gaussian Energy Broadening
IAEA	High-Purity Germanium
INFCIRC	International Atomic Energy Agency
INFCIS	Information Circular
ISOCS	Integrated Nuclear Fuel Cycle Information System
KMP	In situ Object Counting System
$LaBr_3$	Key Measurement Points
LANL	Lanthanum bromide
LLNL	Los Alamos National Laboratory
MAC	Lawrence Livermore National Laboratory
MBA	Mass Attenuation Coefficient
MC&A	Material Balance Area
MCNPX	Material Control & Accountability
MFP	Monte Carlo N-Particle Transport Code eXtended
MTU	Mean Free Path
MUF	Metric Tonnes of Uranium
NaI	Material Unaccounted For
NDA	Sodium Iodide
NNWS	Nondestructive assay
NUCP	Non-Nuclear Weapons States
NWS	Natural Uranium Conversion Plant
ORNL	Nuclear Weapons States
PCA	Oak Ridge National Laboratory
PIV	Principal Component Analysis
PM	Physical Information Verification
PP18	Process Monitoring

ROI	IAEA Policy Paper 18
RPM	Region of Interest
SAGSI	Revolutions per Minute
SBD	Standing Advisory Group on Safeguards Implementation
SNRI	Safeguards by Design
SQ	Short Notice Random Inspection
TUrND	Significant Quantity
UCF	Transverse Uranium Neutron Detector
UF_4	Uranium Conversion Facility
UF_6	Uranium tetrafluoride
UN	Uranium hexafluoride
UNCLE	Uranyl nitrate
UO_2	Uranyl Nitrate Calibration Loop Equipment
UO_3	Uranium dioxide
UOC	Uranium trioxide
U_3O_8	Uranium ore concentrate
U.S.	Uranous uranyl oxide
	United States

SUMMARY

Conversion, the process by which natural uranium ore (yellowcake) is purified and converted through a series of chemical processes into uranium hexafluoride gas (UF_6), has historically been excluded from the nuclear safeguards requirements of the ^{235}U-based nuclear fuel cycle. With each step in the conversion process, from yellowcake to feedstock for UF_6, intermediary uranium oxide and uranium fluoride compounds become progressively more attractive products for diversion toward activities noncompliant with international treaties. The diversion of this product material could potentially provide feedstock for a clandestine or undeclared enrichment for weapons development for state or non-state entities. With the realization of this potential, the International Atomic Energy Agency (IAEA) has only recently reinterpreted its policies to emphasize safeguarding this feedstock in response to such diversion pathways.

This project employs a combination of simulation models and experimental measurements to develop and validate concepts of nondestructive assay monitoring systems in a natural uranium conversion plant (NUCP). In particular, uranyl nitrate (UN) solution exiting solvent extraction was identified as a key measurement point (KMP), where gamma-ray spectroscopy was selected as the process monitoring tool. The Uranyl Nitrate Calibration Loop Equipment (UNCLE) facility at Oak Ridge National Laboratory was employed to simulate the full-scale operating conditions of a purified uranium-bearing aqueous stream exiting the solvent extraction process in an NUCP. This work investigated gamma-ray signatures of UN circulating in the UNCLE facility and evaluated various gamma-ray detector (HPGe, $LaBr_3$, and NaI) sensitivities to UN. Several predictive modeling techniques were explored where satisfactory agreement with experimental measurements was achieved.

It may be concluded that transmission-corrected gamma-ray spectra provides a reliable way to monitor the ^{235}U concentration of UN solution in transfer pipes in NUCPs. Furthermore, predictive and analysis methods are adequate to design and realize practical designs. The ^{137}Cs transmission source employed in this work is viable but not optimal for ^{235}U densitometry determination. Validated simulations assess the viability of ^{133}Ba and ^{57}Co as alternative densitometry sources. All gamma-ray detectors are viable for monitoring natural uranium feed; although high-purity germanium (HPGe) is easiest to interpret, it is the least attractive as an installation instrument. Overall, for monitoring throughput in a facility such as UNCLE, an error of less than 0.17% is required in order to detect the diversion of 1 significant quantity (SQ) of UN. Although calibrated gamma-ray detection systems are capable of determining the concentration of uranium content in NUCPs, it is only in combination with supporting data (such as flowrate, enrichment) and verifiable declarations that safeguards conclusions can be drawn. Consequently, lessons learned and recommendations are provided.

In addition to the technical assessments and sensitivity analyses presented, the proposed changes in IAEA safeguards policy are described, as are the political and operational challenges associated with advancing front-end safeguards monitoring.

CHAPTER 1. INTRODUCTION

The nuclear safeguards requirements of the ^{235}U-based nuclear fuel cycle historically began with uranium hexafluoride gas (UF_6), having precluded any precursor products in the conversion part of the fuel cycle. Conversion is the process by which natural uranium ore (yellowcake) is purified through a series of chemical processes into UF_6. With each intermediary step in the conversion process, unmonitored intermediary uranium oxide and uranium fluoride compounds could become attractive products for misuse or diversion to clandestine or undeclared activities. The International Atomic Energy Agency (IAEA) has recently revised its policies to recommend safeguarding this potential feedstock material in response the increased availability of dual-use nuclear technology in the changing global political environment.

1.1 Project Significance

Recent IAEA circulars and policy papers have sought to implement safeguards when any purified aqueous uranium solution or uranium oxides suitable for isotopic enrichment or fuel fabrication exist. Under the revised policy, IAEA Policy Paper 18 (PP18), "Safeguards Measures Applicable in Conversion Plants Processing Natural Uranium," the starting point for nuclear material under safeguards was reinterpreted and a new definition of source material in this category was introduced [1]. Under IAEA PP18, the IAEA suggests that these purified uranium compounds should be subject to safeguards procedures no later than at the first point in the conversion process. In response, the IAEA and the U.S. Department of Energy (DOE) have become interested in developing instruments, tools, strategies, and methods that could be used in safeguarding materials and detecting diversion in the front end of the nuclear fuel cycle prior to the production of UF_6 [2]. Efforts thus far have largely

focused on conceptual approaches, not integrated technology development for safeguards monitoring, to determine if IAEA requirements can be met.

1.2 Problem Statement and Objectives

The aim of nuclear safeguards is to deter diversion of nuclear material from peaceful uses by maximizing the chance of early detection. This work evaluates whether passive nondestructive assay (NDA) techniques using gamma-ray spectroscopy can be used as a technical method for drawing safeguards conclusions, and if the IAEA detection requirements of 1 significant quantity can be met. In the scope of natural uranium conversion plants (NUCPs), 1 SQ translates to 10 metric tons of natural uranium over a period of 1 year with a detection probability of 50% [2]. This project creates and evaluates a technical design basis using passive gamma-ray spectroscopy for the safeguarding of nuclear material at the first identified key measurement point (KMP) in an NUCP. PP18 articulates that the uranyl nitrate (UN) stream exiting solvent extraction during conversion is the first point at which uranium is of suitable purity for enrichment or fuel fabrication.

Trials of the proposed NDA system in operational settings will test and evaluate new applications of safeguards instrumentation. The precision, capabilities, and applicability limitations of the NDA-based integrated safeguards system is to be determined through validating existing plant operations, as well as providing a sensitivity analysis of instrumentation to proposed misuse/diversion cases.

1.3 Research Questions

The following key research questions will be addressed in the scope of this project: First, although there is precedence for reinterpretation of Integrated Nuclear Fuel Cycle Information Circular (INFCIRC) 153 in response to technology changes, there will be plurality of legal and political hurdles to implement safeguards earlier in the fuel cycle. A dichotomy between states with and without Complementary Access (CA) will become evident, as will the safeguards burdens further imposed on non-nuclear weapons states (NNWS) versus those of nuclear weapons states (NWS). With increased interest in civilian nuclear energy and a subsequent increase in demand for conversion capacity, this legal and political issue will have to be imminently addressed for existing facilities and new facility builds. With the evolution of new nuclear fuel cycle technology, the requirement for the Non-Proliferation Treaty (NPT) as a binding legal and policy agreement must continue to evolve with these technology changes. The technology-policy nexus is evaluated with respect to the recommendations of PP18 in the purview of technological progress.

Second, given that passive gamma-ray techniques have long been employed in front-end enrichment monitoring, this tradition continues to be applicable for process monitoring (PM) of UN. Although high-resolution semiconductor detectors provide the most precise signatures, lower-resolution scintillator detectors will likely prove to be more robust under field operating conditions, but require advanced techniques to unfold lower resolution signatures from high interference/background. Based on these premises, this project evaluates what gamma-ray detection system is suitable for safeguards monitoring of intermediate compounds during the conversion process. Also, the capabilities and limitations of these NDA gamma-ray systems provide for PM of UN in NUCPs are assessed.

Third, due to the high uranium throughput of conversion facilities, meticulous monitoring will be required along the entire conversion process. Although PM at a single KMP will provide essential safeguards data for a small NUCP, the complex structure of large NUCP facilities will require more extensive in-line monitoring points in order to differentiate diversion activities from inventory differences and material unaccounted for (MUF). The IAEA's criteria for diversion detection of 1 SQ at an NUCP corresponds to a diversion of 10%, 1%, and 0.1% production from small, medium, and large production plants, respectively. Although it may be easier to detect a 10% diversion with a smaller production facility, the nature of the diversion threat becomes increasingly more complex with increasing facility size, and the burden for accurate detection becomes increasingly challenging. Once the capabilities of each of the tested detection systems are ascertained, the robustness of the NDA instrumentation is evaluated for detecting undeclared diversion, misuse, or "spoofing" activities during conversion. Detection limits and sensitivities from detection capabilities are then translated into an assessment of safeguards conclusions that can be drawn.

1.4 Dissertation Overview

To address the posed research questions, this dissertation is structured as follows: In Chapters 2–4, current natural uranium conversion facilities subject to IAEA inspections and inspection approaches are identified. Potential measurement locations and associated technologies for doing so based on previous technical and policy work are also summarized. The potential impact and benefits of unattended PM for both the operator and the IAEA are also be evaluated from an implementation strategy perspective.

Chapter 5 outlines the methodology for developing the proof-of-principle for NDA monitoring at NUCPs. Candidate NDA systems are further explored in Chapter 5, where IAEA technical requirements, compliant instrumentation, and methods are identified. Experimental measurement designs are described and serve to assess each instrument's PM capability in determining instrumentation sensitivities and limitations. This includes fully characterizing the UN source term, with calculations provided in Chapter 6. As Uranyl Nitrate Calibration Loop Equipment (UNCLE) employs UN from uranium that is 40 years old, a source term analysis is required to determine aged-based signature changes vis-à-vis freshly solvent-extracted UN in NUCPs. Once the source term has been characterized and potential monitoring signatures have been identified, attenuation measurements are conducted in Chapter 7. At the established KMP, UN exiting the solvent extraction stream in an NUCP flows through an intricate array of stainless steel piping. Consequently, for gamma-ray detection, UN emissions must penetrate stainless steel piping. In addition, use of an external gamma-ray source for densitometry measurements must be calculated to determine emission intensity through the entire diameter of the UN-bearing pipe.

Chapter 8 outlines the simulation geometry, source term, and tallies that are conducted via Monte Carlo simulations, which are validated via the subsequent measurements. Results of experimental dilution measurements in a controlled laboratory setting for validation, as well as for operational measurements in the UNCLE facility, are provided in Chapters 9 and 10, respectively. Chapter 11 provides the results of the Monte Carlo simulations in order to simulate the detector response function based on the dilution experiments. With validated simulation models at each of the dilution concentrations, the detector responses for both passive and a variety of transmission sources are simulated to determine the optimum transmission source for UN densitometry measurements. In addition, simulation measurements are conducted in

order to assess instrumentation sensitivity to varying enrichments of UN solution. Based on dilution and facility data, the robustness of monitoring signatures is assessed via statistical analysis and error propagation in Chapter 12. Chapter 12 further provides a more detailed sensitivity analysis of the detector response to a variety of key factors affecting detection efficiency (geometry, attenuation, sample self-attenuation, intrinsic efficiency).

From data obtained from both the experimental measurements and simulations, in combination with a detailed sensitivity analysis, evaluations are made in Chapter 13 regarding the optimization of gamma-ray NDA instrumentation for PM at this KMP. Assessments are made regarding whether the IAEA timeliness and detection goals are feasible, and whether passive gamma-ray techniques are capable of detecting undeclared, misuse, or diversion scenarios at an NUCP. Finally, Chapter 14 provides conclusions and recommendations for ensuing work, as well as lessons learned regarding design optimization, IAEA implementation challenges, and further policy investigations.

CHAPTER 2. BACKGROUND

At present, the IAEA's Integrated Nuclear Fuel Cycle Information System (INFCIS) database lists 22 conversion facilities currently with a total design capacity of 155.6 kt of heavy metal (uranium)/yr. [3] [4]. Approximately 75% of the current capacity is held in NWS. Four new facilities are either in planning or under construction in Brazil and France, increasing the projected capacity by 31.5 kt HM/yr. All projected, operational, and decommissioned conversion facilities and statuses from INFCIS are summarized in *Appendix A*.

Distributed worldwide, the conversion facilities provide fuel to a growing number of nuclear power plants (currently totaling 495) [5]. Conversion facilities worldwide can be broadly grouped into the following three distinct sizes, based on production in metric tonnes uranium (MTU): [6]

- Small (S) ~ 100 MTU/yr,
- Medium (M) ~ 1000 MTU/yr, and
- Large (L) ~ 10,000 MTU/yr.

2.1 Conversion Methods in the Nuclear Fuel Cycle

To develop a framework for assessing the technical basis of a safeguards system employing NDA technology, it is first necessary to outline the chemical processes common to NUCPs. In the ^{235}U-based nuclear fuel cycle, conversion is considered to be part of the front end of the fuel cycle, following the mining and milling steps.[1] Conversion is necessary in order to purify the uranium compounds from the ore components resulting from the milling phase of the fuel cycle. In the conversion process, uranium ore concentrate (UOC) containing 75–80% U_3O_8 [7] is purified and converted through a series of chemical procedures into uranium dioxide (UO_2), uranium trioxide (UO_3), or uranium metal for fuel fabrication, as well as uranium hexafluoride gas (UF_6), as feedstock for enrichment prior to fuel fabrication [8]. The main conversion processes are shown in Figure 2-1, which depicts conversion to UO_3.

[1] Note that this is not applicable to the products of in situ leach mining.

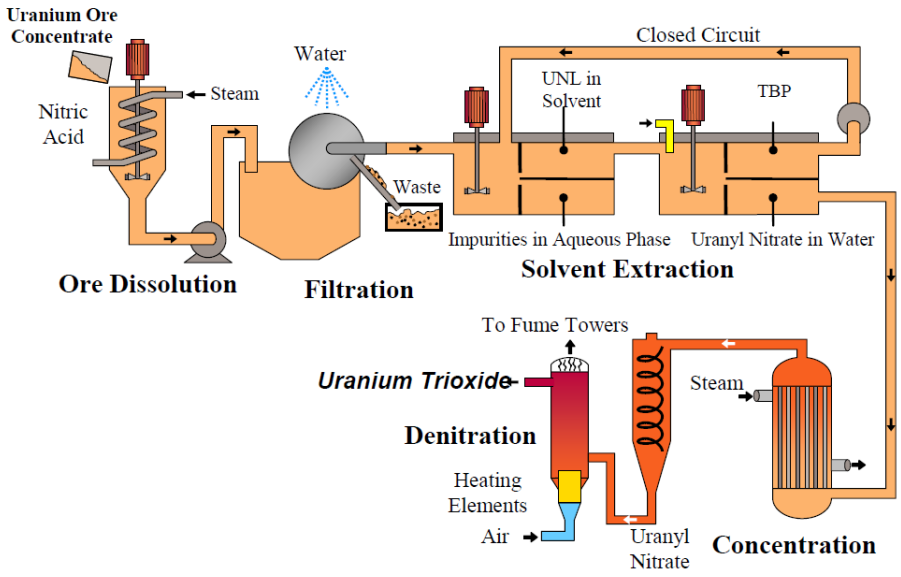

Figure 2-1. Typical Processing Phases for Conversion (UO_3).

Reproduced from Francis [9].

Two methods are commercially employed for converting UOC to UF_6 in the conversion process: (1) the dry hydrofluor process *[Figure 2-2(A)]*, in which fractional distillation is employed in the final stages to purify the feed materials to produce UF_6, and (2) the wet solvent extraction process *[Figure 2-2(B)]*, in which yellowcake is dissolved, purified, and converted via a series of chemical processes to UF_6 or uranium metal [7] [10].

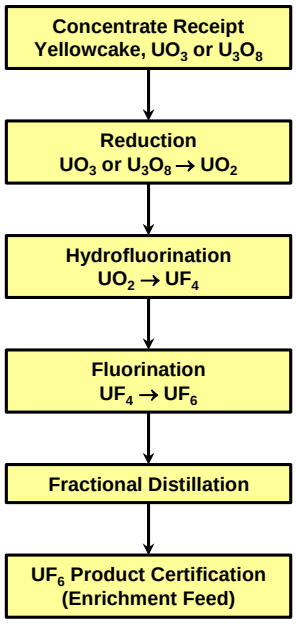

(A)

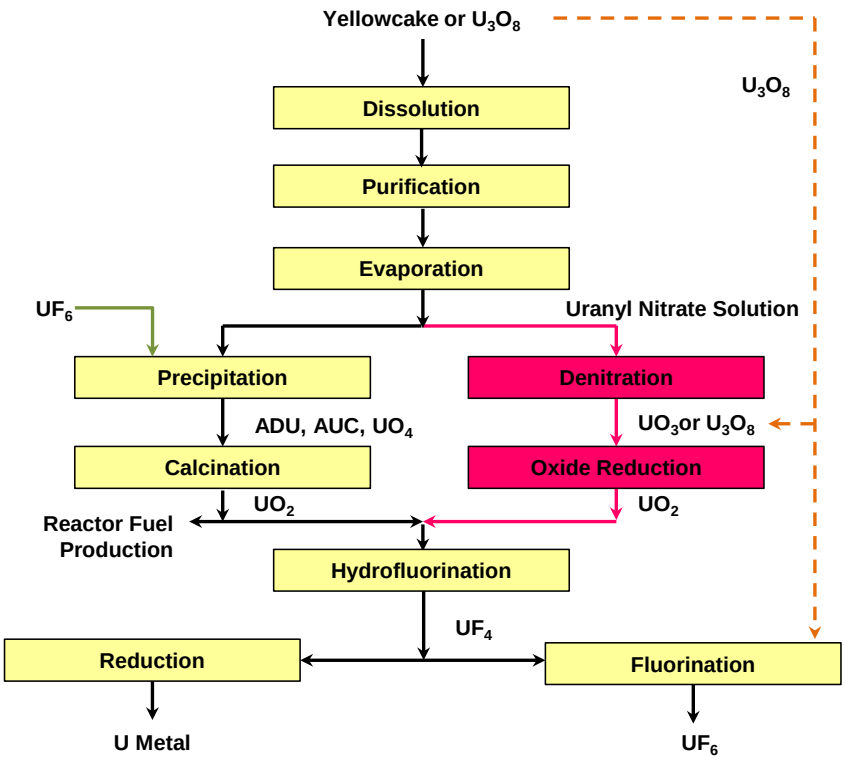

(B)

Figure 2-2. Uranium Conversion (A) Dry Hydrofluor (B) Wet Solvent Processes.

Figure 2-2(B)-Small-scale batch NUCP (left chain) and medium/large-scale continuous (right chain). Reproduced from Faulkner et al. [11].

2.1.1 Dry Hydrofluor Process

For an NUCP employing the dry hydrofluor process *[Figure 2-2(A)]*, the chemical processes can be summarized as follows [6] [7].

- Roasting and fluidized-bed reduction of yellowcake or uranium oxides (U_3O_8 or UO_3) to UO_2 using hydrogen from cracked ammonia [5]:

$$U_3O_8 + 2H_2 \rightarrow 3UO_2 + 2H_2O \quad [2\text{-}1]$$

or

$$UO_3 + H_2 \rightarrow UO_2 + H_2O \quad [2\text{-}2]$$

- Fluidized-bed hydrofluorination of UO_2 to produce crude UF_4 using anhydrous HF
- Fluidized-bed fluorination of UF_4 to UF_6 using elemental fluorine
- Fractional distillation to purify UF_6 of volatile fluorides from fluorination

2.1.2 Wet Solvent Extraction Process

As the production capacity of a conversion facility increases, so does the complexity of the processing system. Depending on the size and throughput of the NUCP, the intermediary processing steps vary in the conversion of uranium ore to fluoride gas. For an NUCP employing the wet solvent extraction process [*Figure 2-2(B)*], the chemical processes (according to plant size) can be summarized as follows [5] [6] [7].

Common to all sizes of natural uranium conversion facilities employing wet solvent extraction, the conversion process begins as follows.

- Dissolution of yellowcake with hot nitric acid to form a uranyl nitrate (UN) solution as $UO_2(NO_3)_2 \cdot 6H_2O$
- Purification of UN using solvent extraction with tributyl phosphate in kerosene or dodecane
- Evaporation, stripping the uranium from the organic phase, and washing with dilute nitric acid, producing a purified and concentrated UN solution

For a selection of small plants (100 MTU/year), and most medium- to large-sized plants (1000 MTU to 10,000 MTU per year), denitration is employed in continuous operation to accommodate higher production.

- Heat is applied to dehydrate and denitrate pure UN, producing UO_3.
- Hydrogen induces oxide reduction from UO_3 to UO_2.

For all plant production sizes, the final phases converge.

- Anhydrous HF is used to produce UF_4 via hydrofluorination of UO_2:

$$UO_2 + 4HF \rightarrow UF_4 + 2H_2O. \quad [2\text{-}3]$$

- UF_4 can follow one of two routes:
  - Fluorinated into UF_6 using F_2 by being fed into a fluidized bed reactor or flame tower with gaseous fluorine;

$$UF_4 + F_2 \rightarrow UF_6 \quad [2\text{-}4]$$

  - Reduced to uranium metal by using magnesium or calcium and heat

The resulting UF_6 is moist and highly corrosive and is prepared as a gas for enrichment activities [12]; however, under pressure at lower temperatures, UF_6 can be liquefied and stored in thick-walled steel shipping cylinders, weighing over 15 tons when filled [5]. The cooled UF_6 crystallizes from liquid to form a white solid within these cylinders.

It is possible for a small size plant to operate continuously, as outlined in the above process, but it is also suited to batch production techniques, where denitration is replaced by the following.

- Ammonia/ammonium hydroxides are used to precipitate ammonium diuranate, or carbon dioxide is used to precipitate ammonium uranyl carbonate (AUC).

- Calcination in a fluidized bed reactor in the presence hydrogen is employed to produce UO_3, or UO_2 if heated sufficiently.

The typical process steps for the conversion from yellowcake to UF_6 for small-, medium-, and large-scale production plants are summarized in Figure 2-2.

2.2 Potential Diversion Pathways in Conversion Facilities

Each step in the conversion process at an NUCP increases the nuclear material attractiveness for diversion as the uranium is successively purified. Products created later in the conversion process are more attractive products for diversion. Although uranium in liquid form as UN is the first attractive diversion point, the handling of solid material (uranium oxides and fluorides) in a solid phase may be a more attractive medium, as solids are more easily handled than liquids. Naturally, the most desirable product for diversion would be a UF_6 cylinder for diversion to a poorly safeguarded or clandestine enrichment facility. A variety of potential diversion paths exist for a generic NUCP, as shown in *Figure 2-3*. Thus, a detailed understanding of the processes during conversion operations is essential to selecting instrumentation and strategies for NUCP safeguards and controls. At various points in the conversion process, the intermediary material becomes attractive in relevant scenarios, where the level of appeal for each of these diversionary activities is contingent upon the state facilities available. For example, diversion to a laser enrichment facility only becomes a major point of interest if the host state has access to such a facility, or access to a clandestine means of transferring it to a complicit state with the required infrastructure. Consequently, not only does the intermediary product become more attractive, it holds a higher strategic value.

As UN is denitrated to UO_2 or UO_3, these compounds produce UCl_4 via chlorination, which is an attractive feedstock for electromagnetic isotope separation chemical-ion exchange enrichment [11]. Alternatively, following reduction, UO_2 can be hydrofluorinated into UF_4 or metallothermically reduced to uranium metal for use in atomic vapor laser isotope separation or for plutonium production [11]. Thus, unmonitored UF_6 could be shipped to a clandestine location for distillation prior to

enrichment in gaseous diffusion or centrifuge facilities. In essence, diversion could be as simple as draining UN into a drum in a trickle-diversion ("garden-hose") scenario.

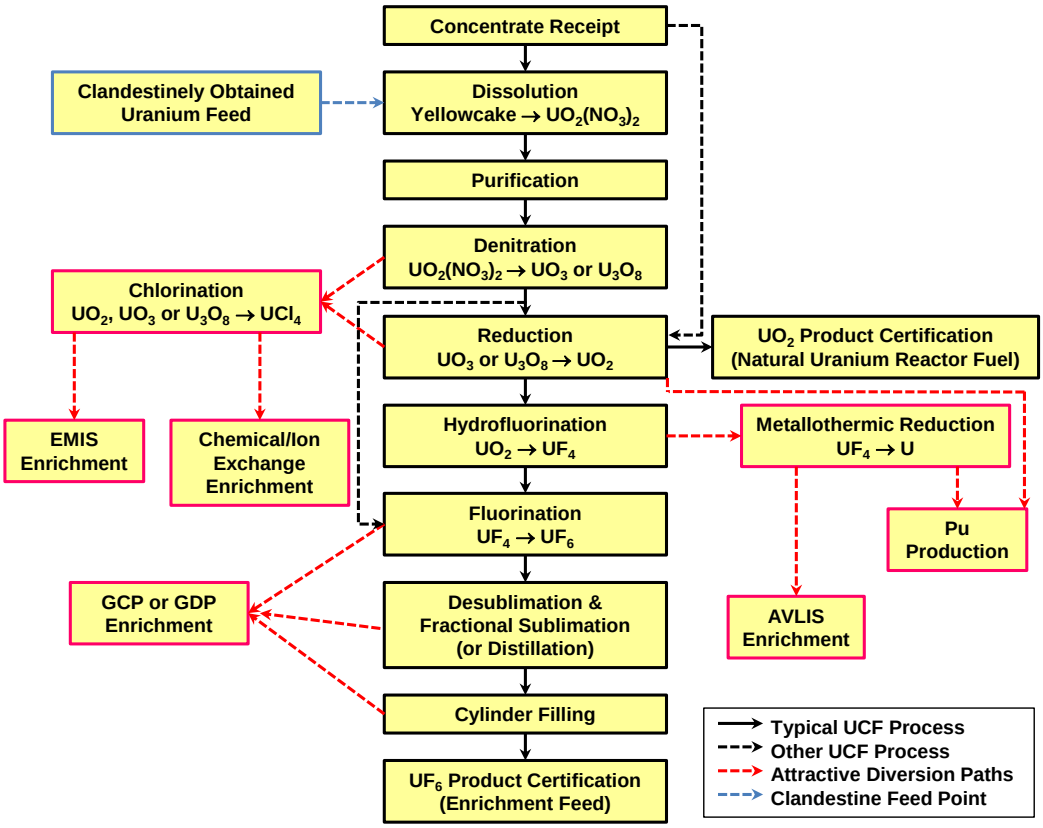

Figure 2-3. Generic Conversion Wet Process (Central Axis) and Potential Diversion Paths (Periphery) for a Natural Uranium Conversion Facility.

Reproduced from Faulkner et al. [11].

2.3 Drivers for New Conversion Capacity Production

With global interest in civil nuclear energy production gaining momentum, aspiring nuclear energy states will undoubtedly be placing increasing demand on current facilities. *Nuclear Engineering International* has projected a nearly 100% increase in UF_6 demand from conversion facilities *(Figure 2-4)* in the next two decades [13].

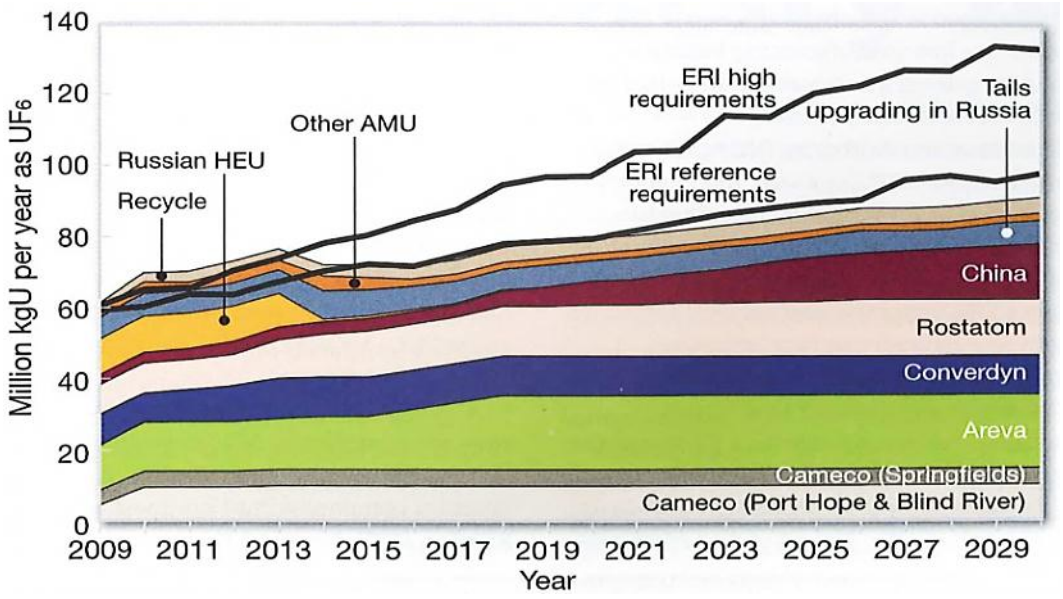

Figure 2-4. Conversion supply and requirements (reference and high cases) forecast.

Reproduced from Schwartz and Steyn [13].

In tandem with IAEA drivers for reinterpreting early fuel cycle safeguards policy, this increase in projected demand presents a complex technology-policy nexus that must be rectified for existing and new facilities in order to ensure the peaceful civilian development of nuclear energy, on a global scale.

CHAPTER 3. POLICY CONTEXT: IAEA POLICY-DRIVEN TECHNOLOGIES

3.1 International Atomic Energy Agency Changes in Early Fuel Cycle Policy

Prior to 2003, the IAEA did not consider the feedstock (UOC) or intermediary products (UO_3, UF_4) within the conversion process to be of safeguards relevance [14]. The two principal products from the NUCPs that fall under IAEA safeguards are UF_6, feedstock for subsequent enrichment at commercial facilities, and UO_2, used for fuel in heavy-water-moderated reactors [i.e., the Canada Deuterium Uranium reactor (CANDU)] and, to a limited extent, in light water reactors. Industrial practices have changed at the front end of the fuel cycle, resulting in high-purity uranium-bearing products. Consequently, IAEA safeguards practices must remain current with technology developments and industrial practices in order to ensure safeguards are operating with efficacy. With the ambiguous technical interpretation of INFCIRC/153 (Corrected) paragraph 34(c), the IAEA has been inconsistent in the implementation of safeguards at NUCPs. Traditionally, states have only been bound by comprehensive IAEA safeguards under INFCIRC/153, beginning with the end product of NUCPs [15]. As such, the IAEA has limited access to early fuel cycle activities, which would fall under the scope of the Model Additional Protocol (AP) for subscribing states (INFCIRC/540), limiting IAEA monitoring capabilities [16]. Thus, the declared final product (UF_6 or UO_2) from an NUCP was the starting point for safeguards accountability, with no assurance or accountability metrics for any undeclared production.

The new approach to safeguarding NUCP intermediate compounds was first outlined by *Doo et al.* in reference to INFCIRC/153 (Corrected) paragraph 34(c), when it was

first stated that the IAEA considers all purified aqueous uranium solutions or uranium oxides suitable for isotopic enrichment or fuel fabrication as products as candidates for safeguards under 34(c) [14] [15]. Paragraph 34 (c) of INFCIRC/153 (Corrected) reads [1] [15] as follows:

> (a) When any material containing uranium or thorium which has not reached the stage of the nuclear fuel cycle described in sub-paragraph (c) below is directly or indirectly exported to a non-nuclear-weapon State, the State shall inform the Agency of its quantity, composition and destination, unless the material is exported for specifically non-nuclear purposes;
>
> (b) When any material containing uranium or thorium which has not reached the stage of the nuclear fuel cycle described in sub-paragraph (c) below is imported, the State shall inform the Agency of its quantity and composition, unless the material is imported for specifically non-nuclear purposes; and
>
> (c) When any nuclear material of a composition and purity suitable for fuel fabrication or for being isotopically enriched leaves the plant or the process stage in which it has been produced, or when such nuclear material, or any other nuclear material produced at a later stage in the nuclear fuel cycle, is imported into the State, the nuclear material shall become subject to the other safeguards procedures specified in the Agreement.

Under the revised interpretation, Doo *et al.* highlight that "full safeguards procedures should be applied no later than the first point in the conversion process at which such material leaves the process stage or the plant in which it is produced" [14]. This was later codified in 2003 in PP18, "Safeguards Measures Applicable in Conversion Plants Processing Natural Uranium," stating that the point for nuclear material under safeguards was reinterpreted, and a new definition of source material in this category was introduced [1].

Under IAEA PP18, the IAEA suggests that these purified uranium compounds should be subject to safeguards procedures no later than the first point in the conversion process. Before the issue of this policy, only the final products of the uranium conversion plant were considered to be of a composition and purity suitable for fuel fabrication or for being isotopically enriched and, therefore, subject to all the safeguards procedures described in the safeguards agreements. The IAEA now considers that the UN solution meets the above requirement, and if there are no procedures to account for this material in a particular facility, the full safeguards procedures should be extended upstream in the process. Further points addressed in PP18 to support advancing the starting point of safeguards include (1) a new definition of source material, which potentially brings yellowcake under safeguards; (2) new requirements for design information verification (DIV) and provision; and (3) use of a complementary access-type concept [1] [17] [18].

The IAEA's Standing Advisory Group on Safeguards Implementation (SAGSI) was formed to address the issue of UOC materials meeting 34(C) criteria. Recent work by the SAGSI has begun to more concretely define where safeguards should start in the conversion process, as conversion plants in some states produce high-purity uranium oxides that meet nuclear industry standards, such as those of the American Society for

Testing and Materials (ASTM) [19] [20]. SAGSI's analysis and recommendations of where safeguards should be applied in the fuel cycle and in conversion facilities are provided in *Appendix B.* SAGSI advised that measures should be determined on a state-by-state basis, taking into account safeguards by design (SBD), integrated safeguards, and state-level concept activities [21].

3.2 Legal Context and State-Level Concepts

As noted by SAGSI, a variety of technical and strategic implementation challenges exist in response to implementing PP18. This analysis extends into a comprehensive assessment of the motivations, impacts, and effectiveness of such safeguards efforts on the overall nonproliferation regime. The recommendations made under PP18 must further be extrapolated for states with Comprehensive Safeguards Agreements (CSA) in effect under INFCIRC/153 [15] versus states with CA under the AP in effect under INFCIRC/540 [16]. Based on the INFCIS, approximately 25% of the global conversion capacity lies in NNWS [3].

3.2.1 Case Study for States with Complementary Access: Canada

From the NNWS with conversion facilities, almost all the conversion capacity (~37 kt HM/yr.) is produced in Canada, which has ratified the AP [3] [22]. Canada represents a case study for a state with CA in effect that was successfully able to implement the requirements under PP18 [23] [24]. From 2003 to 2005, Canada was able to bring two of the world's largest conversion facilities – Port Hope and Cameco Blind River – into compliance with PP18. In PP18, the primary recommended measurement point was the UN stream exiting solvent extraction, which the Canadians noted was a well-measured point by the operator for sampling. However, due to the intermixing of unsafeguarded recycle streams, this point prove to be an unacceptable

point for PM, as safeguarded and unsafeguarded material were intermixing. Flexibility among the IAEA, Canadian regulatory authorities, and the operators was instrumental in eventually establishing the two facilities, each as a single material balance area (MBA) to meet PP18 requirements.

Two key challenges were faced by the Canadians in bringing their conversion facilities into compliance with the requirements under PP18: First, the Canadians noted that it was difficult to implement safeguards in facilities with throughput that were built prior to safeguards implementation, thus lacking an integrated safeguards design. Second, a sizeable effort was required to characterize the large inventory of historical waste, as well as to account for the large difference in their inventory, which is a natural result of large-scale chemical operations. This latter statement was similarly echoed by the Brazilians, who are non-signatories of the AP, during the joint study between DOE and Brazilian Nuclear Energy Commission (CNEN) [25].

3.2.2 Case Study for States without Complementary Access: Brazil and Argentina

Brazil and Argentina hold the minority remainder of the world's NNWS conversion capacity (~357 kt HM/yr.) [3]. For Argentina and its Brazilian regional counterpart in the Brazilian Argentine Agency for Accounting and Control of Nuclear Materials (ABACC), the starting points of safeguards and the requirements for any changes of this definition have been legally outlined in the Quadripartite Agreement [17] [18]. Both parties of the Quadripartite Agreement are not signatories to the AP [22], and both ascertain that the recommendations under PP18 are beyond the legal framework and requirements of the Quadripartite. Beyond legal precedence, challenges cited by the Quadripartite echo the challenges aforementioned by the Canadians. Like the

Canadians, the Quadripartite parties also identified waste management optimization and process recycling as being limited under PP18. The Quadripartite also challenges the use of CA echoed in PP18, as neither enforce the AP, which also permits CA. Ultimately, ABACC feels that the new safeguards recommendations would require additional effort by all stakeholders "without having profitable return" [17]. Instead of legally binding the recommendations under PP18, the Quadripartite recommends the use of mail-box declarations by the operator on a weekly basis, noninvasive containment and surveillance (CS) measures as a deterrent for misuse, and the use of short notice random inspections (SNRI) [17].

Based on these case studies, it seems that implementing recommendations under PP18 are more intuitive to states with the AP in force, as seen with Canada. Having prepared for the requirements of complying with the CA requirements of INFCIRC/540, which extend to facilities beyond those in INFCIRC/153, states with this requirement are more readily compliant and equipped to address changes in interpretation of 34c materials. However, regional bilateral politics have contributed to the rationale behind why the Quadripartite has not signed the AP, and thus feels that there is no legal precedence under PP18 to implement the recommendations. However, recommendations were made by ABACC on how safeguards could be improved in a non-binding manner for existing facilities, in order to comply with the broader safeguards concerns regarding front-end monitoring. These case studies represent the successes of and obstacles facing existing conversion facilities in NNWS. However, the implementation of PP18 in new facilities gives rise to implementation using safeguards-by-design (SBD) principles, which may potentially alleviate some of the identified obstacles and challenges.

3.3 Integrating Safeguards by Design

The challenge of meeting the recommendations of PP18 involved retrofitting existing conversion facilities that were not originally designed in the purview of safeguards activities. The emergence of SBD becomes especially pertinent in the implementation of safeguards in future conversion facilities. SBD is defined as the "approach wherein international safeguards are fully integrated into the design process of a nuclear facility—from initial planning through design, construction, operation and decommissioning" [26]. The IAEA further identifies three critical enablers for implementation of SBD: (1) defining the requirements and acceptance criteria for the design and SBD processes; (2) developing the design process for SBD based on interactions and agreements amongst all stakeholders; and (3) motivating all stakeholders to apply SBD [26].

In the case of NUCPs, SBD must address providing adequate measures for either limiting diversion pathways from declared feed or detecting the processing of undeclared/substituted feed to produce undeclared purified uranium products. Conversion facilities are essentially large complex chemical facilities containing interconnecting pipework, tanks, vessels of uranic and non-uranic chemicals, and recycle loops. For existing facilities, diversion can occur in an infinite number of ways but can be mitigated using SBD through optimizing DIV and process design for physical inventory verification (PIV), as well as establishing MBAs for PM at sample/flow measurement points in conjunction with CS [9]. In the purview of the latter case study, Brazil is undertaking the construction of a new the pilot plant in Sorocaba [27]. SBD may mitigate some of the aforementioned challenges – both legal and technical – in implementing front-end safeguards in such new conversion facility builds. In essence, the design basis of any new conversion facility will directly impact the burden for providing DIV or developing a nuclear MC&A system. Integration of

consultative DIV and accommodating MC&A in SBD can consequently lead to a more efficient and cost-effective safeguards regime in new conversion facilities.

3.4 Safeguards System Requirements

From a technical perspective, a safeguards system for monitoring processes and facilities producing 34(c) material would require the following capabilities [28] [29]:

- verify production and shipments of 34(c) source material;
- detect excess production of 34(c) source material; and
- support detection of undeclared both within the state and auxiliary activities in other states.

CHAPTER 4. RELATED WORK ON SAFEGUARDING URANIUM CONVERSION FACILITIES

In response to the issuance of IAEA PP 18, DOE has become interested in developing instruments, tools, strategies, and methods that could be used by the IAEA in the application of safeguards for materials in the front end of the nuclear fuel cycle, prior to production of UF_6 [2]. Previous work has investigated monitoring locations using conventional, non-NDA instrumentation for an NUCP.

4.1 Previous Approaches to Safeguarding Conversion Facilities

This work started with Doo *et al.* at the IAEA in 2003, which proposed the first mass-balance measurement points for operations monitoring at NUCPs [14]. Since then, several DOE national laboratories have become involved in developing tools or techniques for safeguarding conversion plants. In 2004, Elayat *et al.* at Lawrence Livermore National Laboratory (LLNL) developed a system of analysis of safeguards effectiveness in conversion plants using digraph and fault tree analysis [30]. The digraph and fault tree analysis assessed the deviation of input parameters required to indicate diversion and how the same safeguards system could deviate from the base case. This simulation involved employing decision-making based on input inspector verification of material declaration and on the output probability of diversion success. The statistical analysis was based on mass difference and material unaccounted for (MUF) indicators, proposing various scenarios of gross, partial, and bias defects. Although statistical methods have been recently investigated theoretically through the development of generic error models by Burr *et al.* [31], no PM data specific to NUCPs have been experimentally tested for verification or diversion operations at an NUCP.

An overall safeguards approach was proposed in 2004 by Boyer *et al.*, who suggested the use of unattended PM equipment to measure flows of uranium through unit processes [2]. Boyer states that traditional CS could provide some detection capability, but the IAEA has revised its approach for NUCP safeguards to rely on SNRIs to permit more flexibility and unpredictability in conducting inspections [2]. Ideally, a continuous presence or continued monitoring of unattended monitoring systems by IAEA inspectors would be effective for detecting the processing of undeclared materials in an NUCP; however, resource shortages require that more innovative approaches be employed. Boyer recommends that the use of unattended PM equipment would suffice or that the facility operator could make daily "Mailbox" declarations of nuclear material quantities and operating parameters on a periodic basis. Boyer states that resources should be allocated according to the following criteria [2]: (1) unattended monitoring instruments to monitor uranium content flow and (2) generation of PM data that will enable the inspector to determine if undeclared feed or misuse is occurring. As per IAEA guidelines, the safeguards goal of 1 SQ of natural uranium over a period of 1 year must be within a detection probability of 50%. Boyer describes this detection probability (P_D) as [2]

$$(P_D) = (P_S) \times (P_R) \times (P_P) , \qquad [4\text{-}1]$$

where
(P_S): probability that a falsified item is selected for verification measurement,
(P_R): probability that measured falsified item is identified as falsified, and
(P_P): probability based on operator's falsification strategy, residence time (duration over which diversion would occur), and number of SNRIs.

Nusbaum *et al.* further ascertain that although the IAEA prescribed limit is 1 SQ of 10 MTU/year, a rogue diverter with a clandestine enrichment capability requires only 5 MTU to produce 1 SQ (25 kg U) of highly enriched uranium (HEU) [32].

4.2 Previous Technology Development for Process Monitoring in Uranium Conversion Facilities

Work at ORNL began in 2004, when Faulkner *et al.* investigated material balance approaches to safeguards through preliminary research at the ORNL UNCLE facility [11]. In addition, the FLOW simulation platform was developed to simulate generic conversion plants of various throughputs. It was limited to mass balance, not energy balance or source term analysis. At ORNL, international safeguards approaches for NUCPs were addressed by Raffo-Caiado *et al.* in conjunction with the Brazilian Nuclear Energy Commission in 2009 [33]. This work proposed to establish a technical basis for NUCP safeguards, primarily outlining process modeling and configuration, from which the proposed material balance points in Faulkner *et al.* were integrated into IAEA-focused monitoring and verification activities. However, that report only loosely addressed NDA radiation detection technologies by proposing technologies that may be fruitful for safeguards purposes but were never simulated, implemented, or evaluated for verification monitoring or diversion purposes.

More recently, Pickrell *et al.* and Ladd-Lively *et al.* have benchmarked a Coriolis flow rate meter in addition to testing the 20-array ^{3}He tube clamp neutron detector developed at Los Alamos National Laboratory (LANL) (now installed at the ORNL UNCLE facility), originally tested at the Springfields NUCP in the United Kingdom [34] [35]. Equipment calibration of the ^{3}He detector was later completed by Ladd-Lively at the UNCLE facility [6] [36] [37] [38] [39]. Operations monitoring at the UNCLE facility have been preliminarily analyzed by Lee, employing the second-generation Transverse Uranium Neutron Detector (TUrND) developed by LANL, based on the first-generation design by Miller and Pickrell in 2004 [40] [34] [41]. Neutron monitoring efforts have not met performance specifications, nor have they been analyzed for drawing conclusive safeguards conclusions with respect to the 1 SQ

requirement by the IAEA [42] [43] [44]. Employing neutron detection does not meet performance specifications due to ^{3}He shortages in addition to the inability to distinguish (α,n) interactions in nitrogen and oxygen in the UN solution, and cosmic-ray-induced spallation neutrons in an outdoor operational environment. This results in poor signal-to-noise discrimination using such principles. With the ^{3}He shortage and the associated high costs of development, employing commercially available gamma-ray detectors in this study provides an ideal opportunity to test alternatives to ^{3}He technology and neutron detection.

Ladd-Lively has proposed multivariate statistical methods involving singular value decomposition to develop a framework to detect the diversion of intermediate products at an NUCP using only material-balance points [45]. Nuclear source term and radiation detector responses have not been evaluated for statistical determination of diversion. According to Boyer *et al.,* the verification of declared material based on material balance alone is insufficient to detect undeclared production or diversion of material in larger NUCPs [2]. Thus additional safeguards measures are necessary to detect undeclared processing. This dissertation work builds upon this recommendation by addressing how detection techniques and low-cost distributed PM technologies can be used to create an effective safeguards system that is operational and verifiable.

4.3 Proposed Monitoring Points

Optimal locations for PM in an NUCP have been discussed by Doo, Boyer, and Faulkner in detail [2] [11] [14]; however, none of the proposed methods or key measurement points (KMPs) has been tested operationally, nor have the limits of instrumentation capability been ascertained for providing a technical basis for drawing

safeguards conclusions. The placement of KMPs should take into account the following factors [28] [29]:

- measurement of in-process material during PIV;
- interconnecting arrays of piping;
- internal recycle streams;
- storage fluctuations within the facility;
- access to measurement points;
- potential diversion routes; and
- processing undeclared feed.

For a small NUCPs, Boyer has suggested that the following three monitoring points should suffice for PM *(Figure 4-1)* [2].

1) Output of dissolver tank at 400–450g U/L to acquire a measurement of feed material.
2) Where purified uranium becomes available, at the solvent extraction output columns at a concentration of 80–100g U/L. A K-edge or L_{III}-edge densitometer and flowmeter could be installed to measure uranium concentration and volumetric flow, respectively. Spectrometry-based instrumentation may be suitable for this monitoring point.
3) Prior to withdrawal of UF_6 into cylinders, to provide an indication of product produced. CS in addition to load-cell-based weighing systems would be sufficient monitoring.

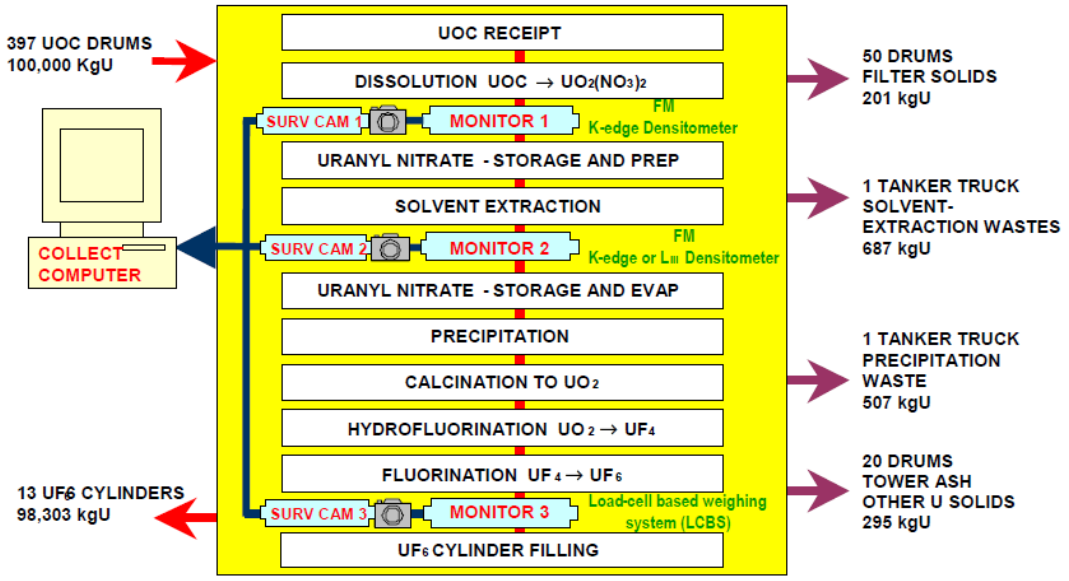

Figure 4-1. NUCP Process Diagram with Proposed Safeguards Instrumentation.

Reproduced from Boyer et al. [2].

Although simple accounting using input/output traditional mass balance would provide some assurance through PM, the use of unattended monitoring would validate accountability and improve safeguards assurances. Eight such KMPs were recommended by Faulkner *et al.* in *Table 4-1* (corresponding to points depicted in *Figure 4-2*) and safeguards systems recommended by Loden and Begovich [29], also integrated in *Table 4-1*. These monitoring points provide a high probability of detecting diversion for small- and medium-sized NUCPs, and the probability for high-throughput plants can be remedied if attention is placed on monitoring waste stream materials.

The recommended measurement techniques for each KMP are drawn from the recommendations and requirements outlined in the *IAEA Safeguards Techniques and Equipment: 2011 Edition* [46]. These techniques include [25] (1) nondestructive analysis (NDA), (2) destructive analysis (DA), (3) containment and surveillance (CS),

(4) unattended monitoring, (5) attended monitoring, (6) remote monitoring, (7) data security, and (8) environmental sampling.

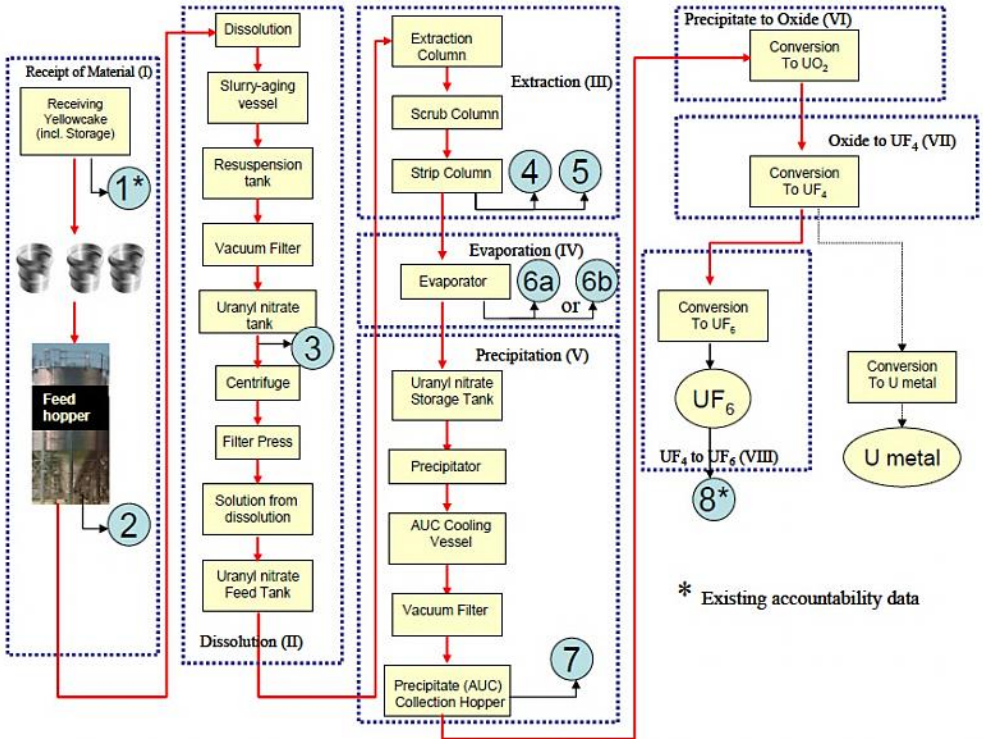

Figure 4-2. Recommended Material Balance Locations for Uranium Conversion Process.

Reproduced from Faulkner et al. [11].

Table 4-1. Monitoring Points Suggested from ORNL Studies.

Monitoring Point	Location	Justification	Safeguards System	Brazilian NUCP (MTU/yr.)
1	Yellowcake feed entering NUCP for processing.	Record of uranium entering plant (required).	Grab samples taken for destructive analysis (DA)	500
2	Solid yellowcake fed from hopper to dissolver.	Independent verification of yellowcake entering. Prevents introducing "unaccounted" material that can be diverted before next monitoring point.	NDA measurement of U in drum.	500
3	Unpurified uranyl nitrate solution exiting tank downstream of dissolver.	First analysis of uranium dissolved from yellowcake; helps prevent diversion of dissolved uranium or misuse of equipment to process unaccounted uranium.	Solid mass flow rate using gravimetric techniques combined with analysis of U content (Point 1) or destructive analysis (Point 2).	498.9
4	"Stripped" organic stream exiting strip column for solvent extraction.	Prevents inefficient stripping and possible diversion of uranium away from main uranium path through solvent recycle/disposal.	In-line monitoring of U concentration, pH, density, conductivity, temperature, and flow rate.	3.4
5	Purified uranyl nitrate solution exiting strip column after solvent extraction.	Mass balance check after purification of uranium (attractive diversion point).	In-line monitoring of U concentration, density, temperature, and flow rate.	495
6 a or b	Concentrated purified aqueous uranyl nitrate solution exiting evaporator: (a) In the line exiting evaporator before passing through valves or equipment; or (b) before the cooler leading to storage tank.	Another attractive diversion point. Each valve provides another opportunity for diversion. Monitor right out of evaporator, or downstream of reflux leg back into evaporator and before cooler leading into storage tank.	In-line monitoring of U concentration, pH, density, conductivity, temperature, and flow rate.	495
7	First purified dry solid uranium (AUC or UO_3) precipitating/ denitrating.	Verifies uranium dissolved and purified, preventing diversion during precipitation/denitration. Sometimes collected in drums for transport to next step (traditional accountability using CS and NDA to estimate U content).	In-line monitoring of U concentration, pH, density, conductivity, temperature, and flow rate.	490.2
8	UF_6 collected in cylinders	Provides product output value for mass balance analysis. Inventory of uranium output plus waste streams should match input uranium value. Point for mass balance (required).	Accounting with grab samples taken for destructive analysis and mass rate on total U produced.	488.4

Data from [11] [25] [28].

LaMont *et al.* developed a conceptual approach for the use of chemical and isotopic tracers as part of an improved safeguards approach at NUCPs, where the latter would be advantageous in verifying declarations in waste streams and MUF [47]. Chemical tracers would be useful for UOC products prior to dissolution (where they would be stripped) in order to verify that undeclared UOC batches were not introduced. As NDA techniques are a standard complement to IAEA methods and technologies employed, these approaches are investigated herein.

4.4 UNCLE Facility at ORNL

The completion of a field trial of safeguards monitoring equipment by Ladd-Lively *et al.* at the Springfields NUCP demonstrated the need for a facility to perform full-scale equipment testing under controlled conditions prior to field deployment of safeguards systems at additional plants [34] [35]. UNCLE serves as a calibration facility for safeguards monitoring instrumentation (e.g., flowmeters, density probes, neutron detectors) and as a test facility for simulation of diversion of UN products in NUCPs. This unique facility within the US DOE is designed to simulate the operating conditions for a purified uranium-bearing aqueous stream exiting a solvent extraction process conducted in an NUCP operating up to 6000 MTU/year throughput [40]. The UNCLE facility represents a test bed of monitoring points 4 and 5 in Faulkner's monitoring scheme in *Figure 4-2* [11]. Monitoring instruments, including the neutron detector and the second-generation TUrND, both developed at LANL, and the Endress+Hauser Promass 83F Coriolis flowmeter, are currently installed at the UNCLE facility. The UN solution circulating in UNCLE contains decay products that are more than 40 years old, dating back to approximately 1968, and was produced from ground fuel pellets (see Chapter 5). This facility, which was modeled based on the design specifications of the Springfields conversion facility, now decommissioned in the United Kingdom, circulates UN of near-natural uranium compositions. A photo of UNCLE is shown in *Figure 4-3*, and schematics with design specifications of UNCLE are provided in *Appendix C*.

Figure 4-3. UNCLE Facility with First-Generation TUrND Neutron Detector.

Reproduced from [36].

As shown in Figure 4-3, Tanks A and B represent sources of holdup, as well as a source of changing background in UNCLE. Preliminary work regarding the source term and age effects modeling of the UN in UNCLE, simulated detector responses to the UN-filled pipe, and validated experimental measurements were conducted by Dewji *et al.* [48] [49], [50] in accordance with the scope of this dissertation .

4.5 Challenges for Developing a Safeguards System

An objective of a rogue diverter would be employing NUCP equipment to process undeclared feed for a weapons program with diversion of intermediary products prior to any KMPs. Specific categories of diversion must be identified before an adequate strategy can be applied to meet safeguards objectives of (1) detecting the processing of undeclared feed and (2) verifying that declared feed is not being diverted [2]. The categories of concealment of diversion are described as follows [11] [32].

- **Introduction of undeclared feed:** Substitution of feed materials with higher-than-declared uranium content. This can be accomplished by introducing undeclared UOC into the dissolution vessel or during recycle processing.
- **Material substitution:** Material could be substituted with higher concentrations or enrichments. Uranium concentration is either understated in the product/feed streams or overstated in the waste stream. In either case, the uranium quantity is understated in accounting procedures. The substitution of dummy product materials with similar characteristics but no uranium content is also consistent with such activities.
- **Equipment alteration:** Operating procedures and/or equipment configurations are modified to alter the physical uranium output quantity through diversion earlier in the process or through unreported activities. This is also manifested through the installation of valves or bypasses to syphon material, or the modification of equipment to produce excess uranium in the waste/tails. This would manipulate the declared amounts of uranium in the MUF.
- **Falsification of records and/or data tampering:** Material balance records are adjusted, such as understating throughput, or incorrectly recorded to reinforce diversion activities.

Accountability systems, enhanced by conventional surveillance methods, provide some capability measures for detecting diversion. Unattended monitors based on NDA detection systems would provide real-time accountability information, thus making diversion a more arduous undertaking. Effective monitoring to enhance diversion detection requires combining accountability principles with unattended

monitors. Optimization of such a system would supersede the verification of accountability data with the assistance of inline PM systems, comprising both conventional and radiation detection instrumentation.

CHAPTER 5. INSTRUMENTATION AND METHODS

Assessing the use of NDA instrumentation for PM of UN in transfer pipes of NUCPs entails theoretical, simulation, and experimental methods to investigate the viability of gamma-ray methods for safeguards applications.

The theoretical basis is described in Chapter 6, with a source term analysis of the UN circulating in UNCLE. Since the UNCLE employs 40-year-old UN with decay products, which varies from freshly solvent extracted commercial UN, the source term analysis evaluates the subsequent age effects on potential measurement signatures. Based on the emission properties of the UN, the attenuation analysis detailed in Chapter 7 of the UN-filled Schedule 40 304L pipe determines the transmission of signatures of photon emissions in this detection geometry. In addition, investigation of potential transmission sources for densitometry measurements correlating uranium concentration was conducted. Finally, an analytical model of a self-attenuation correction factor is investigated as a way to determine the effects of self-attenuation on detection efficiency. This analysis also sets up the framework for distinguishing changes in attenuation (self, piping) with changes in material properties (enrichment, concentration, density) with respect to the peak efficiencies of the monitoring signature emissions.

Experimental measurements were conducted in two settings: The first measurements were taken in a low background environment, where the sensitivities in detector responses are determined for concentrations of UN diluted from 90g U/L to 10g U/L. These are described in Chapter 9. Dilution measurements were taken for each of the selected gamma-ray detectors with a UN-filled pipe segment. This pipe segment was created from the same Schedule 40 304L pipe used in UNCLE, which was chosen to mimic the Springfields NUCP in the UK. The source UN at 90g U/L was obtained from UNCLE for the dilution experiments. Passive measurements of ^{235}U emissions are

conducted for dilution concentrations to determine monitoring signatures. Transmission source measurements were also conducted to determine the densitometry source sensitivity to uranium content and UN density for sample dilution concentrations. Finally, spatial offset measurements are taken vis-à-vis the central detection axis to determine spatial effects on detection efficiency for a pipe containing 90g U/L solution. This is important in assessing variation due to reproducibility and control of the geometry.

Chapter 10 describes further experimental measurements conducted at UNCLE to determine detector responses in an operational environment. Steady-state measurements are taken at a two flowrate values, which mimics the throughput at the Springfields' NUCP. Shadowshield measurements are also taken at UNCLE to determine the leakage into the collimator from adjacent UN-filled transfer pipes and tanks.

Simulations were conducted using Monte Carlo photon transport codes, as explained in Chapters 8 and 11, to determine the pulse height detector response for high-intensity ^{235}U emissions from the UN-filled pipe configuration employed in the dilution experiments. Comparing dilution measurement data with the constructed Monte Carlo models, the intrinsic detection efficiency was determined for a high-resolution detector system. Subsequently, various transmission sources were tested to determine the optimal gamma-ray source for UN densitometry and sensitivity to uranium content in UN.

Finally, a comprehensive statistical and sensitivity analysis is summarized in Chapter 12. Estimates of the optimal counting time for each of the tested gamma-ray detectors to meet a 5% and 10% uncertainty threshold due to Gaussian count-rate statistics are provided. The sensitivity analysis provides insights regarding how variables, such as pipe thickness, material properties, and source-detector geometry, affect the overall detection efficiency of the assayed ^{235}U signatures. The analysis provides a benchmark from which performance can be reliably scaled to other conditions. Monte Carlo models were created

to determine the particle flux of signature ^{235}U emissions traversing each shielding boundary. Ray-tracing simulations were modeled to determine the peak efficiencies for the specific source-detector geometries. This geometry-specific efficiency calibration is applied to spectra acquired in the dilution and UNCLE measurement spectra to determine the mass and activity of ^{235}U in the UN-filled pipe segment. The ray-tracing simulations were also employed to determine how variations of specific absorber thicknesses and source-detector locations affect the signature peak efficiencies. Ray tracing is more rapid than Monte Carlo but provides only full energy peak efficiency scaling, rather than the full pulse height distribution. Furthermore, Monte Carlo simulations are employed to determine how changes in material properties affect the detection efficiency of ^{235}U signature peak emissions in UN.

Harnessing all the passive and densitometry gamma-ray measurement data with the effects of the statistical, absorber, geometry, and source material variations determines whether IAEA guidelines can be met to detect diversion of 1 SQ of 10 MTU/yr. with a 50% probability. As the UN concentration increases, ^{235}U assay emissions are expected to increase; however, as the ^{235}U content increases, so does the solution density and hence self-attenuation, counteracting an otherwise proportional relationship. This discussion of assessing whether the tested detectors can acquire statistically relevant data in a timely way is discussed in Chapter 13. Whether in-line transmission source can monitor the UN concentration independently is further discussed.

5.1 Source Term Analysis

As UNCLE employs UN from uranium that is 40 years old, a source term analysis is required to determine aged-based signatures changes vis-à-vis freshly solvent-extracted UN in NUCPs. This is accomplished through harnessing the program, RadSrc [51], which solves the Bateman equations to determine age effects of fresh (0 years) and aged

(~1 year, secular equilibrium) uranium in the UN source term for various concentrations (10, 50, 75, 85, 90 g U/L). In conjunction with Sources4C [52], gamma-ray and neutron radiation emissions are calculated for the UN source term, in order to characterize the radiation signatures of UN.

5.1.1 Solution Preparation of Uranyl Nitrate in UNCLE

A variety of intermediary uranium compounds are connected with the conversion process. UNCLE was designed to reproduce the conditions of the purified aqueous UN stream exiting the solvent extraction process in an NUCP. The scope of this project is focused on this specific phase of the conversion process containing purified aqueous UN. Traditionally, UN salt is a water-soluble yellow salt that forms uranyl nitrate hexahydrate in water. Uranyl nitrate is soluble in water up to ~660g/L at 20^{o}C [53].

The UN (molecular formula $UO_2(NO_3)_2$) for UNCLE was prepared in 2004 using UN acid-deficient solution in a two-step process [54]: First, UO_2 pellets were oxidized to U_3O_8 powder in air at 450°C. Second, the U_3O_8 was dissolved using concentrated nitric acid in several batches. The resulting stock solution had a pH of 1.65 and uranium concentration of 630 g/L.

$$U_3O_8 + 6HNO_3 \rightarrow 3UO_2(NO_3)_2 + 2NO_2 + 4H_2O. \qquad [5\text{-}1]$$

Preparation using acid-deficient UN was conducted because the lower acid concentration led to a quicker precipitation reaction, resulting in a stock solution with a NO_3/U mole ratio of 1.53. The stock solution was diluted with water from 630 g U/L to 90 g U/L.

The UN solution circulating through the UNCLE facility contains 90 g of naturally enriched uranium dissolved per liter of water, with a measured solution density of

1.122 g/cm^3 at 20^{o}C. The elemental solution composition was calculated stoichiometrically for a 1 L (= 1000 cm^3) volume of natural uranium-bearing UN with the density and concentration of UNCLE. These properties are summarized in Table 5-1.

Table 5-1. Uranyl Nitrate Composition in 1 L (1000 cm^3) Volume of UNCLE Solution.

Element	Molar Mass (g/mol)	Weight Fraction	Mass (g)	Isotope	Isotopic Weight Fraction (per g Element)	Isotope Mass (g)
U	238.03	0.080	90.00	^{234}U ^{235}U ^{238}U	0.0059% 0.76% 99.2%	89.31 0.68 0.01
N	14.01	0.007	7.94	Nat.		
O	16.00	0.815	914.64	Nat.		
H	1.01	0.098	109.42	Nat.		
TOTAL	364.90		1122.0			

5.1.2 Radiation Signatures for Assaying Uranyl Nitrate

From an NDA-monitoring perspective, two radiation decay modes are of potential interest: (1) gamma-ray production due to radioactive decay of natural uranium and (2) neutron production from spontaneous fission, (α,n) and cosmic-ray interactions in the UN solution. To assess the radiation signature from the UN in the UNCLE facility, the decay properties of the daughter products of the dissolved uranium must be assessed as a function of time.

Two primary decay series ensue from the decay of ^{235}U and ^{238}U in natural uranium, via the actinium and radium (uranium) series, respectively. These series are summarized in Figure 5-1. As decay time progresses, the varying half-lives of daughter products cause the decay product quantities to change. As secular equilibrium in natural uranium (between ^{238}U and ^{234}U specifically) is reached, where the half-life of the daughter product is smaller than that of the parent, the concentration of such daughter isotopes will

reach a near-constant ratio over time. As shown in Figure 5-1, decay chains can branch into more than one excited daughter product, resulting in more than one pathway for gamma-ray emission. As such, there are 30 possible decay paths from ^{238}U to ^{206}Pb, where the probability of a specific decay is quantified by its branching fraction [51].

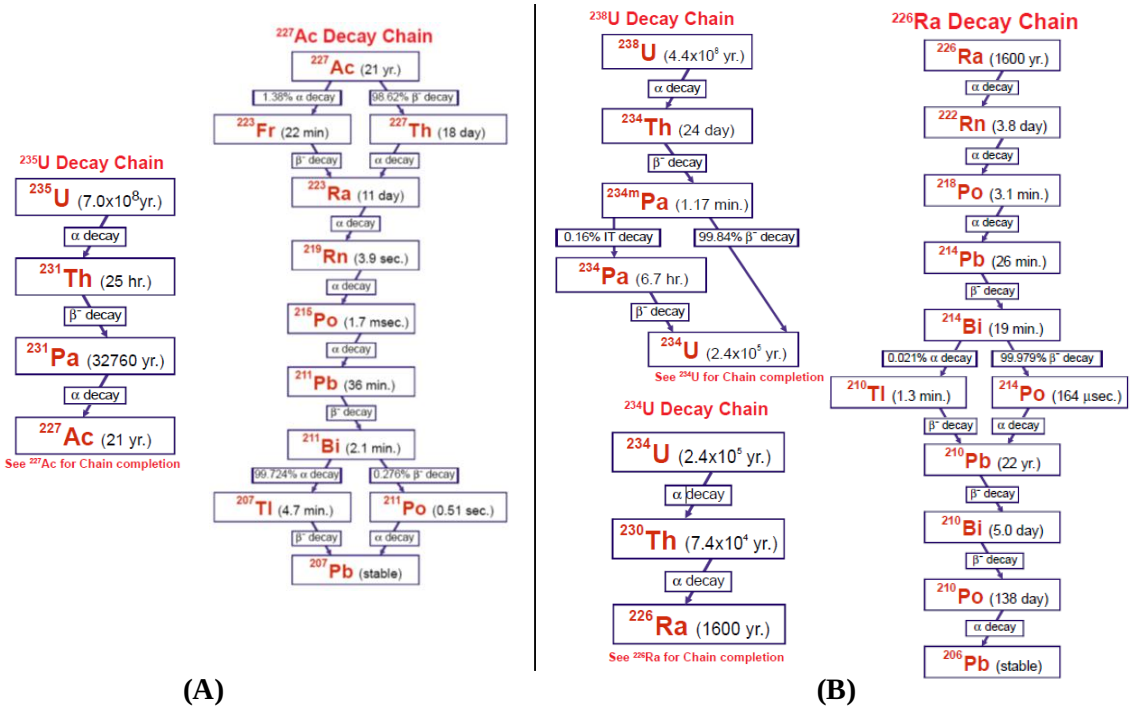

Figure 5-1. (A) Actinium and (B) Uranium Radioactive Decay Series for Natural Uranium.

Reproduced from [55].

The behavior of decay chains is governed by the Bateman equations, which describe the serial radioactive decay of a parent into multiple daughter products [56]. The Bateman equation reduces each individual decay scheme into an inherently recursive solution from which each decay chain can be represented as a linear system of differential equations for each decay pathway. Equations [5-2] and [5-3] describe the relationship between the concentration of parent nuclide (N_0) and first daughter product (N_1) as a function of time, *t*.

$$\frac{dN_0(t)}{dt} = \lambda_0 N_0(t) \qquad \text{and} \qquad [5\text{-}2]$$

$$\frac{dN_1(t)}{dt} = \lambda_0 N_0(t) - \lambda_1 N_1(t) \quad [5\text{-}3]$$

where
λ_0 = decay constant of parent nuclide and
λ_1 = decay constant of daughter nuclide.

The UN solution circulating in UNCLE contains decay products over 40 years old, dating back to approximately 1968. Aged UN is atypical for commercially produced UN, which is freshly processed following solvent extraction during conversion. Solvent extraction was not available to process the UN in UNCLE. Thus, the following section focuses on identifying radiation signatures for freshly processed and aged UN, specific to gamma-ray responses as a function of decay time. By comparing signatures of the aged with freshly processed UN, we can focus on characterizing the signatures associated with freshly processed UN. Results of signature identification and age effects are explored in Chapter 6.

5.1.3 Age Effects of Decay Products in UN

Accounting for the aged UN employed in UNCLE vis-à-vis freshly processed UN in conversion facilities, the predominant photon sources maintained a relatively constant emission rate as a function of time within a year. As secular equilibrium in natural uranium (between ^{238}U and ^{234m}Pa specifically) is reached, where the half-life of the daughter product is smaller than that of the parent, the concentration of such daughter isotopes will reach a near-constant ratio over time, given in Equation 5-4 and shown in Figure 5-2 [57]. In this decay chain, ^{238}U (half-life 4.47×10^9 y) decays via α-emission to ^{234}Th (half-life 24.10 d), which subsequently decays via β- emission to ^{234m}Pa (half-life 1.17 m), where a signature 1001 keV photon is emitted with a probability of 0.837%.

$$A_{234mPa} \sim A_{234Th} = A_{238U}(1 - e^{-\lambda_{234Th}t}) \quad . \quad [5\text{-}4]$$

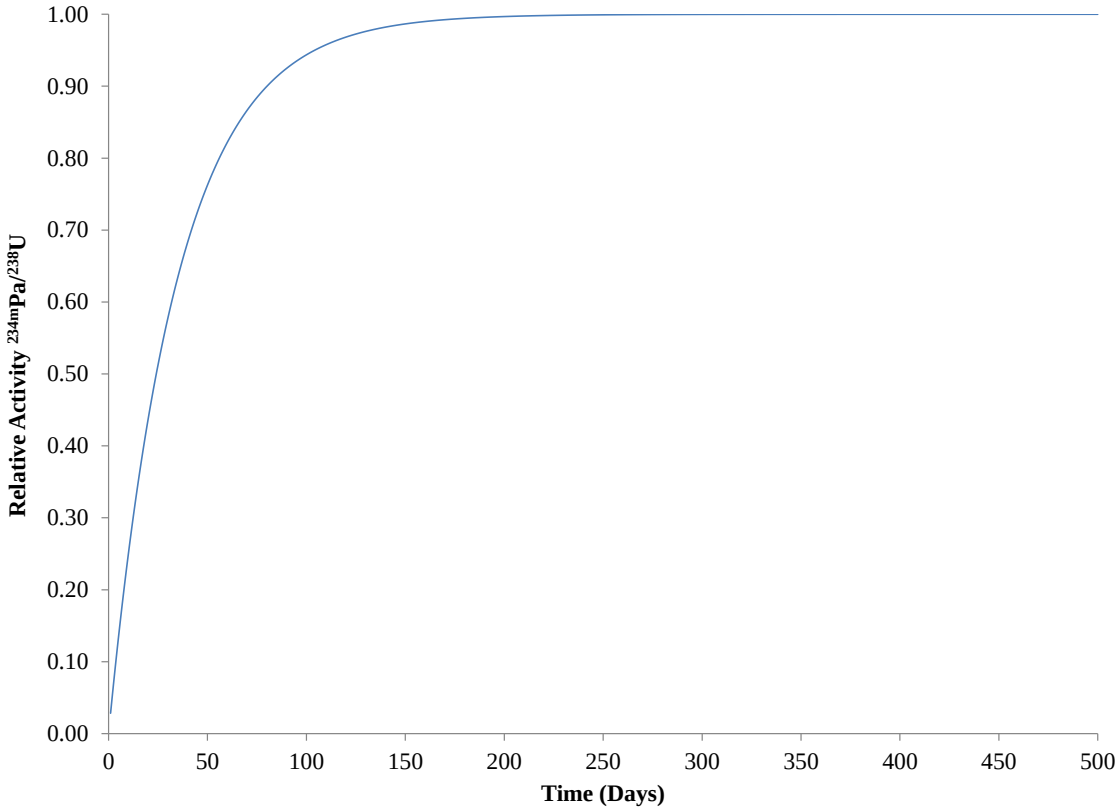

Figure 5-2. Secular Equilibrium of ^{234m}Pa in ^{238}U-Decay Chain.

Subsequently, as the UN in UNCLE is ~40 years old and in equilibrium, the UN from commercial conversion facilities cannot be assumed to be in equilibrium. As a result, the scope of this project assumes that secular equilibrium cannot be ensured, hence focusing on the direct ^{235}U-based assay signatures, though the other lines are available to measure experimentally in this special situation to add complementary information.

5.2 Attenuation Analysis

Monitoring ^{235}U gamma-ray emissions from freshly processed UN provides insights into the characteristics of the material flowing in conversion facilities. Identifying gamma-ray interactions occurring in the UN media flowing through pipes of an NUCP will help determine the probability of photon interactions to identify detection signatures for

verifying uranium presence, flow, concentration, and enrichment. First, attenuation and transmission calculations for uncollided particles in UN can be made using *XCOM: Photon Cross Sections Database* [58]. The mean free path (MFP) of the UN flowing in a pipe of an NUCP must be calculated in order to determine the fraction of the sample that will reach the detector uncollided. Also, use of external gamma-ray transmission sources can provide further insights regarding the density, concentration, and enrichment of UN. Finally, determination of the correction factor due to self-attenuation enables the observed signal, which is essentially proportional to the fraction of the signature photons emitted in the direction of the detector that actually reach the detector, to be placed on a common reference scale for qualitative comparison. Using the source term composition values for dilution concentrations, mass attenuation coefficient (MAC) values were calculated (without coherent scattering) for each of the dilution UN concentrations.

An ideal monitoring signature would be an intense, penetrating gamma ray ($>10^4$ gammas/g-s), with an energy of several MeV [59]. This is because between 1 and 5 MeV, the mass attenuation of all materials show a broad minimum (Figure 5-3); very few natural gamma rays exist above 1 MeV. In the purview of freshly purified UN, where decay products have been removed during solvent extraction, such gamma rays do not exist until secular equilibrium of ^{234m}Pa with ^{238}U occurs. In the scope of this work, the dominant gamma-ray signatures most suitable for assaying ^{235}U for solvent-extracted UN would be the 185.7 keV emissions.

5.2.1 Mass Attenuation Properties of Uranyl Nitrate

The probability of a photon interacting in a medium is characterized by the mass attenuation coefficient (MAC), μ (cm^2/g). In the range of ^{235}U high-intensity emissions (~100–200 keV), photoelectric effects are the predominant interactions, followed by Compton scattering. As photon energy increases, scattering interactions become the

predominant mode of interaction. Coherent (Raleigh/Thompson) scattering makes a minor contribution to MAC attenuation in high-resolution gamma-ray measurements by scattering the photon through the combined action of the atom. Coherent scattering results in elastic scattering of photons, yielding no net energy loss, conservation of momentum of the photon and the atom, and no ionization or excitation of the atom [60].

Transmission at full energy through a medium with the energy-dependent MAC (without coherent scattering) is the ratio of the transmitted (I) and incident (I_o) photons through an attenuating medium of thickness, x (cm), and density, ρ (g/cm^3), is governed by Equation 5-5 for narrow-beam (good) geometry.

$$T = \frac{I}{I_o} = e^{-\mu\rho x} \, . \qquad [5\text{-}5]$$

As shown in Figure 5-3, the attenuation behavior of elemental uranium, plutonium, californium, and lead are compared. Furthermore, the k-edge x-ray for uranium falls at 115.6 keV in Figure 5-3 [61].

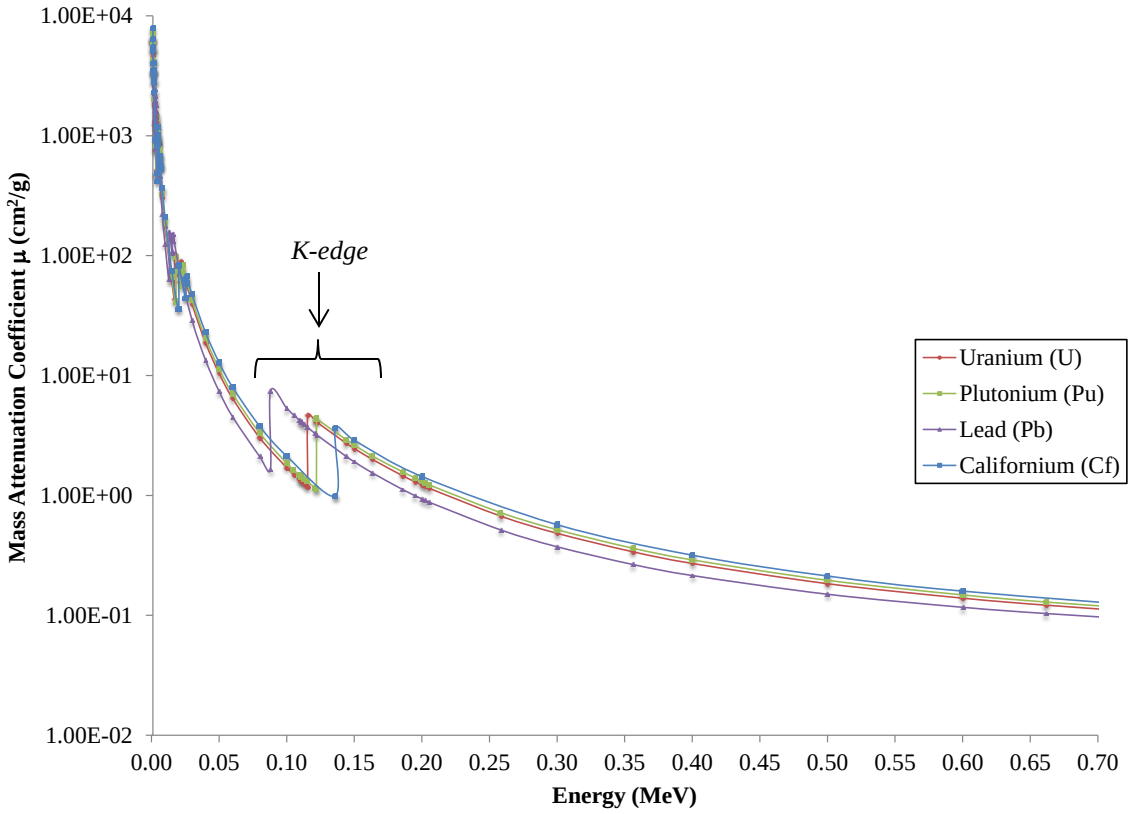

Figure 5-3: Total Mass Attenuation without Coherent Scattering of Uranium (Z=92) Compared with Plutonium (Z=94), Californium (Z=98), and Lead (Z=82).

Identification of the photon interactions occurring provided an assessment of the behavior of the 185.7 keV photons as a monitoring signature. Furthermore, attenuation analysis provides a basis for identifying which external densitometry transmission sources were optimal for monitoring density and uranium content. Results of the full attenuation analysis for the 304L pipe, UN, and UN-filled pipe are explored in Chapter 7.

5.3 Detection Efficiency

Gamma rays must undergo interaction with the detector crystal before being registered. The efficiency of a detection system is typically defined as the observed peak area count rate divided by the source gamma emission activity, as given in Equations 5-6a and 5-6b [62].

$$Total\ Efficiency = \frac{number\ of\ photons\ recorded\ by\ detector}{number\ of\ photons\ emitted\ by\ source} \quad . \qquad [5\text{-}6a]$$

$$Full\ Energy\ Peak\ Efficiency = (\text{total detector efficiency}) \times \frac{counts\ in\ full{-}energy\ peak}{total\ counts\ in\ spectrum} \ . \qquad [5\text{-}6b]$$

Variation of the variables that contribute to the total detection efficiency originates from any of the of four factors contributing to the overall efficiency [63] [64]:

$$\varepsilon_{full} = \varepsilon_{geom} \cdot \varepsilon_{absp} \cdot \varepsilon_{sample} \cdot \varepsilon_{int} \quad . \qquad [5\text{-}7]$$

- **Geometric efficiency (ε_{geom})** is explicitly dependent on the point-to-point source-to-detector distance (R) as the inverse square law (i.e., $\varepsilon_{geom} \propto \frac{1}{R^2}$) [64]. It is essentially independent of the photon energy. In the scope of this work, spatial offset measurements during the dilution experiments were taken for each of the three detectors. This experimental data is coupled with simulation data from the In Situ Object Counting System (ISOCS).
- **Absorption efficiency (ε_{absp})** accounts for the effects of intervening materials. In the case of the NUCP measurements, these include the detector housing, detector collimator/endcap, and shielding, in addition to attenuation due to pipe thickness. This is an energy-dependent parameter (i.e., $\varepsilon_{absp} \propto e^{-\Sigma \mu \rho x}$, where Σ denotes the

sum over all materials and gamma-rays) dependent on exponential attenuation by the MAC (μ), in addition to density (ρ) and attenuator thickness (x) for the detector housing, shielding, collimators, and sample containers [64]. This factor should be <<1 for low-energy photons, at which absorption effects are most pronounced, making it very sensitive to the exact dimensions in an absolute sense. In the scope of this work, the effect of pipe thickness on the absorption efficiency was tested using ISOCS simulations.

- **Sample efficiency (ε_{samp})** quantifies the self-attenuation within the sample material, yielding the fraction of emitted gamma rays that actually emerges from the source (UN) material. This value is the reciprocal of the self-attenuation correction factor, *CF(AT)*, elaborated by Parker's method calculated as a function of transmission values (T) in Chapter 7 ($\varepsilon_{absp} \propto \frac{1}{CF(AT)} = \frac{1-T}{-\ln(T)}$) [64]. In the scope of this work, measurement data and MCNPX simulations were calculated to determine the *CF(AT)* for sample efficiency values.
- **Intrinsic efficiency (ε_{int})** is the probability that the gamma ray entering the detector will interact and produce a full-energy peak. The intrinsic efficiency is dependent upon the interaction probability of the detection material ($\varepsilon_{int} \propto 1 - e^{-\mu\rho x}$) [64]. Only a fraction of the interactions results in complete energy deposition, and a combination to the full energy peak. In Equation 5-6b, the ratio by which the total detector efficiency is multiplied is called the peak-to-total ratio.

The energy dependence of the detection efficiency causes the detected photons recorded by the detector to differ from the emission intensities. If multiple ^{235}U signatures are employed, each with different intensities, this energy dependence must be taken into account by correcting the efficiency.

Subsequently, evaluation of the sensitivity of each of these parameters to the overall detector response will provide insights into interpretation of variations affecting assay signatures. A detailed assessment of factors affecting detection efficiency (geometry, attenuation, sample self-attenuation, intrinsic efficiency) is made by conducting a sensitivity analysis of the detector response to changes in pipe thickness, material properties (density/concentration/voiding), and source-detector placement/offset. These are conducted using the ISOCS software [63], as well as Monte Carlo simulation tools. The sensitivity analysis is presented in Chapter 13.

5.3.1 Self-Attenuation Correction Principles

The NDA of nuclear material often encounters large sample containers with high self-absorption properties. If the detector efficiency is accurately known as a function of source position and energy and if the geometry and source emission rates are also accurately known, calibration standards are not necessarily required to determine the attenuation correction factor due to self-absorption.

Nondestructive assay of UN flowing in NUCP piping presents a geometry configuration that is susceptible to high self-attenuation. In determining the correction factor for self-attenuation, *CF(AT)*, we are addressing what fraction of the signature photons emitted in the direction of the detector actually reaches the detector. The MAC calculated in the previous section quantifies material composition and density; however, these are restricted to narrow-beam (good) geometry. Use of transmission calibration provides a reference for assay using transmission techniques to determine the self-attenuation for a sample, in this case, for UN-filled piping. In order to conduct the calibration, transmission detection measurements are taken for both the empty and UN-filled pipe. The transmission ratio of the full to empty container is used to determine the sample-specific *CF(AT)* using the method developed by J. L. Parker [65], which has previously

been employed in NDA field measurements for waste-drum assay [66] and pipe slurry measurements [67]. In these approaches and applications, the *CF(AT)* is empirically derived for a cylinder in far field geometry and is best applied using high-resolution gamma-ray detectors.

Following the methods for the characterization of a passive gamma-ray detection system recommended by Parker formed the basis of the efficiency analysis conducted in the scope of this work [65]. To determine the *CF(AT)* contribution to the overall detection efficiency, Parker recommends the following approach:

- measurement of the raw data acquisition rate;
- determination of gamma-ray self-attenuation correction;
- computation of corrected as proportional to the mass of the isotope being assayed; and
- determination of the efficiency calibration for both the non-attenuating geometrical shape in the same position with respect to the detector.

In the calculation of the correction factor for self-attenuation in the cylindrical pipe geometry, *CF(AT)*, the method based on transmission measurements outlined by Parker [65] is adopted:

$$CF(AT) = \frac{-\ln(T^{\kappa})}{(1-T^{\kappa})} \ , \qquad [5\text{-}8]$$

where
κ= geometrical calibration parameter
(κ <1 for cylindrical samples)
($\kappa \approx \pi/4$ for far-field approximation for reasonably transparent cylinders) and
T= transmission through sample.

The diametrical transmission, T, through the cylindrical sample is the ratio $T=I/I_o$, where I is the detected count rate of the transmission source energy through the pipe with UN and I_o is the detected transmission through the empty pipe. For our purposes, T is the predictive variable, Equation [5-8] provides a convenient functional form, and κ is an empirical parameter chosen to describe the data.

If the sample can be characterized by a linear attenuation coefficient, μ_l, the fraction of photons that detected from the sample can be determined via the following relation:

$$T = e^{-\mu_l \cdot x} \, . \qquad [5\text{-}9]$$

Two key assumptions must be satisfied in the scope of this method in order to ensure that the μ_l can sufficiently compute the photon escape-fraction on a macroscopic scale [65]: First, the gamma-ray source material (i.e., UN solution) is reasonably homogeneous in composition; second, the gamma-ray emitting constituents are small enough such that self-attenuation within the individual particles (i.e., uranium) is negligible.

Employment of the *CF(AT)* method accounts for variation in sample size, shape, composition, and density. In Parker's derivation of *CF(AT)*, the most significant parameters in decreasing order of importance are [65]

1. linear attenuation coefficient of the material;
2. volume and shape of the sample material;
3. linear attenuation coefficient of the sample container;
4. size and shape of the sample container;
5. position and orientation of the sample relative to the detector; and
6. size, shape, and efficiency of the detector.

While the first and third parameters are consistent, the sample (pipe-filled UN) is positioned closer to a collimated detector, which will affect the detector geometry and efficiency. In the purview of the *CF(AT)* calculations, it is preferable to increase the sample-to-detector distance to simplify calculations; however, for NDA in this work, this would reduce the signal count rates and introduce high background signals if the collimator was not positioned close to the sample.

Mathematical simplifications best occur in the far-field case, where the sample and detector dimensions have less impact compared to their separation distance and photons reach the detector along parallel paths. As our detector is in near-field approximation to the source, there is high dependence on detector size/shape, sample-to-detector distance, and sample size, which all affect the fraction of gamma rays escaping from the sample. However, it is possible to calculate *CF(AT)* in such situations through analytic expression of sample shapes (cylindrical in the scope of this work). *CF(AT)* for a cylindrical geometry is less than that of a slab or box-shaped sample. Consequently, if the *CF(AT)* is smaller, the fraction of photons escaping the sample is greater.

Parker provides a baseline example for the computation of *CF(AT)* using depleted UN samples in cylindrical containers [65], whose *CF(AT)* results as a function of uranium concentration are plot in Figure 5-4.

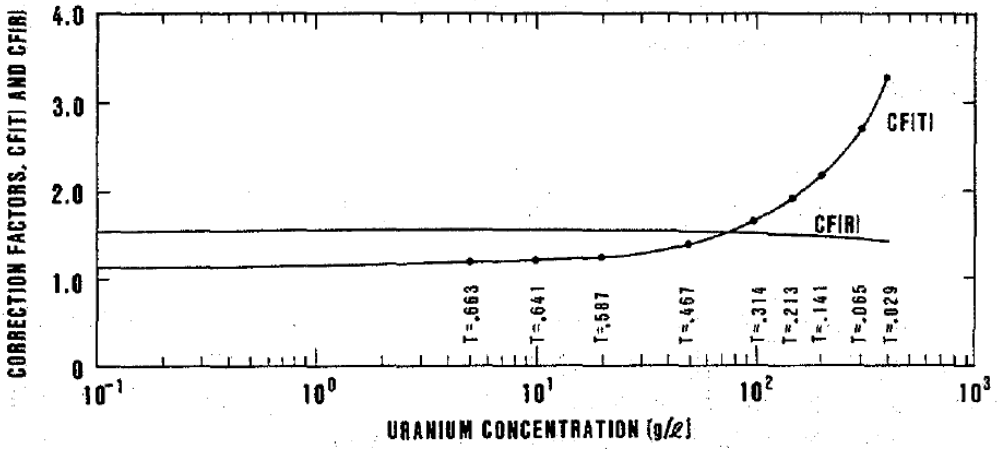

Figure 5-4. Results of Depleted UN Measurements in Parker's Calculation of *CF(AT)* Based on One-Dimensional Model.

Reproduced from [65].

Compared to three-dimensional calculations, the one-dimensional model gives lower values of *CF(AT)* compared to the three-dimensional model. In the one-dimensional model, photons pass through a slightly greater thickness of sample solution than in the three-dimensional model. Also, increasing the container diameter also increases the *CF(AT)* for lower values of *T*. In quantifying *CF(AT)*, Eqn. 5-4 shows that *CF(AT)* is linearly proportional to $-\kappa \cdot \ln(T)$ for $T<<1$ [65].

5.4 Detection Instrumentation Selection

Assessment of instrumentation that could potentially be employed to measure material flow and inventory at NUCPs requires specific criteria in evaluating which systems would be best suited for this purpose. The criteria that were considered included [40] [41] the following.

- **Applicability to uranium measurements:** Differentiating from systems optimized for other common NDA measurements, such as plutonium assay or spent fuel, for example.

- **Cost and complexity:** Cost not only includes the purchase cost of the system but also extends to include the operation, repair and maintenance, and personnel/training costs associated with maintaining the system. Methods should be minimally invasive and not interrupt operator activities.
- **Consistency with current IAEA protocol and procedures:** Employing standard complement of measurement techniques, instrumentation, and practices.
- **Resilience to tampering or spoofing:** The system should be designed for timely detection of the aforementioned safeguards challenges with confidence, where instrumentation is optimized to avoid false positives and false negatives. In addition, the instrumentation should be tamper-proof by a potential diverter. Although many instruments can be employed for PM at NUCPs, not all are capable of being employed for drawing safeguards conclusions.

5.4.1 Detection Principles

Passive gamma-ray methods can be conducted using high- or low-resolution measurements and are provide signatures that are difficult to spoof. Gamma-ray methods are relatively inexpensive and are part of the IAEA standard complement of measurement techniques, although assaying larger volumes is difficult due to insufficient penetration for low-energy photons (^{235}U). The exception is with uranium enrichment determination where an infinitely thick sample is required for the gamma rays of interest.

Selecting gamma-ray radiation detection technology as the basis of the NDA safeguards system was based on previous work by LANL and ORNL. The decision to monitor gamma rays as opposed to neutrons is an alternative to the analysis conducted by Miller *et al.* in 2004 [41]. However, Miller did not provide any comparative quantitative metrics or data upon which the decision to use neutron detection was made. Recent experience with the TUrND at ORNL has also shifted preference from neutron detection (due to the

shortage of ^{3}He technology and the inconclusiveness of recent neutron monitoring data). Neutron detection may be appropriate for operations monitoring, but gamma-ray detection may better lend itself to detecting diversion in a timely manner and is more robust to "spoofing" efforts.

5.4.2 Gamma-Ray Instrumentation Selection

Based on the source term analysis and subsequent calculation of emission intensities from the attenuation analysis, candidate NDA instrumentation for passive gamma-ray acquisition were selected for experimental validation measurements in a controlled laboratory setting, as well as for operational measurements in the UNCLE facility.

A variety of methods exist for assaying fissile material, constituting either active or passive methods for gamma-ray or neutron detection. Robustness and practical implementation must be considered for safeguards monitoring. A suite of detectors, primarily commercial-off-the-shelf (COTS), was selected for testing detection sensitivity to various dilutions and shielding configurations of UN (Figure 5-5). These included the Canberra 2×2-inch NAIS with the Osprey digital tube base, which prevents gain drifts; Canberra Inspector 1000 with 1.5×1.5-inch $LaBr_3$ Probe; and Canberra Falcon BEGe.

In addition, the variety in detector selection permitted comparison of resolution and efficiency parameters in monitoring UN. This includes both scintillators – sodium iodide (NaI) and lanthanum bromide ($LaBr_3$) – as well as semiconductors – high-purity/broad-energy germanium (HPGe/BEGe). The detector properties are summarized in Table 5-2. Walford *et al*. conducted a comprehensive measurement of various uranium compounds using COTS detectors to test a parallel-plate collimator to mitigate scatter from ^{238}U [68]. Although this work characterizes the effects of a novel collimator, the scope of the work

herein is focused upon characterizing the detector responses and sensitivities of UN in transfer pipes of NUCPs in response to specific IAEA safeguards requirements.

Furthermore, the ease of operational implementation and robustness in an operational setting is accomplished through field tests at the UNCLE facility. As a result, an evaluation was made regarding the fidelity with which the system can process monitor throughput, as well as determine the ease/difficulty of detecting "spoofing" scenarios, indicative of diversion/undeclared activities that may occur at an NUCP.

(A) **(B)** **(C)**

Figure 5-5. Gamma-Ray Detectors Employed in Measurement Experiments.

A) Canberra NaI(Tl) Osprey; (B) Canberra Inspector 1000 with $LaBr_3$ Probe; (C) Canberra Falcon BEGe [69] [70] [71] [72] [73].

Table 5-2. Properties of Selected Gamma-Ray Detectors for Validation Experiments.

Instrument Name	Instrument Weight (kg)	Detector Material	Crystal Dimensions (cm)
Canberra 2×2-inch NAIS + Osprey Digital Tube Base	1.28	NaI(Tl)	4.08Ø × 4.08
Canberra Inspector 1000-INPROL-1	2.4	$LaBr_3$	3.81Ø × 3.81
Canberra Falcon BEGe	15.5	Ge	2.985 Ø × 2.0

Data from [69] [70] [71] [72] [73].

The accuracy, capabilities, and applicability limitations of the gamma-ray-based detection system were determined through validating existing plant operations at the UNCLE facility at ORNL. The monitoring of uranium using passive gamma techniques determines the optimal instrumentation to authenticate uranium presence, flow, concentration, and enrichment. Upon completion of simulation activities, the suite of

gamma-ray detectors was tested for safeguards applications in an operational setting. Diversion and "spoofing" activities are computationally simulated to test detector sensitivities and to determine the radiation signature as indicators of diversion activities. Based on an assessment of the detector data and each detector's robustness as a safeguards monitoring instrument, a design concept for an optimal monitoring detection system for PM will be proposed.

5.5 Dilution Measurements

Dilution measurements were taken with a UN-bearing 304L pipe segment (described in Chapter 7) in a controlled, low-background laboratory facility. This is in order to determine each detector response's sensitivity to diluted concentrations of UN prior to operations measurements in the UNCLE facility. A previous study by Scargill analyzed the lower limit of naturally enriched UN using high-resolution gamma-ray spectroscopy for concentrations of UN up to 350g U/L in an 11.2 mL sample vessel [74]. The study determined that the lower limit of detection of natural uranium was a concentration of 30 g U/L within an accuracy of 5% for a counting time of 5 minutes. Another study by Sundar *et al.* investigated a variety of methods to determine sample concentrations ranging from 5 to 450 g U/L using high-resolution gamma-ray measurements, among other methods (potentiometric, x-ray fluorescence, differential pulse volumetric, ultraviolet-vis) using 10 mL aliquot samples [75]. As discussed earlier, the absolute efficiency of a detection system is dependent upon geometry, container wall attenuation, self-attenuation, and intrinsic factors. Thus, varying certain parameters of the experimental setup will determine how each of the three former factors (geometry, container attenuation, self-attenuation) affects the overall sensitivity of the detector response to each parameter. In addition to passive gamma-ray measurements using HPGe, $LaBr_3$ and NaI detectors, a passive gamma-ray transmission source is employed

for densitometry measurements to correlate source transmission and UN density/concentration.

Peak areas for the ^{235}U high-intensity emissions (notably at 185.7 keV and 143.8 keV) were determined as a function of UN density and uranium mass. Canberra's VMS Standard Peak Search in the Genie 2000 Gamma Analysis software was employed. The peak selection, fit and background (continuum) subtraction methods are described in full detail in the Genie 2000 manual [76].

The dilution experiment results and peak area correlations are discussed in detail in Chapter 9. Additionally, spatial resolution is determined from pipe-offset measurements to determine the geometry effects on detection efficiency due to detector offset. These results are discussed as part of a comprehensive sensitivity analysis in Chapter 12.

5.5.1 Dilution Measurement Setup

The following measurements were conducted in order to test the sensitivity of the detector responses:

- **I) Passive Measurements:** Spectra were acquired for 3600 s measuring the ^{235}U high-intensity photons for each of the three candidate detectors for uranium concentrations ranging from 10 g to 90 g U/L of UN.
- **II) Transmission Measurements:** Spectra were acquired for 3600 s measuring the ^{235}U emissions as well as the 661.7 keV ^{137}Cs transmission from an external source through the UN-filled pipe for each dilution concentration. Transmission measurements were taken to determine UN densitometry signatures.
- **III) Spatial Offset Measurements:** Passive ^{235}U spectra were acquired for 3600 s for each of the three detectors at various offset positions from

the centerline of the detector shifted off-center from the pipe in order to determine the sensitivity of pipe positioning to the detector response. This measurement was a component of a comprehensive sensitivity analysis.

Data were taken over 3600 s live time for passive and external source transmission measurements and over 1800 s for each position in the offset measurements. Although spectra were saved in 300 s increments, temporal analysis is beyond the scope of the current work; thus, integrated count rates at 3600 s are analyzed.[2] For all measurements, a ¼-inch (0.635 cm) distance was maintained between the pipe and the face of the detector endcap/collimator. The detector was shielded on all sides with a 20.3cm×10cm×5cm lead brick. Schematics of the dilution measurement setup are depicted in Figure 5-6.

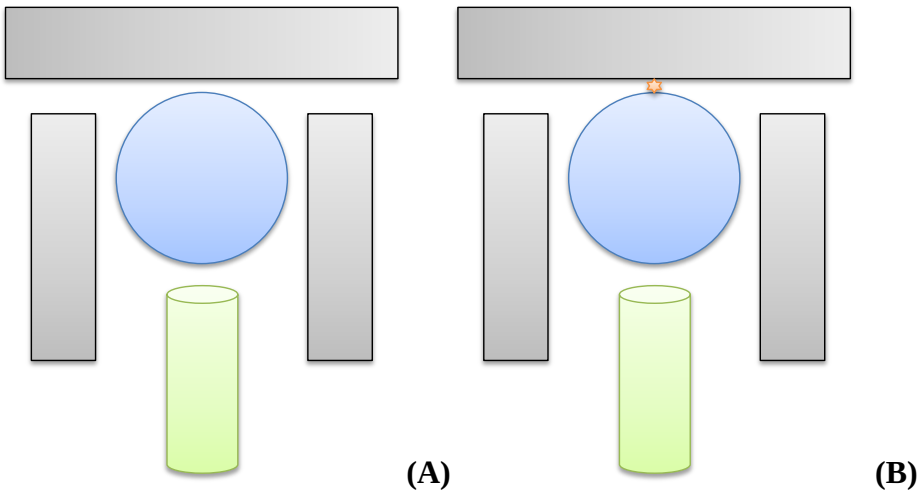

[2] The exception is with passive measurements at 90 g U/L, for which data were only available up to 1800 s live time.

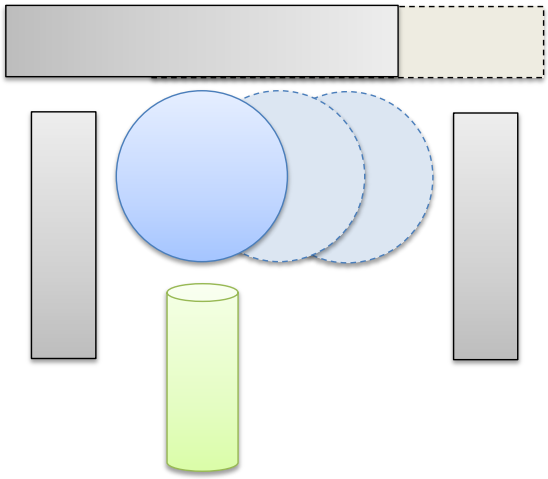

(C)

Figure 5-6. Dilution Measurement Experiment Configurations.

Top view of: pipe (blue); detector (green); and Pb shielding (grey).
(A) Passive setup; (B) Transmission source setup; and (C) Spatial offset setup.

5.5.2 Densitometry Measurements

A transmission-based in-line densitometer using the 661.7-keV gamma ray from ^{137}Cs was selected based upon availability. As investigated in detail in Chapter 7, a 122 keV transmission measurement from the ^{57}Co line is theoretically preferable, as it does not interfere with the 185 keV ^{235}U assay peak or the 115.6 keV k-edge X-ray peak; it does not contribute Compton continuum downscatter to ^{235}U emissions; and ^{57}Co at 122 keV is highly sensitive to uranium content. However, one caveat is that it may be too sensitive to content such that Compton contributions from the ^{235}U emissions in the 140–205 keV range may interfere with densitometry signatures, notably for low-resolution measurements.

5.6 UNCLE Measurements

The dilution measurements in a low-radiation background environment permitted testing the instrument sensitivity and the development of monitoring signatures. Transition to the UNCLE facility provides a test bed for assessing gamma-ray instrumentation monitoring capabilities in an operational setting. Similar to the dilution measurements, passive and

transmission measurements were conducted in UNCLE to determine the detector responses in comparison to the static dilution experiments. Where the dilution measurements employed static UN, the UNCLE measurements provide detection data on dynamic, flowing UN in a small-scale facility representing the KMP following solvent extraction. In actuality, this KMP is where PP18 defines the starting point of 34(C) materials. Operational deployment assesses issues such as high-radiation background, shielding configurations, collimator leakage, voiding and vibration effects due to changes in flow rate, and environmental factors. The UNCLE facility measurement results are provided in Chapter 10.

Both passive ^{235}U and ^{137}Cs transmission densitometry measurements were conducted at UNCLE using the three detectors employed in the dilution experiments: Canberra Falcon BEGe, Canberra Inspector 1000 1.5×1.5 $LaBr_3$, and Canberra Osprey 2×2 NaI(Tl). Detector responses to changes in flowrate, shielding configurations, background determination, and transmission densitometry were assessed in the UNCLE measurement excursion. The detectors employed in the UNCLE field measurements were similarly set up as the dilution experiments, where the detectors were each shielded with lead bricks and collimated.

5.6.1 Monitoring of Fissile Flow

Characterizing mass flowrate in an NUCP provides auxiliary verification data to aid in determining material throughput. Flowrate data alone provides limited information regarding uranium concentration, especially in cases where material substitution, instrumentation tampering, and falsification of records are potential means of misuse/undeclared activities (discussed further in Chapter 13). In addition, the feasibility of installing a flowrate instrument was viewed as intrusive and undesirable by operators

in nation states which would fall under this safeguards effort (identified in Chapter 3) [77]. Non-intrusive flowrate instruments tend to be inaccurate.

As part of a comprehensive NDA safeguards system that accurately provides concentration data, flowrate measurements help correlate mass throughput at an NUCP, as described in Equation 5-10 [42].

$$M(t) = C(t) \times F(t) \ , \qquad [5\text{-}10]$$

where
M(t) = mass flowrate of UN as a function of time, t,
C(t) = uranium concentration (g U/L), and
F(t) = flowrate (L/h).

Ladd-Lively *et al.* describe measurements using the Coriolis flowrate meter installed at UNCLE [39], which benchmarked the mass flowrate of the uranium flowing through UNCLE. The flowrate tests conducted by Ladd-Lively *et al.* on UNCLE included steady-state measurements at the following pump speeds (RPM): 450, 750, 1000, 1250, 1500, 1700, and 1071. The pump speed of 1071 RPM approximates the average flowrate that was used during the field test at Springfields NUCP [39]. From Ladd-Lively *et al.*'s results of the steady-state tests, shown in Figure 5-7, the mass flowrate shows a strong positive linear correlation with the pump speed. Based on this data, the tests conducted in this work at 1070 RPM and 500 RPM correspond to mass flow rates of 7963.4 kg/h and 3528.9 kg/h, respectively. With respect to plant classification at this throughput explained in Chapter 2, if UNCLE was run continuously for a whole year, this would correspond to ~2.5 kt U/yr. and ~5.7 kt U/yr., respectively. The potential of diversion from a facility of this scale is discussed in Chapter 13.

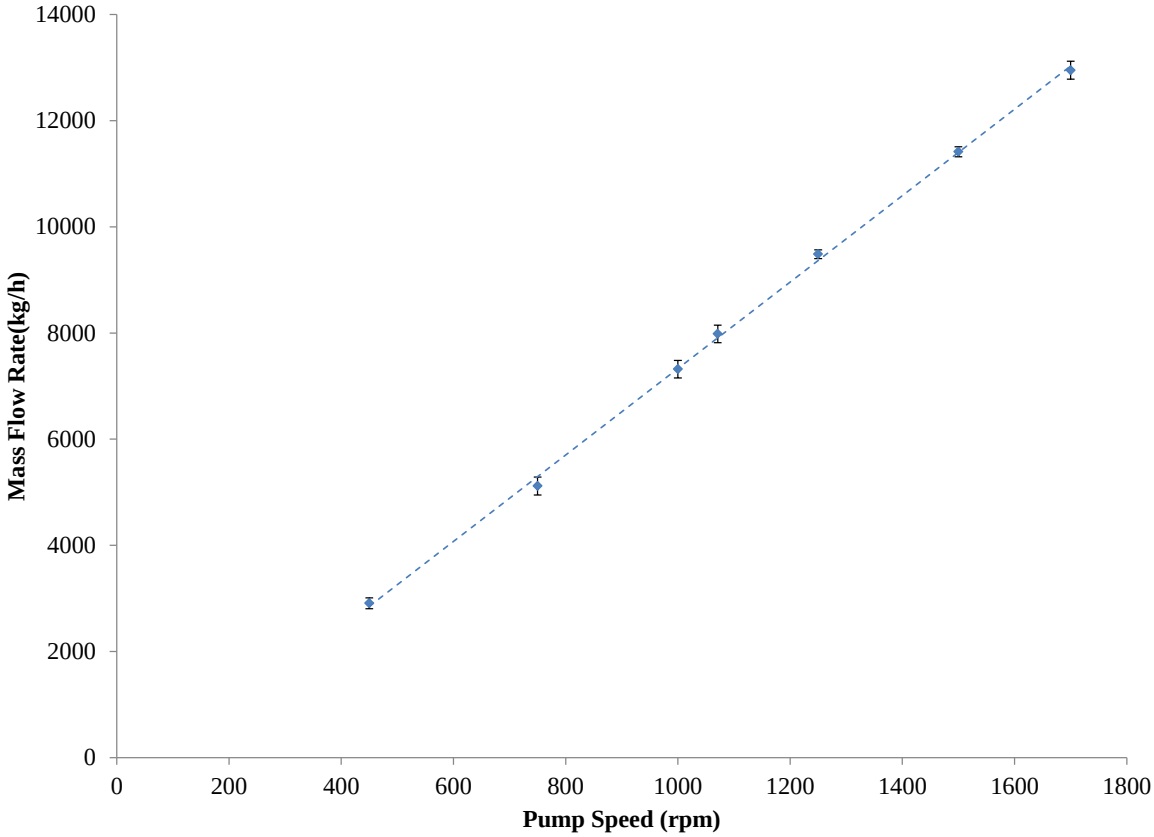

Figure 5-7. Mass Flowrate Averages for Varying Pump Speeds in UNCLE.

Data reproduced from [39].

5.6.2 UNCLE Measurement Setup

Field measurements under steady-state conditions at UNCLE were taken for the following setup configurations.

- **I) Passive-High Flowrate:** Spectra were acquired at a flowrate of 1070 RPM.
- **II) Passive-Low Flowrate:** Spectra were acquired at a flowrate of 500 RPM.
- **III) Transmission:** Spectra were acquired at 1070 RPM of the UN solution with external ^{137}Cs source exposed. Transmission measurements were taken to determine UN densitometry signatures.

- **IV) No Backshield:** Measurements were taken in the absence of the pipe backshield in order to determine environmental background in the operational facility with UN flowing at 1070 RPM.
- **V) Shadow Shield:** A frontshield or "shadow shield" was employed to shield the UN-bearing pipe in order to determine the background signals or "leakage" into the collimator reaching the detector.

Schematics of the experimental setup for the UNCLE measurements are given in Figure 5-8.

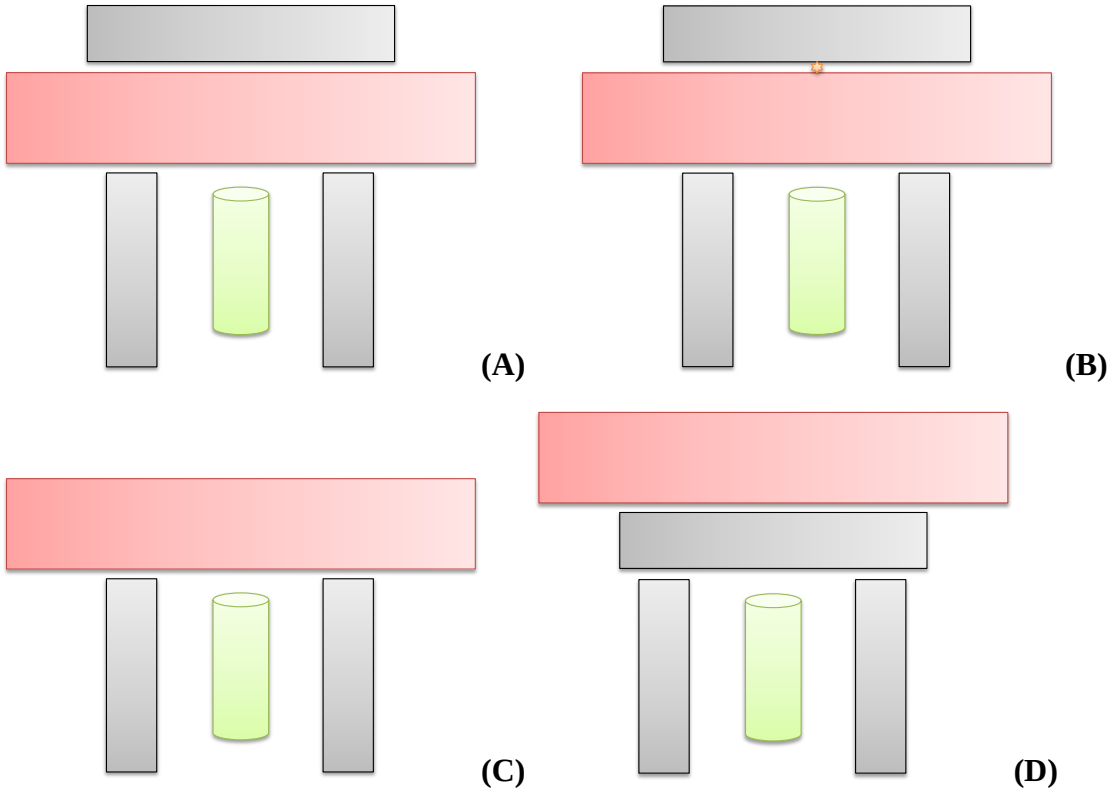

Figure 5-8. Detector Setup in UNCLE Facility.

Top view of: detector (green); pipe (red); and Pb shielding (grey).
(A) Passive change in flowrate setup; (B) Transmission source setup; (C) No backshield setup; (D) Frontshield/Shadowshield setup.

5.7 Validation Simulations

Experimental measurements undertaken in the scope of this project provide an overall assessment of the sensitivity of gamma-ray detection technology to variations in concentration, as well as to determine the monitoring capabilities in an operational conversion facility. However, a myriad of variables – both from solution properties and detector efficiency – were not able to be experimentally tested. Thus, simulations provide detector responses to test variables such as variations in transmission densitometry. Computational models were constructed to simulate the detector responses for passive dilution and transmission measurements. All simulations were conducted using the *Monte Carlo N-Particle eXtended* (MCNPX) photon transport code [78].

The modeled UN was a solution of 90 g of uranium dissolved per 1000 mL of water, 0.76 wt.% enrichment, with a measured solution density of 1.122 g/cm^3. The elemental solution composition was calculated in the UN solution to be 8.0 wt.% U, 0.70% N, 81.5% O, and 9.8% H, as given in Table 5-1. As the detector providing the highest resolution signatures, the Falcon BEGe detector was modeled in detail to determine validated detector responses.

The simulation was modeled after the experimental setup for the dilution measurements, employing lead brick shielding around the perimeter of the collimator, as well as behind the pipe acting as a backshield.

5.7.1 MCNPX Simulations

Simulations were conducted for the following scenarios with the modeled Falcon BEGe.

- **I) Passive Simulations:** Spectra were simulated for the ^{235}U source emissions for uranium concentrations ranging from 10 g to 90 g U/L of UN and compared with experimental dilution measurement spectra.
- **II) Transmission Measurements:** Transmission simulations were taken to determine UN densitometry signatures.
    - **^{137}Cs:** Spectra were simulated measuring the ^{235}U emissions as well as the 661.7 keV ^{137}Cs transmission from an external source through the UN-filled pipe for each dilution concentration (10 g to 90 g U/L). These simulations were compared with the experimental dilution measurement spectra.
    - **^{133}Ba and ^{57}Co:** In the absence of experimental measurements, ^{133}Ba and ^{57}Co measurements were simulated to assess the

sensitivity of the respective 356 keV and 122 keV transmissions through the dilution concentrations of UN (10 g to 90 g U/L).

- **III) Enrichment Measurements:** Spectra were acquired measuring the ^{235}U high-intensity peaks for enrichments ranging from 0.76% (UNCLE) to 10% at a concentration of 90 g U/L. Although the U concentration remains the same, reproduction of the detector response due to subtle changes in enrichment provides data regarding the detection sensitivity.

5.7.2 Gaussian Energy Broadening Calibration

In the unsmoothed MCNPX pulse-height tally, nearly all photoelectric interactions result in a delta function at the photon energy rather than a resolution-broadened photopeak, where only a small fraction may be lost to K-x-ray escape. The Gaussian Energy Broadening (GEB) function [78] in MCNPX was used to simulate the detector resolution, based on the full-width-at-half-maximum (FWHM) data. In principle, the use of the unsmoothed counts at the full gamma-ray energy would also provide photopeak counts, as would smoothing to the monoenergetic output using alternative software. Use of the GEB in MCNPX enables the emulation of the specific detector resolution *in situ* based on a specific detector. The parameters required for the GEB function (*a, b, c*) were calculated based on the measured detector response, and iteratively fit to Equation 5-11 to obtain the GEB parameters.

$$FWHM = a + b\sqrt{E + cE^2} \quad . \qquad [5\text{-}11]$$

In this expression,

E = Energy (MeV)and
FWHM =full-width-at-half-maximum value of photopeak (MeV).

Data obtained from the calibration data of the dilution measurements were used to determine the GEB fit parameters, and are provided in Chapter 8.

5.7.3 MCNPX Tallies

A pulse-height tally (F8) was performed over the active region of the detector crystal to determine the pulse-height spectrum for passive, transmission, and enrichment measurements. The peak efficiency can be determined from the corrected net peak area under the simulated response peaks from ^{235}U as a function of the source emissions from UN. A detailed description of the simulation model is provided in Chapter 8, and juxtaposed with experimental results in Chapter 11.

As part of the comprehensive sensitivity analysis in Chapter 12, a surface current tally (F1) was performed over each of the modeled material boundaries for a UN-filled pipe at 90 g U/L in the dilution measurement setup: (1) UN boundary; (2) pipe boundary; (3) collimator/endcap; and (4) detector housing. The UN boundary provides a simulation complement in the determination of *CF(AT)* by providing data on the fraction of particles that escapes the UN sample. Propagating the tally across the pipe, collimator, and detector housing determines the fraction of signature photons traversing each absorber in the given geometry. The simulations employed for this efficiency analysis are described in detail in Chapter 12.

5.8 Algorithm Development for Peak Area Interpretation

Use of a densitometry source provides a transmission measurement that determines the density of the UN in an NUCP transfer pipe. The transmission, *T*, is calculated by taking a transmission ratio of the UN-filled pipe *(I)* with an empty pipe *(I_o)*. From any the candidate sources tested (^{133}Ba, ^{57}Co, ^{137}Cs), the *T* ratio is related to the density (ρ) of the solution flowing in the pipe (inner diameter d_{eff}) via the following relation:

$$\rho = \ln(\frac{1}{T}) \cdot (\mu \cdot d_{eff})^{-1} \quad . \qquad [5\text{-}12]$$

Using this relation, the density using dilution measurements provided a calibration for UN solution measurements.

Although densitometry measurements may provide the solution density and potentially uranium concentration through calibration, this still does not tell us about the throughput of ^{235}U, specifically. Consequently, a combination of the transmission energy and the 185.7 keV peaks are required to determine not only the uranium concentration in the NUCP transfer pipe but also the ^{235}U content. The concentration *(C)* of ^{235}U in the circulating UN is determined by the peak area count rate of the ^{235}U 185.7 keV signature emission given in Equation 5-13 [67]:

$$C = \frac{r \cdot CF(AT)}{V \cdot \varepsilon \cdot \rho} \quad , \qquad [5\text{-}13]$$

where
r = net count rate of 185.7 keV emission peak (cps),
ρ = solution density (g/cm^3),
CF(AT) = self-attenuation correction factor,
V = volume of solution in detector field of view (cm^3),
ε = peak efficiency of 185.7 keV (cps/Bq), and
C = ^{235}U concentration (Bq/g).

As conducted with densitometry measurements, the use of an empty and full pipe during calibration can determine the ^{235}U enrichment as a function of transmission (Equation 5-14), in addition to analysis of the 185.7 keV emission [79].

$$E = k \cdot \frac{r}{\ln(T)} \qquad [5\text{-}14]$$

where
r = net count rate of 185.7 keV emission peak (cps)
T = external source transmission
k = calibration constant

5.9 Background, Uncertainty, and Sensitivity Analysis

Experimental measurements from both the dilution and operational activities provided a basis for identifying passive gamma-ray signatures from ^{235}U in UN. Detailed uncertainty, statistical and sensitivity analyses are required in order to evaluate the robustness of these monitoring signatures.

Peak area uncertainty due to the underlying Compton continuum from ^{238}U in secular equilibrium from aged UN, in addition to ^{137}Cs emissions during transmission measurements, affect the peak area, uncertainty statistics, and required counting times to meet a specified confidence interval. In addition, background from adjacent tanks and pipes containing uranium in a field setting contributes to background under the assay peak areas, which must be characterized, discriminated, and appropriately shielded during implementation of field instrumentation.

A sensitivity analysis provides an indication of how variables, such as pipe thickness, material properties, and source-detector geometry affect the overall detection efficiency of the assayed ^{235}U signatures. Employment of Canberra's ISOCS software

quantifies the UN mass (hence, activity) in the 304L pipe through a series of ray-tracing calculations, and provides an absolute efficiency for the modeled source-detector configuration. To model the UN-filled pipe geometry, two of the three tested detectors – the Falcon BEGe and the Osprey 2×2 in. NaI(Tl) – were available to model in ISOCS. In addition, MCNPX (F1 tally) simulations were created to determine the effects of source-detector geometry and absorbers in the overall peak efficiency of assay signatures. The details of the statistical and uncertainty analysis are provided in Chapter 12.

5.9.1 Statistical Uncertainty and Error Propagation

In order to determine the net peak area under the ROI, the background must be subtracted (Equation 5-15), and the error from both continuum and background contributions must be propagated to determine the associated uncertainty of the net peak area. Nuclear counting is a random process that obeys Poisson statistics. Consequently the standard deviation of the mean follows as the square root of the true mean number of counts. In ROI peak analysis, the associated statistical error (±σ) with a net count rate (r) is related to the variance by the sum of the errors of each of the gross and background count rates added in quadrature, as defined in Equation 5-16 [80].

$$r = g - b \ , \qquad [5\text{-}15]$$

where
r= net count rate (cpm) in ROI,
g=gross count rate (cpm) in ROI, and
b=background count rate (cpm) in ROI.

$$\sigma_r = \sqrt{\sigma_g^2 + \sigma_b^2} = \sqrt{\frac{\mathrm{g}}{t_g} + \frac{\mathrm{b}}{t_b}} \quad . \qquad [5\text{-}16]$$

In the purview of gamma-ray spectroscopy measurements, for a well-characterized background, it is advantageous to know the optimal sample counting time required to meet a precision of relative standard deviation of *a%* [80]:

$$t_G = \frac{g}{(g-b)^2 \cdot \left(\frac{a}{100}\right)^2 - {\sigma_b}^2} \,. \qquad [5\text{-}17]$$

5.9.2 In Situ Object Counting System (ISOCS)

A detailed assessment of factors affecting detection efficiency is made by conducting a sensitivity analysis of the detector response to changes in pipe thickness, material properties, and source-detector placement/offset. These are conducted using Canberra's ISOCS software [63]. Unlike classical efficiency calibrations, ISOCS can be employed without calibration materials. The geometry is modeled in the ISOCS software and uses ray tracing (described in Chapter 5) to determine the *peak* efficiency of the source-detector system. When this efficiency calibration is applied to an acquired spectrum, the mass (and hence, activity) can be determined for the modeled geometry. The use of ISOCS negates having to run multiple MCNPX simulations, hence permitting testing of a multitude of variables affecting the overall peak efficiency of photon signatures emitted from the UN-bearing pipe.

The ISOCS program works by drawing upon efficiency lookup tables that are generated using pre-simulated and validated MCNPX models. For a given detector, a detailed MCNPX model is created incorporating 30 dimensional parameters. An efficiency is generated for each of the eight source geometries and validated with experimental measurements. The efficiency is computed at 800 spatial locations, where radial symmetry is assumed. ISOCS is valid from 0 to 500 mm source-detector

distances in all directions, spanning an energy range of 45 keV to 7000 keV. *In-vacuo* efficiencies are determined from the "nodal" – or voxel – points of a spatial response grid, where a large number of "sub-nodal" points are generated using a cubic-spline algorithm in between the nodal points. A gridding process is employed to interpolate efficiencies between the modeled points, and the efficiency parameters are supplied into a detector characterization file in ISOCS. The efficiency for the point source is obtained from the characterization file (i.e., lookup table) modified by attenuation through any materials between the source and the detector, given in Equation 5-18:

$$\varepsilon_{ISOCS} = \sum_{voxels}(\varepsilon_{character.pt}) \cdot (attenuation) \; . \qquad [5\text{-}18]$$

In essence, the four-factor efficiency from Equation 5-7 is calculated at the individual voxel level and factor in attenuation. Figure 5-9 depicts the voxel validation technique employed in ISOCS [63].

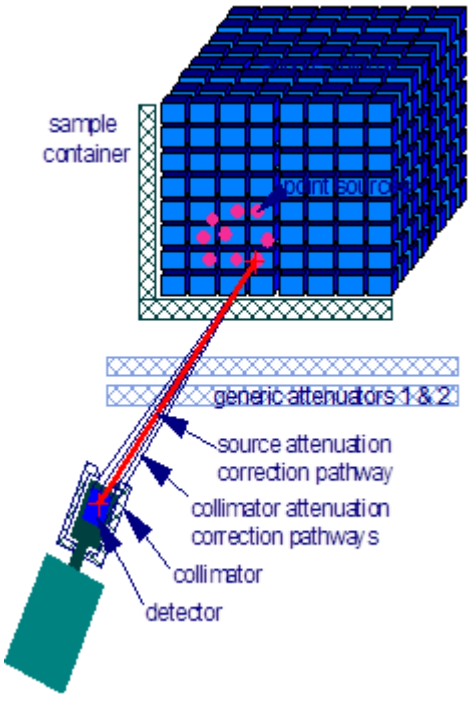

Figure 5-9. ISOCS MCNP Voxel Validation Technique.

5.9.3 ISOCS Peak Efficiency Simulations

Models were created to emulate the geometry employed for both the dilution and UNCLE measurements. The pipe dimensions from Table 6-1 and the UN composition from Table 7-1 were employed in the ISOCS models. When modeling the Falcon and Osprey detectors, the ISOCS template permitted only one collimator/shield. The ISOCS model of the Falcon BEGe was the W collimator, where the endcap modeled as an epoxy absorber to best simulate the Falcon's collimator composition, as shown in Figure 5-10 [81]. The Osprey was modeled approximating the encompassing Pb shielding arrangement to approximate the combined effects of the Pb brick shielding as well as the 7419E Shield/Collimator, as modeling both was not permitted by the template. The Osprey configuration is depicted in Figure 5-11. The input parameters for each of the pipe-detector and collimator/shielding models for the Falcon and Osprey are provided in Appendix K.

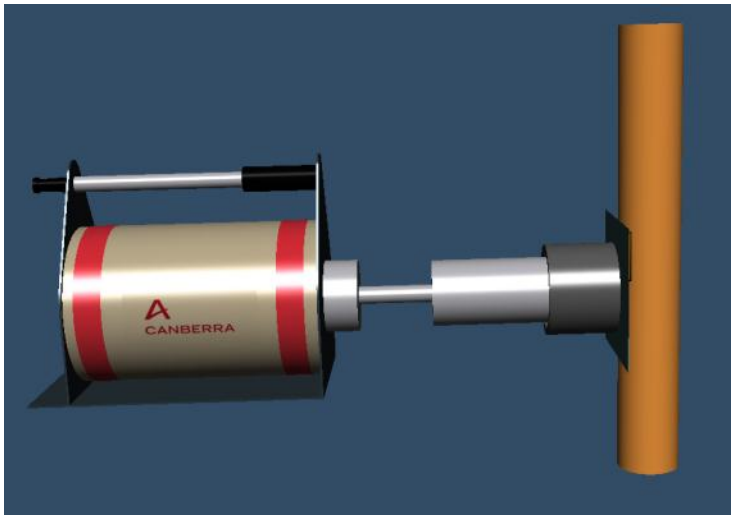

Figure 5-10. Pipe Model of Falcon BEGe with Collimator Using ISOCS.

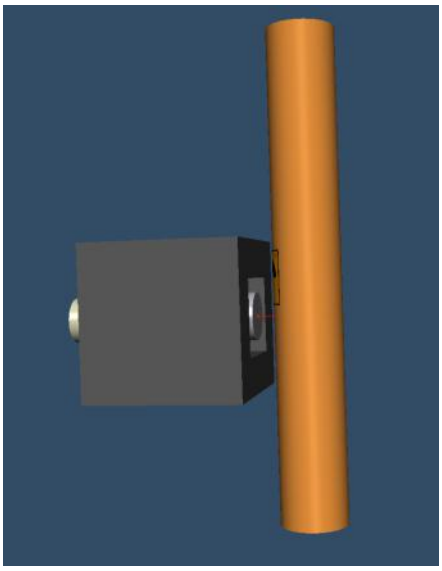

Figure 5-11. Pipe Dilution Model of Osprey NaI(Tl) with Shielding Using ISOCS.

5.10 Discussion and Recommendations

Based on the experimental and simulation data obtained from both the dilution and operational measurements, in combination with a detailed uncertainty, statistical and sensitivity analysis, evaluations will be made regarding the optimizing gamma-ray NDA instrumentation for process monitoring at this KMP in an NUCP. The IAEA requirement for detection of 1 SQ – 10 MTU – in a period of 1 year with 50% detection probability represents 0.1%, 1%, and 10% of plants with throughput of 10, 100, and 1000 MTU/yr., respectively. Although the IAEA prescribed limit is 1 SQ of 10 MTU/year, a rogue diverter with a clandestine enrichment capability requires only 5 MTU to produce 1 SQ (25 kg U) of highly enriched uranium (HEU) [32].

An uncertainty of 0.1–10% due to counting statistics, attenuators, or source material variables must be evaluated in an overall safeguards monitoring regime using gamma-ray instrumentation. This range considers that 10 MTU represents the uncertainty associated with S, M, and L throughput NUCPs. Assessments are made regarding

whether the IAEA timeliness and detection goals are feasible, and whether passive gamma-ray techniques are capable of detecting undeclared, misuse, or diversion scenarios at an NUCP. The discussion of safeguards applicability is presented in Chapter 13.

Based on the culmination of the experimental and simulation data, in addition to the in-depth sensitivity and uncertainty analyses, a prototype design is proposed for full-scale field tests in an NUCP, in addition to exploring operational implementation requirements for this instrumentation in a comprehensive safeguards system. These conclusions and recommendations are discussed in Chapter 14.

CHAPTER 6. THEORY: SOURCE PROPERTIES OF URANYL NITRATE

As UNCLE employs UN from uranium that is 40 years old, a source term analysis is required to determine aged-based signatures changes vis-à-vis freshly solvent-extracted UN in NUCPs. This is accomplished through harnessing the program, RadSrc [51], which solves the Bateman equations to determine age effects of fresh (0 years) and aged (~1 year, secular equilibrium) uranium in the UN source term for various concentrations (10, 50, 75, 85, 90 g U/L). In conjunction with Sources4C [52], gamma-ray and neutron radiation emissions are calculated for the UN source term, in order to characterize the radiation signatures of UN.

6.1 Correlating Uranyl Nitrate Concentration with Density

The UN base solution circulating through the UNCLE facility is a solution of 90 g of uranium, as uranyl nitrate, dissolved per 1000 mL of water, with a solution density of 1.122 g/cm^3. The UN in UNCLE contains 0.0059 wt.% ^{234}U, 0.76% ^{235}U, and 99.2% ^{238}U. The solution properties of natural uranium-bearing UN with the density and concentration of UNCLE are summarized in Table 6-1, as well as the properties of the proposed dilution concentrations.

Table 6-1. Solution Properties of Uranyl Nitrate in Pipe Segment (2.62 L).

Solution Concentration (g U/L)	90	85	75	50	10
Molarity (M)	0.378	0.357	0.315	0.210	0.042
Density (g/cm^3)	1.122	1.115	1.099	1.064	1.008

A variety of studies have examined correlating UN concentration, solubility, and density. Botts *et al.* conducted a thorough investigation of the density, acidity, and

conductivity of UN/nitric acid solutions. Measurements were made on solutions of concentrations ranging from 0.05 to 1.27 M uranium, 0.1 to 2.0 M nitrate, and NO_3/U ratios from 1.56 to 2.3 at temperatures of 25, 30, 40, 50, and 75°C [82]. The densities of the solutions were measured using pycnometric measurement, with an accuracy of ±0.05%. Least-squares curve fitting of the experimental data was conducted (Equations 6-1 and 6-2) in order to relate the density parameters to the uranium and nitrate concentrations (Figure 6-1). Since such customized density measurement techniques were not available for characterizing the UNCLE UN and subsequent dilution solutions, the experimental density measurement used the traditional mass/volume calculation of each solution. The measured results were compared to the least-squares fit parameters calculated from the results of Botts *et al.* (Figure 6-2). The temperature in the UNCLE facility ranges from 12.7–29°C.

$$\text{Density} = \text{DENW} + \text{A(U)} + \text{B}(\text{NO}_3)\ , \qquad [6\text{-}1]$$

where
A=0.265684,
U=uranium concentration of solution (M),
B=0.0282071,
NO_3=nitrate concentration of solution (M), and
DENW= density of pure water (Eqn. 10-3).

$$\text{DENW} = 0.992247 - 0003806 \cdot \text{DT} - 0.00000375 \cdot \text{DT}^2, \qquad [6\text{-}2]$$

where
DT = Temperature – 40 (°C).

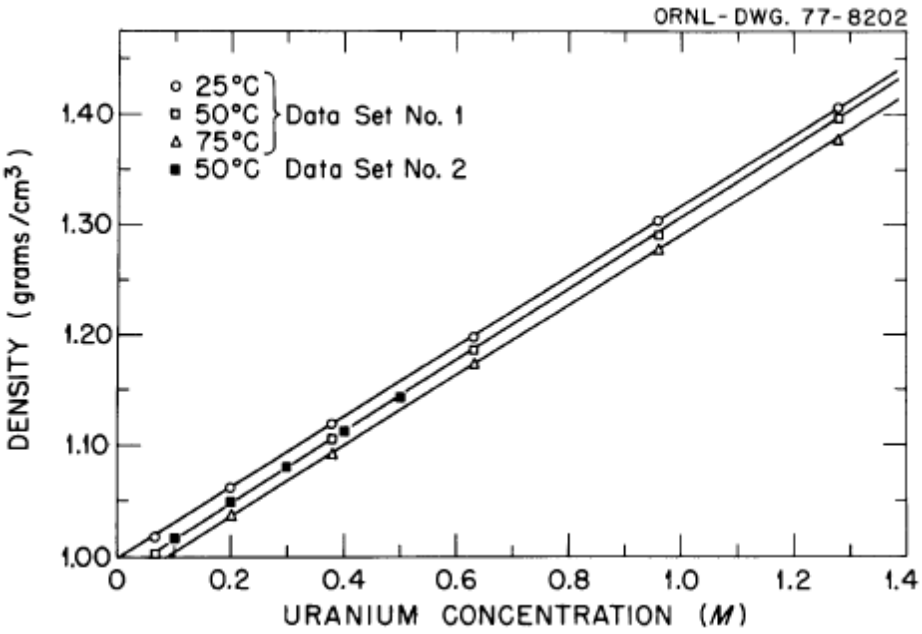

Figure 6-1. Relationship between Density and Uranium Concentration at Various Temperatures (NO_3/U mole ratio = 1.56).

Reproduced from Botts et al. [82].

Given that the ratio of NO_3/U in the UNCLE stock solution is 1.5 [54], Equations 6-1 and 6-2 were applied to determine the correlation between measured solution density and concentration with the validated values at various temperatures. This comparison is plot in Figure 6-2. As expected, the solution density correlates positively with the UN solution concentration.

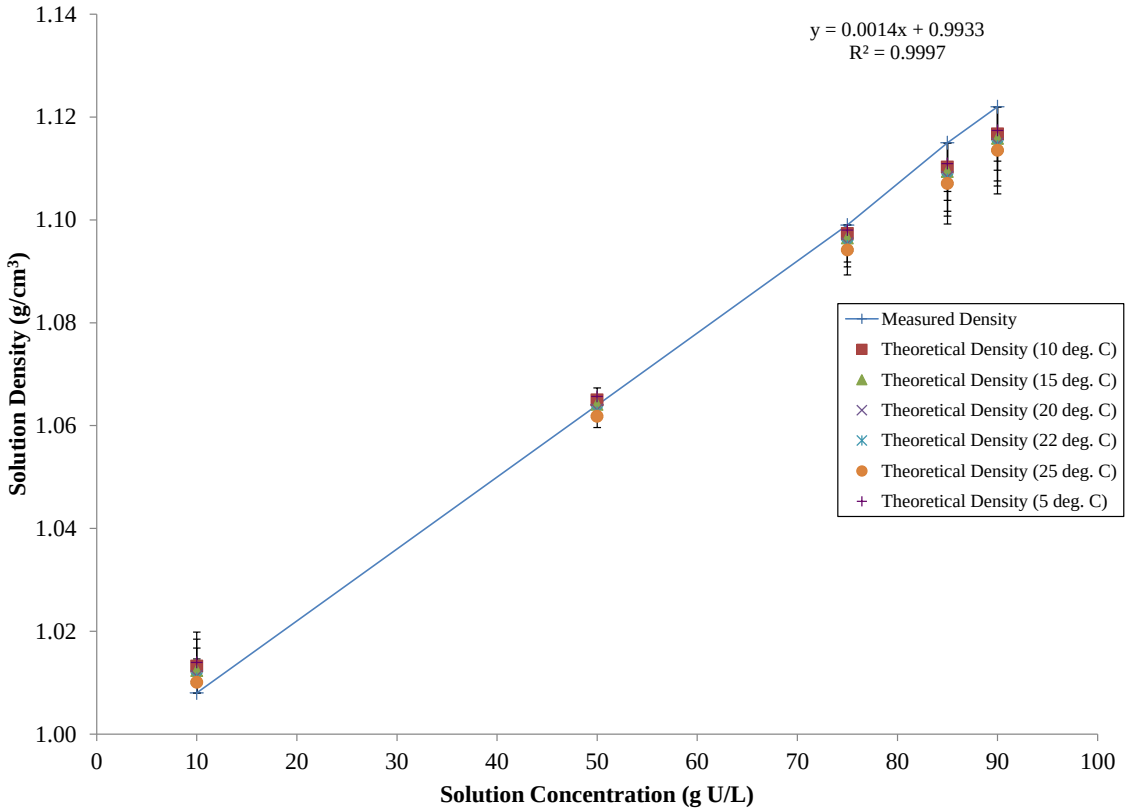

Figure 6-2. Comparison of Measured and Calculated Densities of Uranyl Nitrate as a Function of Uranium Concentration.

6.2 Gamma-Ray Signatures for Uranyl Nitrate Assay

In principle, any of the gamma rays emitted from uranium can be used to determine the isotopic composition in UN. However, in practice, signature gamma rays must be selected based on intensity, penetrability, and isolation from interfering signals. Photon emission from radioactive decay occurs via de-excitation in the nucleus through gamma-ray emission, or de-excitation by atomic electrons via x-ray emission. Alternatively, if charged particles are emitted, this could lead to the production of *bremsstrahlung* radiation. Beta decay of the ^{234m}Pa daughter of ^{238}U can produce *bremsstrahlung* radiation, but this effect in the water-based UN solution is relatively weak.

6.3 Age Effects and Decay Products in UN

Since the UN circulating in UNCLE is approximately 40 years old, which is substantially older than fresh UN in commercial facilities, a time-dependent source-term analysis was required to determine which gamma-ray signatures would best serve PM purposes. Decay product calculations were preliminarily addressed over a 100-year time span by Dewji *et al.* for the UN in UNCLE [48]. Thus, to ascertain the time-dependent radioactive decay and emission of radiation from decay of each of the uranium and actinium decay series, the program RadSrc v.1.5 was employed to computationally solve the Bateman equations [51]. Given the initial isotopic mixture and decay age, RadSrc calculates the decay product concentrations, yielding an output list of gamma rays and x-rays produced by radioactive decay, and the lineage of the decay series producing these photons. From the 1207 lines calculated by RadSrc, predominant photon emitters for fresh (0 y) UN and at secular equilibrium (1 y) for the UN composition in UNCLE are summarized in Table 6-2. Energies above a 100 keV cut-off are sorted by more intense photon intensity emissions (photons/s per gram U in UN).

Table 6-2. Source/Progeny Decay Chains of Predominant Photon Emitters in UN Composition in UNCLE.

Fresh UN (0y)		
Energy (keV)	**Intensity (photons/ s/g U)**	**Decay Chain(s)**
185.72	343.30	$[^{235}U]\blacktriangleright{}^{231}Th$
143.76	65.78	$[^{235}U]\blacktriangleright{}^{231}Th$
163.33	30.49	$[^{235}U]\blacktriangleright{}^{231}Th$
205.31	30.07	$[^{235}U]\blacktriangleright{}^{231}Th$
105.362	11.88	$[^{235}U]\blacktriangleright{}^{231}Th$
120.912	9.29	$[^{234}U,{}^{238}U]^{234}U\blacktriangleright{}^{230}Th$
109.16	9.24	$[^{235}U]\blacktriangleright{}^{231}Th$
202.11	6.48	$[^{235}U]\blacktriangleright{}^{231}Th$
108.99	3.96	$[^{235}U]\blacktriangleright{}^{231}Th$
194.94	3.78	$[^{235}U]\blacktriangleright{}^{231}Th$
110.5	2.96	$[^{238}U]\blacktriangleright{}^{234}Th$
182.61	2.04	$[^{235}U]\blacktriangleright{}^{231}Th$
140.76	1.32	$[^{235}U]\blacktriangleright{}^{231}Th$

UN Secular Equilibrium (1y)		
Energy (keV)	**Intensity (photons/ s/g U)**	**Decay Chain(s)**
185.72	343.30	$[^{235}U]\blacktriangleright{}^{231}Th$
1000.99	103.42	$[^{238}U]\blacktriangleright{}^{234m}Pa\blacktriangleright{}^{234}U$
143.76	65.78	$[^{235}U]\blacktriangleright{}^{231}Th$
766.412	39.69	$[^{238}U]\blacktriangleright{}^{234m}Pa\blacktriangleright{}^{234}U$ $[^{238}U]\blacktriangleright{}^{234}Pa\blacktriangleright{}^{234}U$
163.33	30.49	$[^{235}U]\blacktriangleright{}^{231}Th$
205.31	30.07	$[^{235}U]\blacktriangleright{}^{231}Th$
112.8	29.87	$[^{238}U]\blacktriangleright{}^{234m}Pa\blacktriangleright{}^{234}U$
111.025	12.52	$[^{238}U]\blacktriangleright{}^{234m}Pa\blacktriangleright{}^{234}U$ $[^{238}U]\blacktriangleright{}^{234}Pa\blacktriangleright{}^{234}U$
105.362	11.88	$[^{235}U]\blacktriangleright{}^{231}Th$
742.817	11.66	$[^{238}U]\blacktriangleright{}^{234m}Pa\blacktriangleright{}^{234}U$ $[^{238}U]\blacktriangleright{}^{234}Pa\blacktriangleright{}^{234}U$
120.912	9.29	$[^{234}U,{}^{238}U]^{234}U\blacktriangleright{}^{230}Th$
109.16	9.24	$[^{235}U]\blacktriangleright{}^{231}Th$
258.26	9.00	$[^{238}U]\blacktriangleright{}^{234m}Pa\blacktriangleright{}^{234}U$
786.287	6.83	$[^{238}U]\blacktriangleright{}^{234m}Pa\blacktriangleright{}^{234}U$ $[^{238}U]\blacktriangleright{}^{234}Pa\blacktriangleright{}^{234}U$
202.11	6.48	$[^{235}U]\blacktriangleright{}^{231}Th$
114.866	4.28	$[^{238}U]\blacktriangleright{}^{234m}Pa\blacktriangleright{}^{234}U$ $[^{238}U]\blacktriangleright{}^{234}Pa\blacktriangleright{}^{234}U$
945.9	4.13	$[^{238}U]\blacktriangleright{}^{234m}Pa\blacktriangleright{}^{234}U$ $[^{238}U]\blacktriangleright{}^{234}Pa\blacktriangleright{}^{234}U$
108.99	3.96	$[^{235}U]\blacktriangleright{}^{231}Th$
194.94	3.78	$[^{235}U]\blacktriangleright{}^{231}Th$
131.31	3.53	$[^{238}U]\blacktriangleright{}^{234}Pa\blacktriangleright{}^{234}U$
110.5	2.96	$[^{238}U]\blacktriangleright{}^{234}Th$
880.45	2.62	$[^{238}U]\blacktriangleright{}^{234}Pa\blacktriangleright{}^{234}U$
1737.73	2.61	$[^{238}U]\blacktriangleright{}^{234m}Pa\blacktriangleright{}^{234}U$
883.22	2.60	$[^{238}U]\blacktriangleright{}^{234m}Pa\blacktriangleright{}^{234}U$ $[^{238}U]\blacktriangleright{}^{234}Pa\blacktriangleright{}^{234}U$
569.3	2.51	$[^{238}U]\blacktriangleright{}^{234}Pa\blacktriangleright{}^{234}U$

Data calculated from [51] .

Reilly *et al.* state that an ideal monitoring signature would be an intense gamma ray ($> 10^4$ gammas/g-s), with an energy of several MeV [59]. The gamma-ray emission properties of uranium isotopes are summarized in Table 6-3.

Table 6-3. Gamma-Ray Properties of Uranium Isotopes.

Isotope	Energy (keV)	Specific Activity photons/g-s)
^{234}U	120.9	9.35×10^4
^{235}U	143.8	8.40×10^3
	185.7	4.32×10^4
^{238}U	766.4[a]	2.57×10^1
	1001.0[a]	7.34×10^1

[a] *^{238}U equilibrium with ^{234m}Pa assumed.*
Reproduced from [59].

As the scope of this work is focused on freshly processed UN, monitoring the most intense direct photons from ^{235}U (185.72 keV, 143.76 keV, and where possible, 163.33 keV) is recommended. Given the long half-life of ^{235}U compared to the 40-year decay period of the UN in UNCLE, effects in decay activity for ^{235}U are negligible in the scope of these measurements.

6.4 Conclusions

In anticipation of gamma-ray validation efforts, the time-dependent photon response was modeled with respect to contributions from radioactive decay products of the actinium and uranium decay series. Due to the attainment of secular equilibrium in the UN, notably by ^{234}U/^{238}U within the first year of decay, age effects from circulating 40-year-old UN showed no time dependence in anticipated photon response. Since ^{235}U has a half-life of 7.04×10^8 years, decay over a 40-year time span is negligible.

Identification of decay signatures will become important in analyzing measurement spectra from gamma-ray detectors, for features such as Compton buildup from higher energy ^{238}U gamma-rays influencing the continuum of lower-energy ^{235}U signatures.

These features will be further discussed in the experimental results for the dilution and facility measurements.

The presence of ^{238}U decay products in secular equilibrium in the UNCLE UN solution is not ensured from UN processed in an NUCP. In the scope of these experiments, use of aged UN must first confirm that there are no interferences of concern. Although continuum effects for the BEGe are less imminent than that of lower resolution measurements, the continuum subtraction from these latter spectra is more sensitive to the presence of other nuclides (i.e., ^{238}U). Since the same materials are employed for all measurements, such effects are all proximate. Consequently, it is beneficial to employ the aged UN, as subsequent work can draw on this data to provide multiple energy lines from various sources to confirm our understanding of the behavior of UN.

CHAPTER 7. THEORY: ATTENUATION FACTORS

At the established KMP, UN exiting the solvent extraction stream in an NUCP flows through an intricate array of stainless steel piping. Consequently, for NDA measurements, UN emissions must penetrate stainless steel piping. In addition, use of an external gamma-ray source for densitometry measurements must be calculated to determine emission intensity through the entire diameter of the UN-bearing pipe. Attenuation calculations for the UN and stainless steel piping are made using data from *XCOM: Photon Cross Sections Database* [58] in order to determine emission intensities, mean free paths, infinite thickness requirements, and self-attenuation corrections.

7.1 Attenuation Properties of UN-Bearing Pipe

The pipe employed in the dilution experiments and in UNCLE is from the same 304L pipe inventory, with dimensions summarized in Table 7-1 and depicted in Figure 7-1. The one-wall thickness of the 304L pipe in UNCLE measures 0.52±0.05 cm. As mentioned in Chapter 4, the pipe specifications for UNCLE were modeled on the conversion facility at Springfields, UK, providing a realistic test bed and specifications for NUCP facilities. The uncertainty effects of pipe thickness on the absolute efficiency are discussed in detail in Chapter 11.

Table 7-1. UNCLE Pipe Model Dimensions and Composition

Component	Density (g/cm^3)	Dimensions (cm)
Uranyl Nitrate Solution, 90 g U/L	1.122	7.84Ø × 60.2742
Stainless Steel Pipe, 304L	7.9	8.88Ø × 63.6524

(A) (B)

Figure 7-1: (A) Pipe segment employed in dilution measurements; (B) piping assayed in UNCLE measurements.

The transmission (as defined in Eqn. 7-1) through 304L pipe for 185.7 keV photons is calculated using XCOM and is plot in Figure 7-2. The linear attenuation coefficient at this energy through 304L pipe was found to be 1.14 cm^{-1}, with a 55.4% transmission through 0.52 cm of stainless steel.

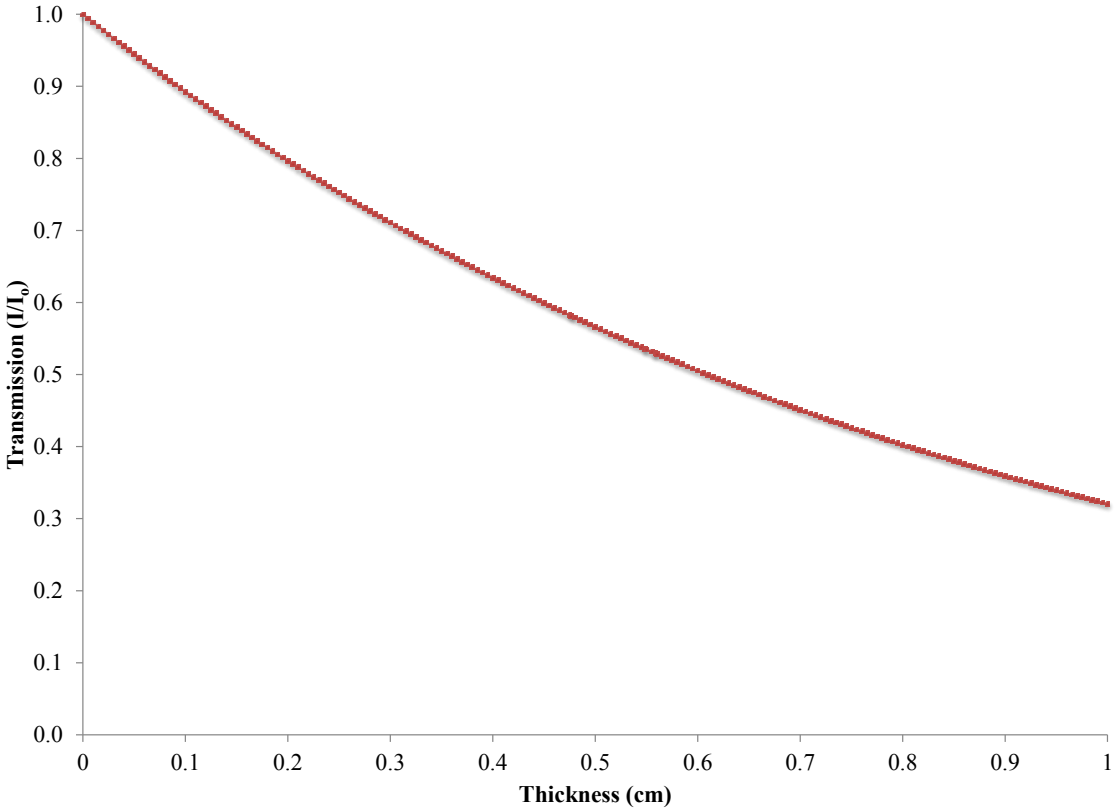

Figure 7-2. Gamma-Ray Transmission through Stainless Steel at 185.7 keV from ^{235}U.

7.2 Attenuation Properties of Uranyl Nitrate

Overall, the "visible volume" is determined by the combination of the detection geometry, collimation, and mean free path (MFP) of the gamma rays assayed [59]. If the uranium sample is large enough, a higher fraction of the 185.7 keV gamma rays emitted from ^{235}U will reach the detector. In addition to attenuation from the piping, strong self-absorption may occur for samples of a large diametric cross section containing high concentrations of uranium. The penetrability of the gamma-ray emissions can be quantified in terms of MFP values. The MFP is the average distance the photon travels before interaction and is quantified as the inverse of the linear attenuation coefficient, $(\mu\rho)^{-1}$ (cm^{-1}).

The linear attenuation coefficients of UN at dilution concentrations were determined using XCOM [58] and are given in Table 7-2. Table 7-2 also summarizes the subsequent calculations for MFP and infinite thickness values for dilution concentrations of the 185.7 keV photons from ^{235}U in UN. As the concentration and density increase, the UN has a higher MAC, indicating that the average distance to interaction decreases.

Table 7-2. Attenuation Properties of 185.7 keV Gamma Ray through Inner Pipe Diameter at Dilution Concentrations of Uranyl Nitrate.

Concentration UN (g U/L)	Density (g/cm^3)	Transmission (%)	MFP (cm)	# MFPs Across Inner Pipe Diameter	Infinite Thickness (cm)
90	1.122	11.65	3.65	2.15	25.53
85	1.115	12.36	3.75	2.09	26.25
75	1.099	13.90	3.97	1.97	27.81
50	1.064	18.75	4.68	1.65	32.78
10	1.008	30.10	6.53	1.20	45.72
0*	1.000	33.66	7.20	1.09	50.40

**100% water.*

Using the source term composition values for dilution concentrations calculated in Chapter 6, the calculated MAC values (without coherent scattering) for each of the dilution UN concentrations is summarized in Figure 7-3. In the range of ^{235}U high-intensity emissions (~100–200 keV), photoelectric interactions dominate in the calculation of the MAC, followed by Compton scattering. The energy range of the gamma-ray spectra resides above the uranium K-absorption edge, and we observe a smooth trend in $\mu(E)$.

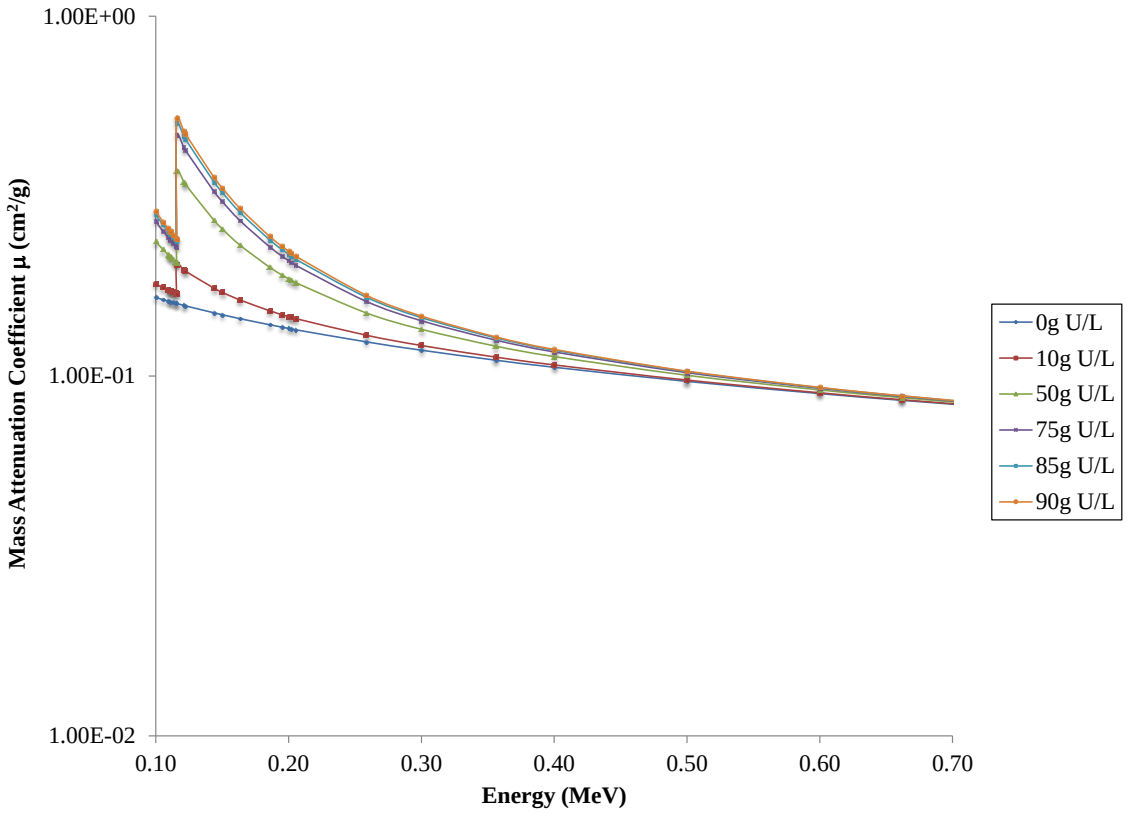

Figure 7-3: Total Mass Attenuation Coefficient at Dilution Concentrations of Uranyl Nitrate.

As shown in Figure 7-4, the diametrical transmission of UN is ~11.7% for 185.7 keV gamma rays at 90 g U/L across the UNCLE pipe (7.84 cm inner diameter). The transmission through UN (independent of pipe) is also summarized in Table 7-2. These calculated transmission values reflect transmission in narrow-beam (good) geometry for a highly collimated source emission traversing the full inner diameter of the pipe.

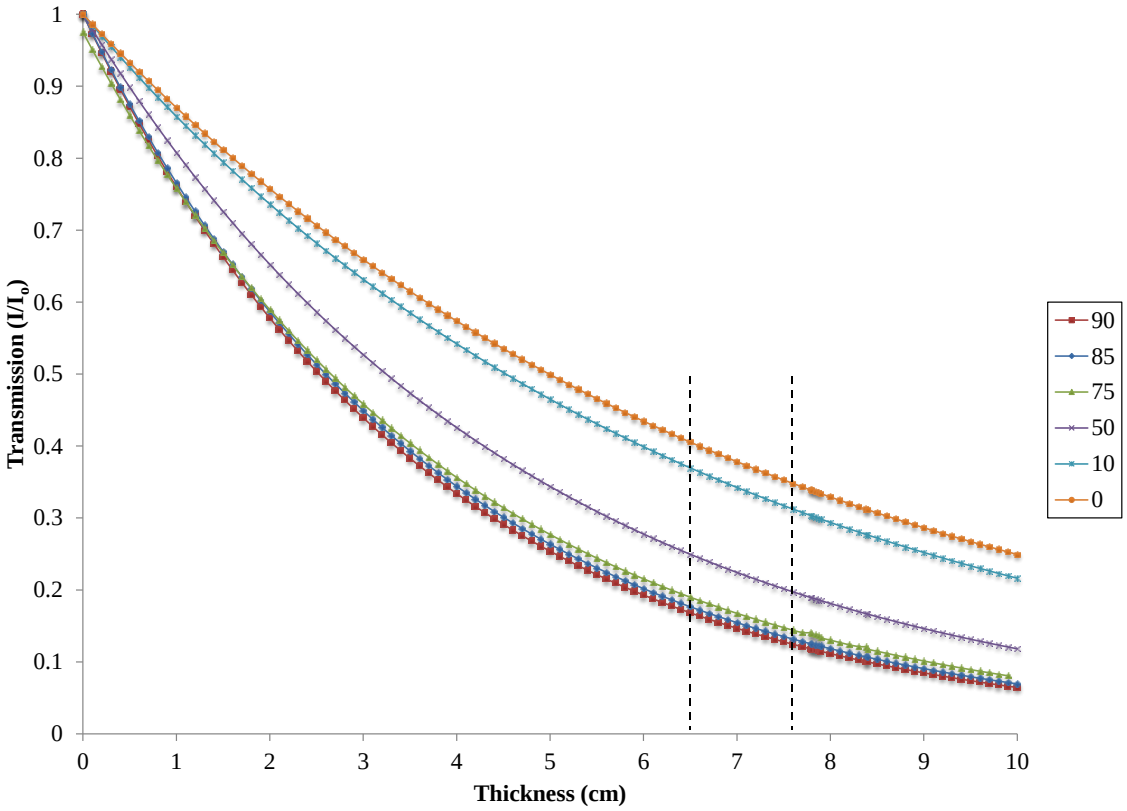

Figure 7-4. Transmission of 185.7 keV Gamma Ray through Various Concentrations of Uranyl Nitrate as a Function of Thickness.

7.3 Emission Intensities from Uranyl Nitrate-Filled Pipe

If we compare the attenuation properties of various dilutions of UN with the penetrability of the 304L piping, 1 mm of piping provides the equivalent of ~ 4 mm of 90 g U/L UN. Using the pipe specifications of Table 7-1, and the subsequent MACs and transmission values (Tables 7-1 and 7-4), the overall transmission of a 185.7 keV photon from the inner edge of pipe diameter penetrating the outer wall of the pipe across the diameter is summarized in Figure 7-5.

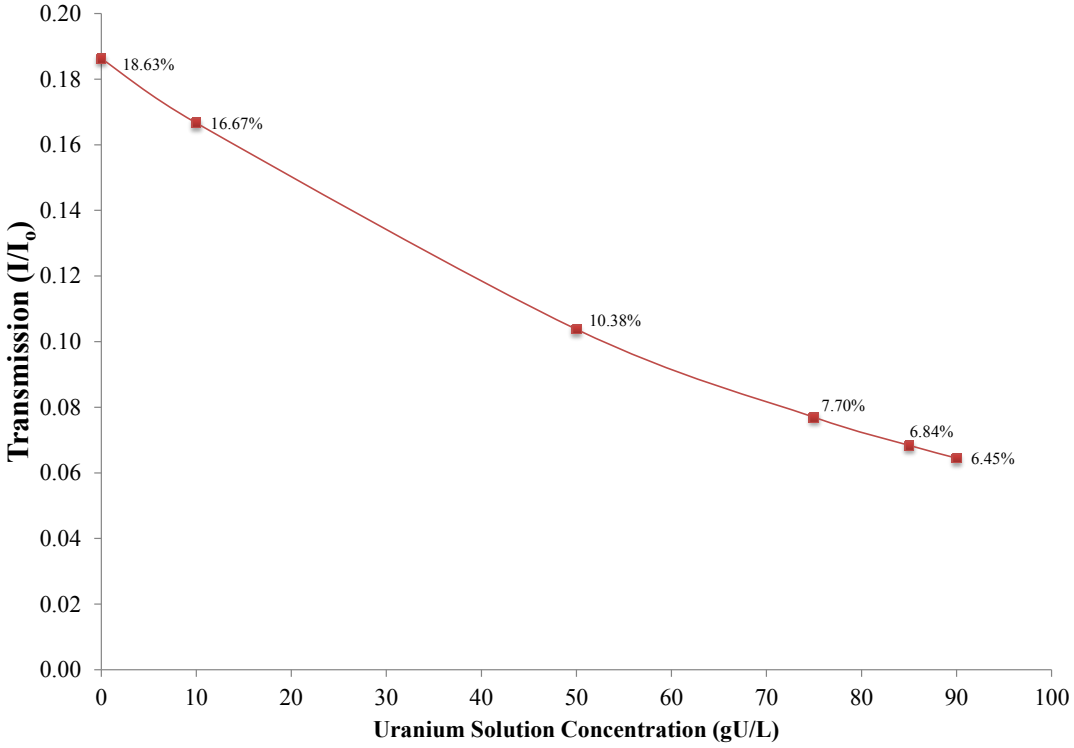

Figure 7-5. Transmission of 185.7 keV Photon within UN-Filled Pipe Segment as a Function of UN Concentration for Narrow-Beam Geometry.

7.4 Properties of Transmission Sources for Densitometry Monitoring

Densitometry is a measurement technique employed for determining the density of a material by determining the degree to which the sample material is attenuated the incident photons. Based on the source and sample attenuation properties, gamma-ray transmission measurements can provide further information on the composition of the sample and provide a measureable assay signal, as attenuation is dependent on both the atomic numbers (Z) and density of the sample. In the scope of this work, external transmission sources penetrating the UN-filled pipe can provide insights into the material concentration, density, and uranium enrichment of UN.

Smith *et al.* identify a range of useful transmission values for a characteristic sample concentration, $\rho_c = 1/\mu x$ [83]. The measurement is favorable when $|ln\ T| > 1$ and $\rho > \rho_c$, which is consistent with the calculated transmission values for UN in the previous section, for which $1.35 < |ln\ T| < 1.48$ and ρ_c (~0.7) $< \rho$ (from Table 7-2). If $\rho_c > \rho$, then the assay signal is too small and the measurement is unfavorable. Determination of the favorable operating range based on ρ_c assists in selecting an optimal sample thickness. On the basis of Smith's analysis, the measurement parameters for passive gamma-ray assay for the UN-filled pipe are favorable.

A transmission-based in-line densitometer using the 662 keV gamma-ray from ^{137}Cs was selected; the 122 keV in ^{57}Co line is certainly more preferable for assaying ^{235}U as explained in Section 7.2, as it does not interfere with 185.7 keV peak, does not contribute to the Compton continuum under lower-energy ^{235}U photons, and is much more sensitive in characterizing attenuation properties of various concentrations of UN (Figure 7-6). Similarly, the 356 keV photon as a transmission source from ^{133}Ba would have been an adequate (though a less preferable substitute to ^{57}Co), but the available source was too weak for laboratory measurements. As seen in Figures 7-3 and 7-6, the MAC at 356 keV still possesses sufficient discrimination for the dilution concentrations of UN. However, ^{133}Ba has three high-intensity photons in the 300–400 keV range, which would interfere in unfolding low-resolution densitometry measurements. The selection of ^{137}Cs is sufficient (though not optimal) for densitometry purposes, as it possesses a strong monoenergetic photon emission at 661.7 keV, which will alleviate any transmission peak overlap discrimination with lower resolution measurements. As the ^{133}Ba and ^{57}Co sources were not available for measurement in this project, their applicability is investigated in Chapter 11 in the purview of validated simulations and attenuation properties described in this chapter.

The MAC and linear attenuation coefficients for transmission sources penetrating dilution concentrations of UN were calculated using XCOM and are summarized in Table 7-3. Transmission values for the external source energies through 304L pipe, as well as UN, are graphed in Figures 7-7 through 7-9 for ^{57}Co, ^{133}Ba, and ^{137}Cs.

Table 7-3. Linear Attenuation Coefficients of External Transmission Sources for Densitometry Measurements.

Solution Concentration (g U/L)	122.1 keV	356 keV	661.7 keV
304L Pipe	1.85	0.76	0.57
90	0.53	0.14	0.10
85	0.51	0.14	0.10
75	0.47	0.14	0.10
50	0.36	0.13	0.09
10	0.20	0.11	0.09

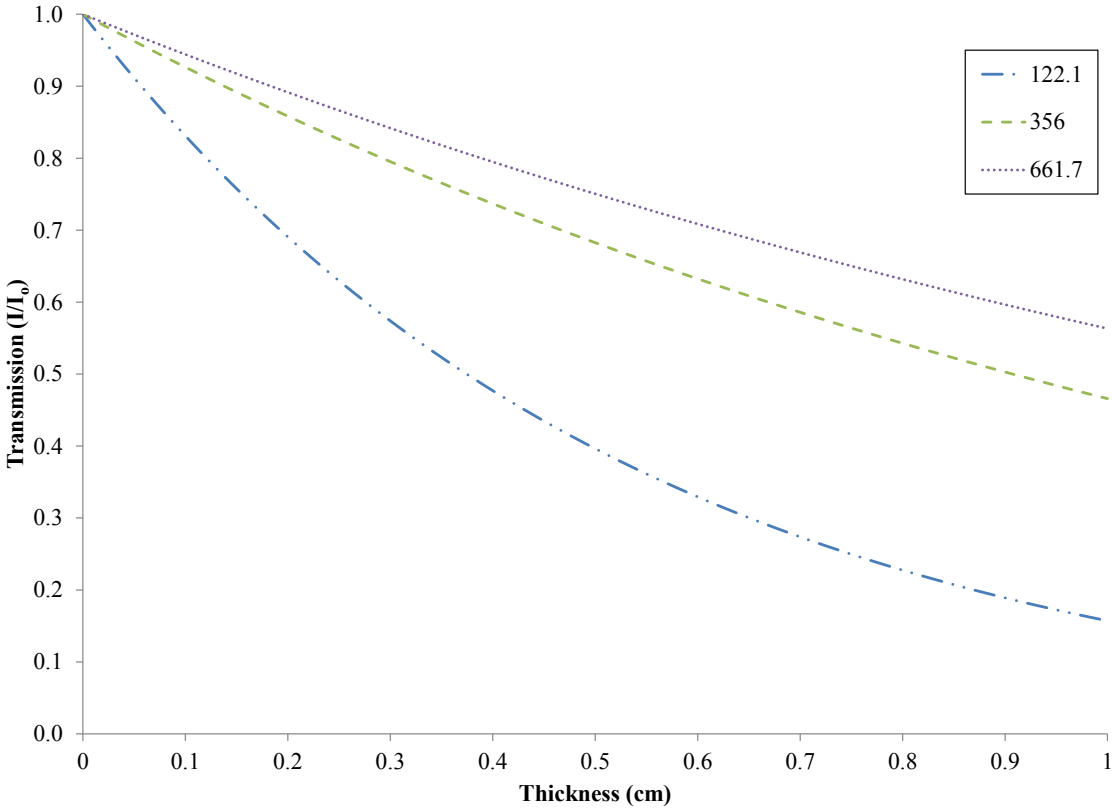

Figure 7-6. Gamma Ray Transmission through Stainless Steel at Various Transmission Energies.

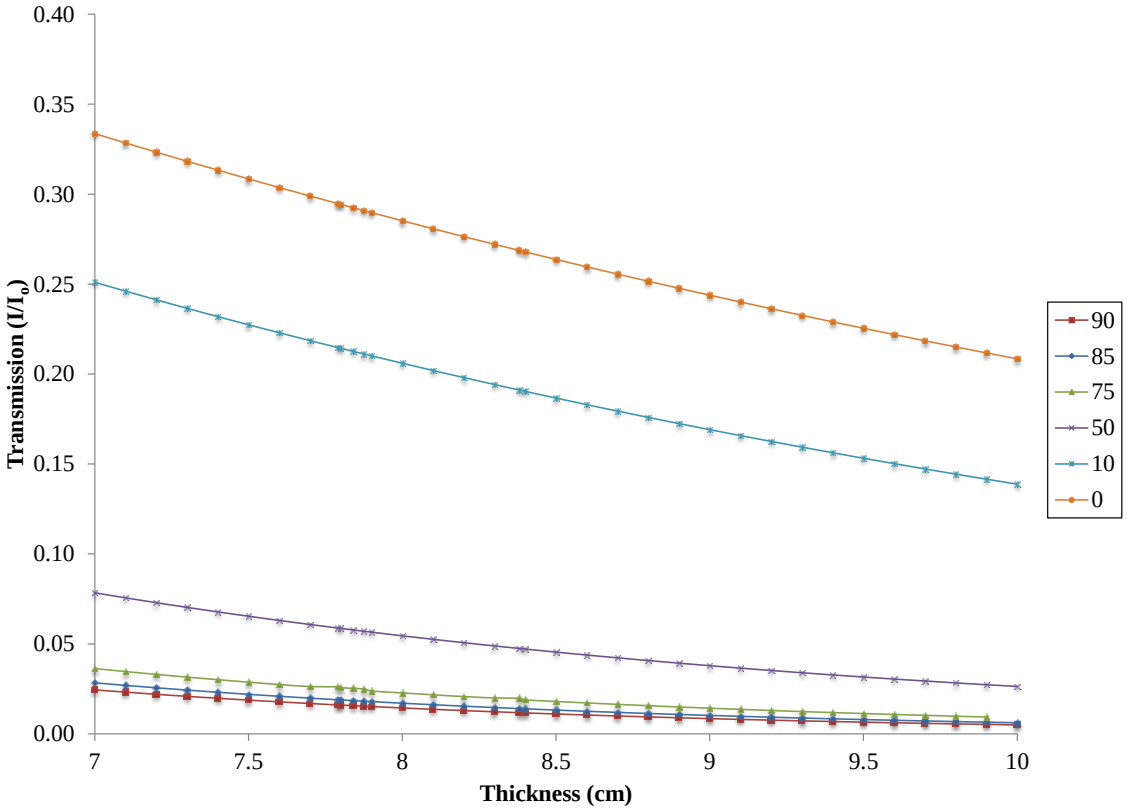

Figure 7-7. Transmission of 122.1 keV ^{57}Co Photon through Various Concentrations of UN as a Function of Thickness.

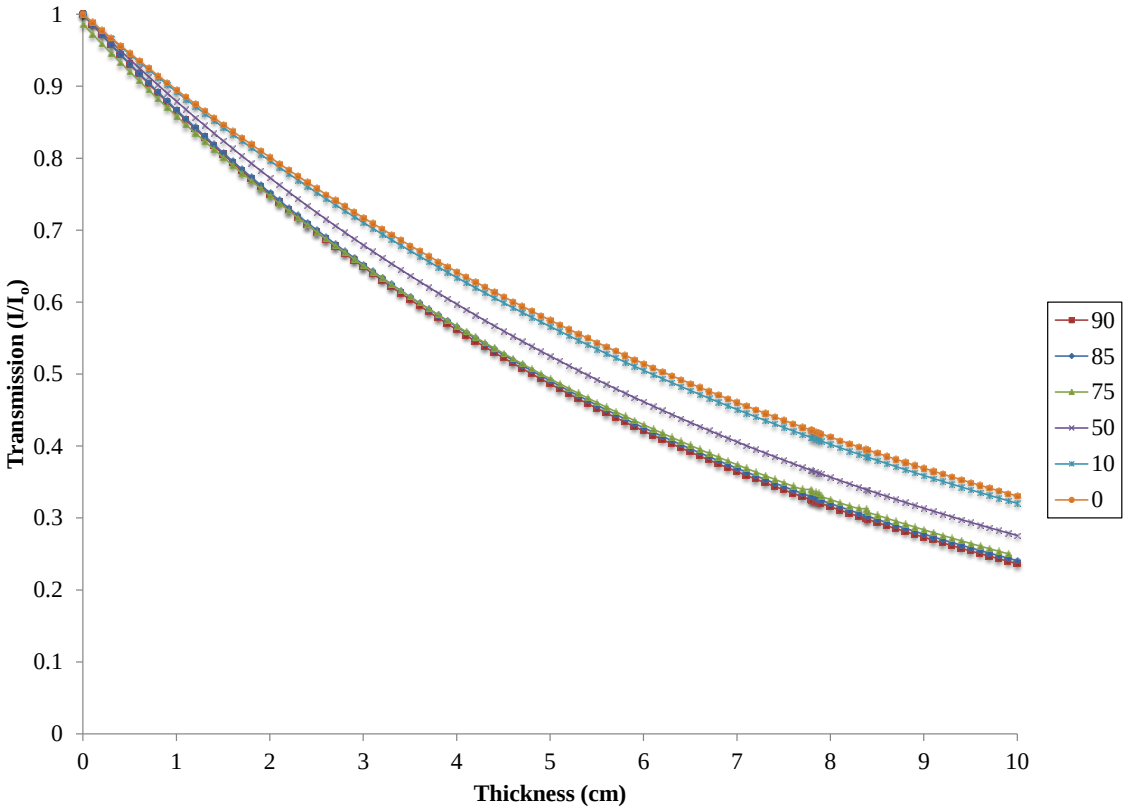

Figure 7-8. Transmission of 365 keV ^{133}Ba Photon through Various Concentrations of UN as a Function of Thickness.

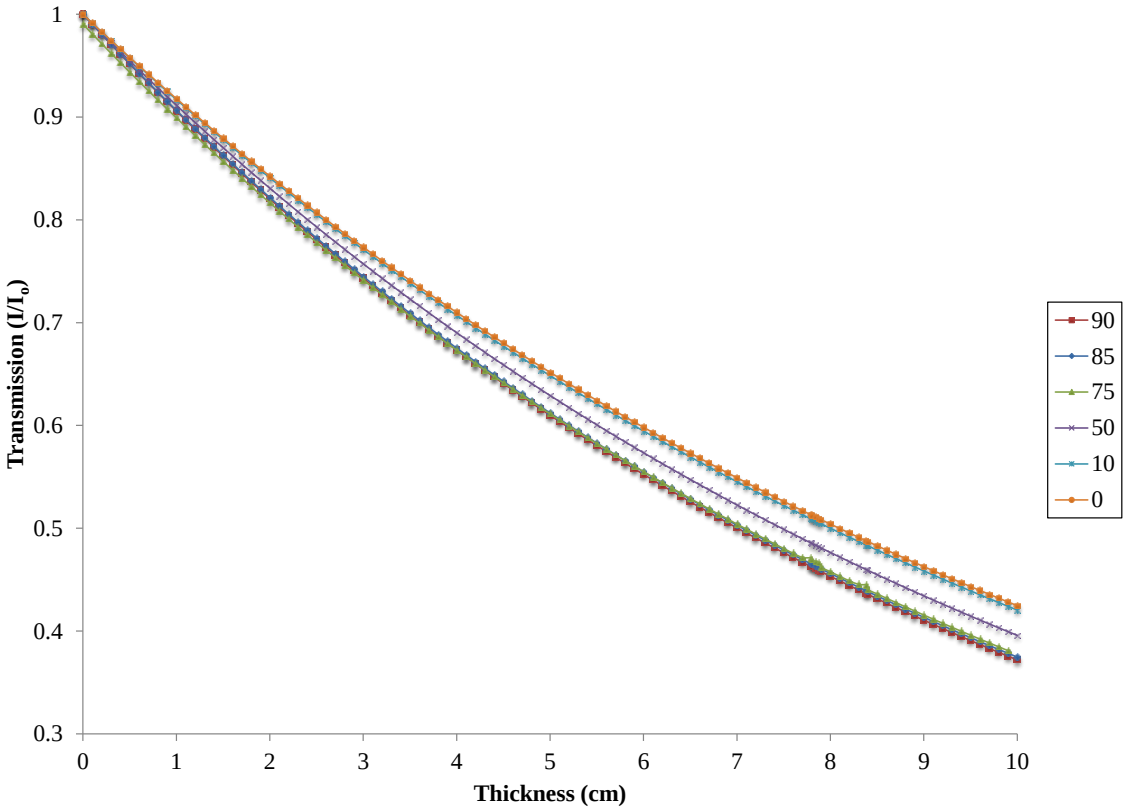

Figure 7-9. Transmission of 661.7 keV ^{137}Cs Photon through Various Concentrations of UN as a Function of Thickness.

The highest energy photon - 661.7 keV from ^{137}Cs – is most penetrative, where the ^{57}Co with the lowest energy at 122.1 keV is the least penetrative, as expected. Where ^{137}Cs may be best suitable for gross densitometry measurements, ^{57}Co and ^{133}Ba provide more discrimination regarding uranium content in the pipe. This is supported by Figure 7-6 and plot in Figure 7-10 for an external transmission source traversing the diameter of the UN-filled pipe. Lower transmission as seen in ^{57}Co can be remedied practically by using a higher activity source. Given that the half-life of ^{57}Co is only 270 days, this may present some practical implementation challenge for safeguards PM. The half-life of ^{133}Ba is more long lived at 7.2 years, which would require less frequency of replacement, but still presents challenges in discriminating transmission in low-resolution systems. The longest half-life is 30 years from ^{137}Cs, which is operationally favorable, but this source provides

lower discrimination in uranium content for PM. Chapter 15 will outline the operational implementation requirements for employing a transmission source form PM.

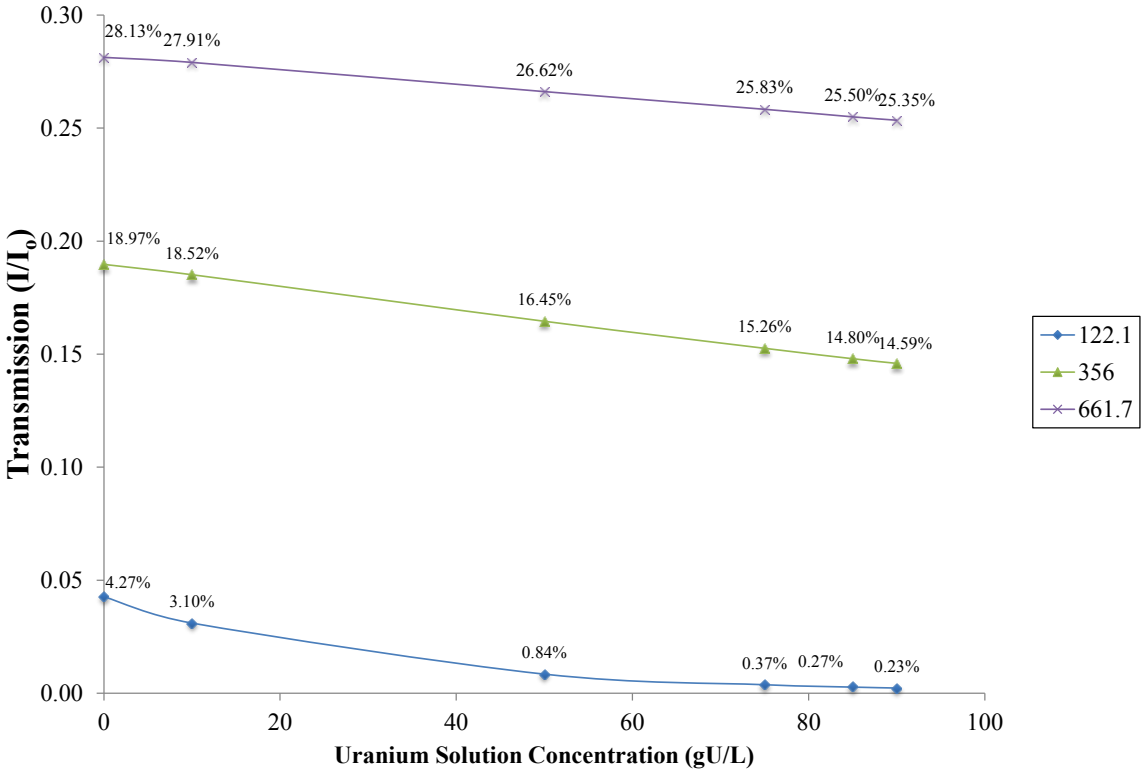

Figure 7-10. Transmission of 122.1 keV, 356 keV, and 661.7 keV Photons in UN-Filled Pipe Segment as a Function of UN Concentration for Narrow-Beam Geometry.

7.5 Self-Attenuation Correction Factor

7.5.1 Measurement and Calculation of Self-Attenuation Correction Factor for UN in Pipe

In determining *CF(AT)* in the scope of this work, *T* was calculated by taking a transmission ratio of the UN-filled pipe *(I)* with an empty pipe *(I_o)*. The signal measured was from BEGe detector measurements of the ^{137}Cs 661.7 keV transmission signal. As empty pipe measurements were not feasible in this experimental work, a Monte Carlo model was developed and validated based on acquired measurements. The measurement data are summarized in Chapter 9, and the parameters of the validation simulations are provided in Chapter 11. The ratio of I/I_o is related to *T* through the inner diameter of the pipe, *d*, via the following relation:

$$\frac{I}{I_o} = T = e^{-\mu\rho d} \ . \qquad [7\text{-}1]$$

The net peak area of the transmitted 661.7 keV photons through the full and empty pipes provided a value for *T*. Applying Eqn. 7-1 to the validated transmission simulations provides *T* for each of the dilution densities/concentrations. The plot of *ln(1/T)* as a function of solution density (for each dilution concentration) is shown in Figure 7-11.

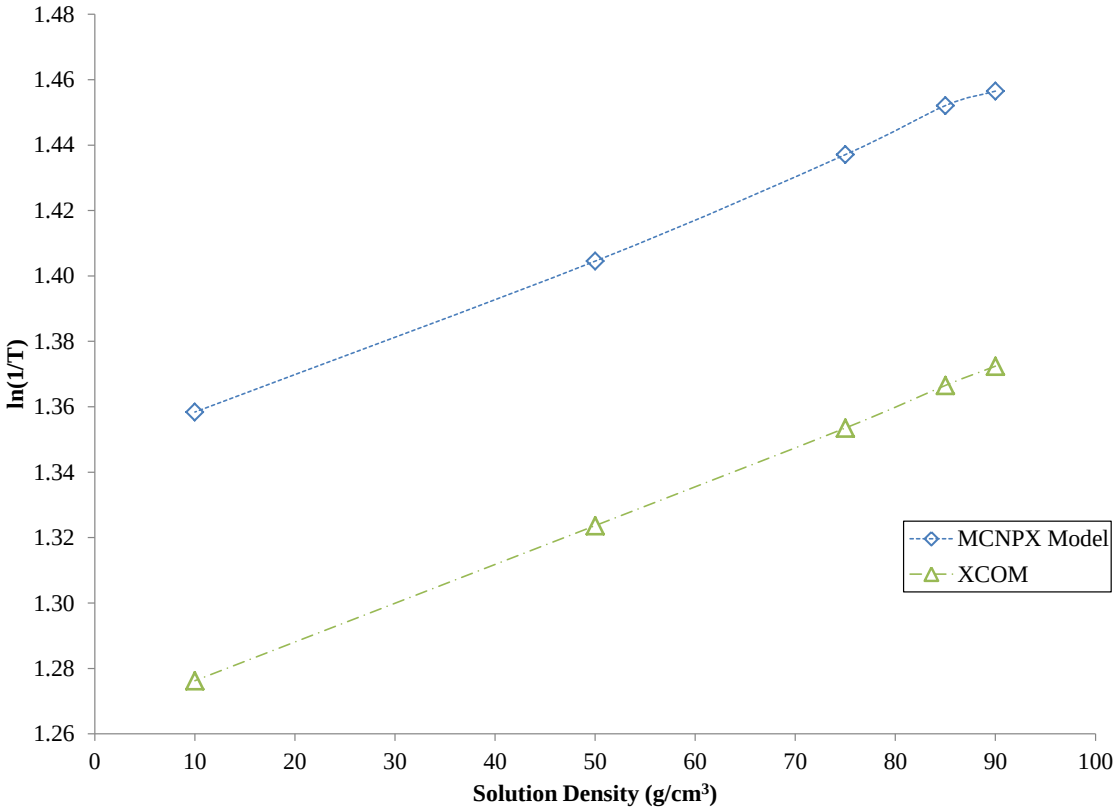

Figure 7-11. ^{137}Cs Source Transmission as a Function of UN Solution Density for Calculation of *CF(AT)*.

Note that in Figure 7-11, the transmission measurements were compared to the transmission values calculated in the previous section with XCOM for narrow-beam geometry. The transmission values for XCOM were much higher compared to the transmission calculated using Parker's method for *CF(AT)*. Taking into account source-detector geometry and self-attention of the material results in a lower transmission value, which is consistent with the results of Figure 7-11.

Finally, applying Eqn. 5-8 for various values of κ (empirically determined) to the ^{137}Cs transmission data provides us the overall calculation of *CF(AT)* for our UN-filled pipe, given Figure 7-12. Figure 7-13 provides an alternative view of *CF(AT)* as a function of

transmission through UN of each of the dilution concentrations. Figures 7-12 and 7-13 are consistent with the similar experiment conducted by Parker (provided in Figure 5-4).

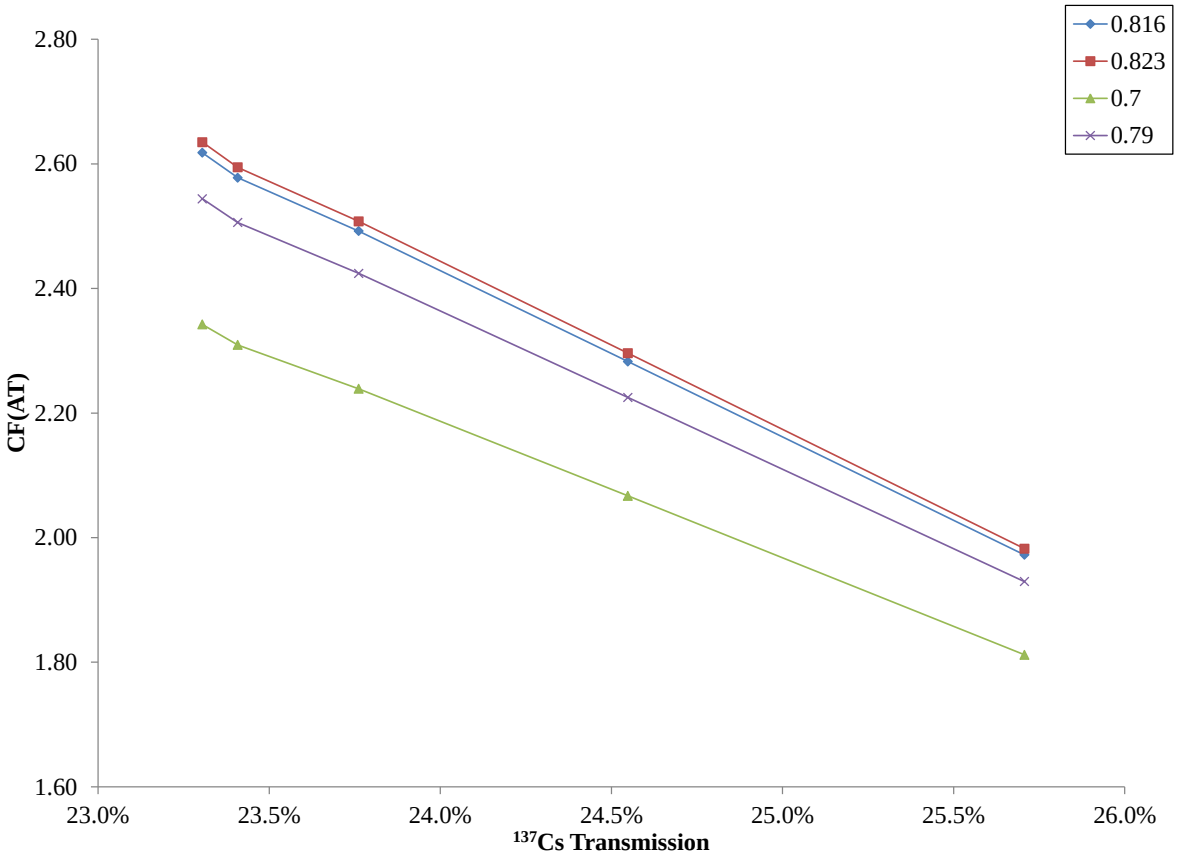

Figure 7-12. Calculation of *CF(AT)* for UN-Filled Pipe as a Function of Transmission through Dilution Concentrations for Various Values of *κ*.

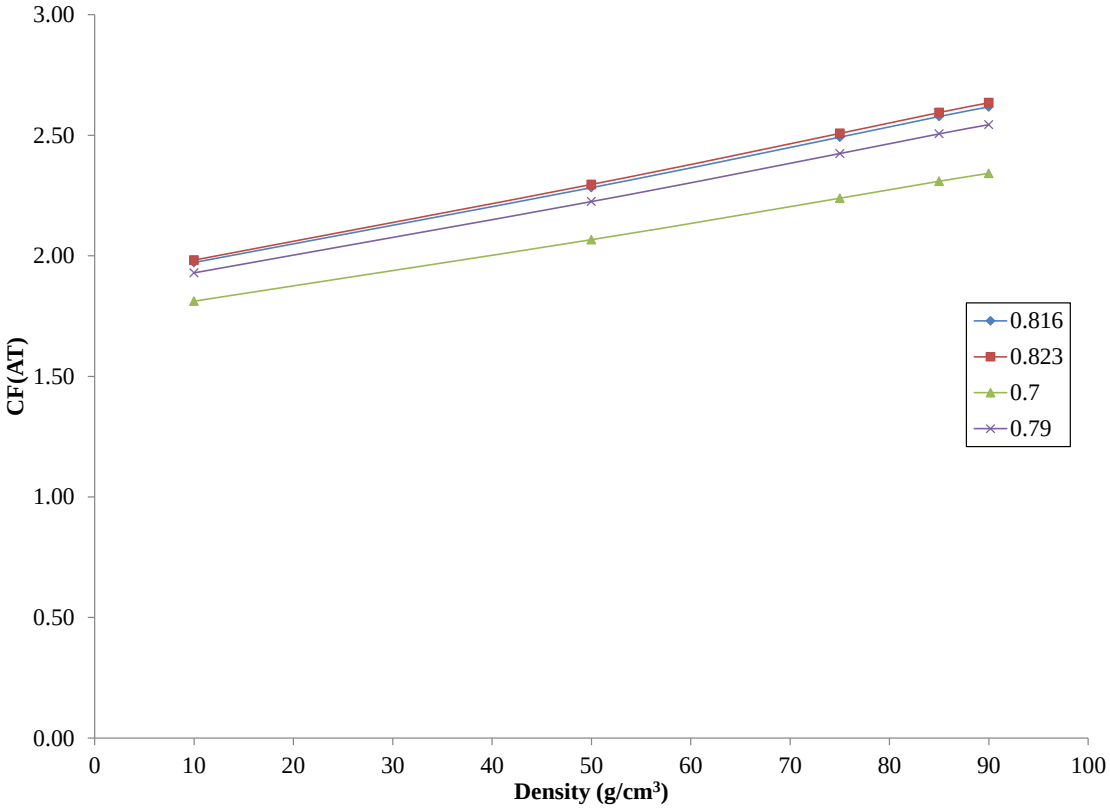

Figure 7-13. Calculation of CF(AT) for UN-Filled Pipe as a Function of Dilution Concentrations for Various Values of κ.

7.6 Conclusions

Analysis of the attenuation effects of the source and detector system provides essential insights into the characteristics of the UN material flowing in NUCPs. Identification of the photon interactions occurring provided an assessment of the behavior of the 185.7 keV photons as a monitoring signature. Furthermore, attenuation analysis provided a basis for identifying which external densitometry transmission sources were optimal for monitoring density and uranium content. Although the ^{57}Co was preferable to ^{235}U transmission measurements, the availability of ^{137}Cs suffices for determining the correction factor due to self-attenuation of the UN-bearing pipe. Determination of the correction factor due to self-attenuation provided a source-detector geometry-corrected

assessment of what fraction of emitted ^{235}U gamma rays actually reached the detector. As expected, narrow-beam geometry theoretically predicted higher transmission values in the absence of accounting for self-attenuation.

CHAPTER 8. COMPUTATIONAL MODELS

The experimental measurements undertaken in the scope of this project provide an overall assessment of the sensitivity of gamma-ray detection technology to variations in concentration, as well as to determine the monitoring capabilities in an operational conversion facility. However, a myriad of variables – including those affecting solution properties and detector efficiency – could not be experimentally tested. Thus, experimentally validated simulations provide a benchmarked detector response to examine these variables including variations in enrichment[3], in addition to detector responses to variations in transmission densitometry. A summary of the computational models to simulate the detector response of the Falcon BEGe detector for the passive dilution and transmission measurements is presented in this chapter. All photon transport simulations were conducted using MCNPX [78].

8.1 Falcon BEGe Detector Model

As the detector providing the highest resolution signatures, the Falcon BEGe detector was modeled in detail to determine validated detector responses. A pulse-height tally (F8) was performed over the active region of the detector crystal to determine the pulse-height spectrum. Since actual measurements were accumulated as 8192-channel pulse-height

[3] The scope detector response to enrichment simulations is reserved for the sensitivity analysis in Chapter 12.

spectra, the MCNPX pulse height spectra were similarly binned and tallied into 8192 channels spanning a total energy range of 0 to 1.59 MeV (0.194 keV/channel).

8.1.1 Simulation Geometry

The dimensions and physical characteristics of the detector are outlined in the sample MCNPX input file in Appendix E, and the detector material properties are presented in Table 8-1. A VisEd [78] rendering of the detector model is given in Figure 8-1. As shown in Figure 8-1, the HPGe crystal is 1.37cm from the endcap surface of the collimator, and the detector endcap is maintained at a ¼-inch (0.635 cm) distance from the pipe surface. In practice, having the detector collimator maintained at a very short (off-contact) distance will prevent degradation in resolution due to vibrations from UN flowing in pipes, in addition to minimizing associated temperature variations. Maintaining the detector at a closer distance increases the rate of counts reaching the detector, while correspondingly lowering the relative background from the facility leaking into the collimator; the open geometry is harder to reproduce and maintain.

Table 8-1. Detector Material Specifications.

Detector Component	Weight Percent Composition	Thickness (cm)	Density (g/cm^3)
High-Purity Germanium Crystal [70], [73]	100.0% Ge	2.985 Ø × 2.0	5.32
Collimator Endcap Face – Epoxy [63], [73], [81]	6.0% H 72.1% C 21.9% O	0.15	11.00
Collimator [63], [81]	98.0% W 1.71% C 0.29% H	0.8	1.03

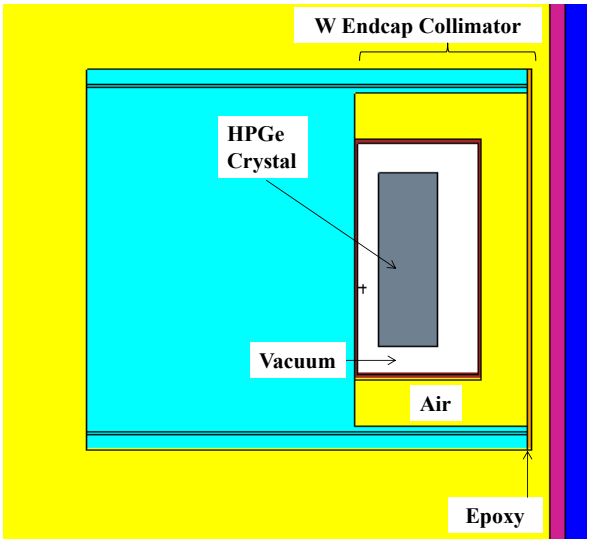

Figure 8-1. VisEd Model of HPGe Detector and Collimator.

The simulation was modeled after the experimental setup for the dilution measurements, employing lead brick shielding around the perimeter of the collimator, as well as behind the pipe acting as a backshield. This encompassing shielding configuration was to compensate for background from surrounding tanks and pipes in an industrial conversion facility. The pipe and brick characteristics are given in Table 8-2 and depicted in Figures 8-2 and 8-3. Figure 8-3 also shows a photograph of the experimental setup juxtaposed with the VisEd models, where dots in Figure 8-3(C) represent collisions by the source particles.

Table 8-2. Pipe, Detector, and Shielding Configurations.

Setup Component	Weight Percent Composition	Dimension (cm)	Density (g/cm^3)
Lead Bricks	100% Pb	20.3 × 10 × 5	11.34
Uranyl Nitrate Solution	Table 8-3	7.84Ø × 60.27	Table 8-3
Pipe [84]	Fe 5.936% Cr 1.743% Ni 0.772 % Mn 0.174%	8.88Ø × 63.65	7.98
Surrounding Air [84]	75.58% N 23.14% O 1.28% Ar	-	0.001293

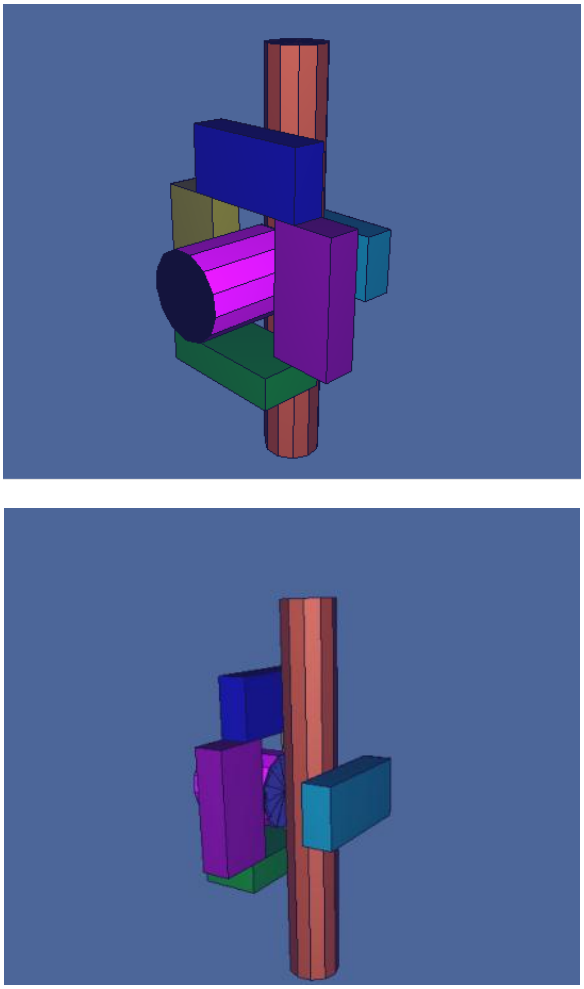

Figure 8-2. VisEd Represenation of Pipe, Detector, and Pb Brick Shielding Configuration Employed in Experimental Measurements.

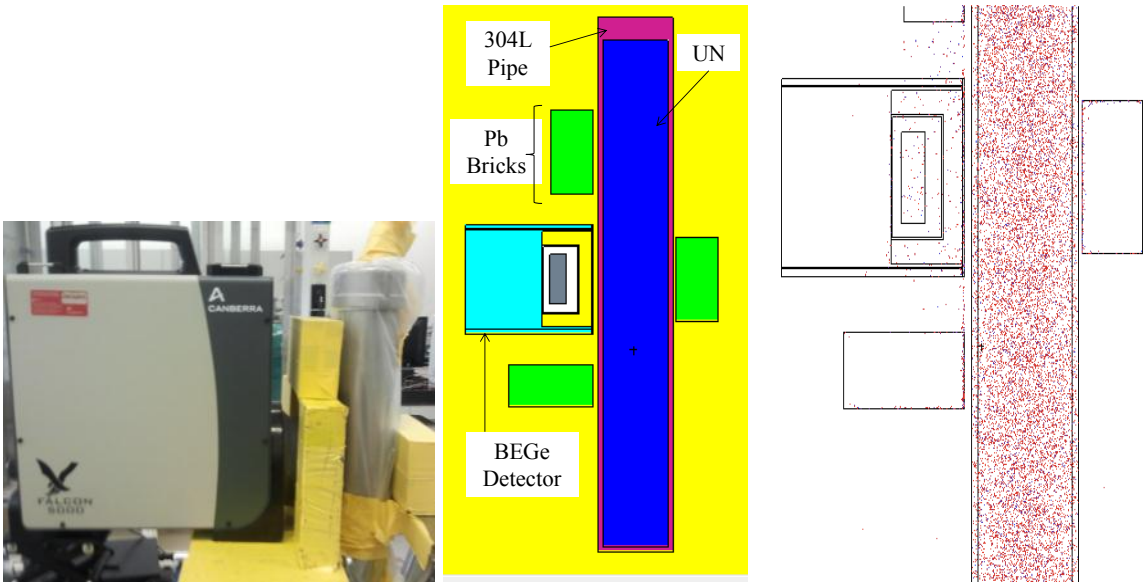

Figure 8-3. Falcon BEGe Detector Setup and Simulation Models.

(A) Photograph of Dilution Experimental Setup of Pipe Segment with Falcon; (B) VisEd Representation of Dilution Experiment; (C) VisEd Simulation of Source Particle-Collisions of Dilution Experiment.

8.1.2 Gaussian Energy Broadening Fit

The GEB function [78] in MCNPX was used to simulate the detector resolution, based on FWHM data obtained from calibration measurements for the dilution experiments. The parameters required for the GEB function (*a*, *b*, and *c*) were calculated based on various gamma-ray sources, and iteratively fit to Equation 5-11 to obtain the GEB parameters.

The detector resolution was determined from calibration sources. The parameters and use of the GEB function may be found in the example MCNP input file in Appendix E. According to the Canberra, the crystal has a FWHM of 0.7 keV at 122 keV, compared to the measured ~0.8 keV FWHM. Any degradation in resolution could be due to mechanical vibrations in the detector, as well as temperature variations. The data from

the FWHM measurements for the GEB fit are plot in Figure 8-4. The GEB parameters were fit using Gnuplot 4.4.3[85] are shown in Figure 8-5.

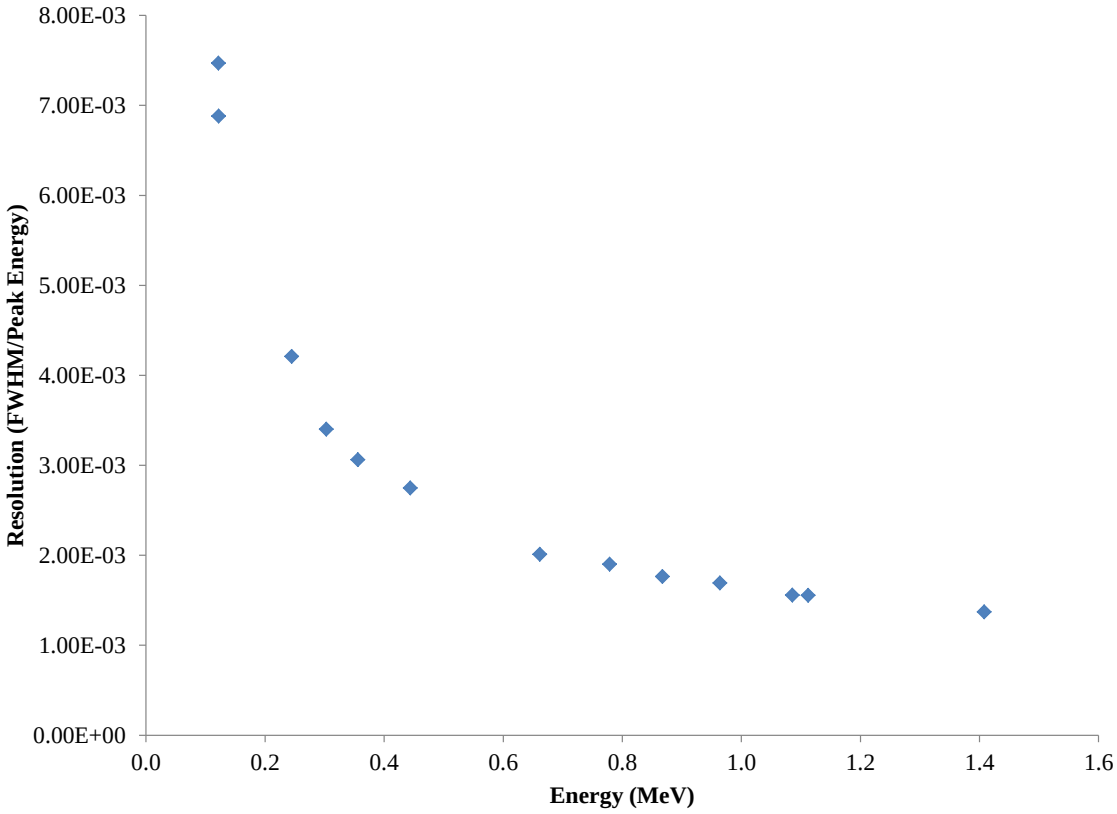

Figure 8-4. Detector Resolution Measured Using Calibration Sources for Falcon BEGe.

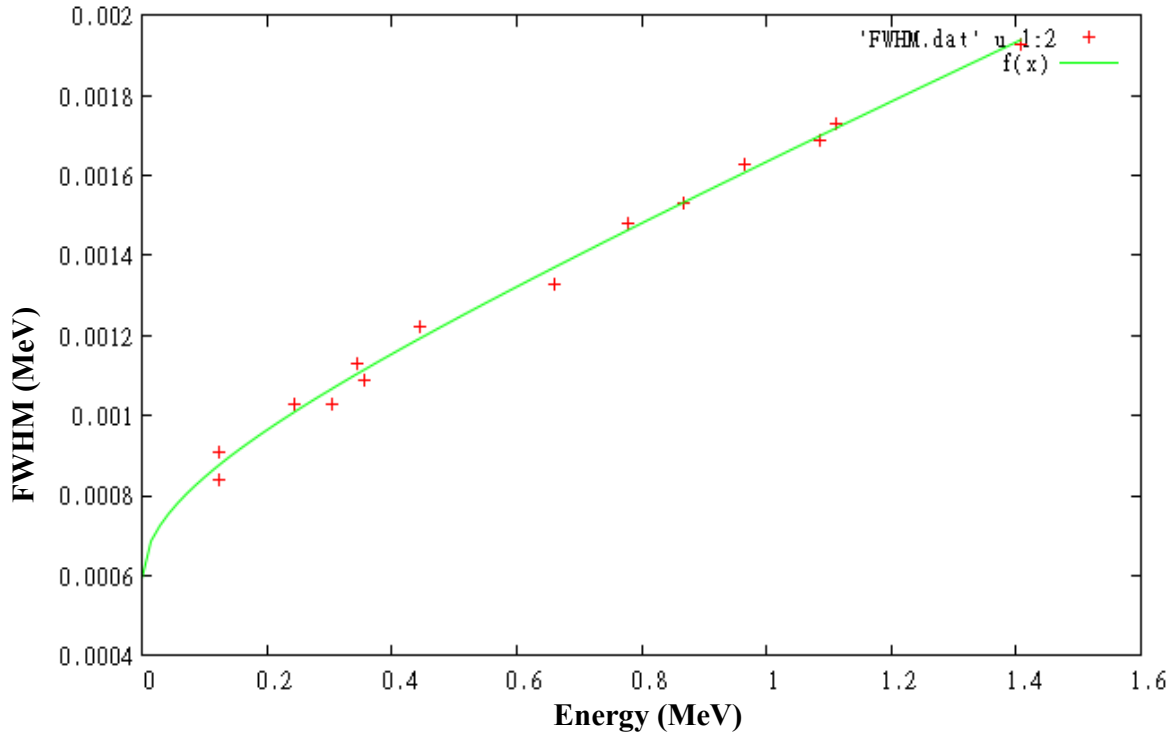

Figure 8-5. Gnuplot Fit of FWHM as a Function of Energy to Obtain the Gaussian Energy Broadening Parameters.

Y-axis: FWHM (MeV) vs. X-axis: Energy (MeV).
Fit parameters: $a=(59.5\pm6.15)\times10^{-5}$, $b=0.000763\pm0.000147$, $c=0.85487\pm0.4942$.

8.2 Passive Dilution Simulations

8.2.1 Passive Dilution Material Composition

At 90 g U/L, the pipe contains 2.62 L of solution with a mass of 2939.64 g, of which ~241 g is natural uranium. The UN material composition employed in each of the validation simulations for passive gamma-ray measurements using the BEGe detector is summarized in Table 8-3. Densities were based on actual measurements taken during dilution.

Table 8-3. Material Composition of Uranyl Nitrate Solution in Pipe Segment (2.62 L).

Solution Concentration (g U/L)	90	85	75	50	10
Molarity (M)	0.378	0.357	0.315	0.210	0.042
Density (g/cm^3)	1.122	1.115	1.099	1.064	1.008
Total UN Solution Mass in Pipe (g)	2939.64	2921.30	2879.38	2787.68	2640.96
Wt.% U	8.02%	7.62%	6.82%	4.70%	0.99%
Wt.% N	0.71%	0.67%	0.60%	0.41%	0.09%
Wt.% H	9.75%	9.82%	9.95%	10.32%	10.94%
Wt.% O	81.52%	81.88%	82.62%	84.57%	87.98%
Wt.% $UO_2(NO_3)_{1.5}$	12.23%	11.63%	10.41%	7.17%	1.51%
Wt.% H_2O	87.77%	88.37%	89.59%	92.83%	98.49%

8.2.2 Passive Dilution Source Definition

Since the MCNP F8 tally is normalized to emissions per source particle, the tally output was multiplied by the exact source activity of the sources employed in the validation measurements and intensities in order to replicate laboratory measurements. These are the number of particles emitted per decay, where ^{235}U emits photons at multiple energies from each decay. Therefore, the sum of each of the emissions must be considered. The intensity of each ^{235}U photon emission is summarized in Table 8-4 for intensities > 0.1%. The full source definition (energies and intensities/probabilities) is provided in Appendix E.

The assay activities of the sources employed in the benchmark measurements are summarized in Table 8-5. The difference between fresh and aged UN for ^{235}U activity is

negligible (< 4×10^{-6} %), given the long half-life of ^{235}U; thus, we can assume the activity at 44 years (as in UNCLE) for ^{235}U approximates the response from fresh ^{235}U.[4]

Table 8-4. Source Photon Emissions from ^{235}U.

Energy (keV)	Intensity (%)
185.712 ***1***	57.2 *5*
143.764 ***2***	10.96 *8*
163.358 ***2***	5.08 *4*
205.309 ***2***	5.01 *5*
109.16 ***2***	1.54 *5*
202.111 ***3***	1.08 *2*
194.94 ***1***	0.63 *1*
182.52 ***2***	0.34 *2*
279.50 ***5***	0.27
140.76 ***4***	0.22 *2*
221.399 ***1***	0.12 *1*
72.7 ***2***	0.11
199.6 ***1***	0.1

Data from [61].

Table 8-5. ^{235}U Activity for Fresh UN at Dilution Concentrations.

Dilution Concentration (g U/L)	Calculated Activity Fresh ^{235}U (Bq)
90	1.59×10^{5}
85	1.51×10^{5}
75	1.33×10^{5}
50	8.84×10^{4}
10	1.76×10^{4}

Although these results simulate the ^{235}U emissions, ^{238}U decay chain emissions will contribute to Compton continuum buildup under the ^{235}U peaks between 140–205 keV compared to UN in secular equilibrium. In the scope of this work, since secular equilibrium for freshly processed UN from an NUCP cannot be ensured, analysis has

[4]Note: ^{238}U was not modeled in the scope of the MCNPX simulations provided in Appendix E in order to accurately reproduce solvent-extracted UN.

been confined to that of the ^{235}U signatures. The simulation results compare the MCNPX output for source definitions of both fresh and secular equilibrium. These are provided as a reference in Appendix F.

8.3 Densitometry Transmission Simulations

8.3.1 ^{137}Cs Transmission Dilution Simulations

As explained in Chapter 5, ^{137}Cs was selected as an external transmission source for densitometry measurements. The UN-filled pipe, collimation, and shielding remained the same as modeled in the passive measurements (sample MCNPX input is provided in Appendix E). In the ^{137}Cs transmission simulations using the same model, a plastic-encased checked source is affixed to the midpoint of the pipe in direct line with the detector's central axis. A VisEd rendering of the transmission source in given in Figure 8-6, where the dots in 8-6(B) represent the source emissions.

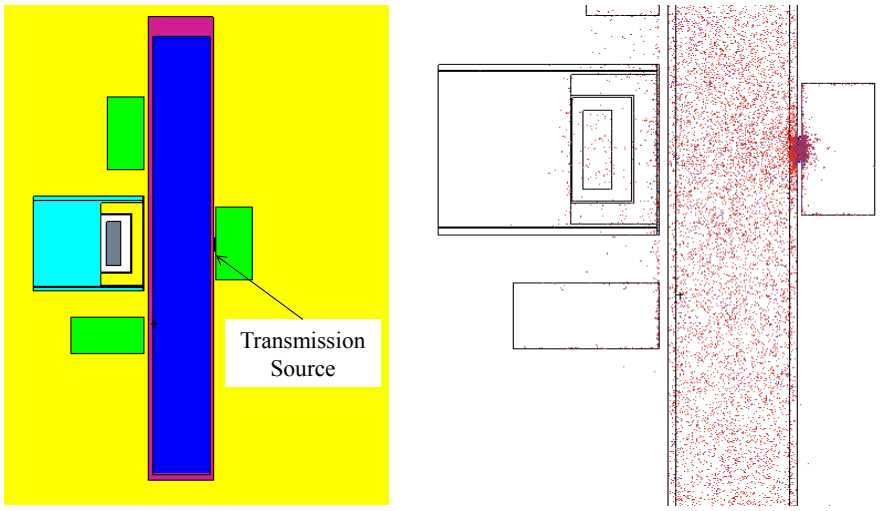

(A) **(B)**

Figure 8-6. External Transmission Source Simulation Models with Falcon BEGe.

(A) VisEd Representation of Dilution Experiment; (B) VisEd Simulation of Source Particle-Collisions of Dilution Experiment.

The ^{137}Cs source employed in the experiments was decay corrected from the date of certification, with an activity of 3.06×10^{4} Bq (0.828 μCi). In the source definition of the external transmission source in the MCNPX model in Appendix E, the 661.7 keV ^{137}Cs source is emitted with an intensity of 85.1%. An F8 pulse height tally was also conducted in this simulation. However, since two sources are employed – ^{235}U in UN and ^{137}Cs transmission source – a *FUn* tally modifier was required in the MCNPX tally card in order to separately tally contributions from each source. Since each tally is normalized to emissions per source particle, each separate tally was calculated using appropriate emission intensities and activities prior to summation to determine an overall detector response.

8.3.2 ^{133}Ba and ^{57}Co Transmission Simulations

As discussed in Chapter 6, the choice of testing the sensitivity of ^{133}Ba and ^{57}Co as alternative transmission densitometry sources would prove more sensitive to uranium content based on mass attenuation coefficient interactions of photons at the 356 and 122 keV energies, respectively. Since these sources were unavailable for experimental testing, use of validated simulations enables assessing the sensitivity of these sources to various concentrations of uranium in UN. The simulations emulated the setup in Figure 8-6, and sample MCNP input decks are provided in Appendix E. The source energies intensities for ^{133}Ba and ^{57}Co are summarized in Table 8-6. The activity required of the sources to penetrate the pipe and provide signature data is analyzed in detail Chapter 11.

Table 8-6. Predominant Source Photon Emissions from ^{133}Ba and ^{57}Co.

^{133}Ba		^{57}Co	
Energy (keV)	**Intensity (%)**	**Energy (keV)**	**Intensity (%)**
276.398 ***2***	7.164 *22*	122.0614 *4*	85.60 *17*
302.853 ***1***	18.33 *6*	136.4743 *5*	10.68 *8*
356.017 ***2***	62.05 *19*		
383.851 ***3***	8.94 *3*		

Data from [61].

8.4 Enrichment Simulations

Finally, a validated simulation model is useful in determining the sensitivity of the HPGe to varying enrichments of uranium in UN, as it was not possible to test varying enrichments through experimental measurements (MCNPX sample in Appendix E). In these simulations, the concentration of 90 g U/L with a density of 1.122 g/cm^3 is maintained; however, enrichments are varied from 0.76% to 10% ^{235}U. The geometry, materials, sources, and tallies employed in the passive and transmission models as described in the previous two sections are the parameters modeled in this enrichment sensitivity simulation. The uranium enrichment in UN that is varied in the material and source definition cards in MCNPX is summarized in Table 8-7.

Table 8-7. ^{235}U Activity at Various Enrichments for Fresh UN at 90 g U/L.

Enrichment ^{235}U (wt.%)	Calculated Mass ^{235}U in Pipe	Calculated Activity Fresh ^{235}U (Bq)
0.76	1.99	1.59×10^5
1	2.62	2.09×10^5
5	13.09	1.05×10^6
10	26.19	2.09×10^6

8.5 Conclusions

The results of each of the validation simulations for passive measurement of UN dilution concentrations and ^{137}Cs transmission source measurements are summarized in Chapter 11. Using these validated simulation models, the results of the ^{57}Co and ^{133}Ba transmission measurement sensitivity to varying concentrations of UN are also provided in Chapter 11. The enrichment sensitivity results are provided as part of a holistic sensitivity analysis in Chapter 12

CHAPTER 9. RESULTS: DILUTION EXPERIMENTS

An assessment of the sensitivity to the different gamma-ray detectors was conducted via a series of dilution measurements to determine emission signatures for monitoring UN in an NUCP. In the chapter, the results of the sensitivity analysis conducted for dilution concentrations of UN at 90 g, 85 g, 75 g, 50 g, and 10 g U/L using COTS gamma-ray detectors are summarized. Both passive ^{235}U and ^{137}Cs transmission densitometry measurements were conducted for three candidate detectors: Falcon BEGe [73], Osprey 2x2 NaI(Tl) [72], and Inspector 1000 $LaBr_3$ [69]. The results of experimental dilution measurements in a controlled laboratory setting are described for detector sensitivity assessments in a low-background environment. The dilution detector responses were imperative in assessing the detection sensitivity to ^{235}U emissions in order to determining monitoring signatures in an operational environment at UNCLE (Chapter 10), in addition to creating a basis for validation measurements for the computational simulations previously outlined in Chapter 8 with results provided in Chapter 11.

9.1 Experiment Setup for Dilution Measurements

The results of the passive and transmission dilution measurements are analyzed in this chapter. The results of the spatial offset measurements are provided as part of a comprehensive sensitivity and uncertainty analysis in Chapter 12. Photos of the experimental setup with each of the Falcon BEGe with the tungsten endcap [73] and Osprey 2×2 NaI(Tl) and Inspector 1000 $LaBr_3$ with the Canberra 7419E Shield/Collimator [86] are given in Figure 9-1.

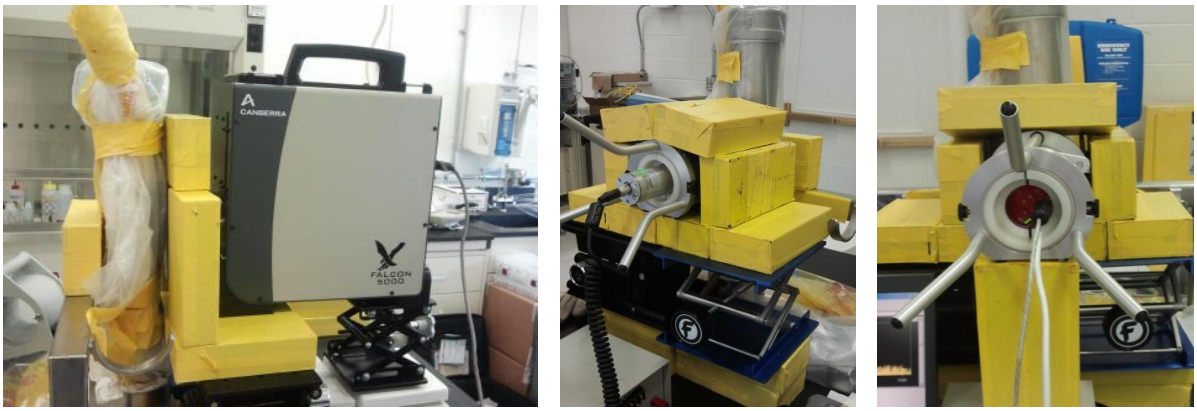

(A) (B) (C)

Figure 9-1. Laboratory Set-up for Dilution Measurements: (A) Falcon BEGe; (B) Inspector 1000 $LaBr_3$; and (C) Osprey 2x2 NaI(Tl).

During the first dilution from 90 g U/L to 85 g U/L, a contamination incident occurred due to leakage from a faulty pipe weld. A new pipe segment was fabricated to the exact specifications of the 90 g U/L. This pipe segment was from the same Schedule 40 304L stainless steel pipe stock used for UNCLE and the first dilution pipe. Although no major contamination was detected in the setup area or in the detection instrumentation, the measurement area was consequently set up as a localized contamination zone. This required that all materials be sealed in plastic and that the pipe segment be wrapped in multiple radiation/leak-proof plastic bags, which challenged optimizing detector alignment and shielding.

Measurements were taken with the first pipe prior to contamination for the Osprey and Inspector at 90 g U/L for 3600 s. The Falcon data were retaken with the new pipe segment for 1800 s for passive measurements and 3600 s for transmission measurements. Any variability in data could be due to these compensations for the contamination incident. Figure 9-2 depicts the added measures following the contamination incident.

Figure 9-2. Experiment Setup following Contamination Incident.

9.2 Energy Calibration

An energy calibration was conducted with the Falcon BEGe detector (with W endcap) using ^{152}Eu, ^{137}Cs, and ^{133}Ba gamma-ray sources. The calibration was fit to a second-order polynomial in Canberra's Genie software, with a multi-channel analyzer spanning 1591.8 keV over 8192 channels. The polynomial fit used for the energy calibration is plot in Figure 9-3.

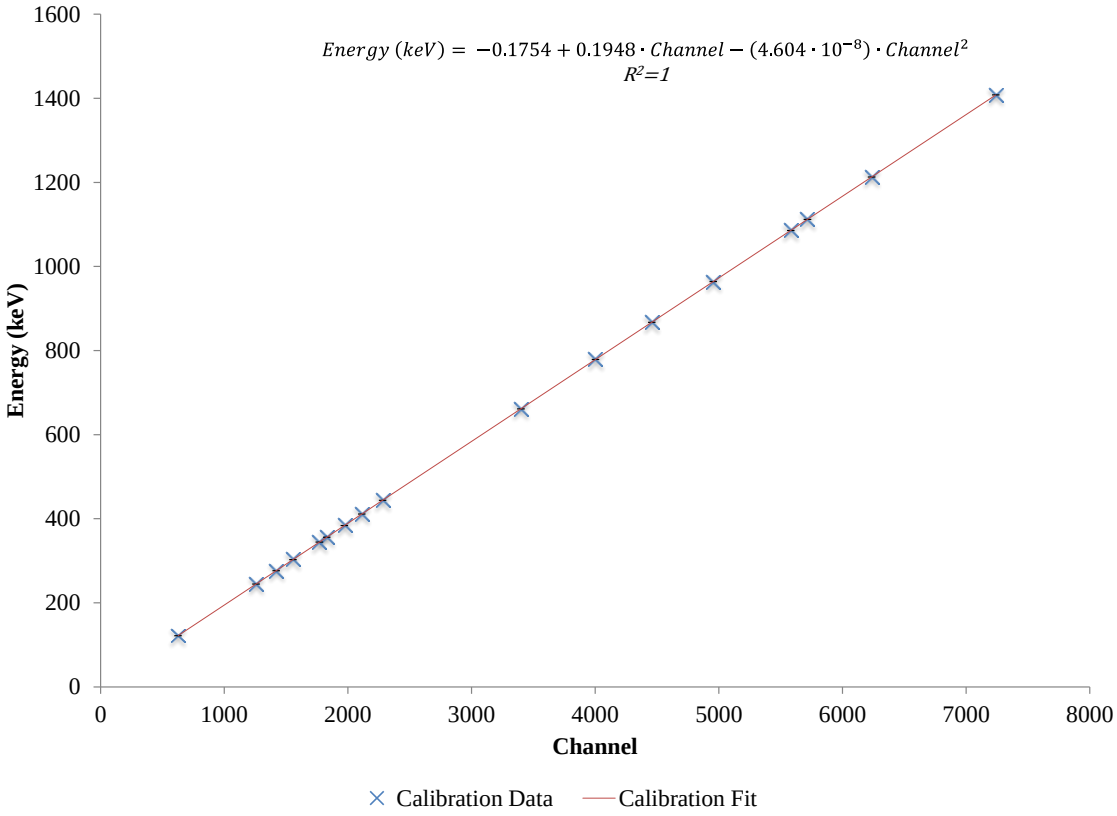

Figure 9-3. Energy Calibration Curve of Falcon BEGe Detector for Dilution Measurements.

An energy calibration was conducted with the Osprey 2×2-NaI(Tl) detector using ^{152}Eu and ^{137}Cs gamma-ray sources. The calibration was fit to a second-order polynomial in Canberra's Genie software, with a multi-channel analyzer spanning 1613.0 keV over 2048 channels. The polynomial fit used for the energy calibration is plot in Figure 9-4.

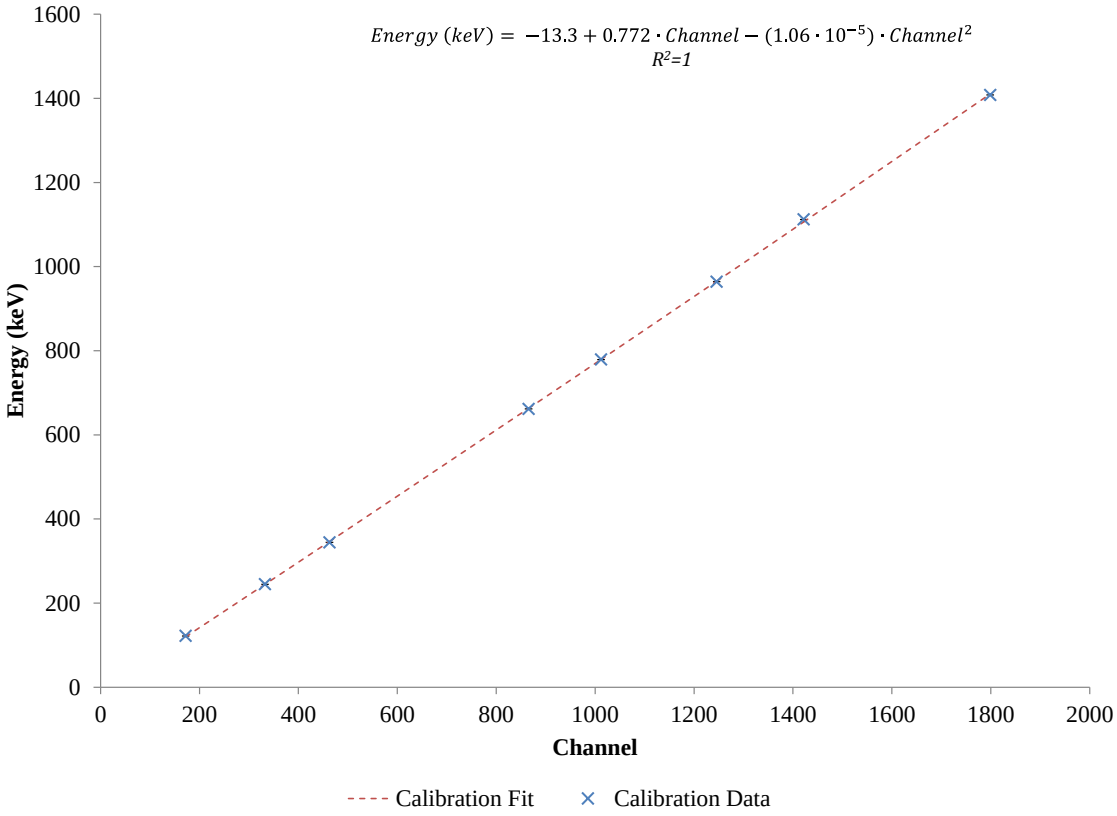

Figure 9-4. Energy Calibration Curve of Osprey 2×2 NaI(Tl) Detector for Dilution Measurements.

An energy calibration was conducted with the Inspector 1000 $LaBr_3$ detector using a ^{152}Eu gamma-ray source. The calibration was fit to a second-order polynomial in Canberra's Genie software, with a multi-channel analyzer spanning 1512.3 keV over 2048 channels. The polynomial fit used for the energy calibration is plot in Figure 9-5.

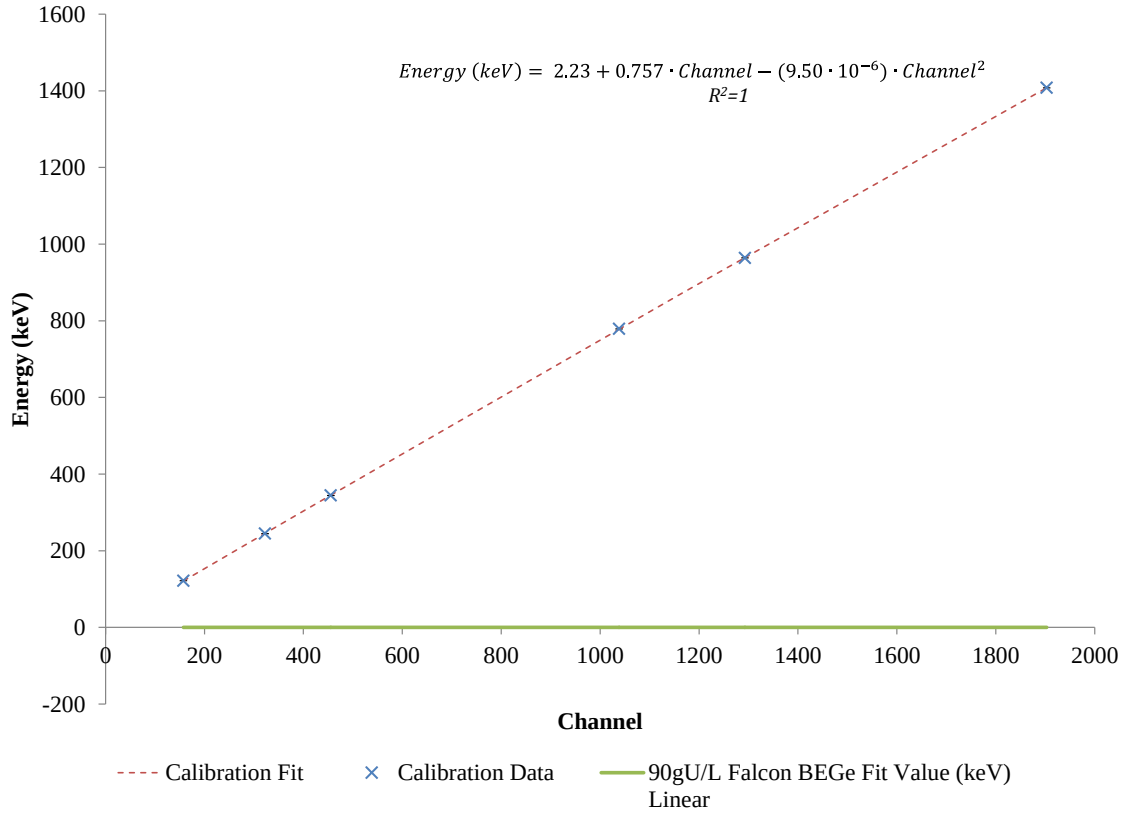

Figure 9-5. Energy Calibration Curve of Inspector 1000 $LaBr_3$ Detector for Dilution Measurements.

9.3 Passive ^{235}U Dilution Measurement Results

Gamma-ray measurements of ^{235}U for a series of dilution concentrations of UN in a 304L Schedule 40 pipe segment were conducted. A comparison of the measured spectra for all the detectors is presented in Figures 9-6 through 9-10. As the UN is 40 years old, the spectra contain contributions from the higher energy ^{238}U emissions, as well as other signatures given in Table 6-2. Although ^{238}U is not a viable signature for measuring freshly solvent extracted UN, these emissions affect the overall detection efficiency, in addition to contributing Compton continuum downscatter underlying the lower energy ^{235}U signatures. The entire energy range of the measured spectra is provided in Appendix G (Figures G-1 to G-5). For the Falcon at 90 g U/L, passive measurements

were only available at a live time of 1800 s, where the remaining detector/concentration count rates were calculated based on a 3600 s acquisition live time. This was due to limitations resulting from the aforementioned contamination event.

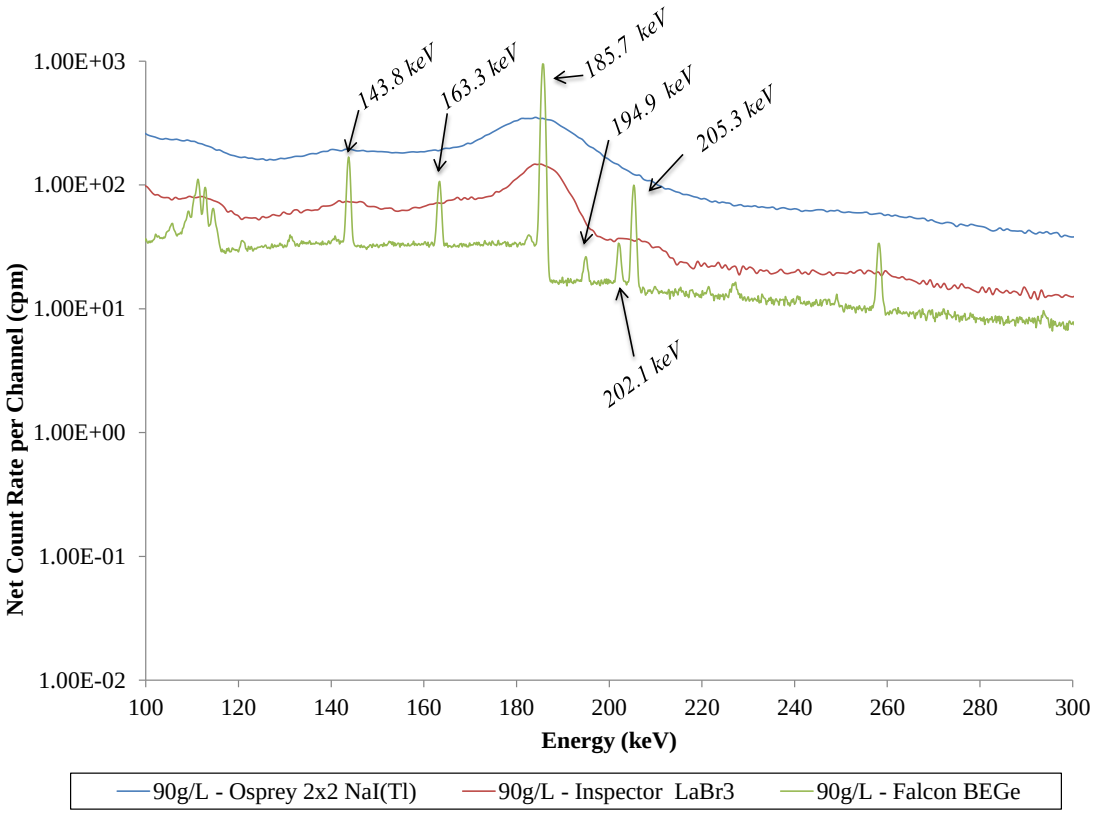

Figure 9-6. 90 g U/L Dilution Measurement Data for All Detectors.

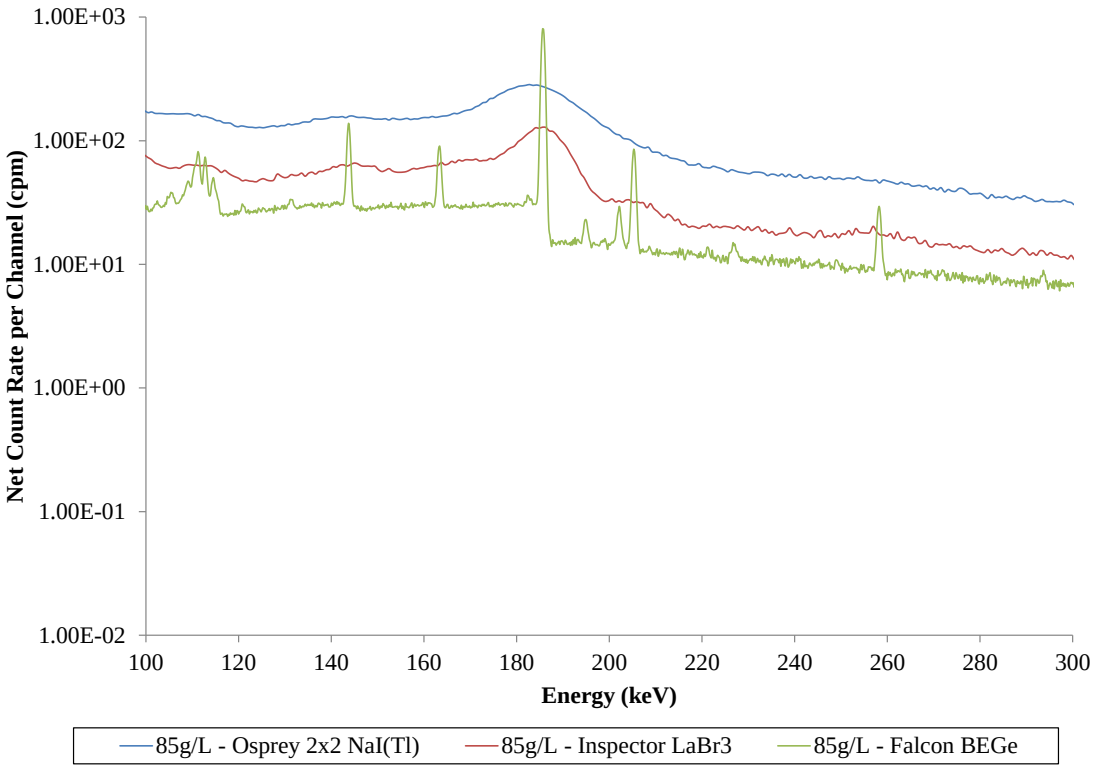

Figure 9-7. 85 g U/L Dilution Measurement Data for All Detectors.

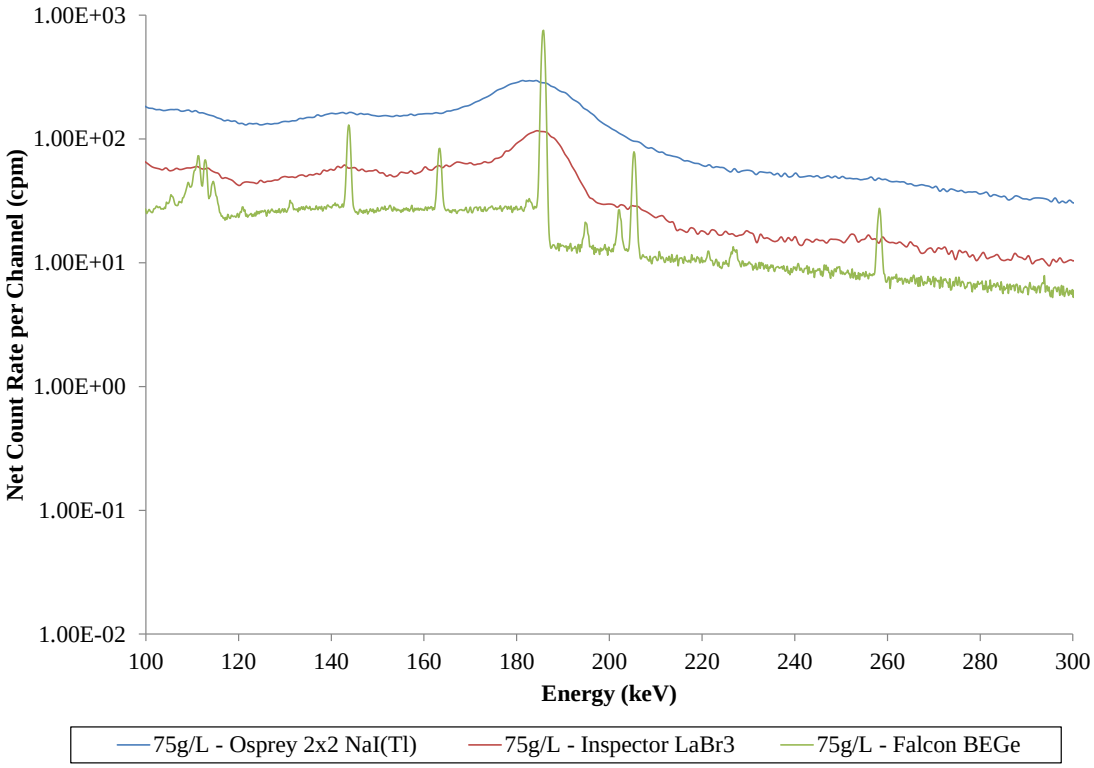

Figure 9-8. 75 g U/L Dilution Measurement Data for All Detectors.

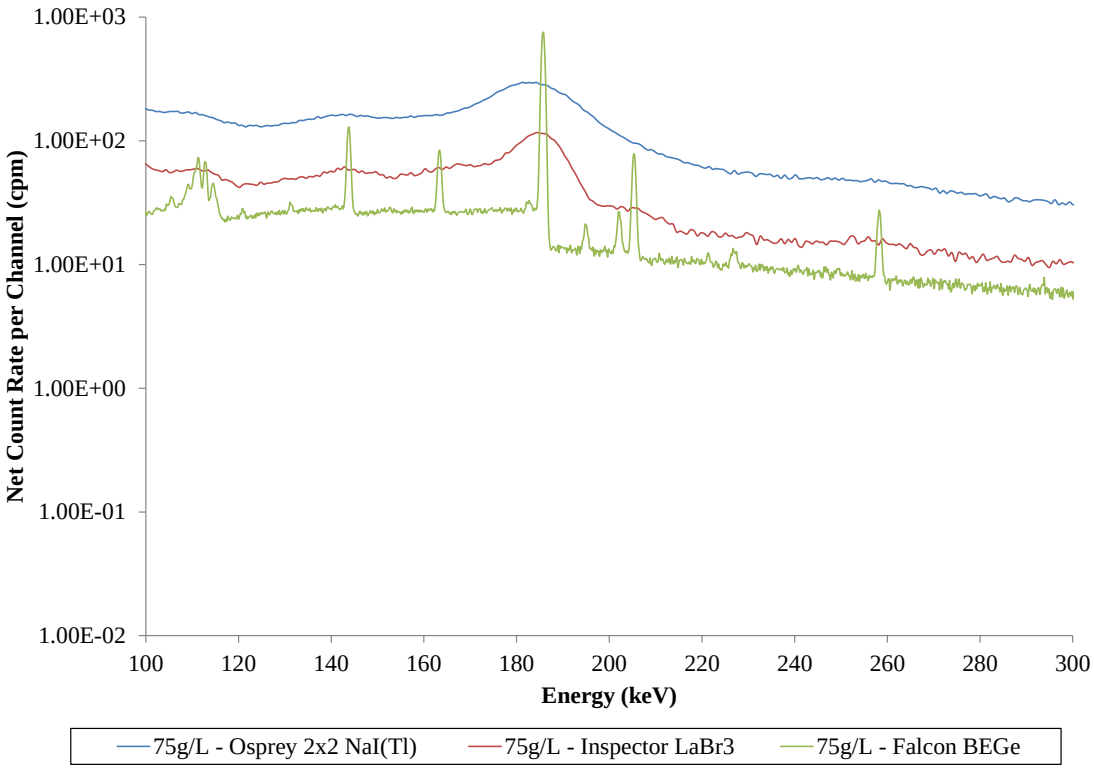

Figure 9-9. 50 g U/L Dilution Measurement Data for All Detectors.

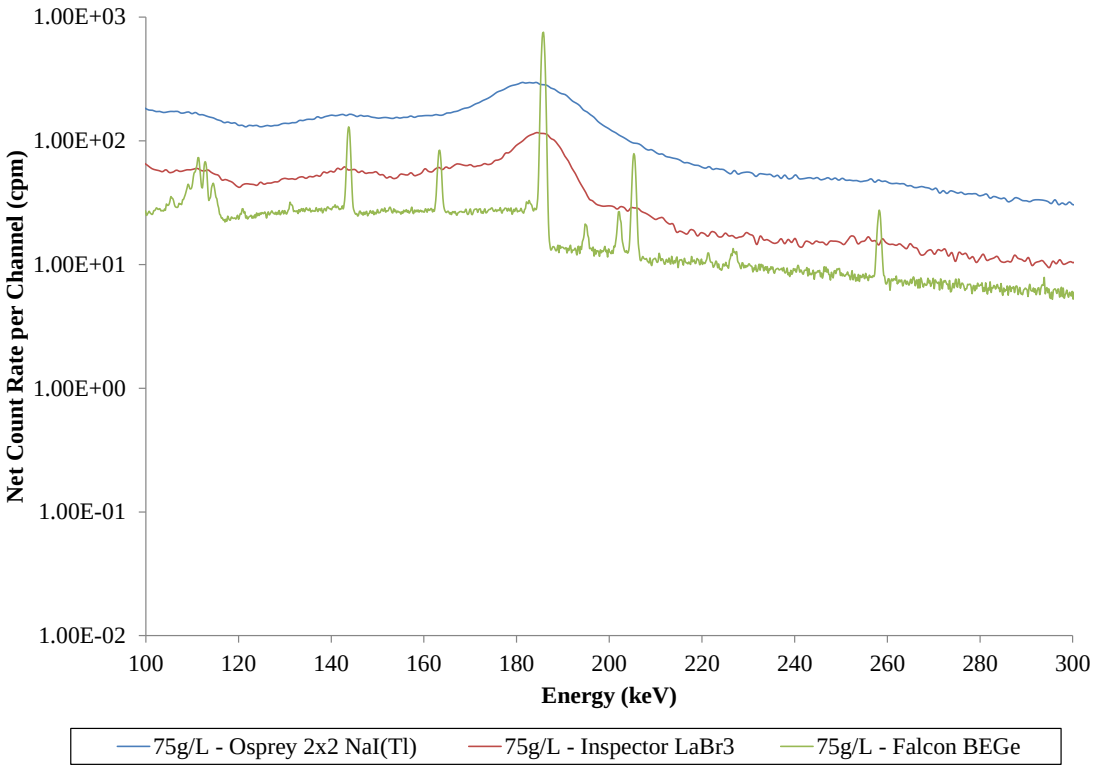

Figure 9-10. 10 g U/L Dilution Measurement Data for All Detectors.

As shown for all dilution measurements in Figures 9-6 through 9-10, the Falcon BEGe possessed the highest resolution, whereas the 2×2 NaI(Tl) Osprey had the lowest resolution, being unable to resolve the 185.7 keV peak from the 163.3, 194.9, 202.1 and 205.3 keV peaks. For the scintillator detectors, the Inspector 1000 provides superior resolution to the Osprey. The peak area boundary (ROIs), FWHM, and resolution values for the 185.7 keV peak are summarized in Table 9-1 for 185.7 keV emissions at 90 g U/L solution concentration.

Table 9-1. Region of Interest (ROI) Boundaries and Resolution Properties of 185.7 keV ^{235}U Peak in Passive Dilution Measurements.

Detector	ROI (keV)	FWHM (keV)	Resolution (%)
Falcon BEGe	[184.3, 187.6]	0.9	0.49
Inspector 1000 LaBr3	[158,204]	11.0	5.93
Osprey 2x2 NaI(Tl)	[124,227]	27.0	14.57

**Includes multiplet peak fit by Genie.*

As shown in the peak area analysis depicted in Figure 9-9, the Osprey had the highest peak area efficiency for the 185.7 keV ^{235}U peak, whereas the Inspector 1000 had the lowest efficiency. At 10 g U/L, the peak for the Inspector was not discernible by Genie as an identifiable peak within the provided confidence limits, and thus no peak area data point is provided at this concentration (Figure 9-10, Figure 9-11). This is consistent with the results from Scargill, who determined the concentration limit for the analysis of natural uranium using the 185.7 keV line is 30 g U/L with an uncertainty of 5% during a counting time of 5 minutes [74].

The correlation fit with dilution concentration is strongly linear, with the net peak area of the 185.7 keV ^{235}U emission. From 90 g U/L down to 10 g U/L, the peak area of 8053 cpm drops overall by 95% at a rate of 85 cpm per g U/L UN for the Osprey detector. For the Inspector dilution concentrations from 90 to 50 g U/L, the peak area of 1133 cpm drops overall by 57% at a rate of 16 cpm per g U/L. Finally, the Falcon net peak area of 3963 cpm drops from 90 to 10 g U/L overall by 88% at a rate of 44 cpm per g U/L. Consequently, the Osprey is the most sensitive to concentration variations in ^{235}U, whereas the Inspector is the least sensitive.

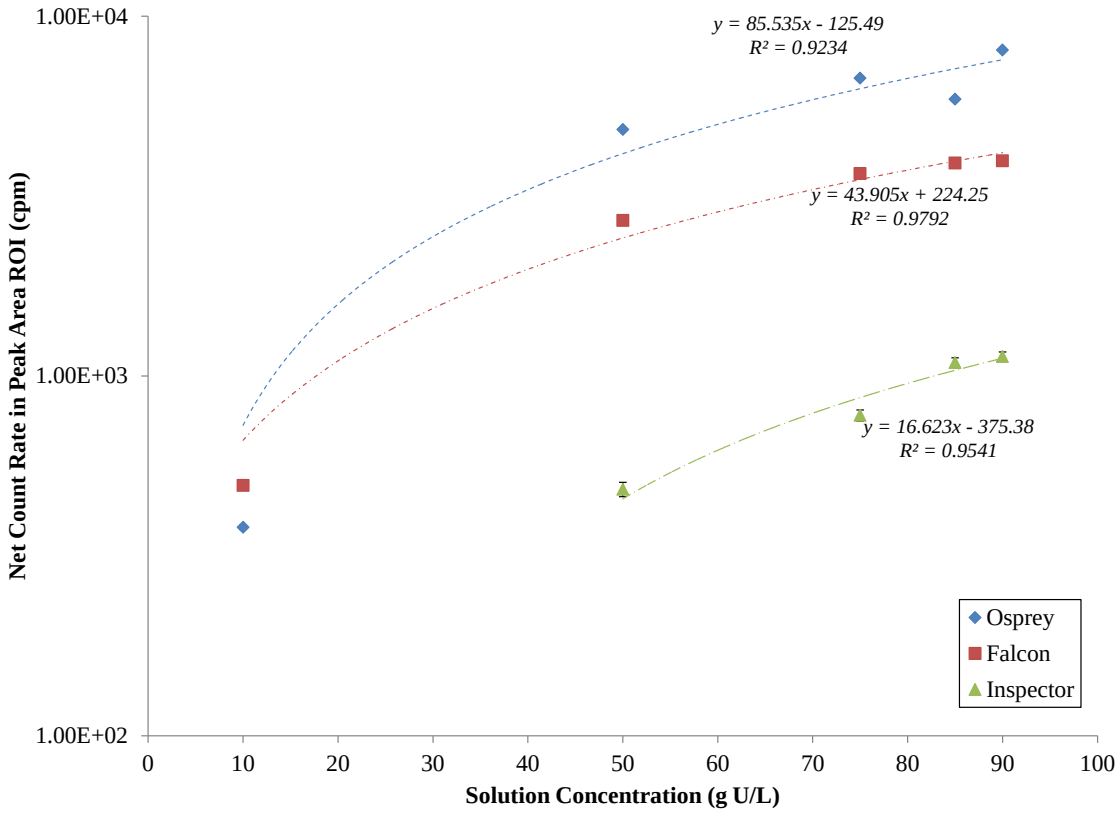

Figure 9-11. Net Peak Area for ^{235}U 185.7 keV Emission as a Function of Dilution Concentration.

Note: Error bars plotted for some data points are smaller than the resolution of the graph.

From 50 to 90 g U/L solution concentration, the statistical error associated with peak area counts for the Osprey is ranges from 0.18–0.22%, where the 10 g U/L has ~1.36% error. With the Inspector 1000, the statistical error from 50 to 90 g U/L ranges from 0.50–1.01%. Finally, the statistical error associated with the Falcon from 50 to 90 g U/L falls within 0.21–0.29%, whereas at 10g U/L, it increases to ~0.87%.

Table 9-2 provides the calculated peak-to-total ratios for each of the three detectors. The peak-to-total ratio is the value by which the total detector efficiency is multiplied by to determine the full energy peak efficiency [80]. At 185.7 keV, the Osprey has the highest peak efficiency vis-à-vis the Inspector and Falcon. Although the Falcon is more sensitive to ^{235}U as a function of UN concentration, it has the lowest peak-to-total ratio, whereas

the Osprey possesses a higher peak-to-total measurement, followed by the Inspector. An in-depth discussion of detector efficiency is provided in the sensitivity analysis in Chapter 12.

Table 9-2. Peak-to-Total Ratios of 185.7 keV Peak at 90 g U/L.

	Lower and Upper Full Spectrum Bounds (keV)	Peak-to-Total Ratio
Osprey	[1.1, 1609.9]	0.28±(0.03%)
Inspector	[1.3, 1514.2]	0.13±(0.03%)
Falcon	[1.4, 1592.4]	0.08±(0.02%)

Since the Falcon is able to resolve the 143.8 and 163.3 keV peaks, peak areas and ratios are provided in Figures 9-12 and 9-13 to show the relative strength of these signatures. Since the 163.3 keV is such a low intensity emission of ^{235}U, the 143.8 is a more favorable monitoring option for a secondary monitoring signature ratio for ^{235}U passive measurements.

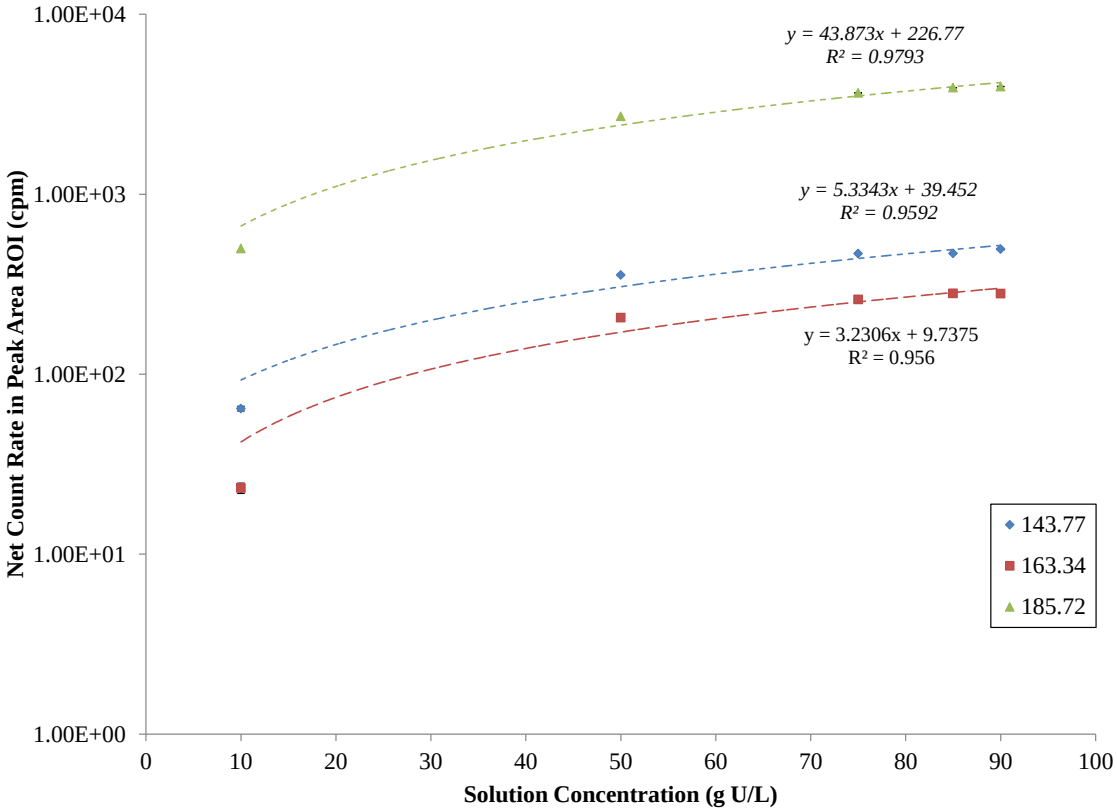

Figure 9-12. Peak Area Values for ^{235}U Emissions as a Function of Solution Concentration for Dilution Measurements for Falcon BEGe.

*Note: Error bars plotted for some data points are smaller than the resolution of the graph.*Data at 90 g U/L only available at 1800 s. Remaining dilution data at 3600 s acquisition time.*

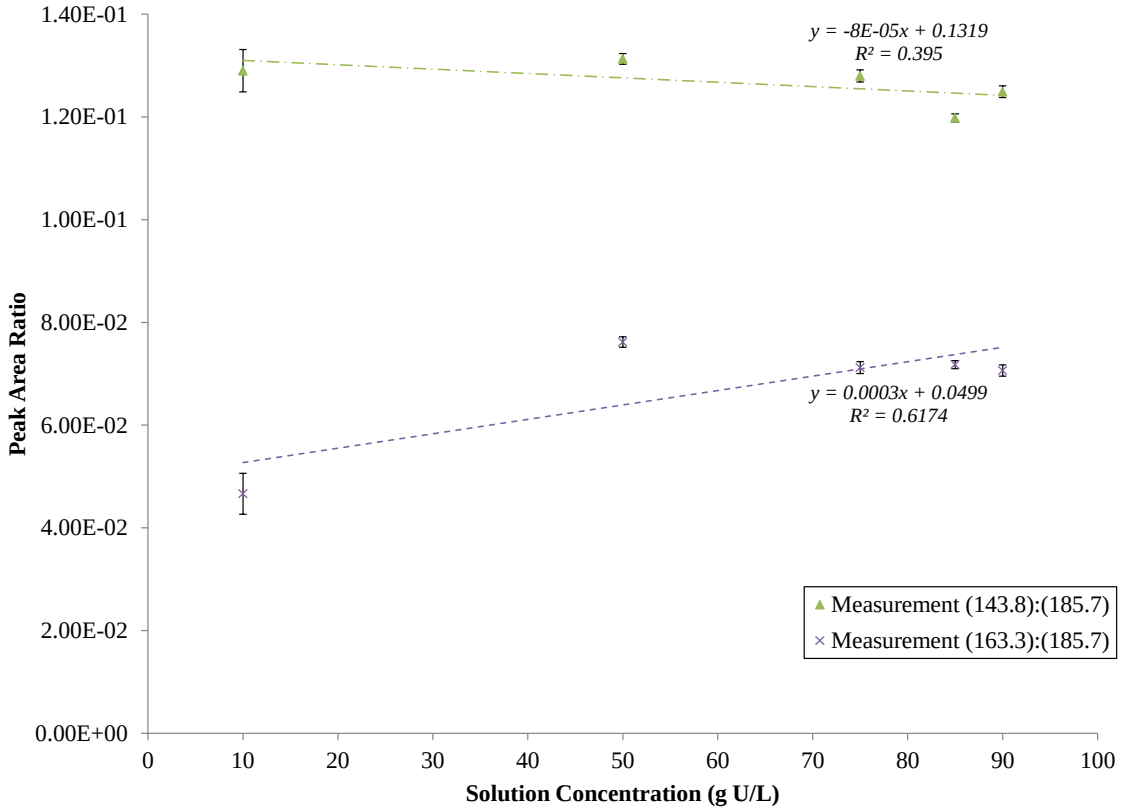

Figure 9-13. Peak Area Ratios of ^{235}U Emissions (143.8 keV, 163.3 keV) to 185.7 keV for Dilution Measurement Data as a Function of Solution Concentration for Falcon BEGe.

**Data at 90 g U/L only available at 1800 s. Remaining dilution data at 3600 s acquisition time.*

9.4 ^{137}Cs Transmission Measurement Results

For each of the dilution concentrations at 90 g, 85 g, 75 g, 50 g, and 10 g U/L, transmission measurements were taken using ^{137}Cs for densitometry measurements for 3600s live time[5]. The spectra for the measurements are given in in Figures 9-14 through 9-18.The corrected source activity from ^{137}Cs employed during measurement acquisition was 0.83 μCi.

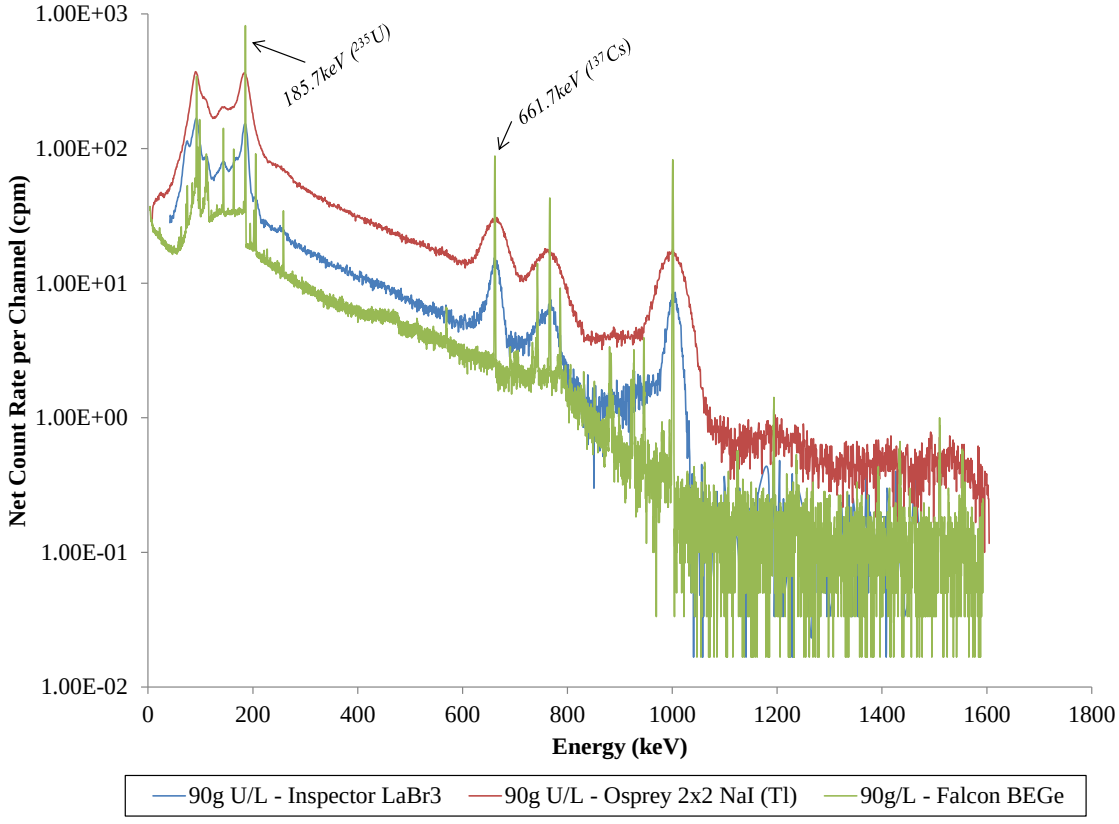

Figure 9-14. 90 g U/L ^{137}Cs Transmission Measurement Data for All Detectors.

[5] All data at 3600 s acquisition time except 75 g U/L = 3311 s live time.

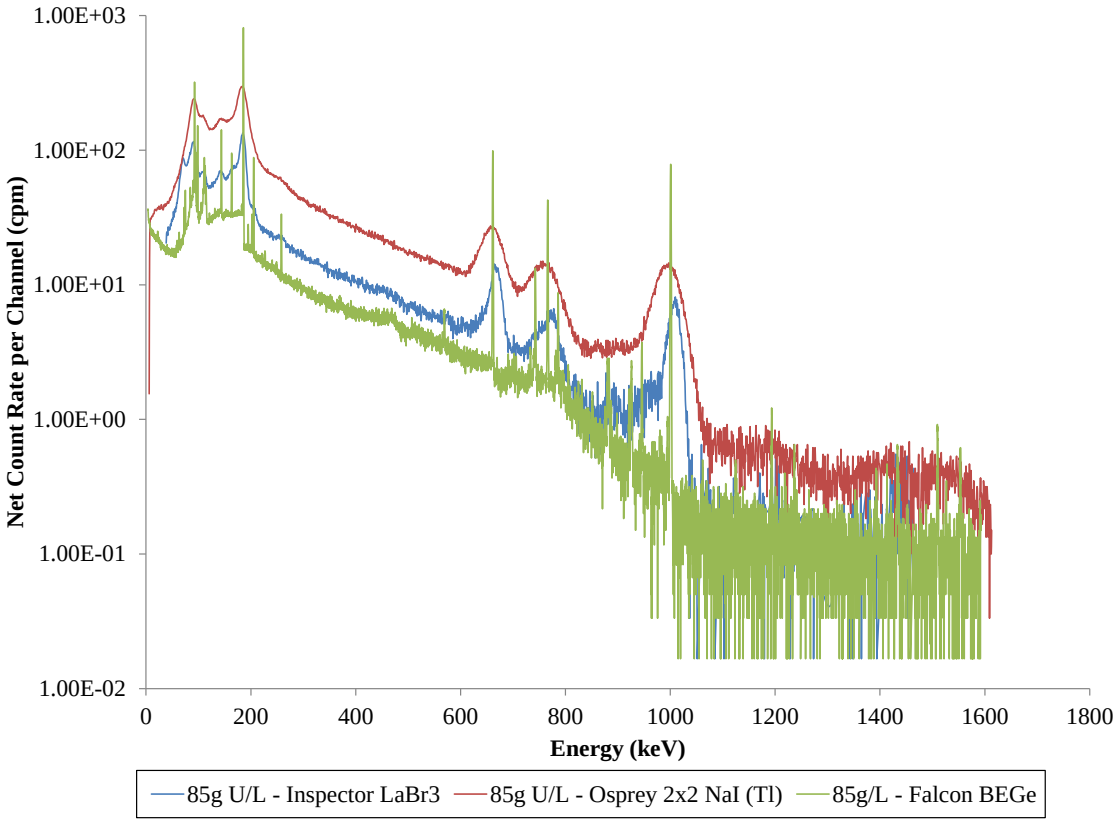

Figure 9-15. 85 g U/L ^{137}Cs Transmission Measurement Data for All Detectors.

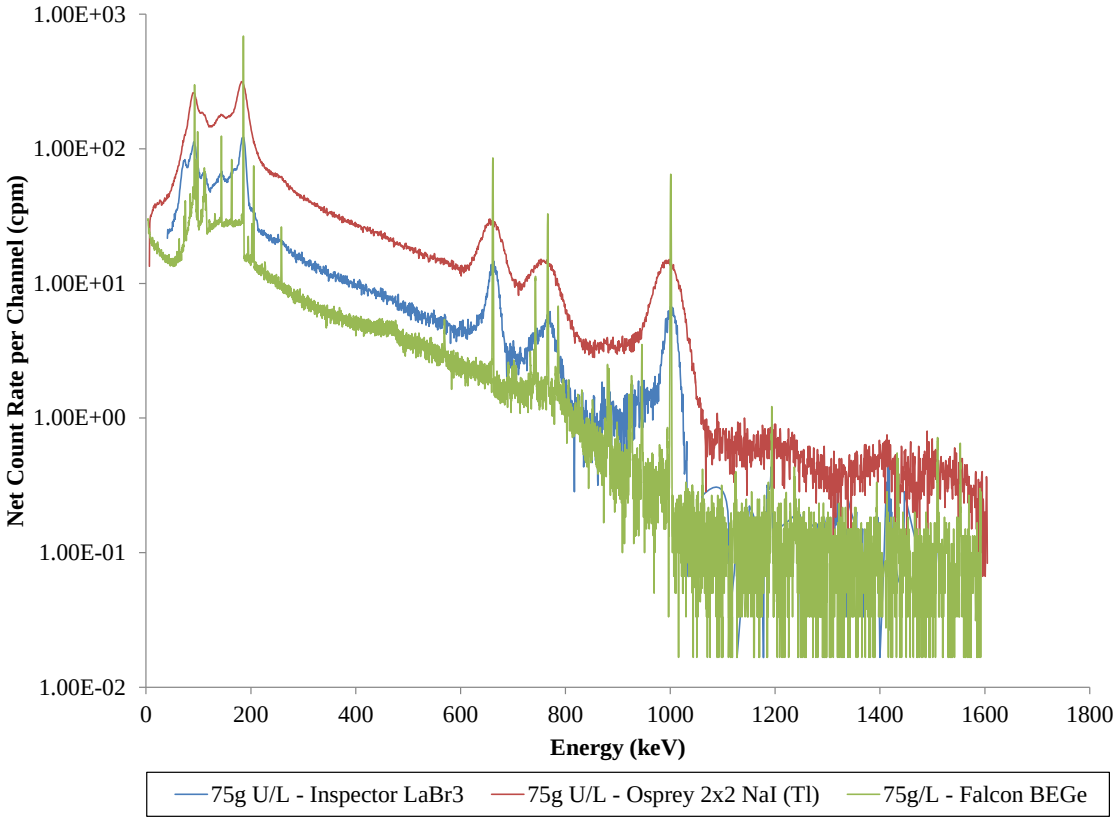

Figure 9-16. 75 g U/L ^{137}Cs Transmission Measurement Data for All Detectors.

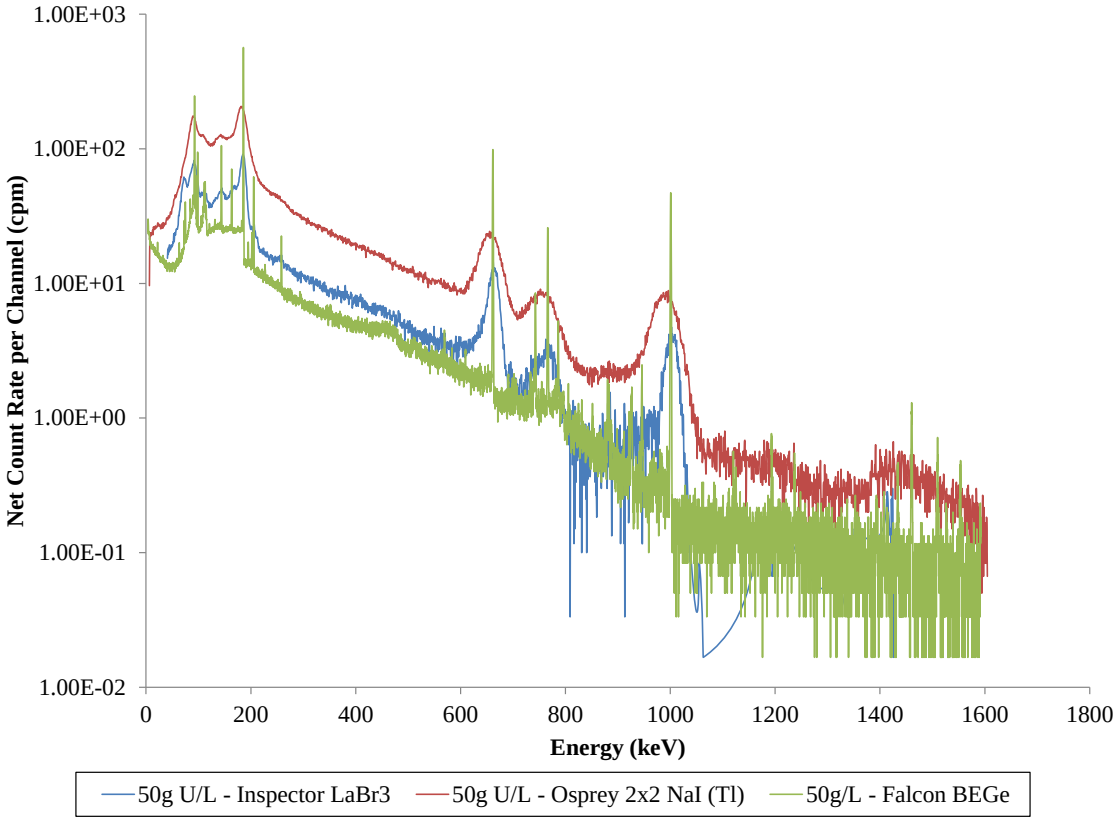

Figure 9-17. 50 g U/L ^{137}Cs Transmission Measurement Data for All Detectors.

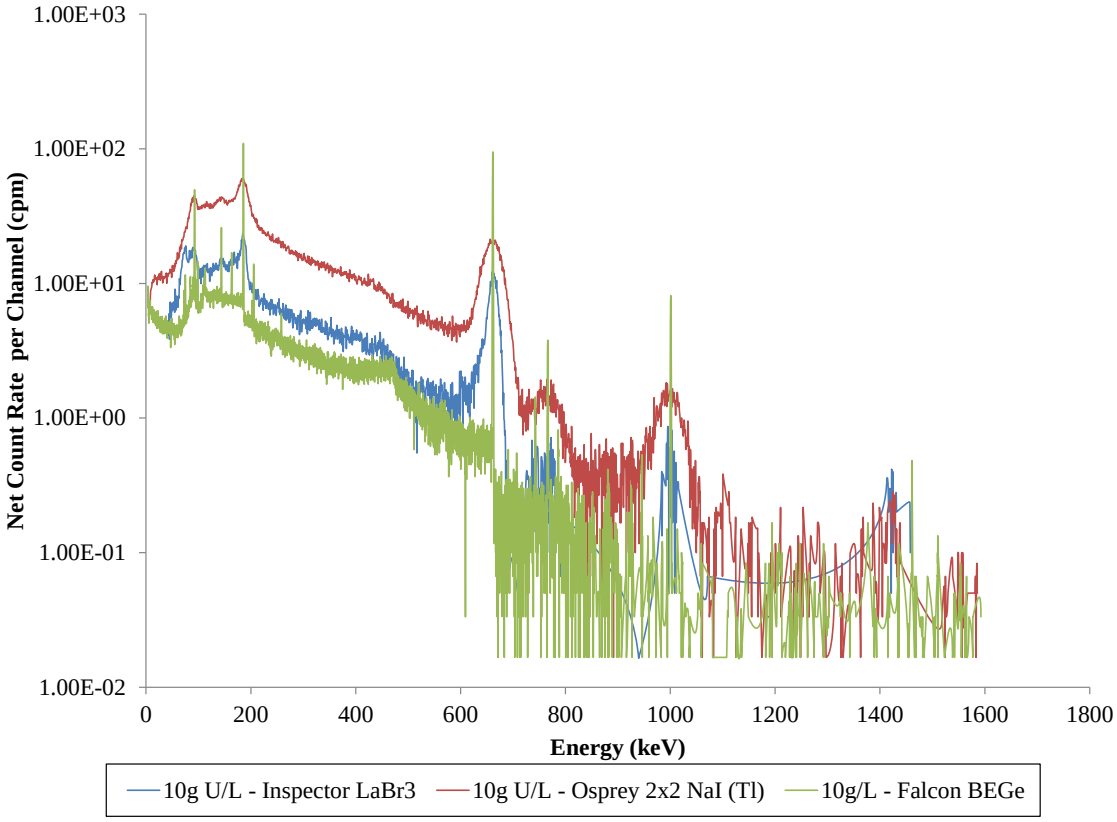

Figure 9-18. 10 g U/L ^{137}Cs Transmission Measurement Data for All Detectors.

A comparison of the detector resolution at the 661.7 keV peak at 90 g U/L is provided in Figure 9-19. At this energy, the Osprey has the poorest resolution, whereas the Falcon has the highest resolution.

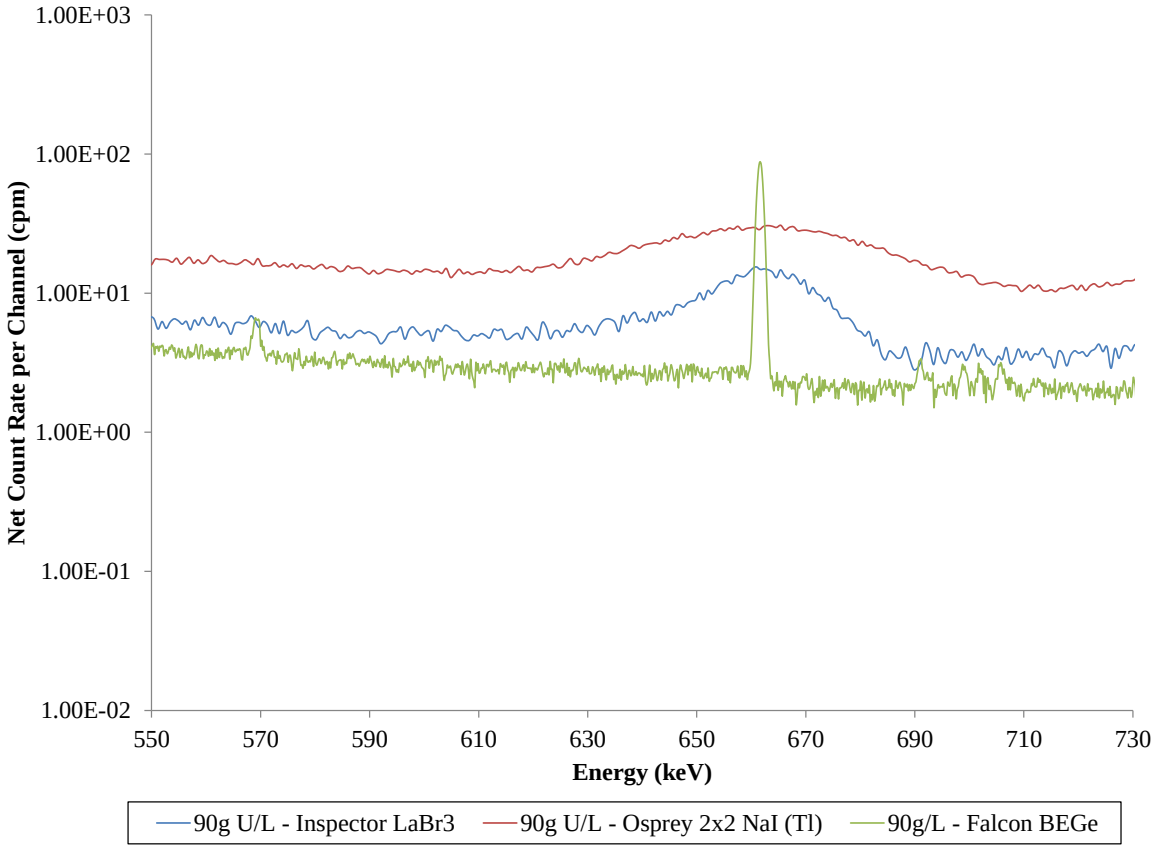

Figure 9-19. Peak Resolution of ^{137}Cs Transmission Measurement Data at 90 g U/L.

The peak area boundary (ROIs), FWHM, and resolution values are summarized in Table 9-3 for 661.7 keV emissions at 90 g U/L solution concentration. Since this energy range does not have any overlapping peaks as the ^{235}U emissions have in the 100–200 keV energy range, the resolution is sufficient for all detectors in assaying the single 661.7 keV ^{137}Cs transmission photon energy.

Table 9-3. Region of Interest (ROI) Boundaries and Resolution Properties of 661.7 keV ^{137}Cs Peak in Passive Dilution Measurements.

Detector	ROI (keV)	FWHM (keV)	Resolution (%)
Falcon BEGe	[659.5, 663.8]	1.3	0.20
Inspector 1000 $LaBr_3$	[620,699]	21.2	3.21
Osprey 2x2 NaI(Tl)	[602,711]	40.6	6.13

Although the resolution does not affect overlapping signature emissions, the transmission peak efficiency becomes of paramount interest in signature identification for PM. Peak area signatures for the 661.7 keV emission for each detector are given in Figure 9-20 as a function of solution concentration. In Figure 9-20, the Osprey has the highest peak area efficiency for the 661.7 keV ^{137}Cs peak, whereas the Inspector 1000 has the lowest peak area value, and hence the lowest efficiency.

The linear correlation with dilution concentrations for the peak area fit of the 661.7 keV ^{137}Cs emission is weak due to the self-attenuation, as well as the lack of MAC sensitivity at higher photon energies, as explained in Chapter 7. From 90 g U/L to 85 g U/L dilution concentrations, the peak area of 969.5 cpm changes by approximately 11.5% for the Osprey detector. For the Inspector dilution concentrations from 90 to 85 g U/L, the peak area of 248 cpm changes by approximately 13.4%. Finally, the Falcon peak area of 629 cpm changes from 90 to 85 g U/L by ~9.1%. Transmission measurement peak areas expect to increase with decreasing solution concentration and density; however, in practice, due to mass attenuation properties, self-attenuation, source-detector geometry, and setup limitations in the contamination area, the 661.7 keV photons of ^{137}Cs transmission measurements were rather insensitive to ^{235}U in UN. In addition, the original pipe segment was assayed at 90 g U/L for the Inspector and the Osprey. Although the newly fabricated pipe replicated the dimensions of the original pipe, and was fabricated from the same stock of 304L pipe, the use of a new pipe provides a source of experimental error.

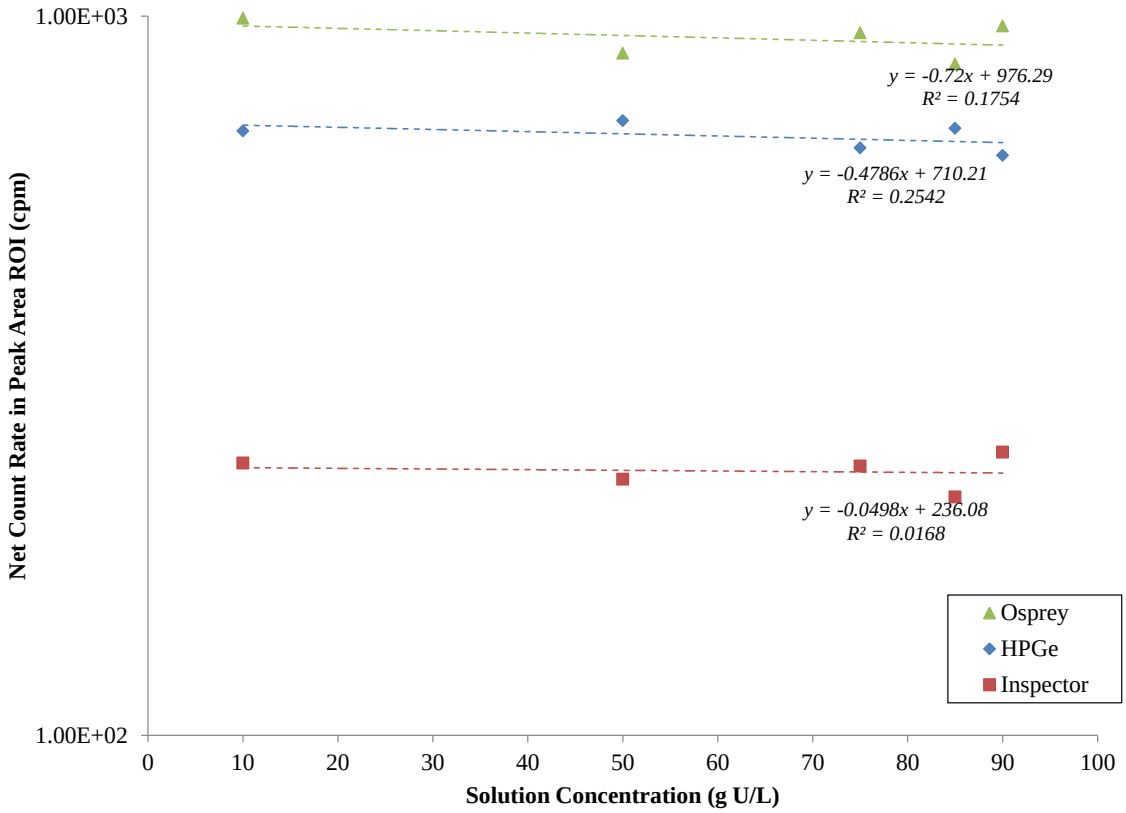

Figure 9-20. Peak Area for ^{137}Cs Transmission Measurements as Function of Solution Concentration for all Detectors.

Note: Error bars plotted for some data points are smaller than the resolution of the graph.

From 10 to 90g U/L solution concentration, the statistical error associated with peak area counts for the Osprey is approximately 3.4%. With the Inspector 1000, the statistical error over the range of dilution concentrations is ~6.5%, where the statistical error associated with the Falcon is ~4%.

Table 9-4 provides the calculated peak-to-total ratios for each of the three detectors. At 661.7 keV, the Osprey has the highest ratio vis-à-vis the Inspector and Falcon. The validated Falcon detector simulations in Chapter 11 provide more in-depth analysis of the peak area signatures and detector efficiency, and the factors impacting peak-to-total ratio are provided in the sensitivity analysis in Chapter 12.

Table 9-4. Peak-to-Total Ratios of 661.7 keV Peak at 90g U/L.

	Lower and Upper Full Spectrum Bounds (keV)	Peak-to-Total Ratio
Osprey	[0.1, 1603.7]	0.038±(0.01%)
Inspector	[3.1, 1512.1]	0.028±(0.01%)
Falcon	[1.4, 1591.2]	0.011±(0.01%)

Since the Falcon is able to resolve the 143.8 and 163.3 keV peaks, peak areas and ratios are provided in Appendix G (Figures G-6 and G-7) to show the relative strength of the ^{137}Cs transmission signatures.

9.5 Dead Time

Dead time losses were also recorded by Genie [76] at each dilution concentration for each of the three detectors employed. As shown in Figure 9-21, the Falcon BEGe has the highest associated dead time losses. The Inspector has the lowest dead time (i.e., highest collection time), and hence has the lowest losses due to limitations with electronics.

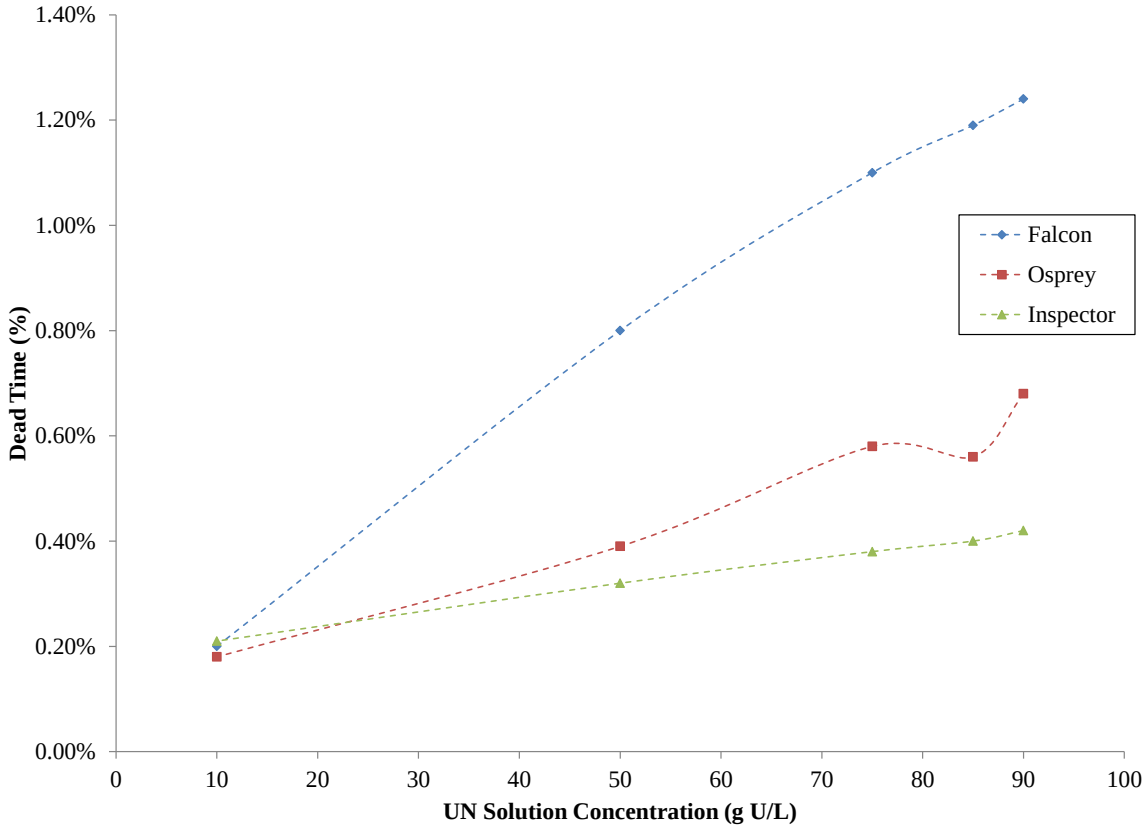

Figure 9-21. Dead Time for all Detectors as a Function of Dilution Concentration.

9.6 Conclusions

Dilution measurements were conducted in a controlled, low-background environment in order to assess the gamma-ray detector sensitivity to various concentrations of uranium, identify the robustness of signatures to these variations, and provide benchmark experiments for subsequent simulation modeling efforts. Using the Falcon 2.985×2.0-cm BEGe [73], Osprey 2×2-inch NaI(Tl) [72] and Inspector 1000 1.5×1.5-inch $LaBr_3$ [69] detectors, gamma-ray signatures were analyzed for dilution concentrations of UN of 90 g, 85 g, 75 g, 50 g, and 10 g U/L.

The passive measurements of the 185.7 keV ^{235}U emissions provided strong sensitivity to dilution concentrations of UN, whereas the 661.7 keV transmission measurements with ^{137}Cs provided poor sensitivity to dilution concentrations. As discussed in Chapter 7, this

is due to convergence of the MAC at higher photon energies for UN, making it relatively insensitive to the uranium content at the 661.7 keV energy range. With regards to resolution, the Falcon BEGe possessed superior resolution, which is useful in discriminating ^{235}U signatures in the 100–200 keV range. However, the Osprey provided greater detection efficiency for both passive and transmission signatures. The 3600 s acquisition time (and even the case of the 1800 s acquisition time at 90 g U/L) provided sufficient counts for measurement statistics to fall within ~1% uncertainty for ^{235}U passive measurements at all dilution concentrations. Overall, ^{137}Cs was not highly sensitive to the uranium content in the UN, as discussed in Chapter 7. The selection of an appropriate monitoring transmission source will be further discussed in the computational simulations in Chapter 11. In addition, since the 661.7 keV peak falls above the 185.7 keV energy range, Compton downscatter from this higher energy peak contributed to higher continuum counts. This affects the continuum background, for which higher continuum will lead to higher uncertainty values associated with the peak area, which will be discussed in detail in Chapter 12.

In Chapter 10, the robustness of the gamma-ray methods is determined through measurements in an operational, high-background environment at the ORNL UNCLE facility.

CHAPTER 10. RESULTS: UNCLE FACILITY MEASUREMENTS

Passive gamma-ray monitoring methods were tested in the UNCLE facility to determine the robustness of gamma-ray instrumentation under operating conditions. The previous dilution measurements provided an indication of instrumentation sensitivity from which PM signatures could be extrapolated. These capabilities were transposed into an operational environment for monitoring of UN following solvent extraction in an NUCP at UNCLE. Where the laboratory dilution measurements provided a controlled, low-background environment, the series of measurements at UNCLE provided more realistic background interference from adjacent pipes and tanks, in addition to introducing voiding and temperature variations from fluid flow.

10.1 Experiment Setup for UNCLE Measurements

The detectors were situated adjacent to one of the 100-gallon stainless steel tanks in UNCLE. Photographs of the experimental setup showing the Falcon BEGe with the tungsten endcap, Osprey 2×2 NaI(Tl), and Inspector 1000 1.5×1.5$LaBr_3$ with the Canberra 7419E Shield/Collimator [86] are given in Figure 10-1.

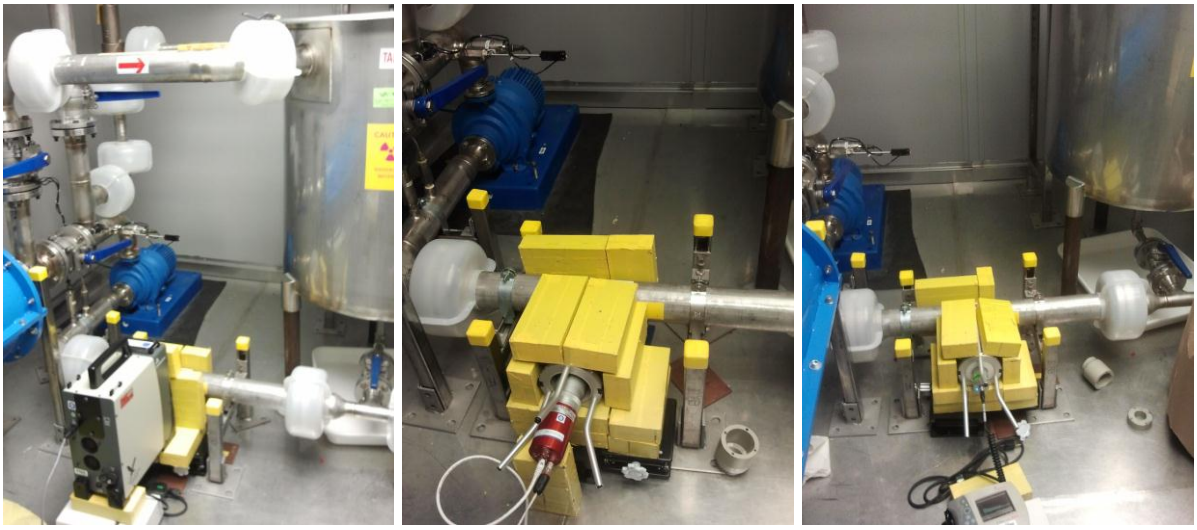

(A) (B) (C)

Figure 10-1. Detector Setup in UNCLE Facility: (A) Falcon BEGe; (B) Osprey 2×2 NaI(Tl); (C) Inspector 1000 $LaBr_3$.

10.2 Energy Calibration

The energy calibration was conducted with the Falcon detector using a ^{152}Eu gamma-ray source. The trend was fit to a second-order polynomial in Canberra's Genie software, with a multi-channel analyzer spanning 1592.5 keV over 8192 channels (0.19 keV/channel). The polynomial fit used for the energy calibration is given in Equation 10-1 and plotted in Figure 10-2.

$$Energy\ (keV) = -1.754 + 0.1948 \cdot Channel - (4.604 \cdot 10^{-8}) \cdot Channel^2 \ . \quad [10\text{-}1]$$

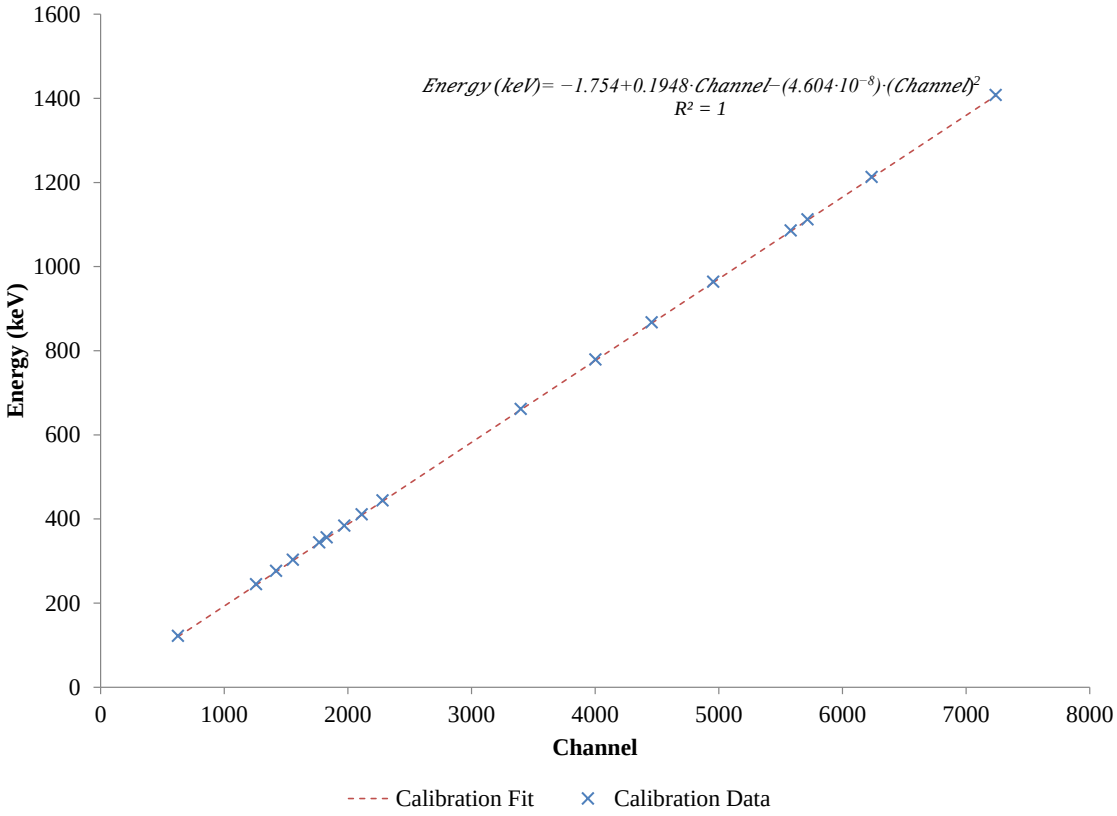

Figure 10-2. Energy Calibration Curve of Falcon BEGe Detector for UNCLE Measurements.

The energy calibration was conducted with the Osprey 2×2-NaI(Tl) detector using a ^{152}Eu gamma-ray source. The calibration was fit to a second-order polynomial in Canberra's Genie software, with a multi-channel analyzer spanning 1616.3 keV over 2048 channels (0.79 keV/channel). The polynomial fit used for the energy calibration is given in Equation 10-2 and plotted in Figure 10-3.

$$Energy\ (keV) = -12.89 + 0.7727 \cdot Channel - (1.123 \cdot 10^{-5}) \cdot Channel^2 \ . \quad [10\text{-}2]$$

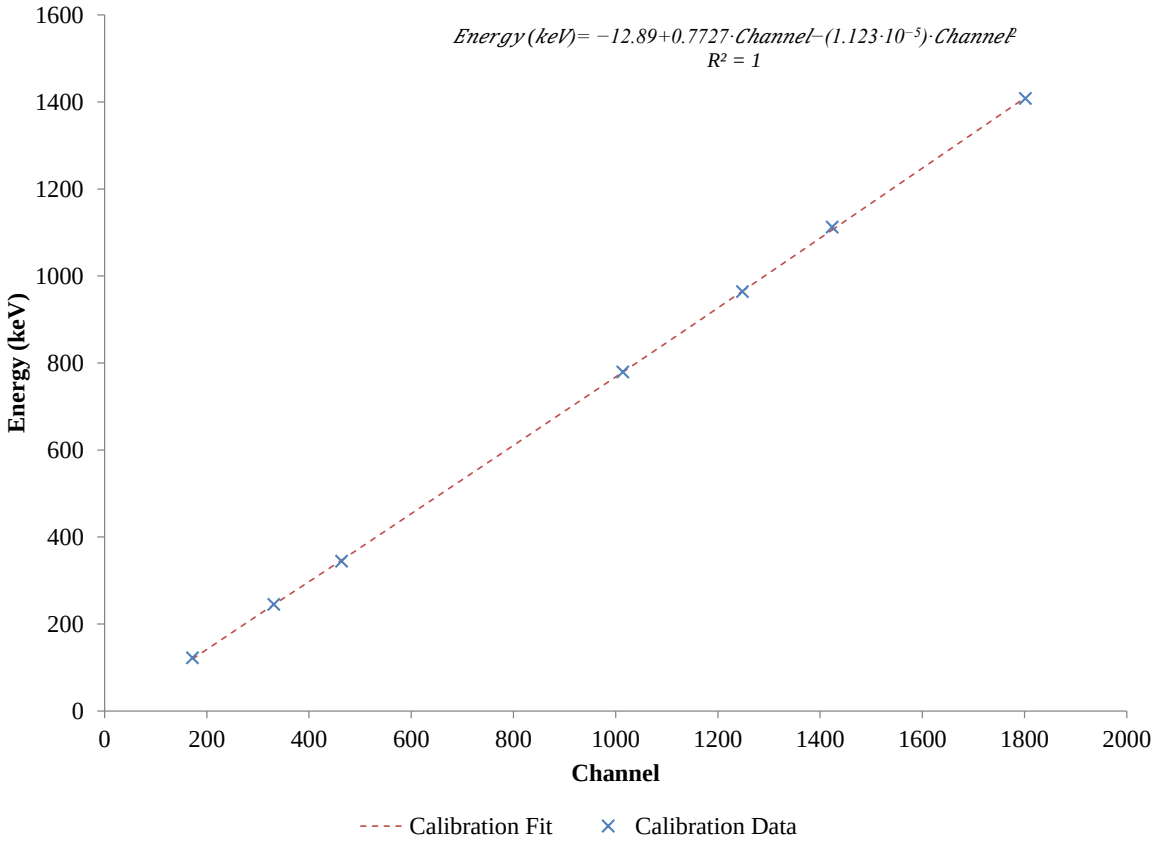

Figure 10-3. Energy Calibration Curve of Osprey 2×2 NaI(Tl) Detector for UNCLE Measurements.

The energy calibration was conducted with the Inspector 1000 $LaBr_3$ detector using a ^{152}Eu gamma-ray source. The calibration was fit to a second-order polynomial in Canberra's Genie software, with a multi-channel analyzer spanning 1517.4 keV over 2048 channels (0.74 keV/channel). The polynomial fit used for the energy calibration is given in Equation 10-3 and plotted in Figure 10-4.

$$Energy\ (keV) = 2.26 + 0.7613 \cdot Channel - (1.049 \cdot 10^{-5}) \cdot Channel^2 \ . \qquad [10\text{-}3]$$

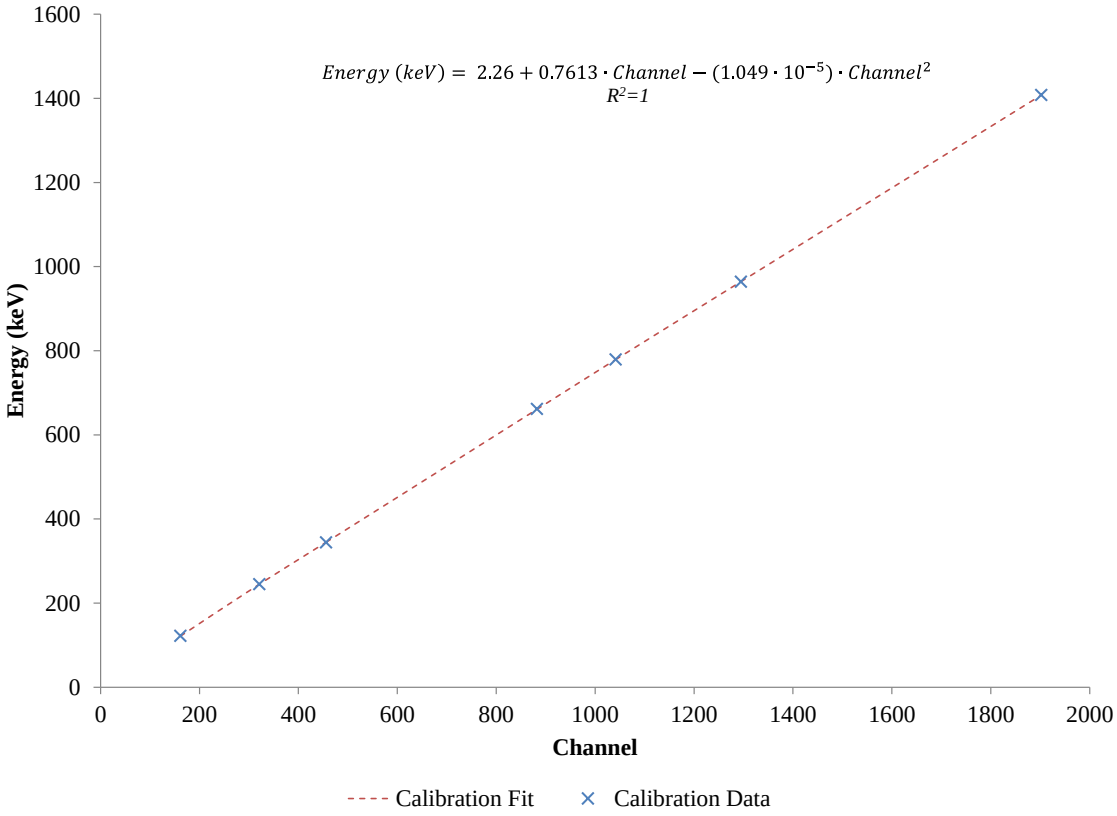

Figure 10-4. Energy Calibration Curve of Inspector 1000 $LaBr_3$ Detector for UNCLE Measurements.

10.3 Change in Flowrate Measurements

The tests conducted in this work at 1070 RPM and 500 RPM correspond to mass flowrates of 7963.4 kg/h and 3528.9 kg/h of UN solution (or 653 kg U/hr and 289 kg U/hr), respectively. With respect to plant classification at this throughput explained in Chapter 2, if UNCLE was run continuously for a whole year, this would correspond to an L-scale NUCP with ~5700 t U/yr. and ~2500 t U/yr., respectively. With respect to flowrate, the conversion from kg UN solution/hr to L UN solution/hr for the UN in UNCLE is given in Figure 10-5.

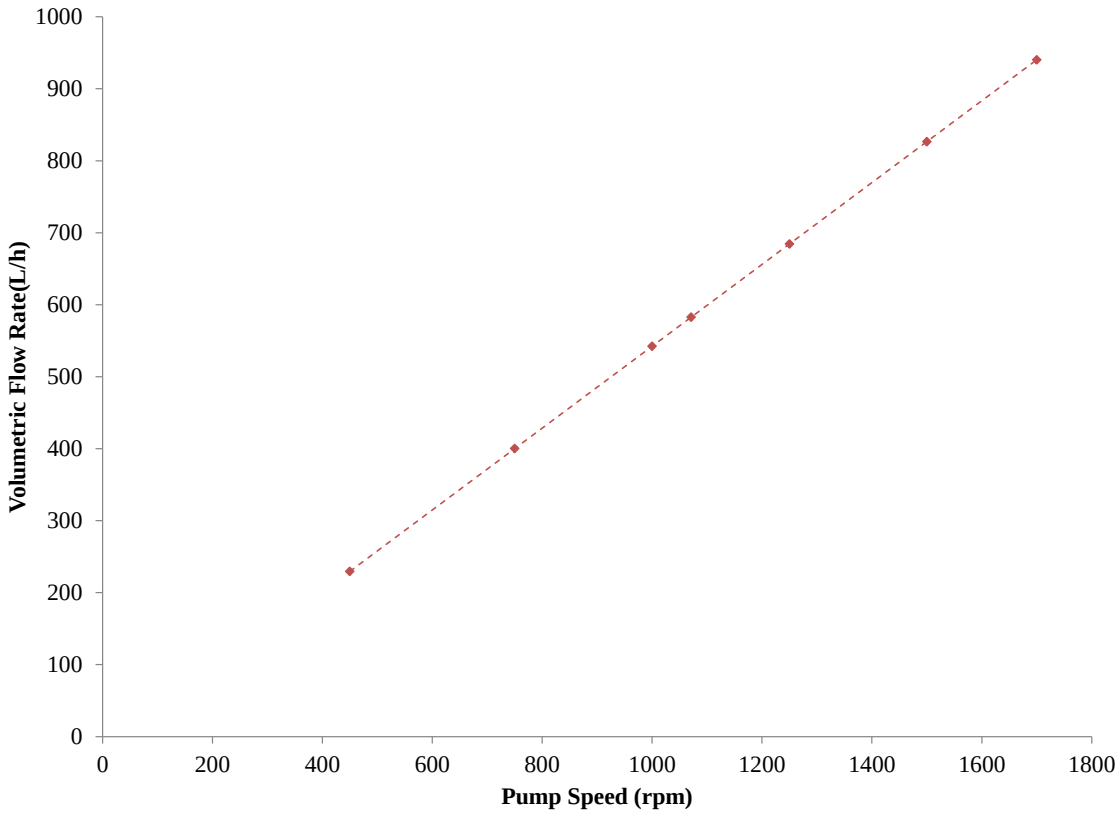

Figure 10-5. Volumetric Flowrate Averages for Varying Pump Speeds in UNCLE.

Data reproduced from [39].

Gamma-ray measurements of ^{235}U were taken in UNCLE at a temperature of 29±3^{o}C and pressure of 58.6±3.5 kPa according to the first temperature and pressure monitors located

adjacent to the detector location before the pump. A comparison of the measured ^{235}U signature spectra in the 100–200 keV range for all the detectors is presented in Figures 10-6 and 10-7 for flowrates under steady-state conditions at 1070 RPM and 500 RPM for a 3600 s live time acquisition time.

Although ^{238}U is not a viable signature for measuring freshly solvent extracted UN, as secular equilibrium of the daughters cannot be guaranteed, the ^{238}U emissions from UNCLE contribute Compton continuum downscatter underlying the lower energy ^{235}U signatures. The full spectra include contributions from ^{238}U from the 40 year old UN in UNCLE, and are provided in Appendix H for the 1070 and 500 RPM flowrates.

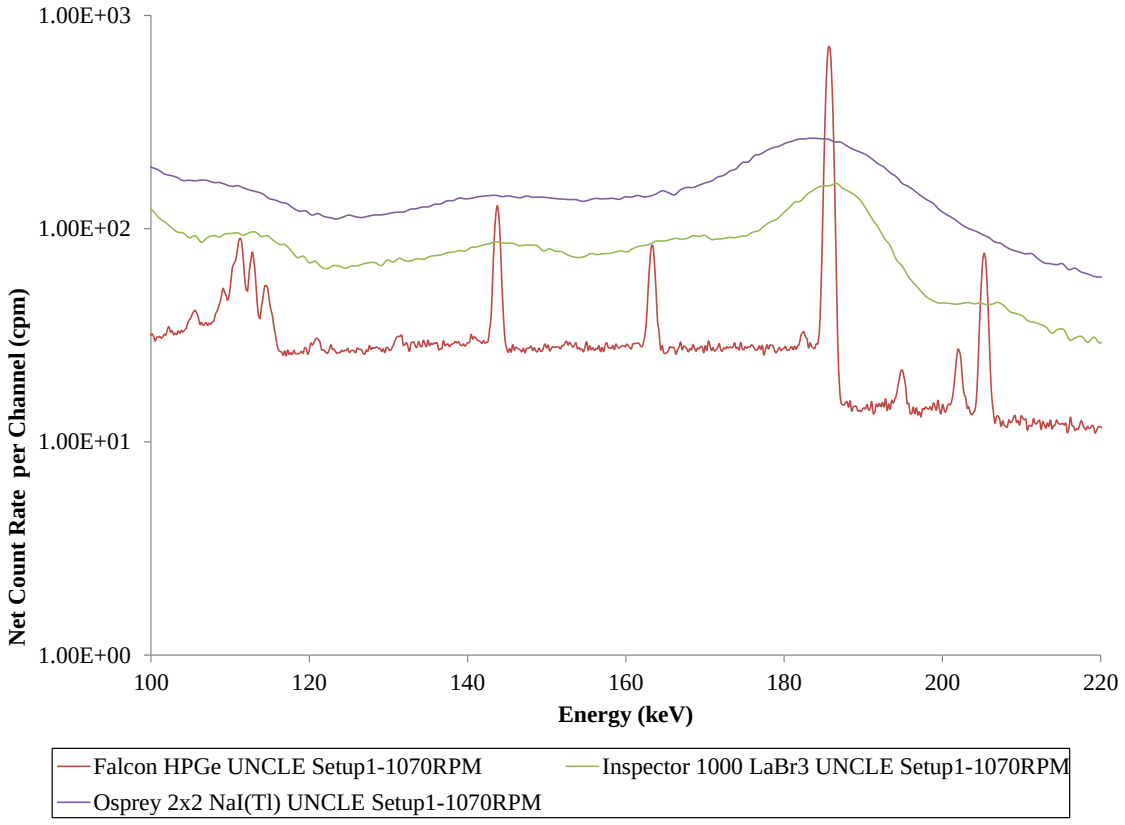

Figure 10-6. Comparison of ^{235}U Spectra for Flowrate Measurements at 1070 RPM at UNCLE.

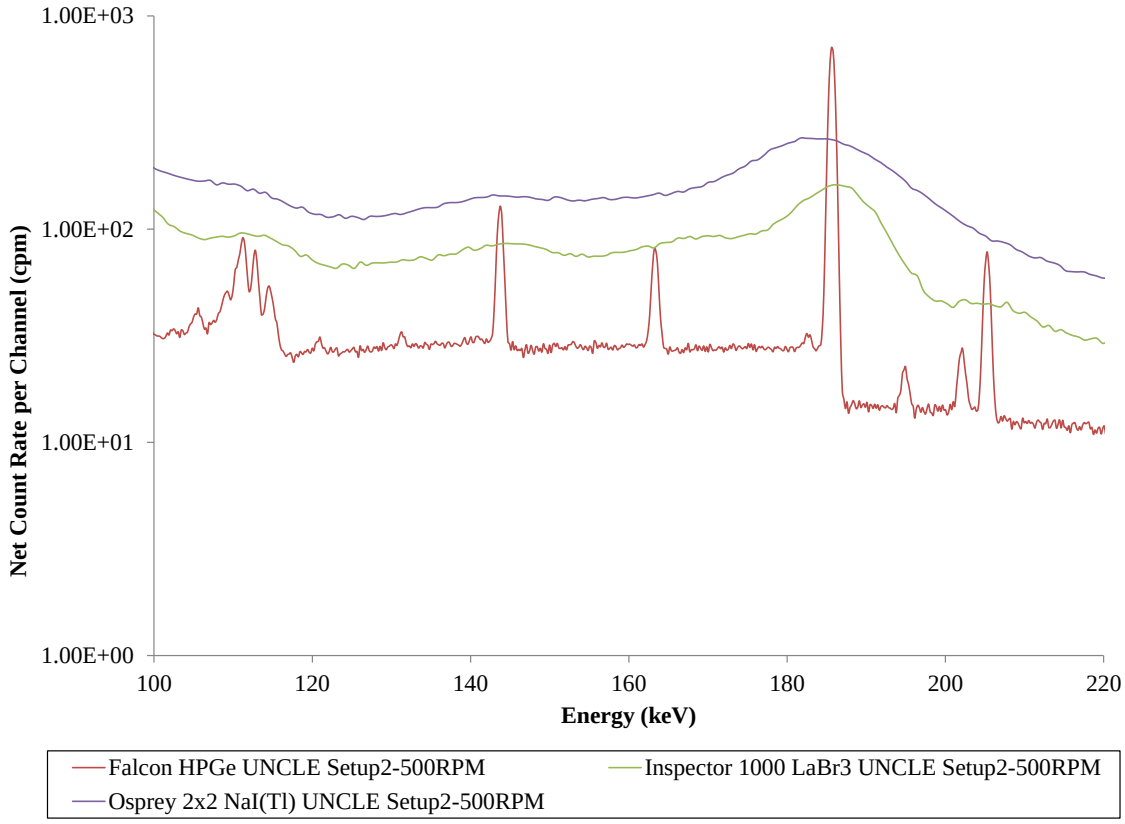

Figure 10-7. Comparison of ^{235}U Spectra for Flowrate Measurements at 500 RPM at UNCLE.

Consistent with the dilution measurement results, the Falcon BEGe has the highest resolution, whereas the 2×2 NaI(Tl) Osprey had lowest resolution, being unable to resolve the 185.7 keV peak from the 163.3, 194.9, 202.1, and 205.3 keV peaks. Similarly, the Inspector 1000 provides superior resolution to the Osprey, but with a lower efficiency. If focused on this energy range and ^{235}U contributes the only signatures at this range, then the lower resolution ROI could be a feasible monitoring signature. However, employment of this multi-peak ROI becomes problematic in a high-background environment of if Compton downscatter increased the continuum under the net peak area. The peak area boundary (ROIs) and peak-to-total values for the 185.7 keV peak are summarized in Table 10-1. As shown in the ROI 185.7 keV peak area depicted in

Figure 10-8, the Osprey has the highest peak area efficiency for the 185.7 keV range, whereas the Inspector 1000 has the lowest efficiency. However, as seen for all detectors, there is very poor discrimination in resolving the change in flowrate from the 1070 RPM to 500 RPM levels. For the Falcon BEGe, the peak area drops by 0.27% with an associated statistical peak area uncertainty at 1070 RPM of 1.68%. The change in peak area from the 1070 RPM to 500 RPM for the Osprey and Inspector is slightly more pronounced at 9.77% and 6.96%, but with associated statistical peak area uncertainties at 1070 RPM of 2.76% and 1.29%, respectively. Consequently, passive gamma-ray detection poorly discriminates flowrate for all detectors in the tested 500 to 1070 RPM range. It is expected that passive gamma-ray discrimination will also be poor for flowrates above this range, since the detectors see the same active detector volume of filled pipe, in addition to being limited by temporal resolution. Activation analysis can perhaps remedy these limitations and will be discussed in the analysis and recommendations in Chapters 13 and 14.

Table 10-1. Region of Interest (ROI) Boundaries and Efficiency Properties of 185.7 keV ^{235}U Peak in UNCLE Measurements.

Detector	ROI (keV)	Peak-to-Total Ratio 1070 RPM	Peak-to-Total Ratio 500 RPM
Falcon BEGe	[184.1, 187.6]	0.0742(±0.21%)	0.0743(±0.21%)
Inspector 1000 $LaBr_3$	[161,199]*	0.1235(±0.22%)	0.1420(±0.21%)
Osprey 2×2 NaI(Tl)	[125,225] *	0.3460(±0.11%)	0.2770(±0.12%)

**Includes multiplet peak fit by Genie.*

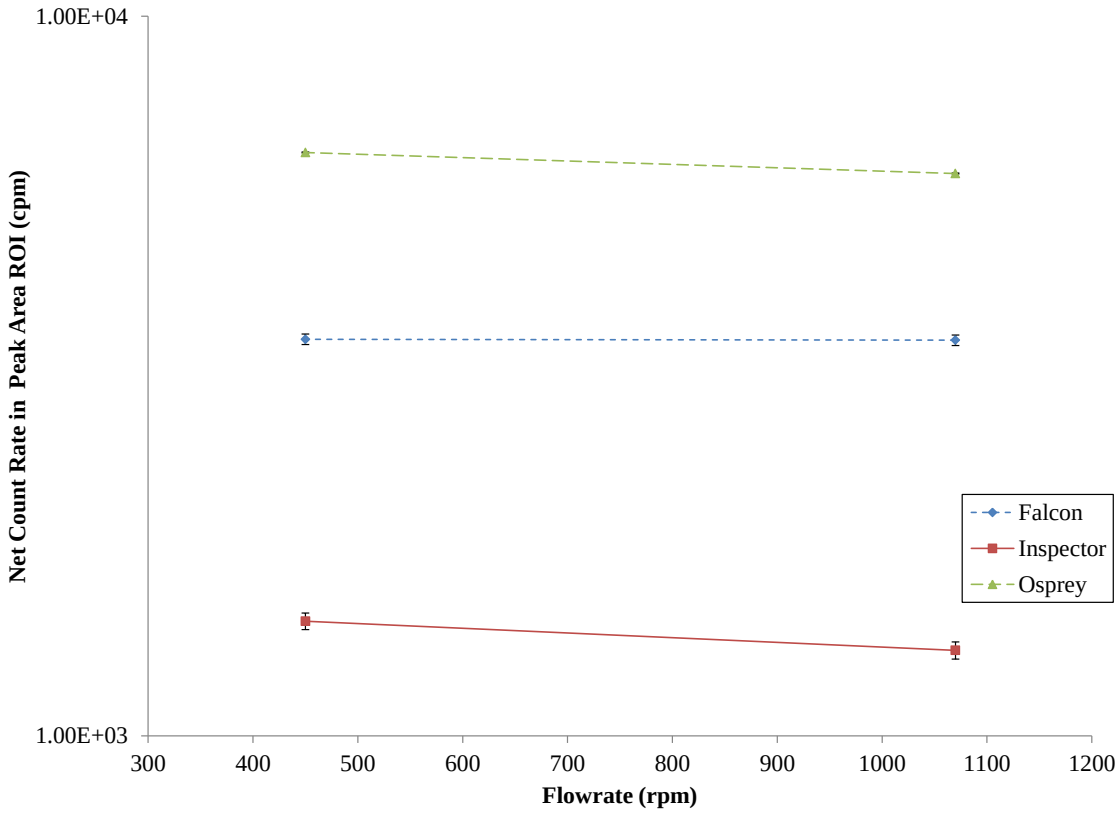

Figure 10-8. Comparison of UNCLE Peak Areas at 1070 RPM and 500 RPM.

The pipe specifications and source-detector geometry employed in the dilution experiments were emulated in the UNCLE facility. In addition, the UN employed for the dilution experiment was extracted from UNCLE. However, despite keeping the aforementioned parameters consistent, variables such as changes in temperature and pressure from dynamic fluid flow, in addition to voiding effects, deviate from the measured gamma-ray static dilution signatures. A comparison of the 1070 RPM, 500 RPM, and dilution peak spectra is given in Figure 10-9, with a zoom in on the 185.7 keV peak from ^{235}U in Figure 10-10. Spectra comparing the UNCLE and dilution measurements for the Osprey and Inspector are similarly given in Figures 10-11 and 10-12, respectively.

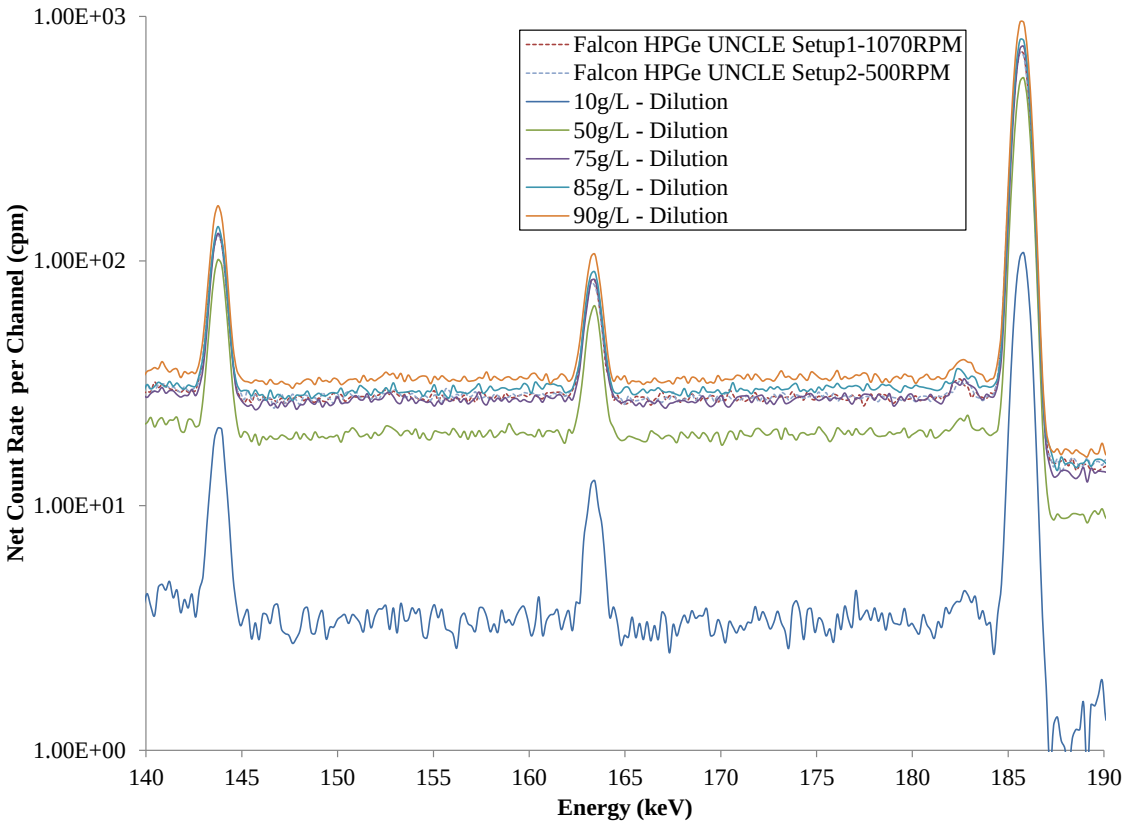

Figure 10-9. Comparison of UNCLE Spectra at 1070 RPM and 500 RPM with Dilution Spectra for Falcon BEGe.

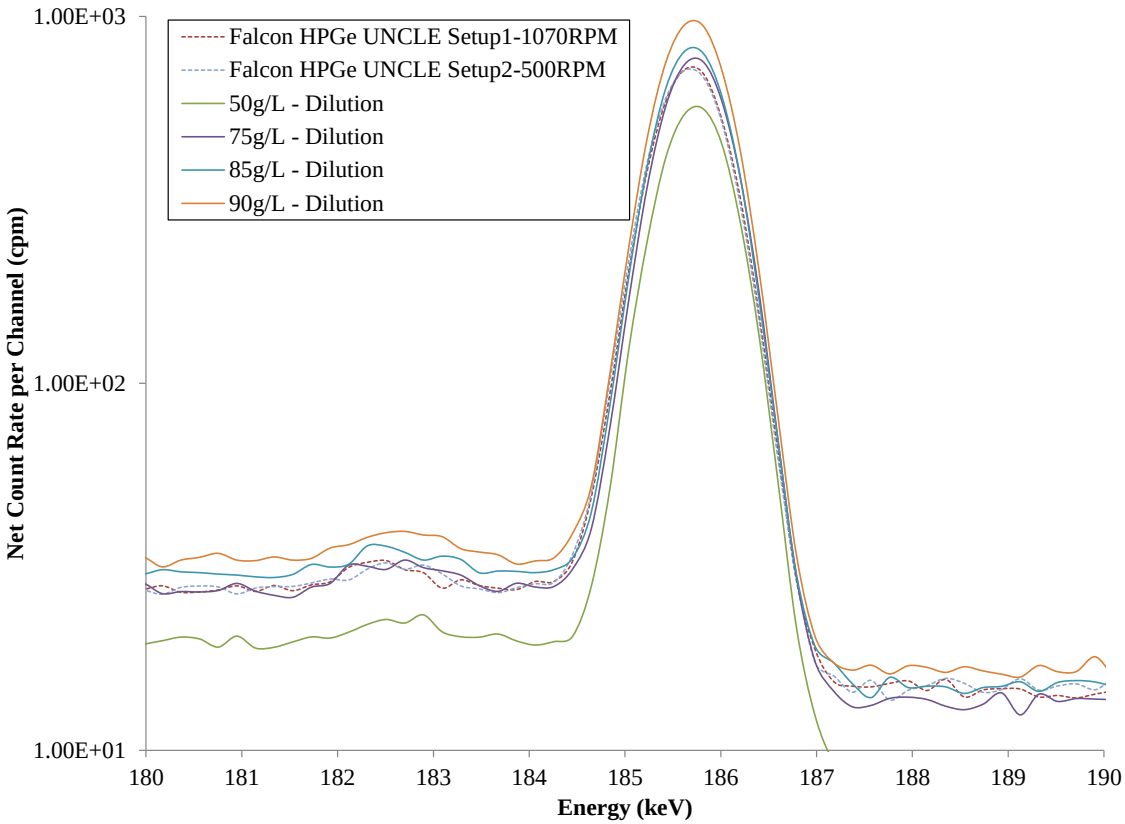

Figure 10-10. Comparison of UNCLE Spectra at 1070 RPM and 500 RPM with Dilution Spectra for Falcon BEGe at 185.7 keV ^{235}U Energy.

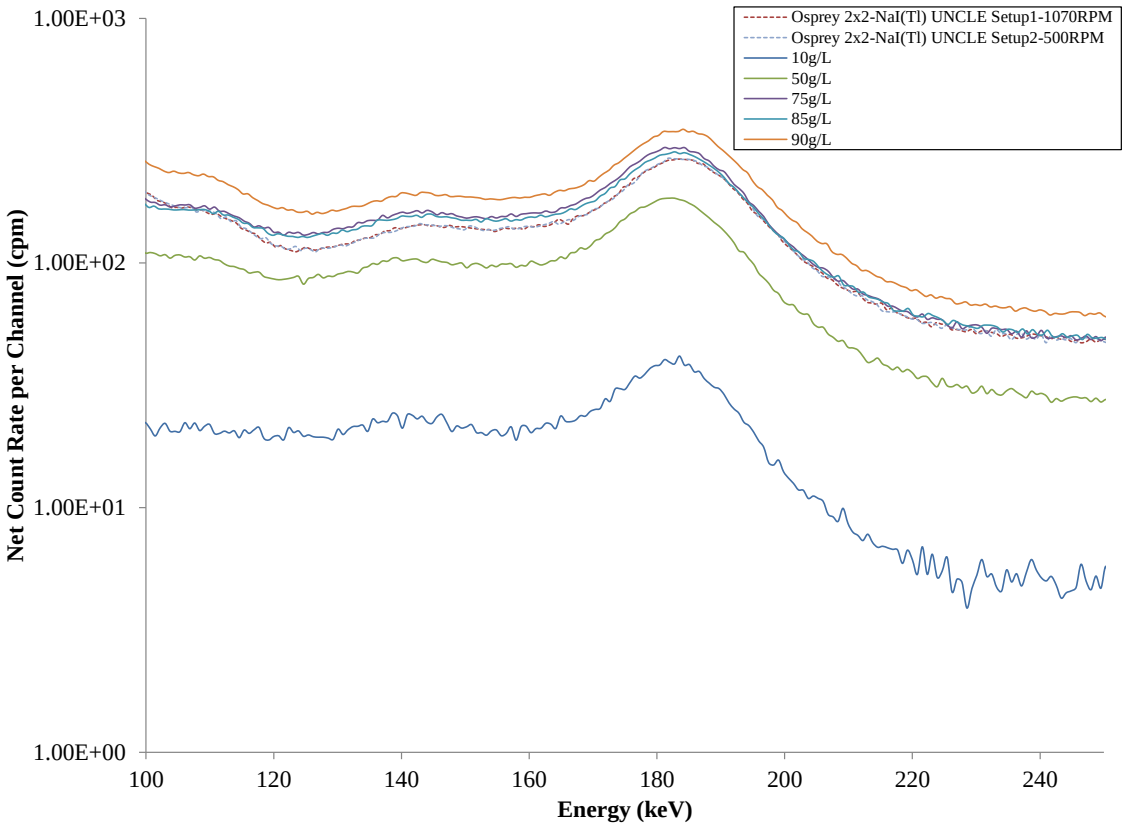

Figure 10-11. Comparison of UNCLE Spectra at 1070 RPM and 500 RPM with Dilution Spectra for Osprey NaI(Tl) at 185.7 keV ^{235}U Energy.

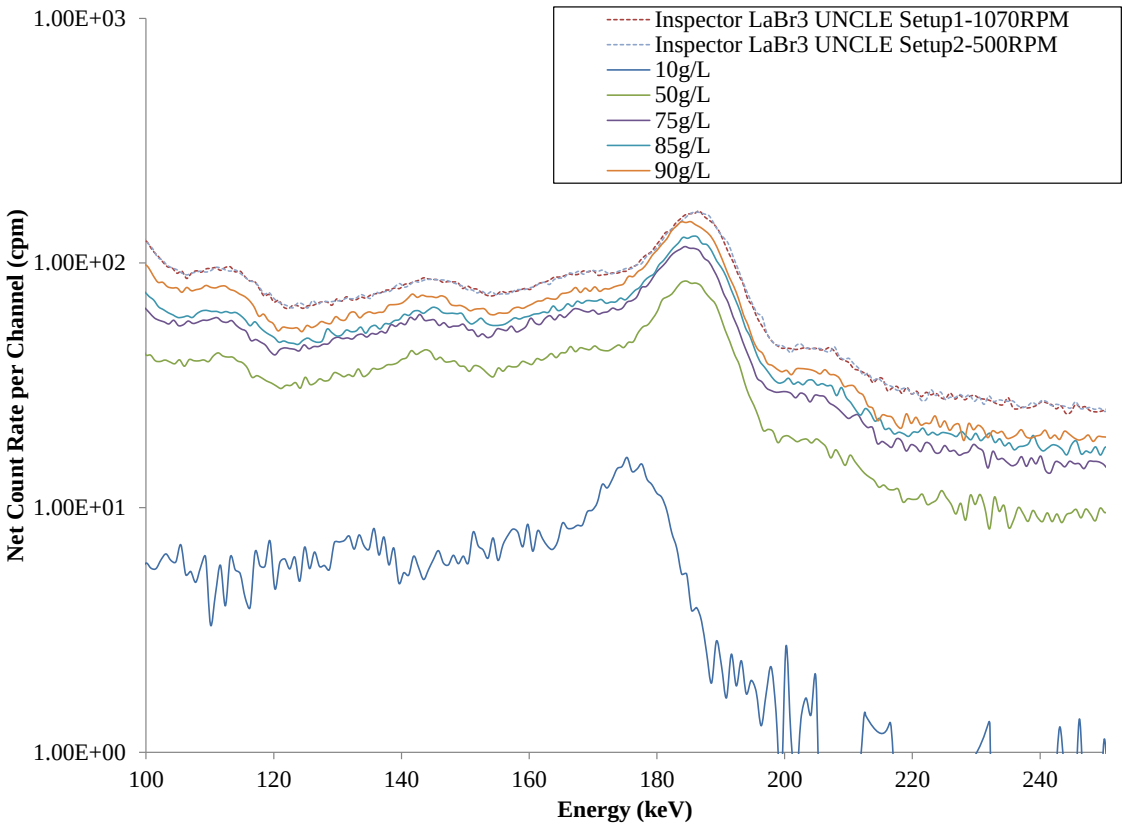

Figure 10-12. Comparison of UNCLE Spectra at 1070 RPM and 500 RPM with Dilution Spectra for Inspector $LaBr_3$ at 185.7 keV ^{235}U Energy.

Even though the UN circulating in UNCLE is the same UN employed in the 90 g U/L dilution measurements, vibrations, environmental temperature, and most importantly, voiding effects due to dynamic fluid flow contribute to an overall effective density lower than that of static measurements. Since Figure 10-8 shows no overall difference in fluid flow, effects due to voiding and localized air bubbles contribute to the overall lower effective uranium content measured in UNCLE. Figure 10-13 compares the 185.7 keV peak area from ^{235}U for both the UNCLE flowrate measurements and the static dilution measurements. The low efficiency of the Inspector measurements is inconsistent with the Falcon and Osprey measurements. Source-detector geometry, ROI selection, and peak discrimination methods employed by Genie, as well as localized voiding, background, and environmental conditions, contribute to interpretations of these results.

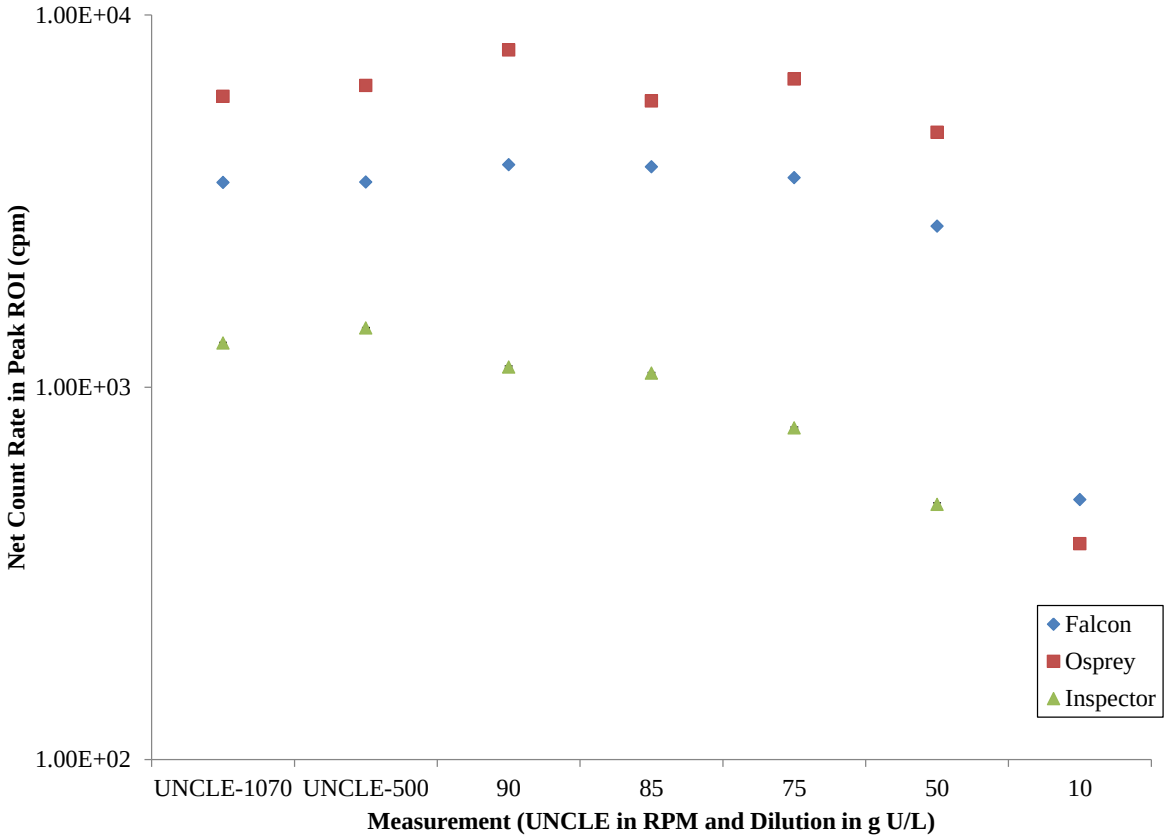

Figure 10-13. Comparison of ^{235}U 185.7 keV UNCLE Flowrate Peak Areas at Dilution Peak Areas for All Detectors.

Note: Error bars plotted for some data points are smaller than the resolution of the graph.

If peak area is indicative of overall uranium content, the UNCLE data, as shown by the Falcon and Osprey measurements, indicate that voiding reduces the effective concentration to that of the 75–85 g U/L, with a corresponding density ranging from 1.099–1.115 g/cm^3.

10.4 UNCLE ^{137}Cs Transmission Measurements

As with the static dilution experiments, transmission measurements were taken with ^{137}Cs to assess the 661.7 keV emission sensitivity to uranium content. Spectra were collected at the same location and setup as the flowrate measurements for 3600 s live time at the 1070 RPM flowrate. A comparison of the full energy spectrum for all detectors is plot in Figure 10-14. In order to compare the 661.7 keV transmission peak area from the UNCLE measurements from the transmission measurements in the dilution experiments, these spectra were overlaid for the Falcon, Osprey, and Inspector detectors.

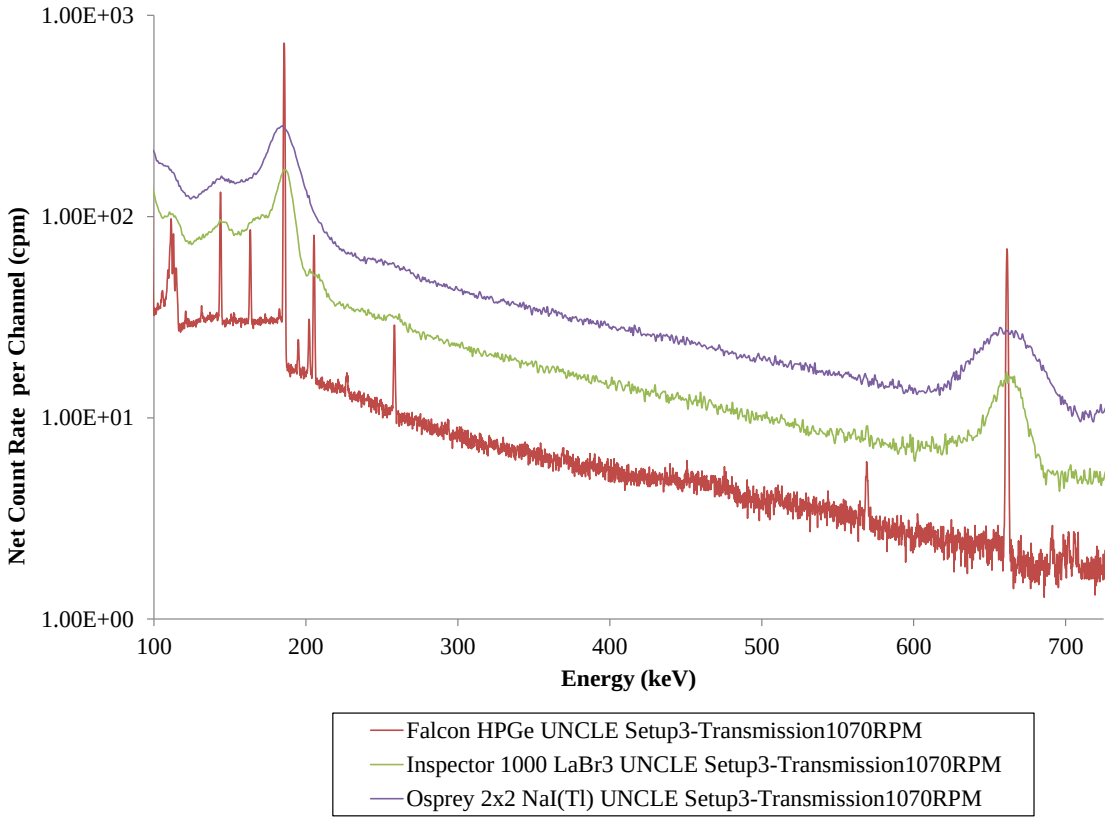

Figure 10-14. Comparison of UNCLE ^{137}Cs Transmission Spectra at 1070 RPM for All Detectors.

The peak area boundary (ROIs) and peak-to-total values for the 661.7 keV peak are summarized in Table 10-2. As shown in the ROI 661.7 peak area depicted in Figure 10-15, the Osprey has the highest peak area efficiency for the 661.7 keV ^{137}Cs

peak, whereas the Inspector 1000 has the lowest efficiency. This is consistent with the flowrate and dilution measurement results. In addition, peak ratio values are provided in Figure 10-16 comparing the 661.7-to-185.7 keV peak areas for the 1070 RPM flowrate with the static dilution measurements.

Table 10-2. Region of Interest (ROI) Boundaries and Efficiency Properties of 661.7 keV ^{137}Cs Peak in UNCLE Measurements.

Detector	ROI (keV)	FWHM (keV)	Peak-to-Total Ratio 1070 RPM
Falcon BEGe	[659.5, 663.9]	1.36	0.0093 (±0.55%)
Inspector 1000 $LaBr_3$	[615.8,696.0]	20.87	0.0304 (±0.40%)
Osprey 2×2 NaI(Tl)	[606.1, 709.9]	41.85	0.0410 (±0.26%)

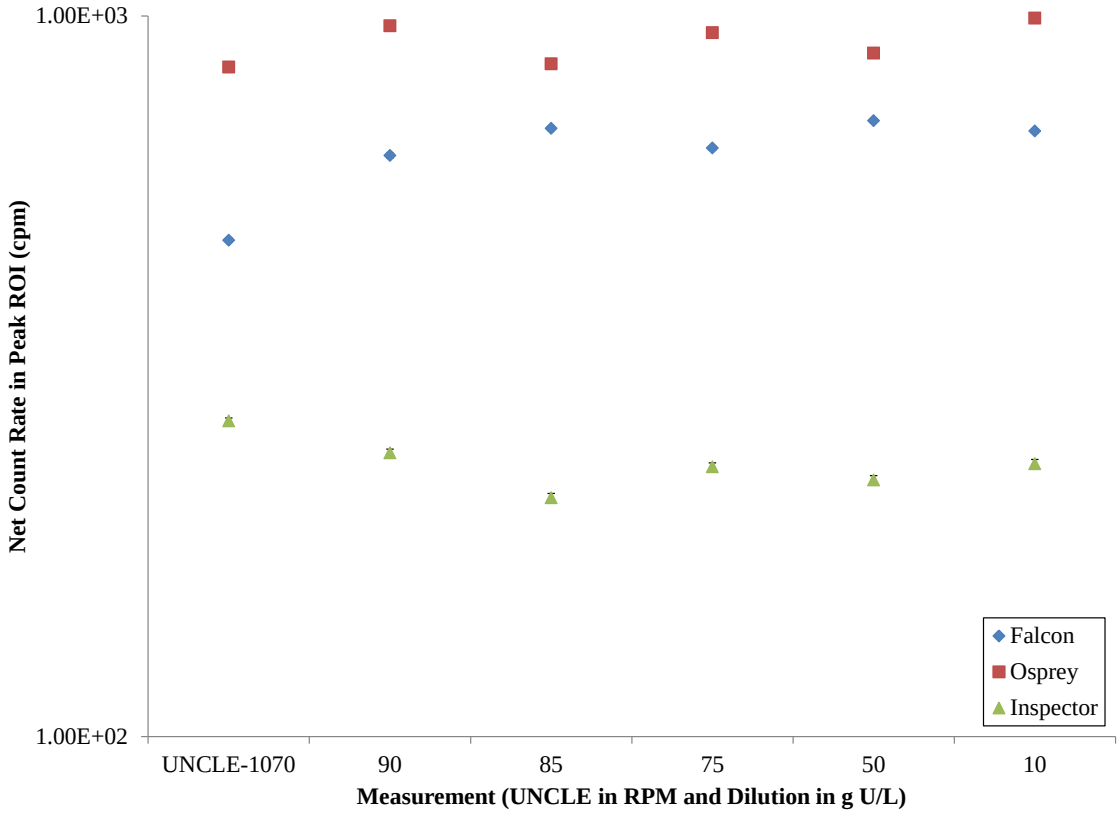

Figure 10-15. Comparison of UNCLE Transmission Peak Areas at 1070 RPM with Dilution ^{137}Cs Transmission Peak Areas for All Detectors.

Note: Error bars plotted for some data points are smaller than the resolution of the graph.

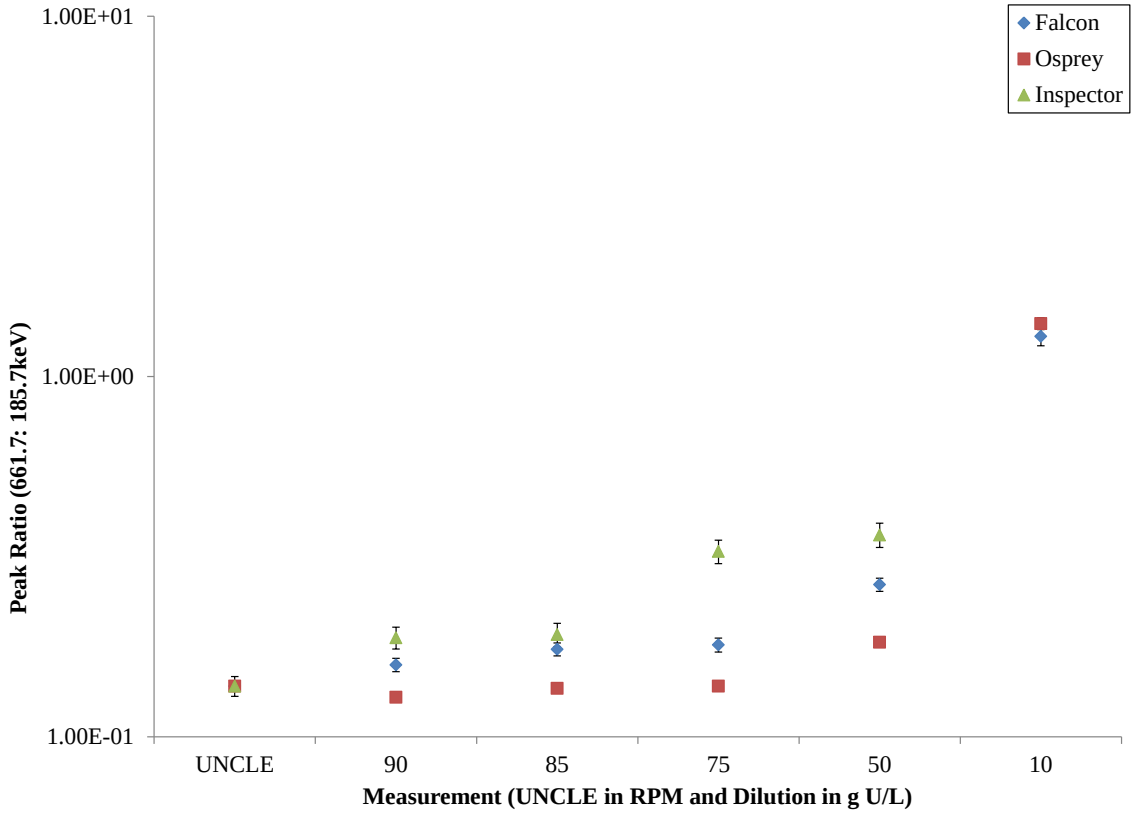

Figure 10-16. Comparison of UNCLE ^{137}Cs Transmission Peak Ratios at 1070 RPM with Transmission Ratios at Dilution Concentrations for All Detectors.

Note: Error bars plotted for some data points are smaller than the resolution of the graph.

Even though the source was UN at 90 g U/L, pipe specifications and source-detector geometry employed in the dilution experiments were emulated in the UNCLE facility, changes in environmental variables, in addition to resettling from fluid flow, deviate from static transmission measurement parameters. A comparison of the transmission measurements at 1070 RPM in UNCLE and dilution peak spectra is given in Figures 10-17 through 10-19, focused on the 661.7 keV energy range for the Falcon, Osprey, and Inspector detectors, respectively.

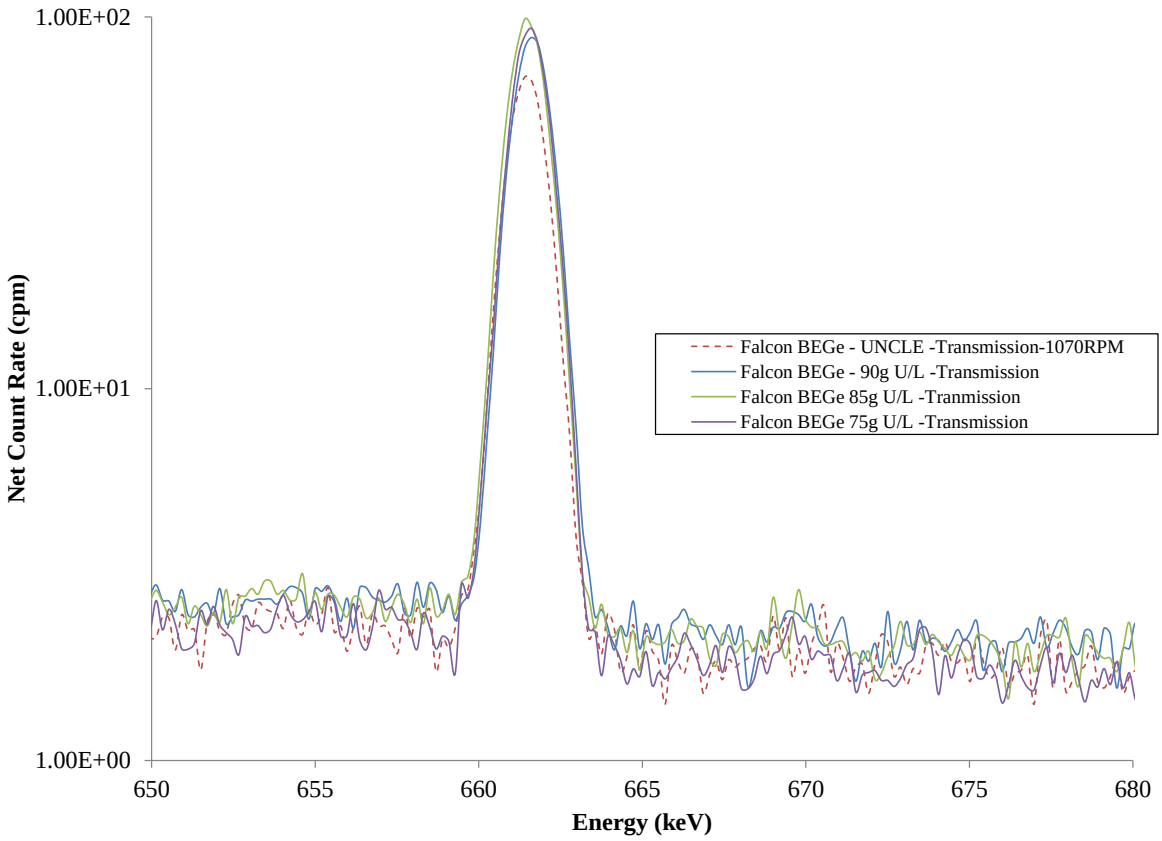

Figure 10-17. Comparison of UNCLE Transmission Spectra at 1070 RPM with Dilution Transmission Spectra for Falcon BEGe.

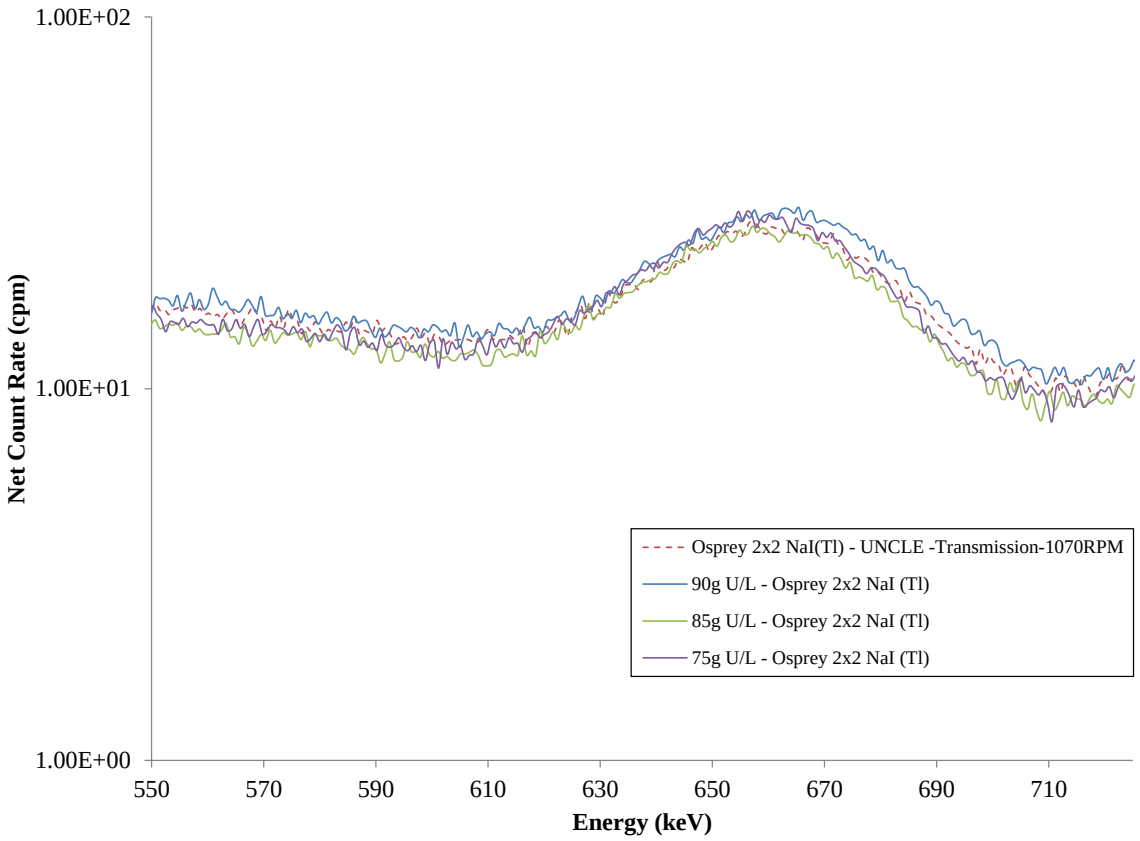

Figure 10-18. Comparison of UNCLE Transmission Spectra at 1070 RPM with Dilution Transmission Spectra for Osprey NaI(Tl).

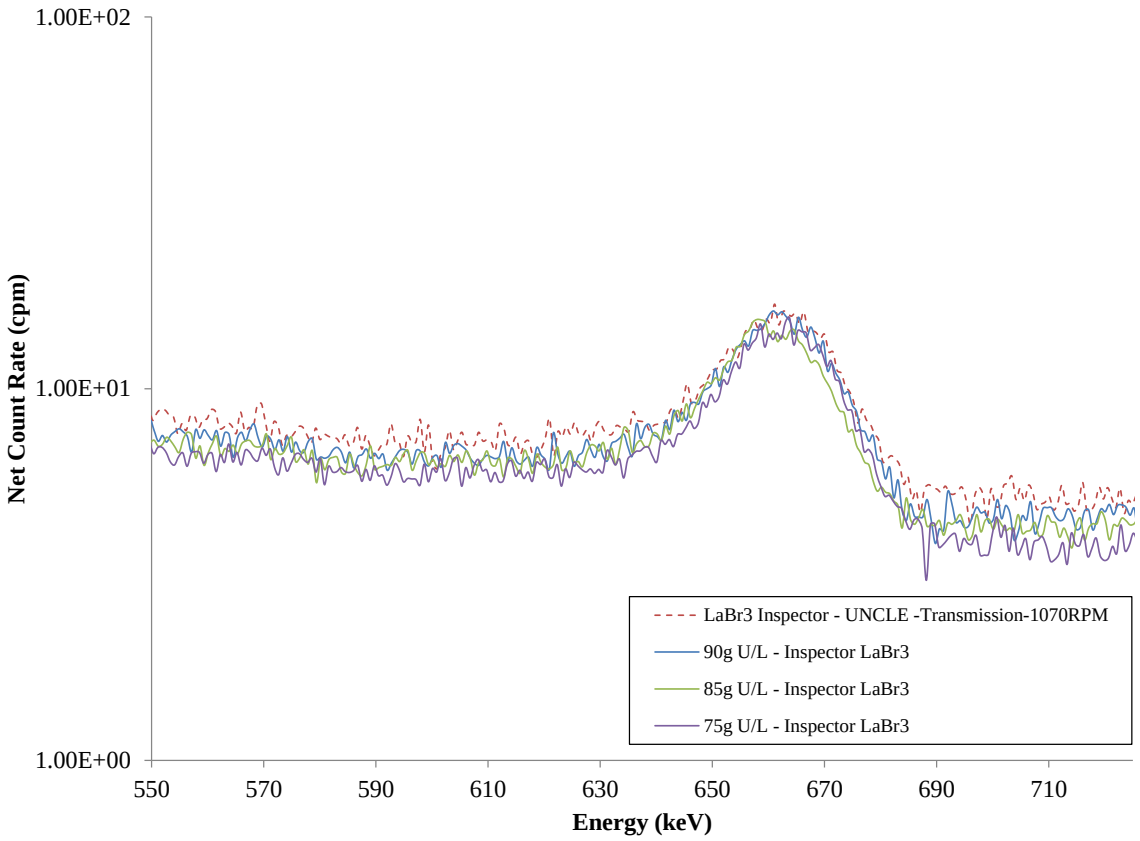

Figure 10-19. Comparison of UNCLE Transmission Spectra at 1070 RPM with Dilution Transmission Spectra for Inspector $LaBr_3$.

As tested with the dilution measurements, the ^{137}Cs peak area and ratios provide a signature of overall uranium content in the UN. The UNCLE data indicates that voiding reduces the effective concentration to that of the 75–85 g U/L range, as seen with the Osprey measurements in Figures 10-15 and 10-16. However, as the dilution measurements found ^{137}Cs to be relatively insensitive to uranium content, this may also be the case with the flowrate measurements.

10.5 Conclusions

Both passive ^{235}U and ^{137}Cs transmission densitometry measurements were conducted in field trials at UNCLE using the three detectors employed in the dilution experiments. The dilution measurements provided indications of instrumentation sensitivity and potential monitoring signatures, which were tested in an operational environment. In the presence of realistic operating conditions, including facility background (pipes/tanks), environmental variables (temperature, pressure), and fluid flow dynamics, the robustness of the Falcon, Inspector, and Osprey were tested under such operating conditions. In the comparative flowrate measurements at 1070 RPM and 500 RPM, ^{235}U signatures were assayed to ascertain whether uranium content could be determined. In comparison to the static dilution experiments, the dynamic flowrate measurements provided results indicating that voiding effects largely contributed to the observed decrease in the 185.7 keV peak area, despite the maintenance of the pipe material, source-detector geometry, and UN material originating from the a common stock 90 g U/L solution. The effective count rate from the 185.7 keV peak from UNCLE was in the range of the 75–85 g U/L measurements from the dilution experiments, indicating a net lower concentration in UNCLE as seen by the detector, likely due to voiding effects. Similarly, ^{137}Cs transmission measurements were conducted at 1070 RPM, emulating the dilution transmission measurements, to determine the effectiveness of ^{137}Cs in assaying uranium content. As seen with the transmission dilution measurements in Chapter 9, ^{137}Cs is relatively insensitive to uranium content over the concentration range of 10–90 g U/L and densities of 1.008–1.122 g/cm^3.

The evaluation of a fieldable COTS detector and transmission monitoring source is finally contingent upon statistical and uncertainty variables, including background effects, peak area continuum, and sensitivity to detector offset positioning, in addition to

further efficiency variables. These factors will be discussed as part of a comprehensive uncertainty and sensitivity analysis in Chapter 12.

CHAPTER 11. RESULTS: VALIDATION SIMULATION MODELS

11.1 Passive Simulation Validation Results

For each of the five measured dilution concentrations outlined in Table 8-5, a comparison of the measured and MCNPX simulated spectra for passive measurements of 90 g, 85 g, 75 g, 50 g, and 10 g U/L of UN are presented in Figures 11-1 through 11-5.

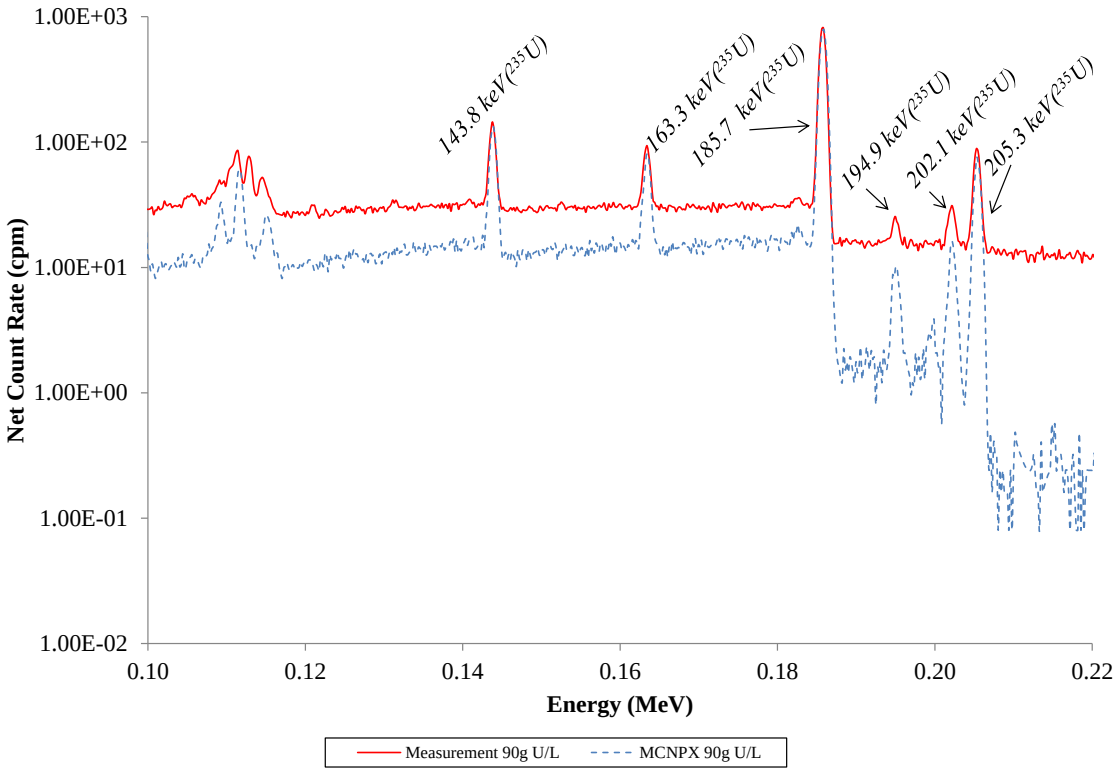

Figure 11-1. 90 g U/L Comparison of Dilution Measurement Data with MCNPX Simulation.

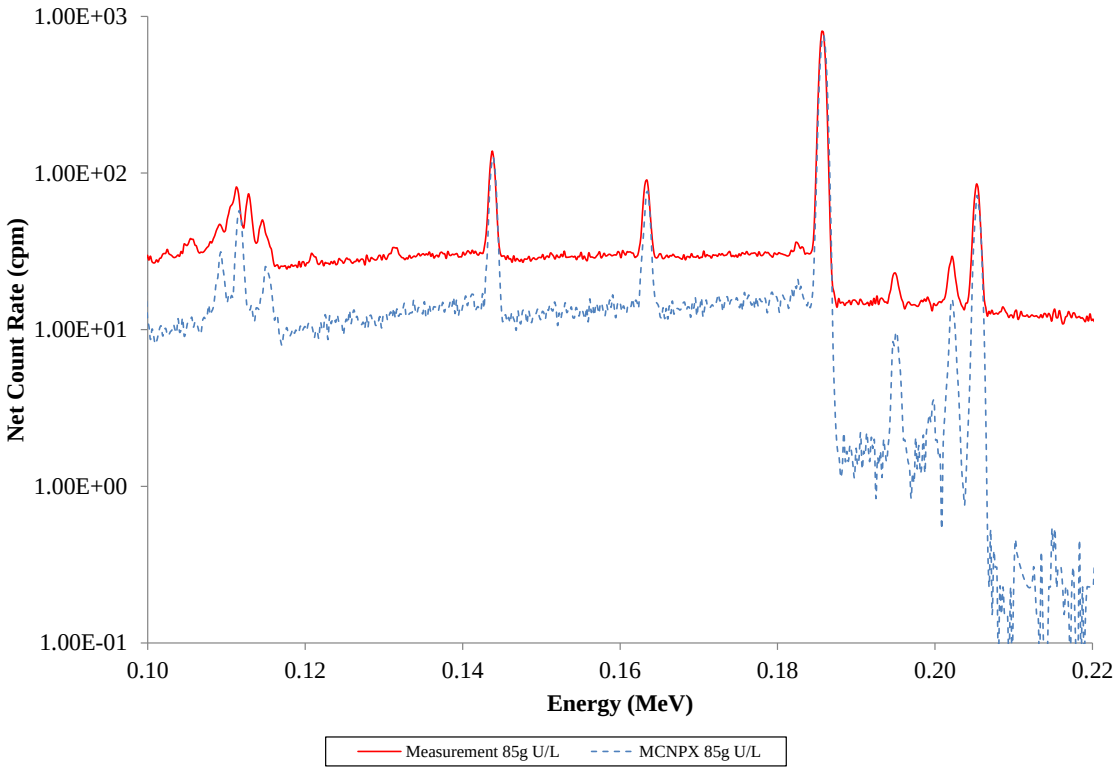

Figure 11-2. 85 g U/L Comparison of Dilution Measurement Data with MCNPX Simulation.

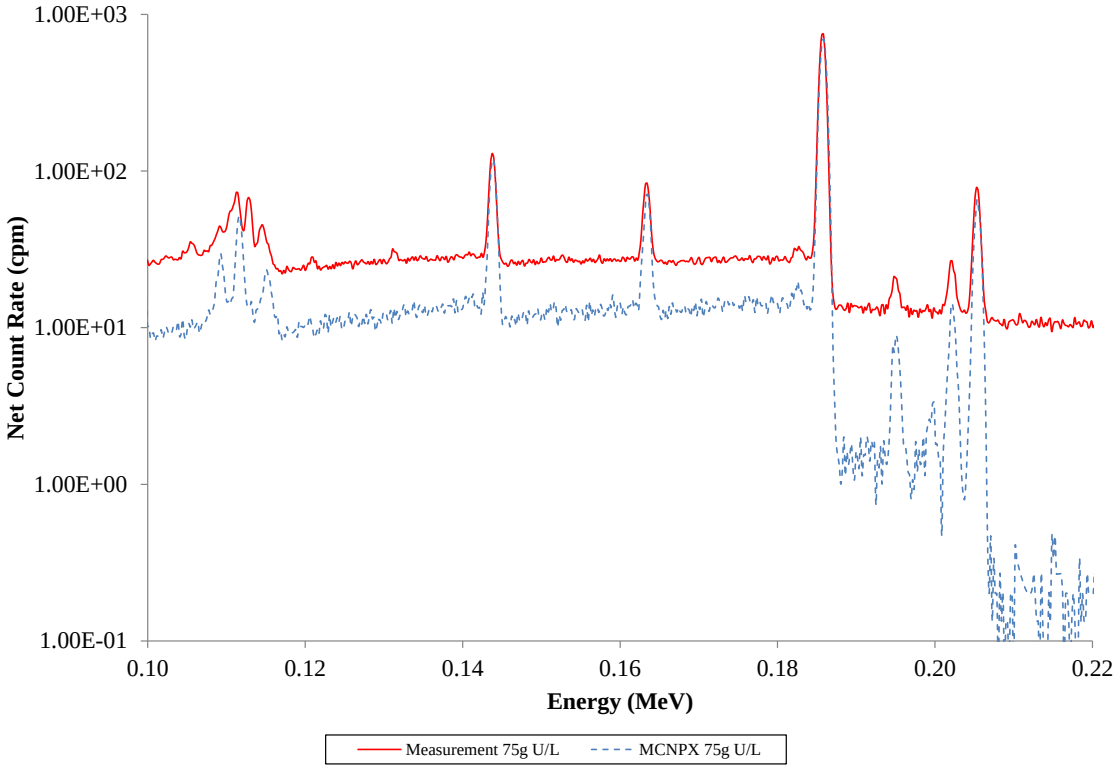

Figure 11-3. 75 g U/L Comparison of Dilution Measurement Data with MCNPX Simulation.

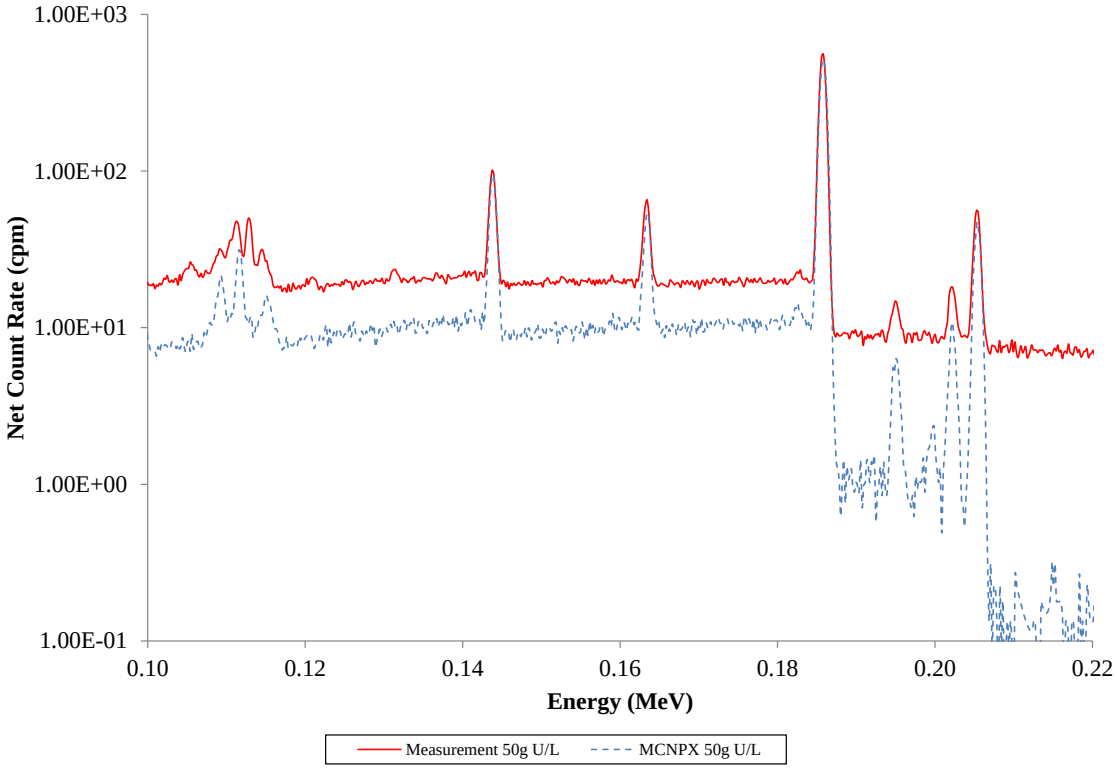

Figure 11-4. 50 g U/L Comparison of Dilution Measurement Data with MCNPX Simulation.

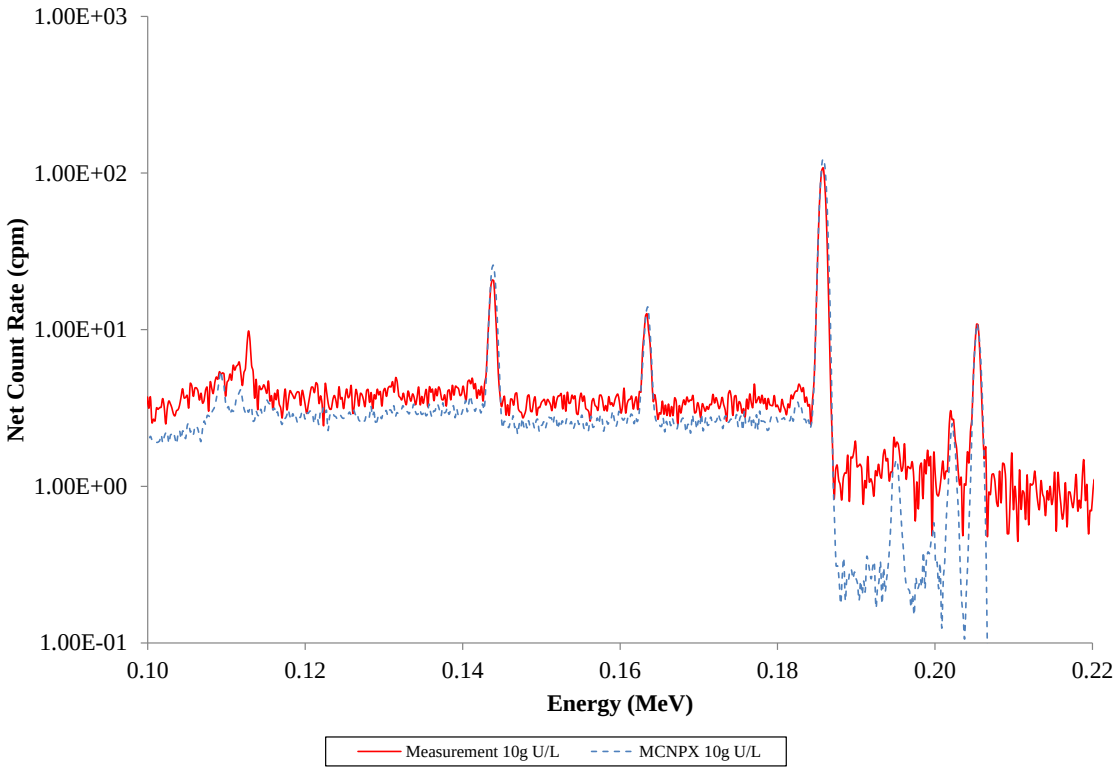

Figure 11-5. 10 g U/L Comparison of Dilution Measurement Data with MCNPX Simulation.

Consistent with the ROI selection in Chapter 9, the ROIs in the experimental measurements were emulated for the simulation spectra in order to determine the net peak areas at each dilution concentration for the high-intensity ^{235}U emissions. These peaks are summarized in Table 11-1. Figure 11-6 plots the peak area of the simulated highest intensity emissions as a function of dilution concentration. Sources of deviations from linearity for both the simulation compared to the experimental data include variables that cannot be simulated, such as electronics variables, detector dead time, and conversion to light from the electron energies.

Table 11-1. Region of Interest (ROI) Boundaries for Gamma-Ray Emissions from Dilution and Transmission MCNPX Simulations of UN for the Falcon BEGe.

Peak Energy (keV)	ROI Energy (keV)
143.76	[142.5, 145.5]
163.33	[161.6, 164.9]
185.72	[184.5, 187.8]
122.1	[120.6, 123.5]
356.0	[354.1,358.0]
661.7	[659.5, 663.8]

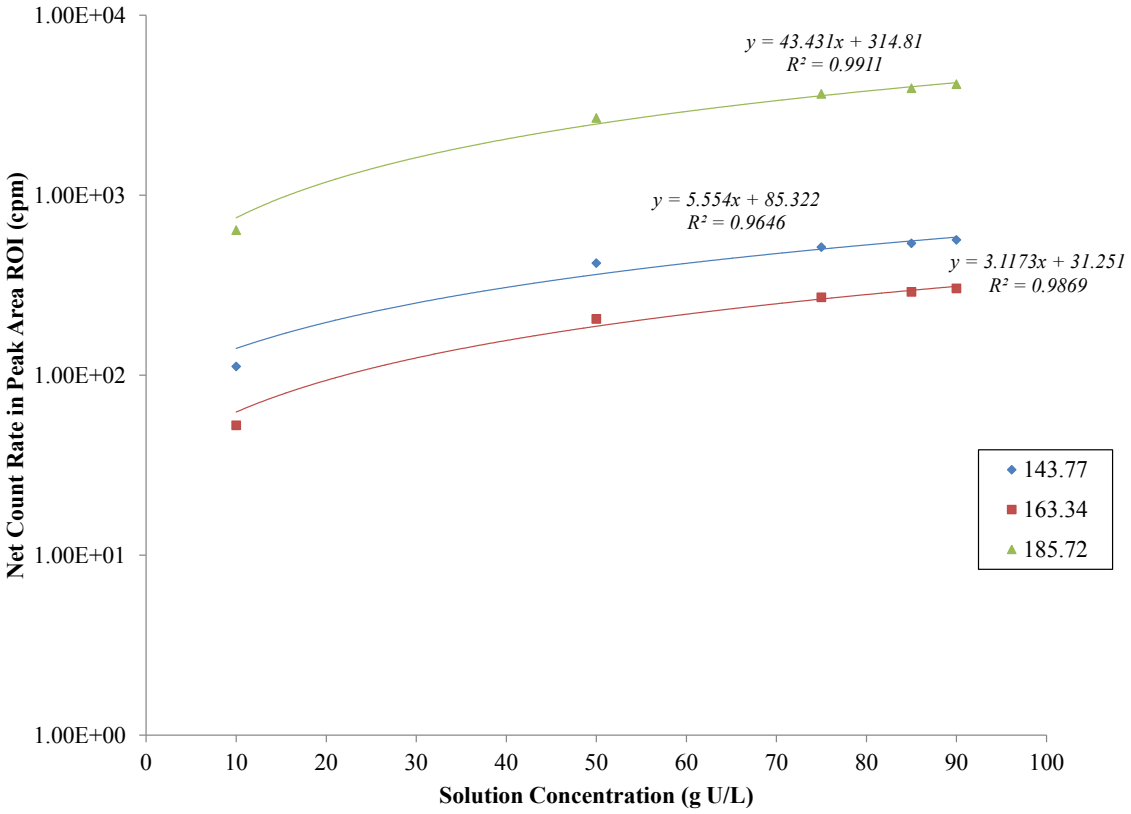

Figure 11-6. Net Peak Area for ^{235}U 185.7 keV Emission as a Function of Dilution Concentration for MCNPX.

The fit values for passive measurements and simulations have correlation coefficient *(R^2)* values higher than 0.9, indicating a strong linear fit for this signature ratio *(y)* as a function of solution concentration *(x)*.

Use of peak ratio methods for peaks within the same energy range ensures that the detector efficiency is also similar between the two peaks. Such peak ratio methods also allow for the uranium concentration to be determined without calibration constants or infinite thickness requirements, making ratios more robust signature indicators [87]. As given in Table 6-2, the highest intensity emissions beyond the 185.7 keV (57.2%) signature emissions from ^{235}U are (in order of decreasing intensity) 143.8 keV (10.96%), 163.3 keV (5.08%), 194.9 keV (0.63%), 202.1 keV (1.08%), and 205.3 keV (5.01%). All energies comparing simulation and experimental ratios are plotted in Figure 11-7 for the dilution concentration of 90 g U/L.

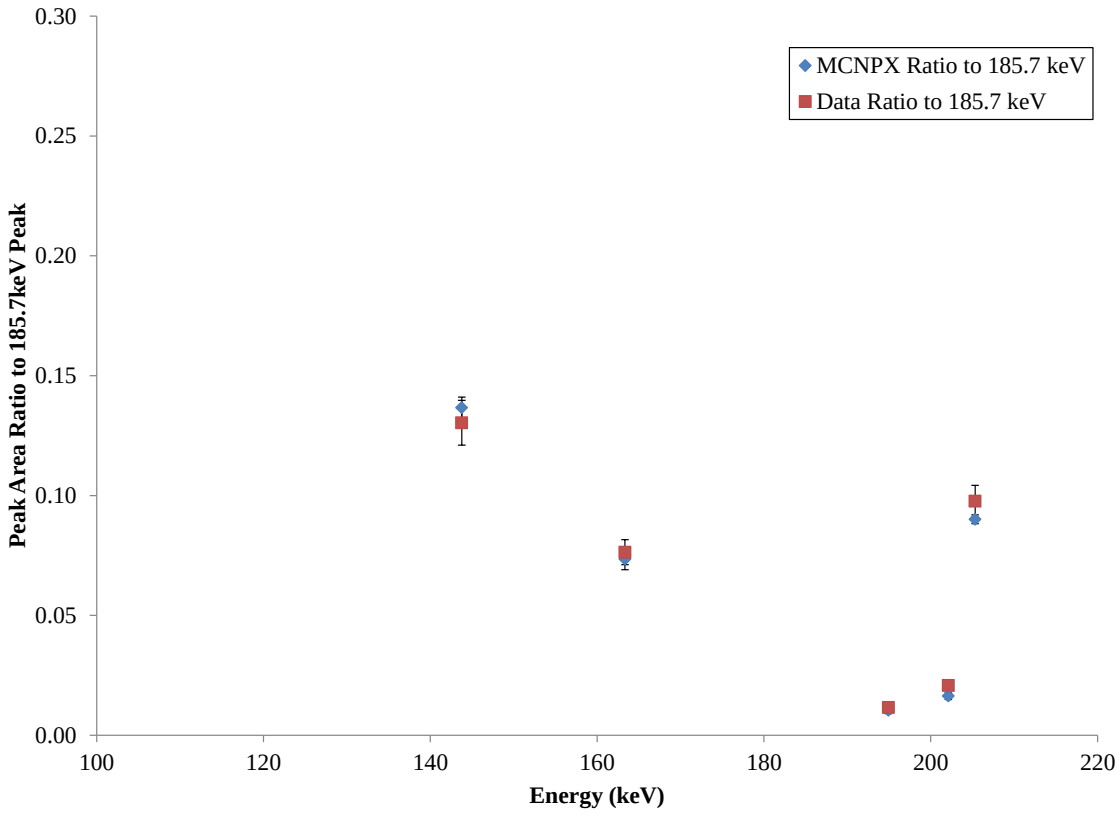

Figure 11-7. Peak Area Ratios of High Intensity ^{235}U Emission Photons to 185.7 keV for Dilution Measurement Data and MCNPX Simulation at 90 g U/L.

In reality, the 143.8 keV signature would best be employed as a signature ratio to the 185.7 keV peak, as its emission intensity is second only to that of the 185.7 keV emission. Diluting from 90 g to 10 g U/L (with a density decrease of ~10.2%), there is a relative 12% increase in the peak ratio values of the peak area of 143.8 keV to 185.7 keV.

11.2 Transmission Simulations of Dilution Experiments

In addition to the passive NDA simulations, detector validation for ^{137}Cs transmission measurements was simulated for 90 g, 85 g, 75 g, 50 g, and 10 g U/L of UN (outlined in Chapter 9). A spectral overlay of the measured and simulated ^{137}Cs transmission is given in Figure 11-8 for 90 g U/L. The spectral overlay plots for the remaining concentrations are given in Appendix F, Figures F-1 through F-4.

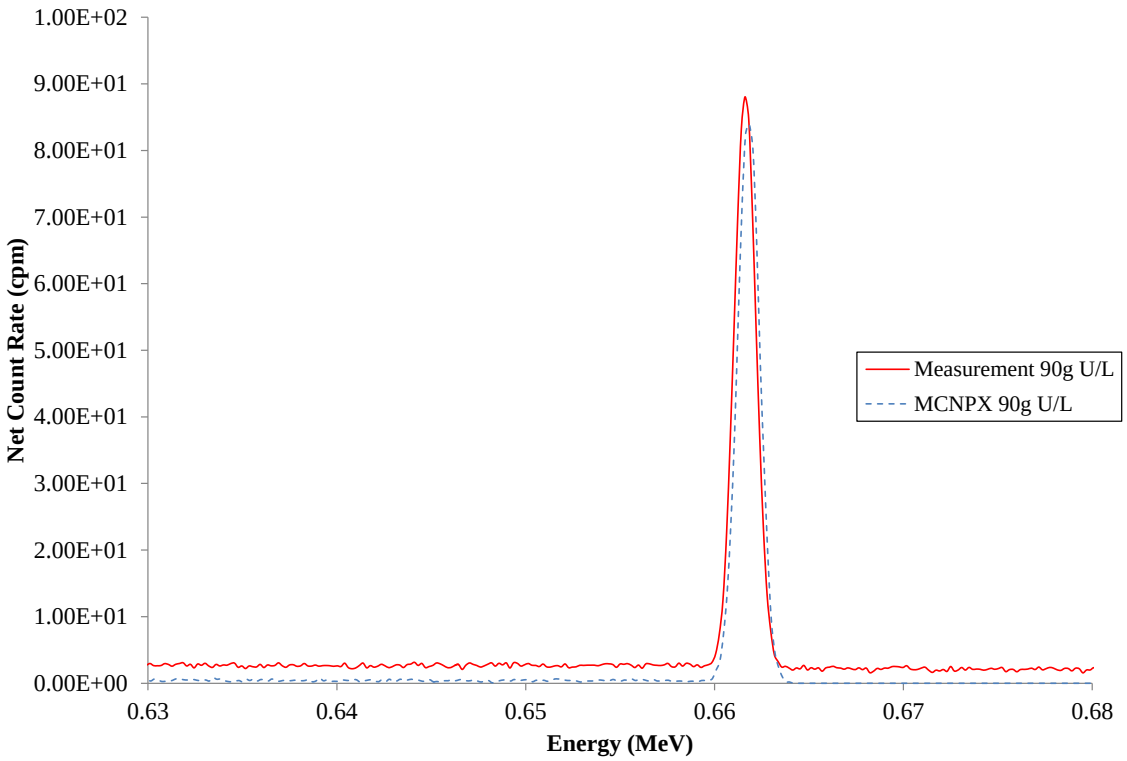

Figure 11-8. 90 g U/L Comparison of ^{137}Cs Transmission Measurement Data with MCNPX Simulation.

Use of the external ^{137}Cs densitometry source ratio methods was not as consistent due to variation in efficiency variables, which will be assessed in the sensitivity analysis in Chapter 12. However, gross peak areas showed strong linear correlation but were not highly sensitive to dilution concentrations to UN. This is consistent with the rationale explained in the attenuation calculations in Chapter 7; as shown in Figure 7-3, the convergence of the MACs for UN at higher energies provides less sensitivity to uranium content. The peak area of 661.7 keV emissions from ^{137}Cs as a function of dilution concentration for both MCNPX and measurements is given in Figure 11-9, and fits with a strong linear correlation coefficient for the validated MCNPX values. Diluting from 90 g U/L to 10 g U/L, there is a relative peak area increase 10.3% of transmitted ^{137}Cs 661.7 keV photons. As shown in Figure 11-9, statistically propagated uncertainty falls within < 1% error.

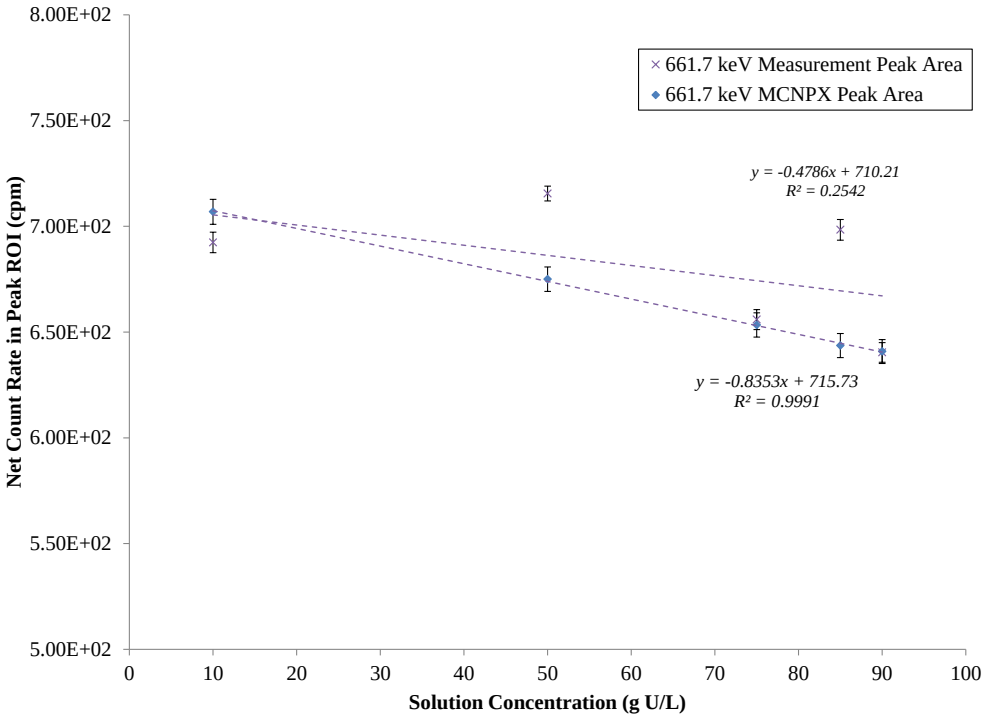

Figure 11-9. Net Peak Area for ^{137}Cs Transmission MCNPX Simulations at 661.7 keV as a Function of Dilution Concentration.

11.3 Transmission Simulations of ^{133}Ba and ^{57}Co

The attenuation analysis in Chapter 7 also proposed that lower energy photon sources from ^{133}Ba and ^{57}Co would be more sensitive to uranium content, as shown in Figure 7-3. Since experimental measurements were not possible to test these sources' sensitivity to uranium content, use of the validated simulations provides insights into transmission sensitivity for PM signature determination.

For each of the five measured dilution concentrations outlined in Table 8-5, a comparison of the MCNPX simulated spectra for transmission measurements of 90 g, 85 g, 75 g, 50 g, and 10 g U/L of UN are presented in Figures 11-10 and 11-11 for ^{133}Ba and ^{57}Co, respectively.

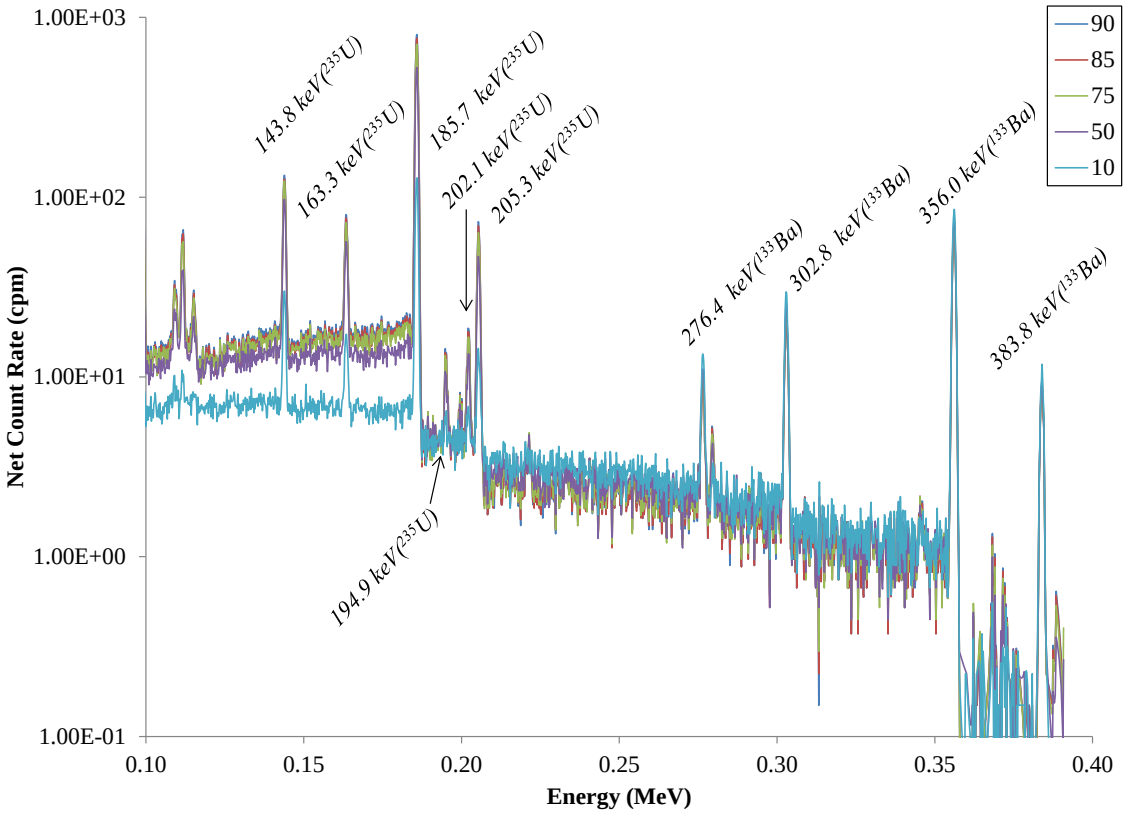

Figure 11-10. ^{133}Ba Transmission MCNPX Simulation Data Spectra at Dilution Concentrations.

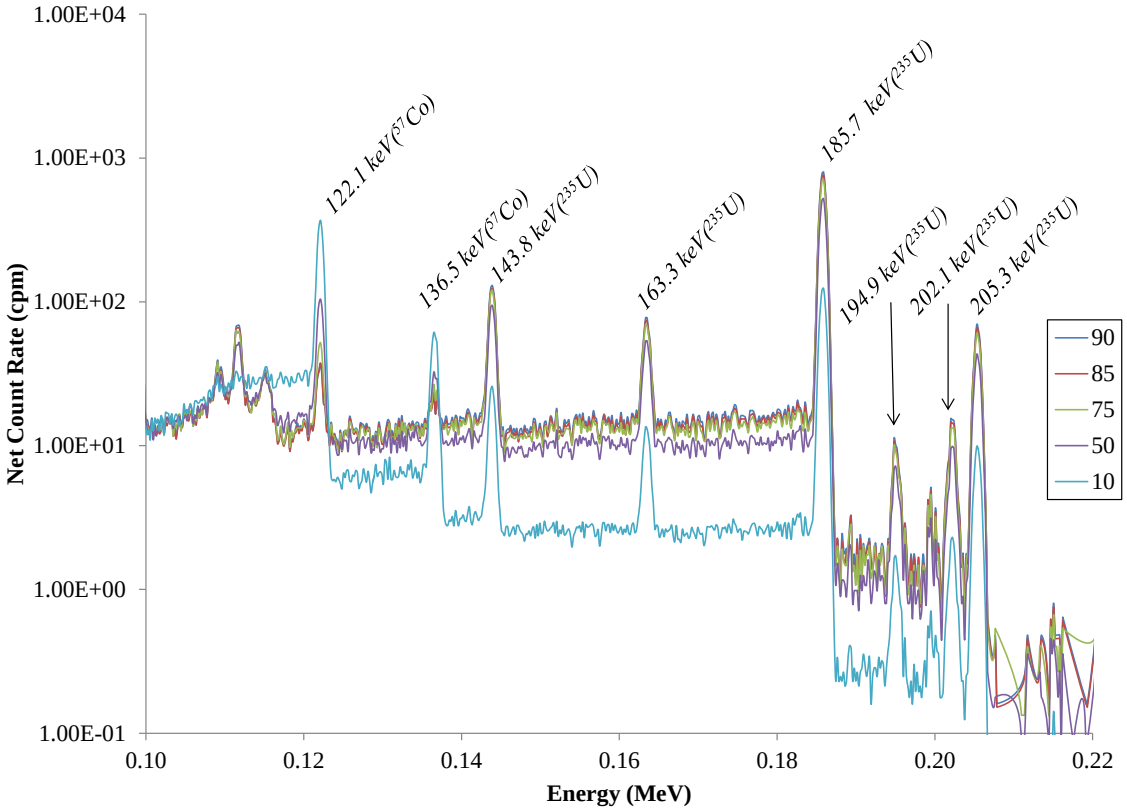

Figure 11-11. ^{57}Co Transmission MCNPX Simulation Data Spectra at Dilution Concentrations.

The 356 keV transmission peak for ^{133}Ba was assessed with the Falcon BEGe detector response for various concentrations of UN. Since the half-life of ^{133}Ba source is approximately 10.5 years, it is favorable from an operational monitoring perspective, as source replacement would need to be less frequent than ^{57}Co (half-life ~271 days). In order to have a peak ratio error < 5% at 90 g U/L (where the highest concentration has the lowest transmission peak area counts and hence the highest statistical uncertainty), use of a 0.7μCi ^{133}Ba source in the simulation model source definition met this 95% confidence level criterion. Since ^{57}Co has such a short half-life, a very high activity source would be required to sufficiently penetrate the UN-filled pipe and provide a statistically confident detection signal. Without introducing a highly

radioactive source in order to meet the 5% criteria, use of a 3 μCi ^{57}Co source in the simulations provides 90% confidence within 10% statistical error for the most conservative model with the lowest transmission (90 g U/L). Peak area values of external transmission source for 356 keV and 122.1 keV photons from ^{133}Ba and ^{57}Co are provided in Figures 11-12 and 11-13, respectively.

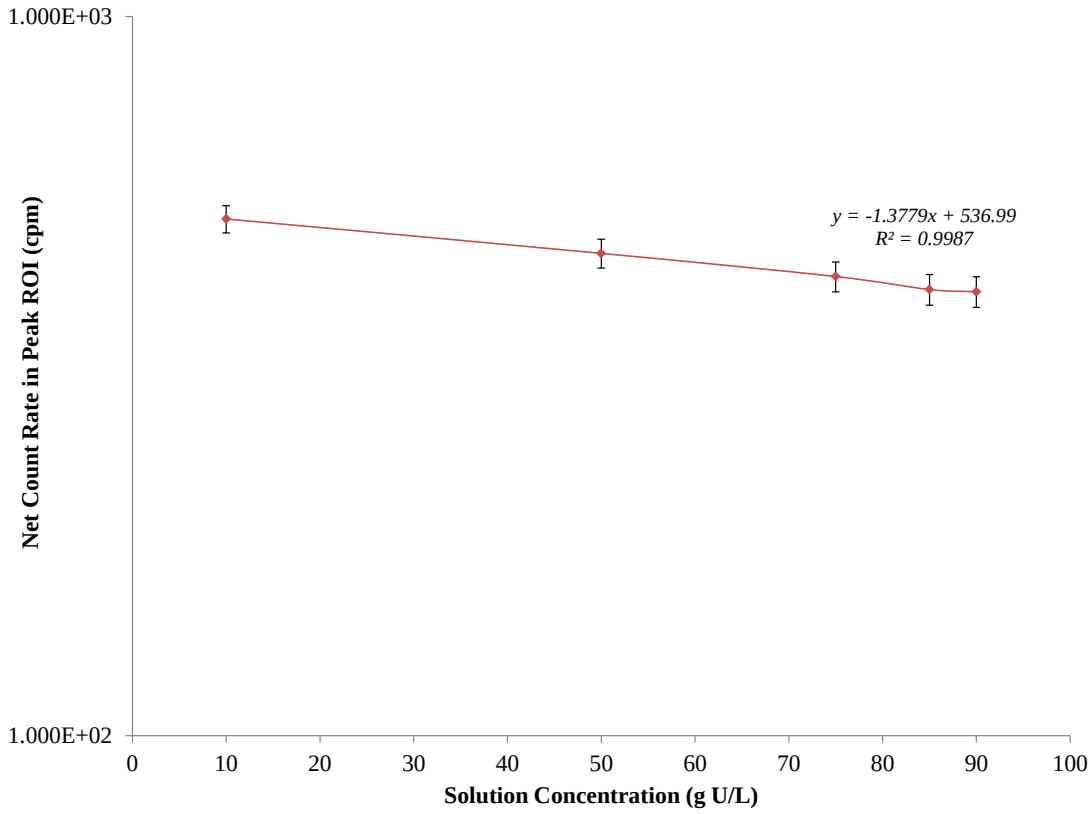

Figure 11-12. Net Peak Area for ^{133}Ba Transmission MCNPX Simulations as a Function of Dilution Concentration.

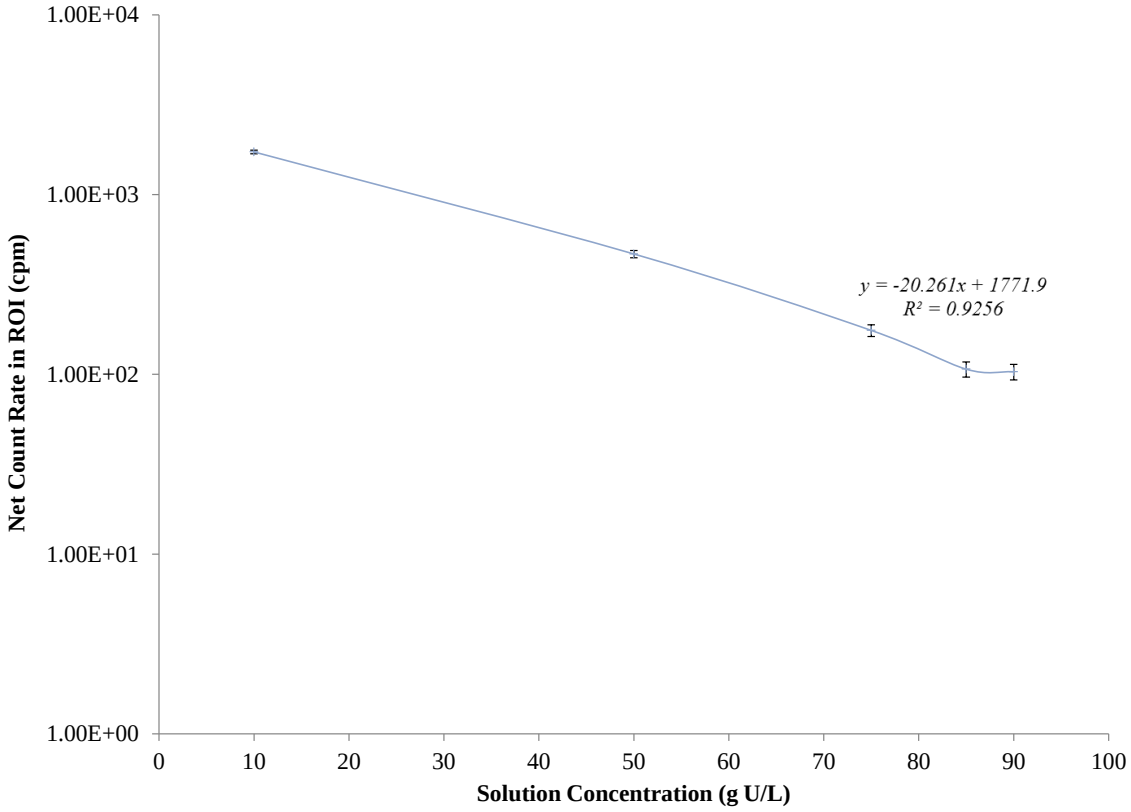

Figure 11-13. Net Peak Area for ^{57}Co Transmission MCNPX Simulations as a Function of Dilution Concentration.

A comparison of all the simulated transmission sources is provided in Figure 11-14.

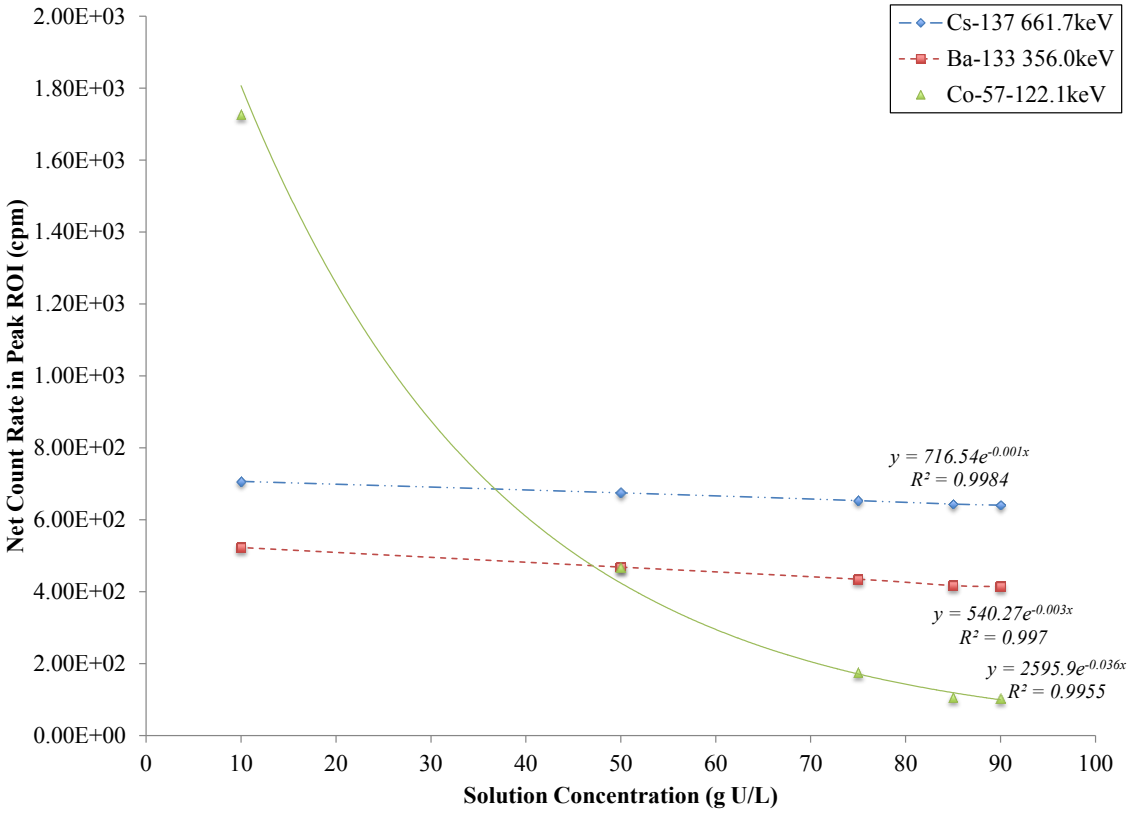

Figure 11-14. MCNPX Simulations Net Peak Area for All Transmission Sources as a Function of Dilution Concentration.

Note: Error bars plotted for some data points are smaller than the resolution of the graph.

11.4 Conclusions

Computational models were created in order to simulate and test the detection response to various concentration and densitometry variables. Passive and ^{137}Cs transmission models were validated with experimental data, and were consistent with experimental measurements. Both ^{133}Ba and ^{57}Co as densitometry transmission sources were simulated to determine the optimal densitometry source for monitoring UN with respect to the highest sensitivity to uranium content.

The slope values of the linear fit for the peak area of the transmission sources as a function of dilution concentration provide an indication of the level of sensitivity of the transmission source to the uranium content in the pipe. As posited in Chapter 7, ^{137}Cs had the lowest slope value (Figure 11-7), with the least sensitivity to uranium content as a function of concentration. This is due to plateauing values of the MAC of UN at higher (500 keV+) energies, as shown in Figure 7-3. For ^{133}Ba (Figure 11-12), the slope of the fit was more pronounced, indicating greater sensitivity to uranium content as a function of concentration. Finally, ^{57}Co (Figure 11-13) had the most pronounced slope with the greatest sensitivity to uranium content. Although most sensitive, the operational implementation of ^{57}Co as a viable monitoring source is deterred by its very short half-life and the need for a high source activity for the low-energy 122 keV photons to penetrate the UN pipe. However, 122 keV also sits below the major uranium emissions and may be too sensitive to continuum subtraction, unless high-resolution instrumentation is employed (HPGe). The ^{133}Ba provides a superior sensitivity compared to ^{137}Cs and a sufficiently longer half-life compared to ^{57}Co. However, if lower resolution measurements are to be considered in a monitoring scheme, degraded resolution would require corrections from the adjacent high-intensity peaks in the 300–400 keV range from ^{133}Ba. Finally, the validated ^{137}Cs provided the least sensitivity to uranium content, but provided sufficient penetration with the singular high-intensity 661.7 keV emission and long half-life.

Although the lower energy transmission peaks provided the greatest sensitivity, from a detection perspective, the ^{133}Ba and ^{137}Cs also contribute higher Compton downscatter, increasing the continuum under the 100–200 keV ^{235}U photon emissions. As we are evaluating natural uranium, higher Compton contributions could eclipse peak measurements in this low energy range, as well as increase the peak area

uncertainty associated with the underlying continuum. This latter concept is now explored in the next chapter (Chapter 12).

CHAPTER 12. STATISTICAL, UNCERTAINTY, AND SENSITIVITY CALCULATIONS

Experimental measurements from both the dilution and operational activities provided a basis for identifying passive gamma-ray signatures from ^{235}U in UN. Detailed statistical, overall uncertainty, and sensitivity analyses are required in order to evaluate the robustness of these monitoring signatures. Systematic and random errors are further considered in the evaluation of monitoring signatures to meet a specific safeguards task.

Peak area uncertainty due to the Compton continuum from ^{238}U in secular equilibrium from aged UN, in addition to the ^{137}Cs emissions during transmission measurements, affect the net 185.7 keV precision peak area and required counting times to meet a specified confidence interval. In a field setting, background from adjacent tanks and pipes containing uranium in a field setting additionally contribute to background under the assay peak areas, which must be characterized, discriminated, and appropriately shielded during implementation of field instrumentation.

A sensitivity analysis provides an indication of how variables, such as pipe thickness, material properties, and source-detector geometry affect the overall detection efficiency of the assayed ^{235}U signatures. Canberra's ISOCS software quantifies the UN mass (hence, activity) in the 304L pipe through a series of ray-tracing calculations (explained in Chapter 5) and provides an absolute efficiency for the modeled source-detector configuration modeled. To model the UN-filled pipe geometry, two of the three tested detectors – the Falcon BEGe and the Osprey 2×2 in. NaI(Tl) – can be handled in ISOCS. In addition, MCNPX simulations were created to determine the

effects of source-detector geometry and absorbers in the overall peak efficiency of assay signatures.

12.1 Statistical Uncertainty and Error Propagation

12.1.1 Dilution Background Measurements

The background uncertainty as part of the overall statistical uncertainty was quantified for the laboratory environment where the dilution measurements were taken. Measurement spectra were taken for 1800 s live time and are provided for each of the three detectors in Figure 12-1. The Inspector 1000 detected the highest environmental ^{40}K at 1460 keV.

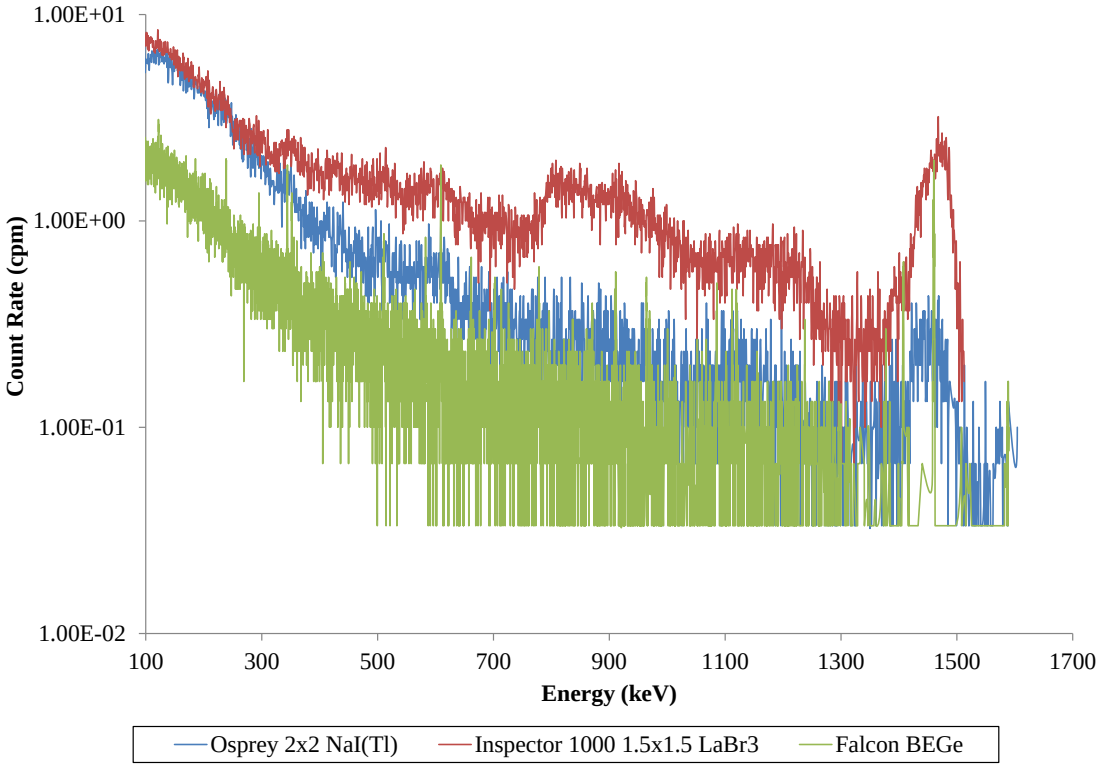

Figure 12-1. Laboratory Background for Dilution Measurements.

ROI gross and background values[6] for the ^{235}U high-intensity emissions were employed for each of the three detectors. The required counting (live) time to meet predetermined uncertainties of 5% and 10% for the Falcon, Inspector, and Osprey detectors are calculated in Tables 12-1, 12-2, and 12-3, respectively.[7]

Table 12-1. Falcon BEGe Optimal Counting Time for Passive and Transmission Dilution Measurements for Predetermined Precision

Dilution Concentration (g U/L)	Peak Energy (keV)	Room Background, *b* (cpm)	Room Background Uncertainty, σ_b (cpm)	Counting Time (s)	
				5%	10%
90	185.7	418.57	3.74	6.65	1.66
	661.7	54.30	1.35	40.30	10.06
85	185.7	435.92	2.70	6.77	1.69
	661.7	34.42	0.76	74.84	18.68
75	185.7	375.15	2.50	7.19	1.80
	661.7	27.88	0.68	78.68	19.65
50	185.7	254.85	2.06	9.60	2.40
	661.7	43.02	0.85	35.23	8.81
10	185.7	29.82	0.70	101.57	25.34
	661.7	6.88	0.34	70.06	17.51

[6] ROI values from Tables 9-1 and 9-3 were employed in this calculation.

[7] For Tables 12-1 through 12-3, 185.7 keV ^{235}U emissions were calculated from passive dilution measurements; 661.7keV ^{137}Cs emissions were calculated from transmission dilution measurements.

Table 12-2. Inspector 1000 $LaBr_3$ Optimal Counting Time for Passive and Transmission Dilution Measurements for Predetermined Precision

Dilution Concentration (g U/L)	Peak Energy (keV)	Room Background, *b* (cpm)	Room Background Uncertainty, σ_b (cpm)	Counting Time (s)	
				5%	10%
90	185.7	2166.10	8.50	42.03	10.40
	661.7	1028.43	5.86	86.77	21.24
85	185.7	2492.82	6.45	52.78	13.10
	661.7	540.85	3.00	198.66	48.42
75	185.7	1674.57	5.28	56.55	14.04
	661.7	468.30	2.79	169.17	41.45
50	185.7	1182.95	4.44	75.22	18.63
	661.7	444.70	2.72	152.96	37.58
10	185.7	500.58	2.89	470.39	109.87
	661.7	218.12	1.91	101.52	25.18

Table 12-3. Osprey NaI(Tl) Optimal Counting Time for Passive and Transmission Dilution Measurements for Predetermined Precision

Dilution Concentration (g U/L)	Peak Energy (keV)	Room Background, *b* (cpm)	Room Background Uncertainty, σ_b (cpm)	Counting Time (s)	
				5%	10%
90	185.7	11365.33	19.46	6.36	1.59
	661.7	3580.13	10.92	32.38	8.03
85	185.7	8393.20	11.83	8.49	2.12
	661.7	1466.70	4.94	69.13	17.13
75	185.7	9143.40	12.34	7.27	1.82
	661.7	1603.83	5.17	62.53	15.51
50	185.7	8048.58	11.58	10.80	2.70
	661.7	1019.20	4.12	52.79	13.12
10	185.7	1471.35	4.95	88.08	21.76
	661.7	575.28	3.10	34.49	8.60

For the measurements conducted, count rates from signature 185.7 keV ^{235}U emissions and 661.7 keV ^{137}Cs emissions were sufficiently intense to satisfy counting times in Tables 12-1, 12-2, and 12-3 to meet the counting statistics of 5–10% uncertainty range.

12.1.2 UNCLE Background Measurements

The background in UNCLE was characterized by first measuring background in the absence of the backshield, and second, by measuring background with a Shadowshield (as shown in Figure 12-2).[8] By shielding the source emissions from the UN-filled pipe, the shadowshield provides measurements for background signals or "leakage" reaching the detector penetrating the shielding arrangement (Figure 12-3). There is no evidence of a peaked background. Thus, the net 185.7 keV intensity simply requires a continuum subtraction. This is determined for each assay from the collected spectrum. In relation to Equation 5-17, this means that $t_g = t_b$.

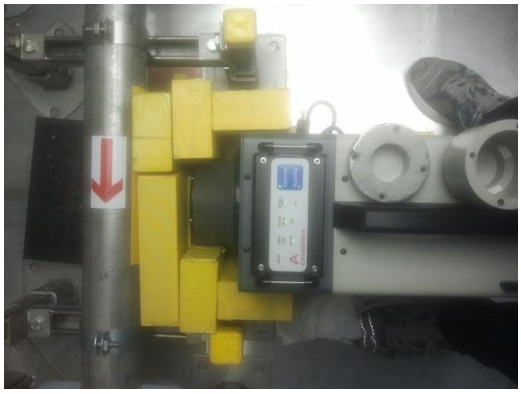

Figure 12-2. Falcon Detector Setup in UNCLE (Setup 5: Shadowshield/Frontshield) Measuring Leakage into Collimator.

[8] Environmental measurements were taken unshielded at a standoff distance at the entrance of UNCLE. This measurement spectrum is provided for all three detectors in Appendix I: Figure I-1.

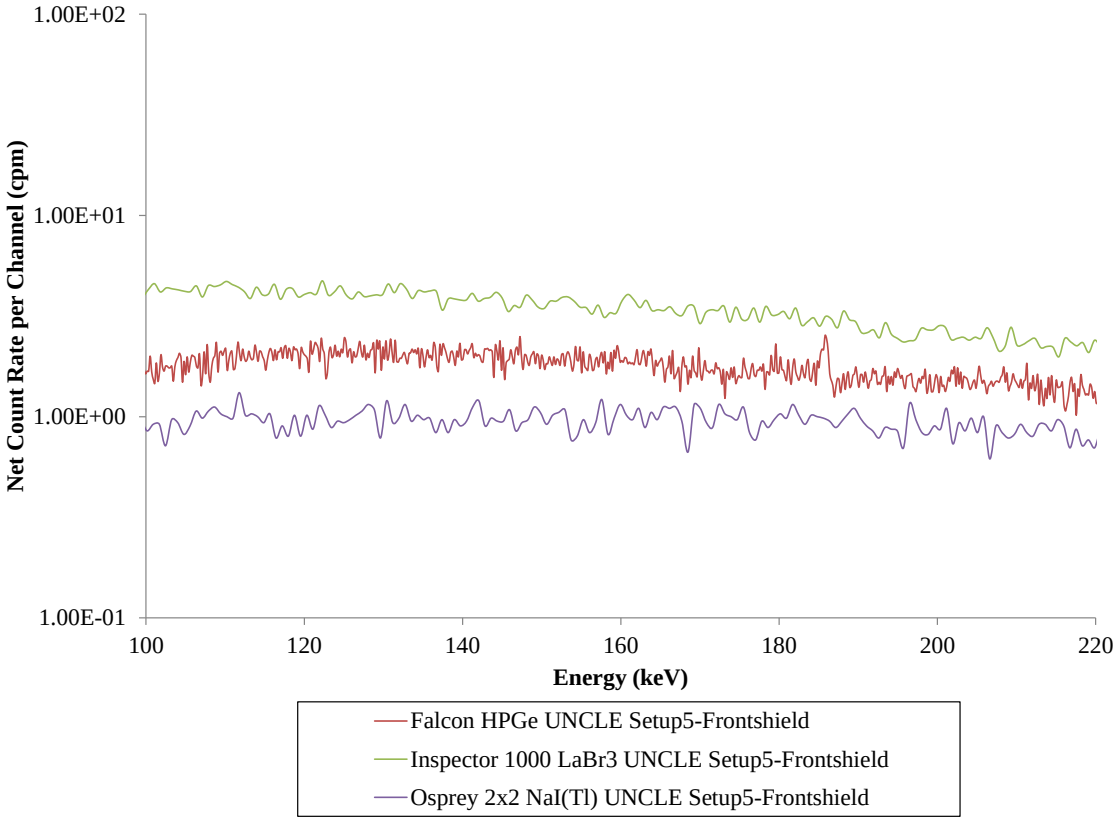

Figure 12-3. Detector Comparison UNCLE - Setup 5: Shadowshield (Frontshield) Leakage into Collimator at 1070 RPM.

Measurements taken in UNCLE in the absence of a backshield are given in Figure 12-4 for each of the Falcon, Inspector, and Osprey. Subtracting these measurements taken in Setup 1 (1070 RPM) with the backshield in UNCLE (given in Chapter 10) provides the background contribution from surrounding pipes and tanks reaching the detector. The background contribution from adjacent tanks and pipes is given in Figure 12-5.

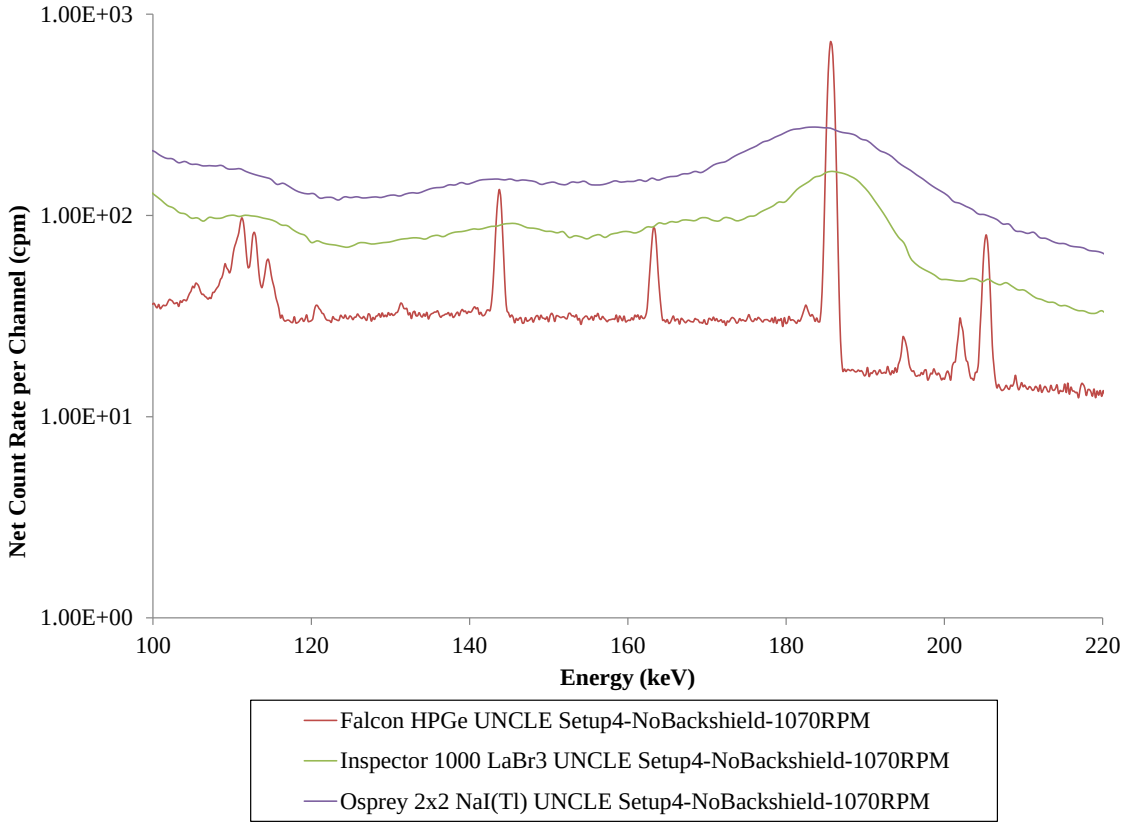

Figure 12-4. Detector Comparison UNCLE - Setup 4: No Backshield 1070 RPM.

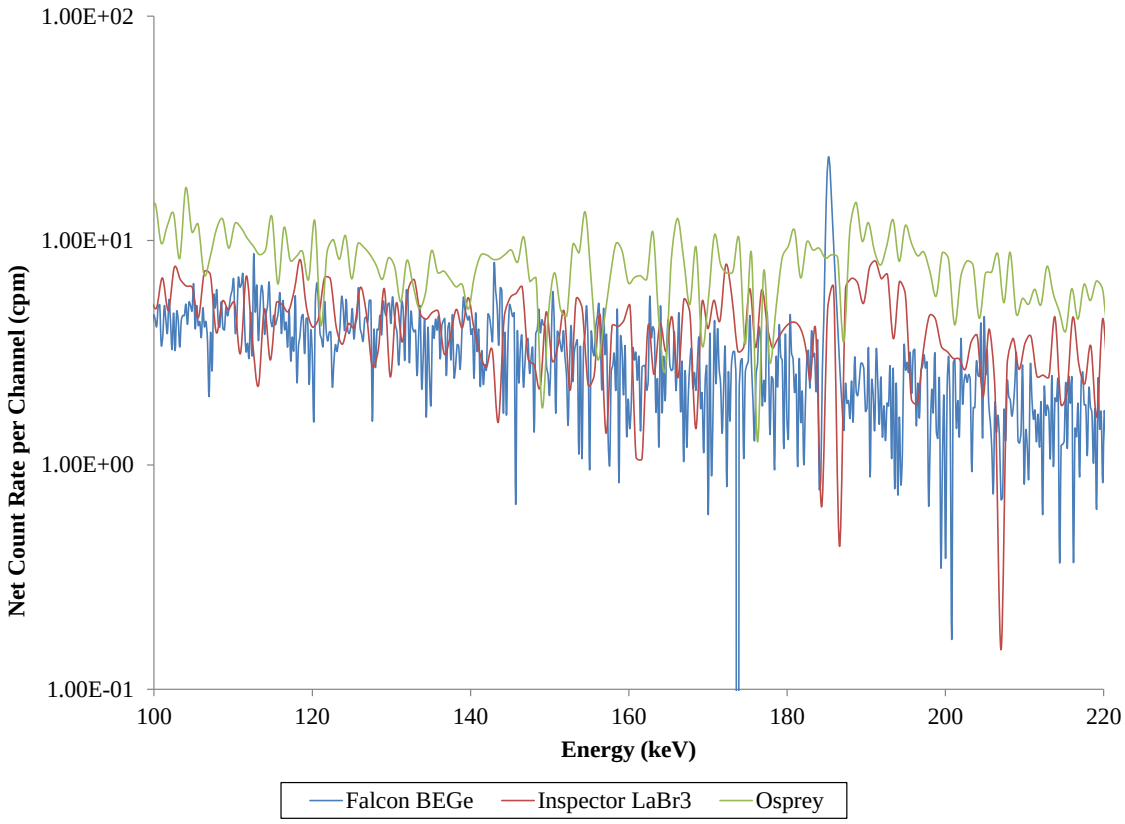

Figure 12-5. Full Energy Spectra of Counts Shielded by Backshield in UNCLE.

Background signals from adjacent tanks/piping provide a ^{235}U interference source that could alter the pipe signals assaying uranium content. However, since the emission range we are focusing on for ^{235}U falls in the 100–200 keV range, the use of a Pb backshield, in conjunction with optimized shielding encasing the detector, sufficiently shields against these external emissions.

ROI gross and background values[9] for the ^{235}U high-intensity emissions were employed for each of the three detectors. The required counting (live) time to meet predetermined uncertainties of 5% and 10% for the Falcon, Inspector, and Osprey detectors are calculated and summarized in Table 12-4.[10]

Table 12-4. Optimal Counting Time for UNCLE 1070 RPM Flowrate Measurements for Predetermined Precision

Detector	Peak Energy (keV)	Room Background, *b* (cpm)	Room Background Uncertainty, σ_b (cpm)	Counting Time (s)	
				5%	10%
Falcon BEGe	185.7	422.23	2.65	7.49	1.87
	661.7	59.55	1.00	54.17	13.53
Inspector 1000	185.7	2372.65	6.29	41.39	10.29
	661.7	739.15	5.53	218.59	53.02
Osprey	185.7	7129.00	10.90	8.41	2.10
	661.7	1594.95	5.16	76.79	19.00

12.1.3 Compton Continuum Effects

In addition to environmental background contributing to ROI count rates, contributions from the Compton continuum shelf affect the associated uncertainty of the background (i.e., environmental background plus Compton continuum). Compton continuum, whether from a ^{137}Cs transmission source or from higher energy ^{238}U, in the case of natural UN in secular equilibrium, contributes to the continuum under the peak ROI. In principle, two 185.7 keV measurements may have the same net peak

[9] ROI values from Tables 9-1 and 9-3 were employed in this calculation.

[10] For Table 12-4, the 185.7 keV ^{235}U emissions were calculated from passive dilution measurements; 661.7 keV ^{137}Cs emissions were calculated from transmission dilution measurements.

ROI (indicative of the same uranium content). However, in the presence of Compton downscatter, this increases continuum background, which increases the overall uncertainty associated with the measured peak area.

In Figure 12-6, the integral ROI for the 185.7 keV peak area at 85 g U/L is shown. Figure 12-6 also assesses the same 185.7 keV ROI, but for measurements with the 661.7 keV ^{137}Cs transmission source present. The change in background in each situation was negligible between the two measurements, given the low-background environment, and the solution remained unchanged at 85 g U/L. Comparing both figures, the high-resolution measurements from the Falcon BEGe show comparatively no change in Compton effects between the passive and transmission measurements. However, for the lower-resolution scintillator detectors, continuum effects are very pronounced with the introduction of a higher energy 661.7 keV source, increasing the continuum under the net peak area. With the highest detection efficiency and low resolution, the Osprey yielded the greatest sensitivity in continuum contributions in the presence of high-emission Compton effects. These effects are echoed in the UNCLE flowrate measurements at 90 g U/L at 1070 RPM in Figure 12-7.

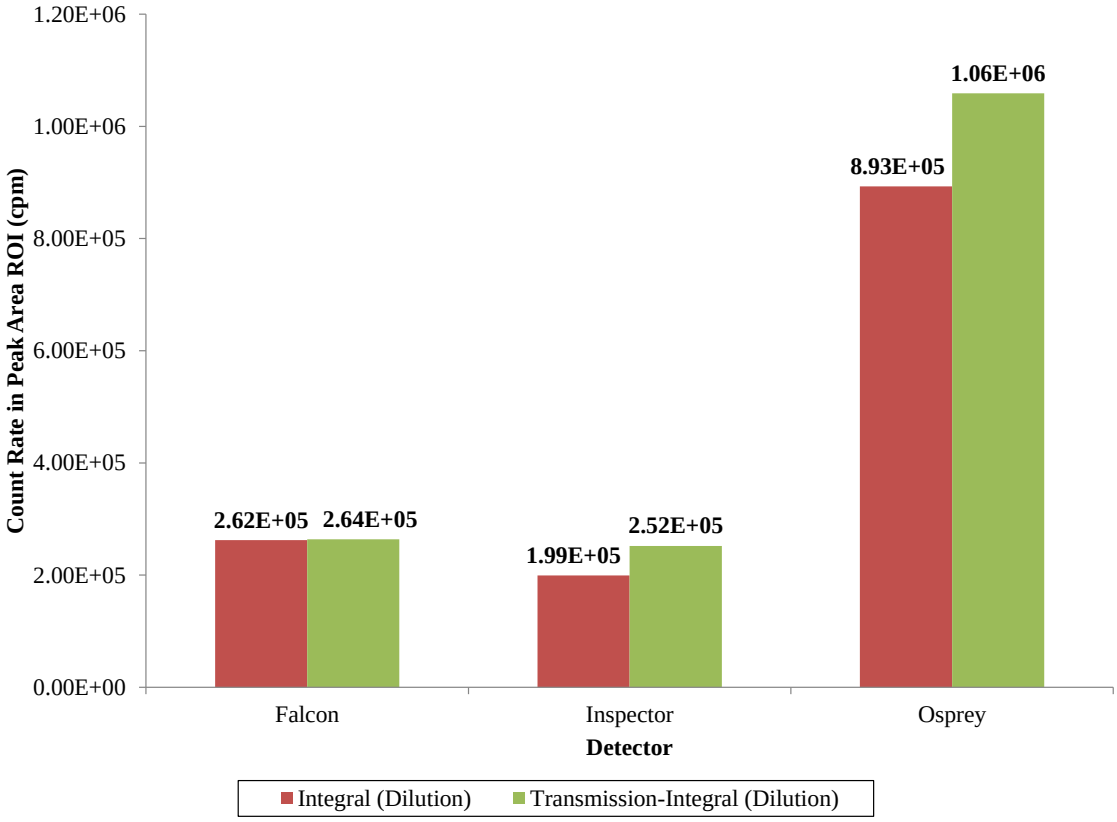

Figure 12-6. 185.7 keV ^{235}U Integral Counts in the Absence and Presence of ^{137}Cs at 85 g U/L Dilution.

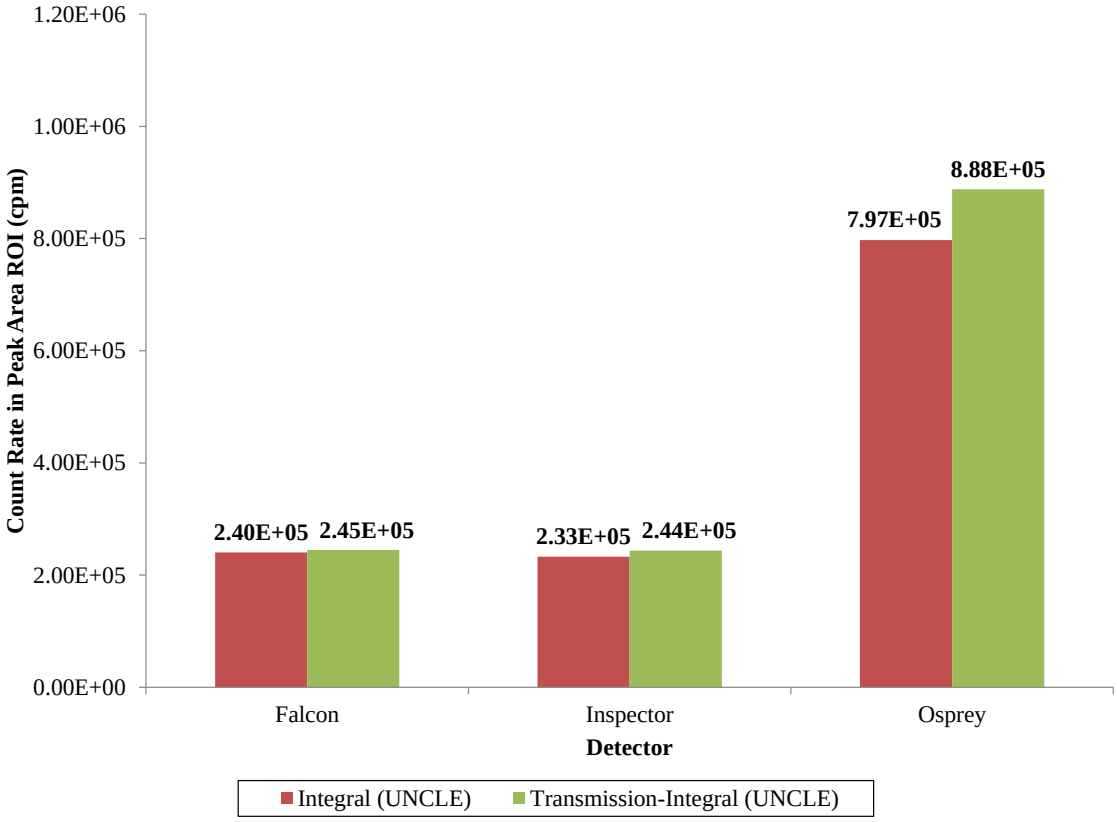

Figure 12-7. 185.7 keV ^{235}U Integral Counts in the Absence and Presence of ^{137}Cs at UNCLE.

If process monitoring ^{235}U in UN included regular Compton downscatter from either high-energy transmission sources or from higher energy ^{238}U in secular equilibrium, then a Compton suppression system could be explored to quantify such effects [80]. However, since ^{235}U in UN is expected to be freshly processed, such measures are not a foreseeable requirement for an NUCP.

12.2 Detection Efficiency

Gamma rays must undergo interaction with the detector crystal before being registered. The efficiency of a detection system is typically defined as the observed peak area count rate divided by the source gamma emission activity. Quantification of

the peak efficiency values of the ^{235}U 185.7 keV and ^{137}Cs 661.7 keV emissions according to Equation 12-2 for the dilution and transmission measurements for the Falcon, Osprey, and Inspector is given in Figures 12-8 and 12-9, respectively.

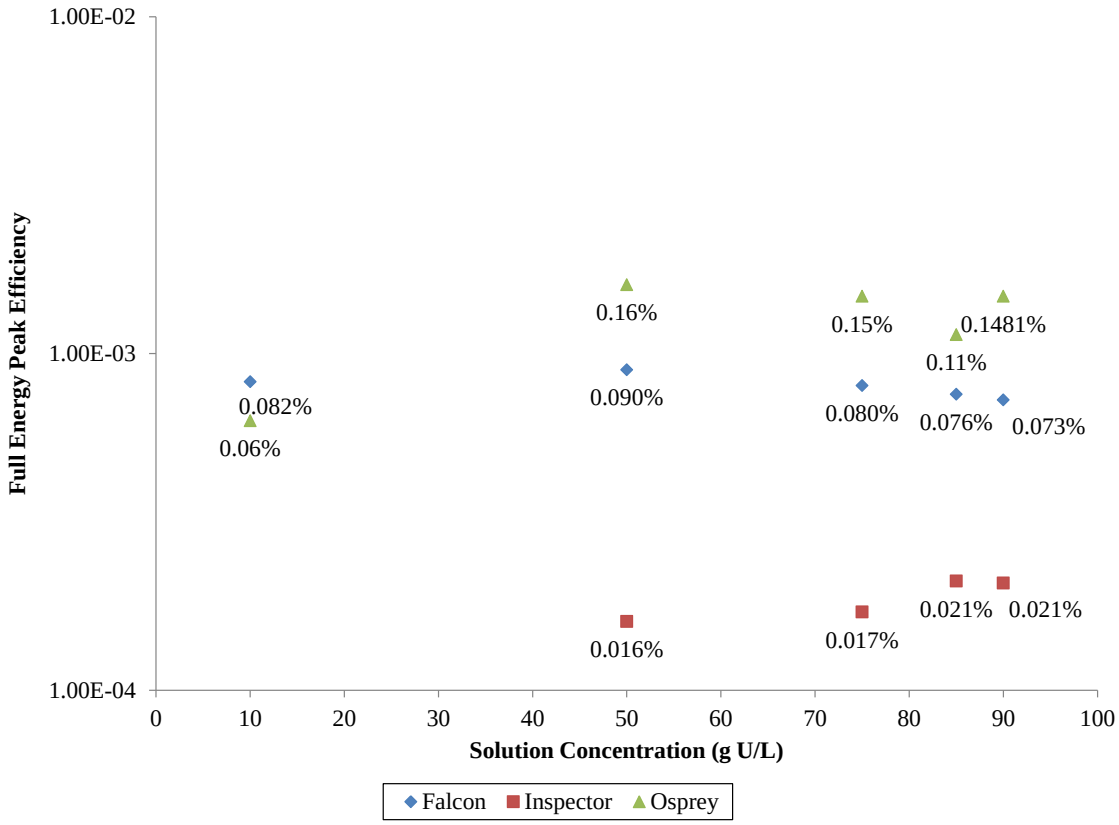

Figure 12-8. Peak Efficiency of 185.7 keV Emissions from ^{235}U from Dilution Measurements.

Note: Error bars plotted for some data points are smaller than the resolution of the graph.

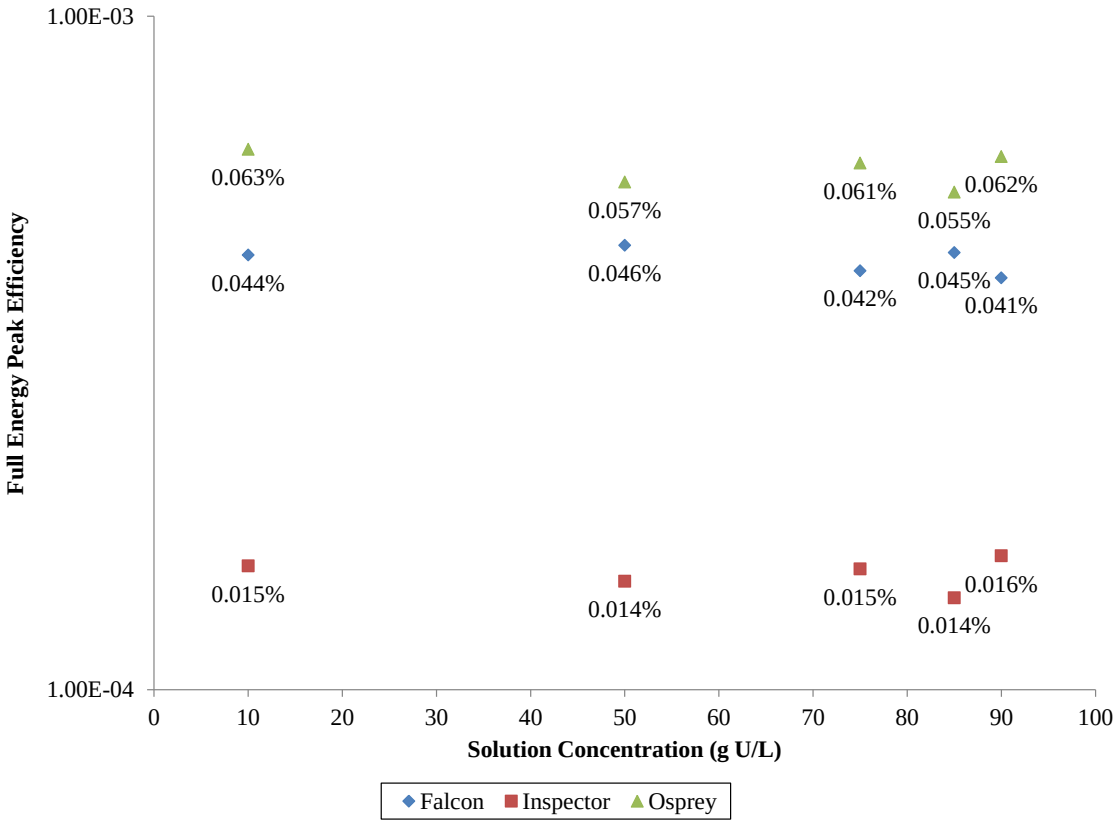

Figure 12-9. Peak Efficiency of 661.7 keV Emissions from ^{137}Cs from Transmission Measurements.

Note: Error bars plotted for some data points are smaller than the resolution of the graph.

As seen in Figures 12-8 and 12-9, deviation from expected values is due variations in any of the variables that contribute to the total detection efficiency. As described in Chapter 5, the total efficiency is the product of four factors [63] [64]:

$$\varepsilon_{full} = \varepsilon_{geom} \cdot \varepsilon_{absp} \cdot \varepsilon_{sample} \cdot \varepsilon_{int} \cdot \qquad [12\text{-}1]$$

Subsequently, evaluation of the sensitivity of each of these parameters to the overall detector response will quantify the effects on the assay signatures.

12.3 MCNPX Analysis

Differentiating each of the four factors contributions to the total efficiency in Equation 12-1 is difficult to determine experimentally. However, the simulation models developed in Chapter 8 can be harnessed to determine the particle flux at each boundary in the experimental setup. Using the energy calibration parameters and detector geometry for the Falcon BEGe outlined in Chapter 8, an F1 flux tally was conducted over interacting surfaces (Figure 12-10). In Figure 12-10, the dots represent the source particles and collisions in the MCNPX model. The MCNPX input is provided in Appendix J.

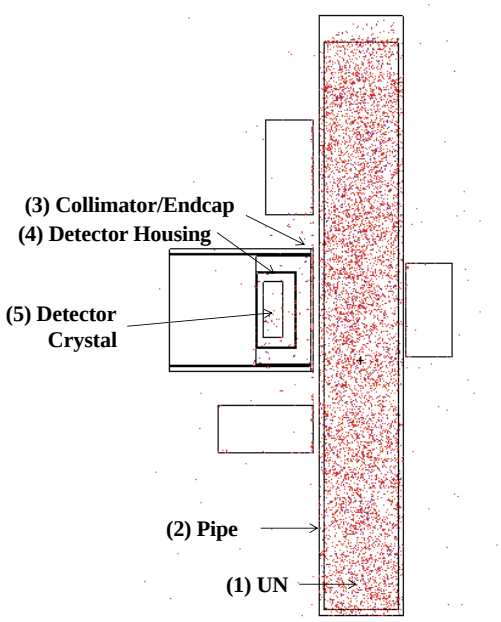

Figure 12-10. VisEd Model of MCNPX Simulation Source Particle Interactions.

To determine the peak efficiency for the 185.7 keV emissions from the UN, the F1 tally is was multiplied by the UN activity and sum of emission probabilities (SP card), and taken as a ratio of the ^{235}U activity emitted by the source UN, with a ^{235}U

branching ratio of 57% for 185.7 keV photons (Equation 12-2). This value provides the fraction of source 185.7 keV photons that escape the UN.

$$Peak\ efficiency = \frac{F1\ Tally\ Output \cdot Source\ Activity\ (Bq) \cdot Source\ Intensity\ (\frac{photons}{decay})}{Source\ Activity\ (Bq) \cdot Branching\ Ratio}. \quad [12\text{-}2]$$

- **(1) UN Boundary:** The first F1 tally was conducted over the boundary of the source UN at 90 g U/L. The peak efficiency of Equation 12-2 provides the ε_{samp}, the self-attenuation effects due to the sample UN. The inverse of this value provides the *CF(AT)* described in Chapter 7.

The following three surface tallies contribute to the evaluation of ε_{absp} and ε_{geom} parameters in Equation 12-1.

- **(2) Pipe Boundary:** The second F1 tally was conducted over the boundary of the 304L stainless steel pipe.

- **(3) Collimator/Endcap:** The third F1 tally was conducted over the boundary of the W endcap of the Falcon BEGe detector.

- **(4) Detector Housing:** The fourth F1 tally was conducted over the Al housing of the detector.

The final tally provides the intrinsic peak efficiency (ε_{int}) values by determine what fraction of the photons reaching the detector crystal actually interact with the crystal to produce a full-energy photopeak.

- **(5) Crystal Surface:** The final F1 tally was conducted over the surface of the HPGe detector crystal. The ratio of the F8 (energy deposition) from Chapter 8 for the 185.7 keV peak to this F1 tally value provides the intrinsic peak efficiency value, ε_{int}.

The peak efficiency at each of these tally points in the MNCPX model is summarized in Figure 12-11.

Figure 12-11. 185.7 keV Peak Efficiency Values from MCNPX F1 Tallies.

Note: Error bars plotted for some data points are smaller than the resolution of the graph.

From the MCNPX F1 tally over the (1) UN boundary, the sample efficiency for the 185.7 keV peak, ε_{samp}, is (40.2±0.2)%. The ε_{int} calculated for the ratio of emissions

reaching detector of the crystal surface [F1 tally at (5) Crystal Surface] with the emissions that interact with the crystal volume creating full energy depositions (F8 peak area) is 46±6%. The culmination of the tallies from (2) Pipe Boundary, (3) Collimator/Endcap and (4) Detector housing contribute to the ($\varepsilon_{absp}\cdot\ \varepsilon_{geom}$) parameters. These efficiency values collectively contribute (0.415±0.001)% to the 185.7 keV peak efficiency. From the source emissions of 185.7 keV photon activity of 9.08×10^{4} Bq with the detected photopeak area of 68.9 cps, the overall peak efficiency based on this validated MNCPX simulation is (0.076±0.009)%.

In addition, tallies were made to determine the effects of the Pb brick arrangement, as well as the W collimator. Consequently, the emissions were tallied in the presence of both Pb shielding and collimator, without Pb with collimation, and without either Pb or collimation. A comparison of the Pb shielding arrangement and collimator is given in Figure 12-12.

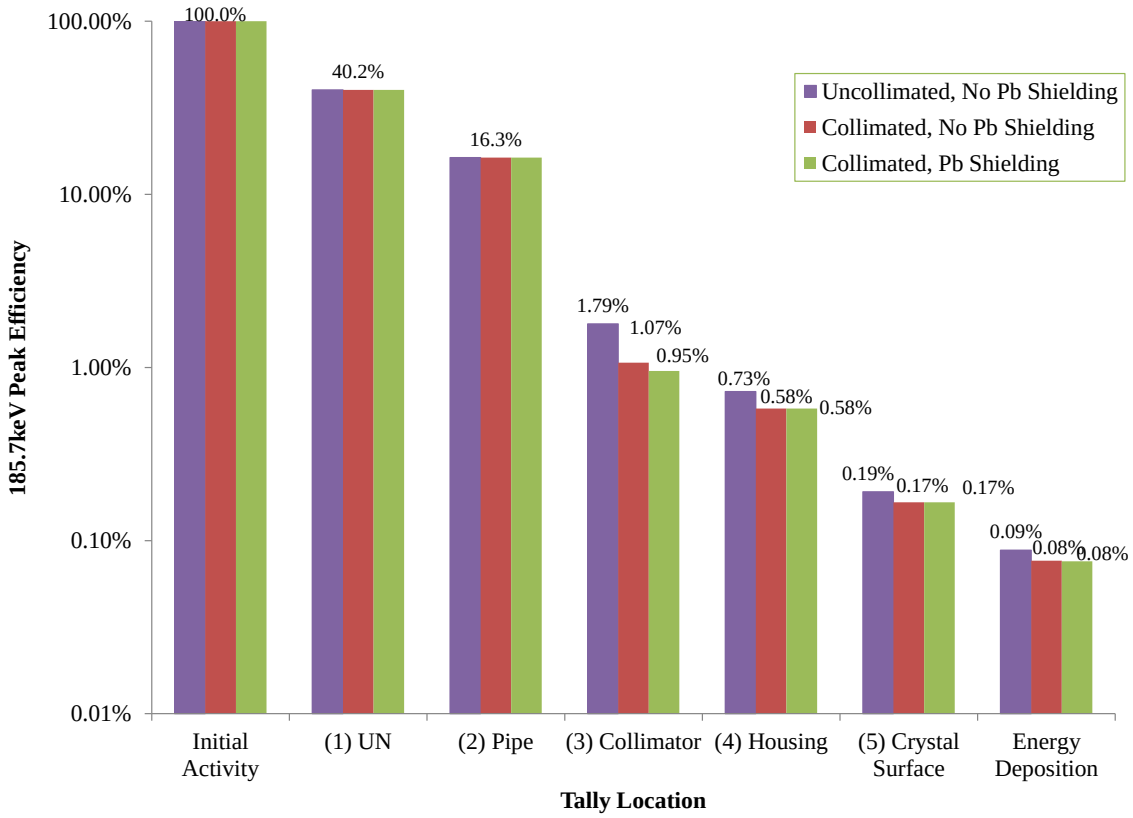

Figure 12-12. 185.7 keV Peak Efficiency Values

In the absence of Pb shielding, the peak efficiency increases from 0.95% (of initial 185.7 keV activity) to 1.07%. Further elimination of the W collimator/endcap increases the efficiency by 0.72% to 1.79%. However, thereafter, the absolute peak efficiency only increases from 0.08% to 0.09% efficiency in the absence of collimation and shielding. The MCNPX models quantify the effects of the Pb shielding arrangement employed in the dilution measurements; optimization of source-detector geometry in a field setting, as well as optimizing shielding, will mitigate background contributions from adjacent pipes and tanks in an NUCP facility.

12.4 In Situ Object Counting System (ISOCS) Simulations

A detailed assessment of factors affecting detection efficiency is made by conducting a sensitivity analysis of the detector response to changes in pipe thickness, material properties, and source-detector placement/offset. These are conducted using Canberra's ISOCS software [63]. Unlike classical efficiency calibrations, ISOCS can be employed without representative calibration materials. A response model of the detector is established at the factory by a combination of measurement and MCNP modeling. The geometry is modeled in the ISOCS software and uses ray tracing (described in Chapter 5) to determine the absolute efficiency of the source-detector system. When this efficiency calibration is applied to an acquired spectrum, the mass (and hence, activity) can be determined for the modeled geometry. The use of ISOCS negates having to run multiple MCNPX simulations, hence permitting testing of a multitude of variables affecting the overall peak efficiency of photon signatures emitted from the UN-bearing pipe. ISOCS executes in a short time relative to MCNP, but generates only the full energy peak efficiency, not the energy deposition profile.

12.4.1 ISOCS Peak Efficiency Simulations

Models were created to emulate the geometry employed for both the dilution and UNCLE measurements. The peak efficiency values determined using ISOCS were calculated within 5% convergence error. The results for the Falcon BEGe are provided in Figure 12-13 and are plotted as a function solution density for the 185.7 keV peak efficiency in Figure 12-14. The Osprey NaI(Tl) ISOCS results are plot in Figure 12-15 as a function of energy and in Figure 12-16 as a function of solution density for the 185.7 keV peak efficiency. All data are plot with 5% error bars. One prominent feature of both these simulations in Figures 12-13 and 12-15 is the efficiency drop after

100 keV. This local drop in efficiency is due to the K-edge absorption of uranium at 115.6 keV. At lower uranium concentrations, the K-edge effect is less pronounced.

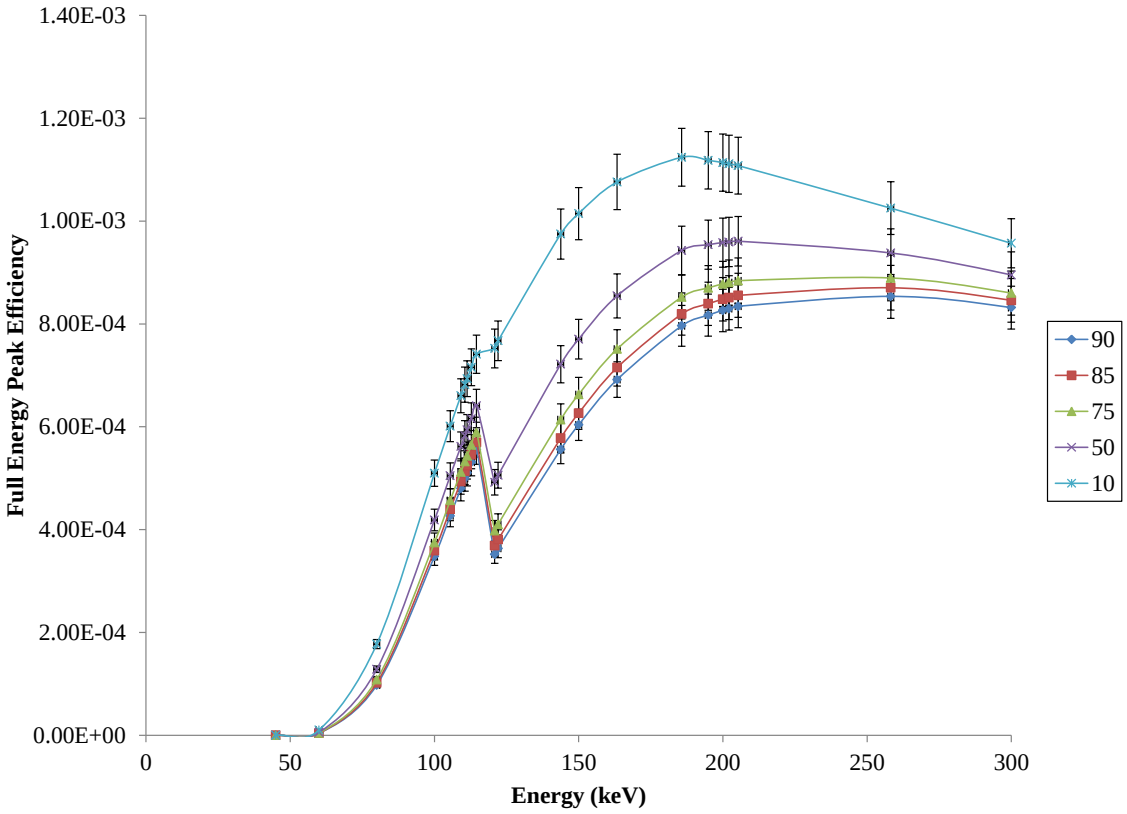

Figure 12-13. ISOCS Calculated Peak Efficiencies for Collimated Falcon at Dilution Concentrations as a Function of Energy.

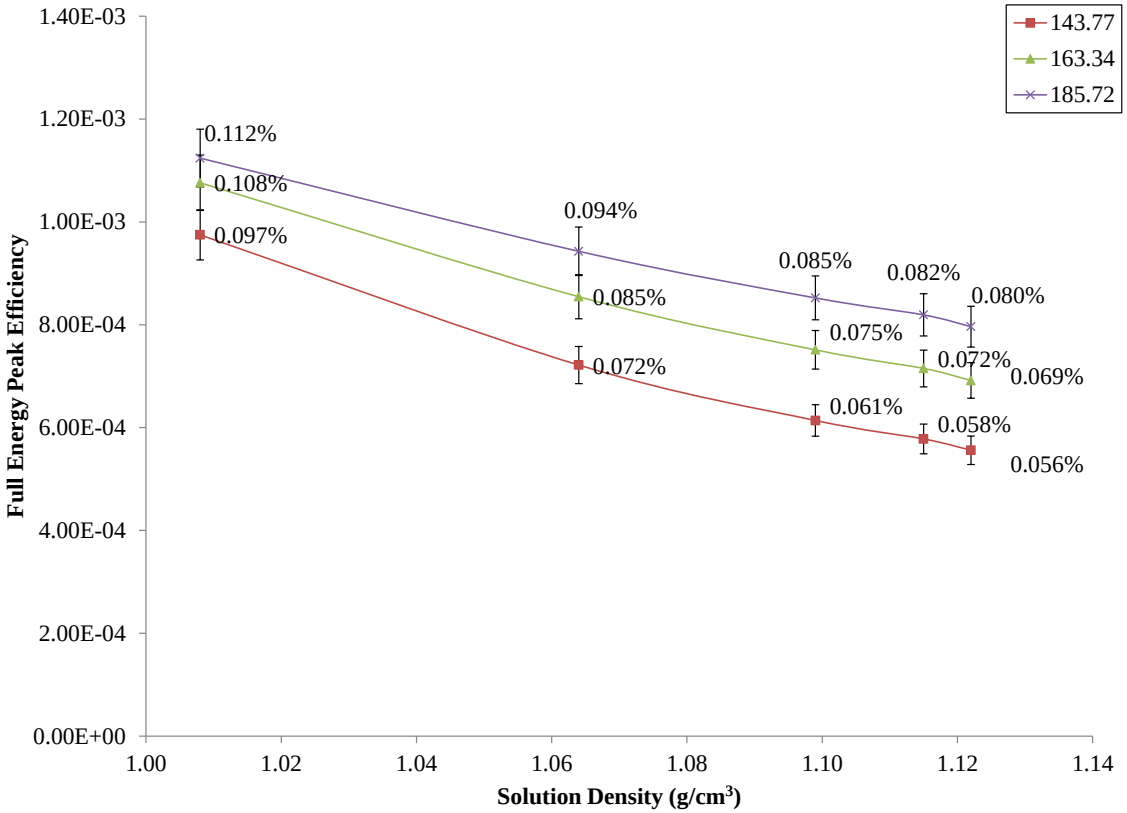

Figure 12-14. ISOCS Efficiency Calculations for Collimated Falcon Measurements as a Function of UN Solution Density.

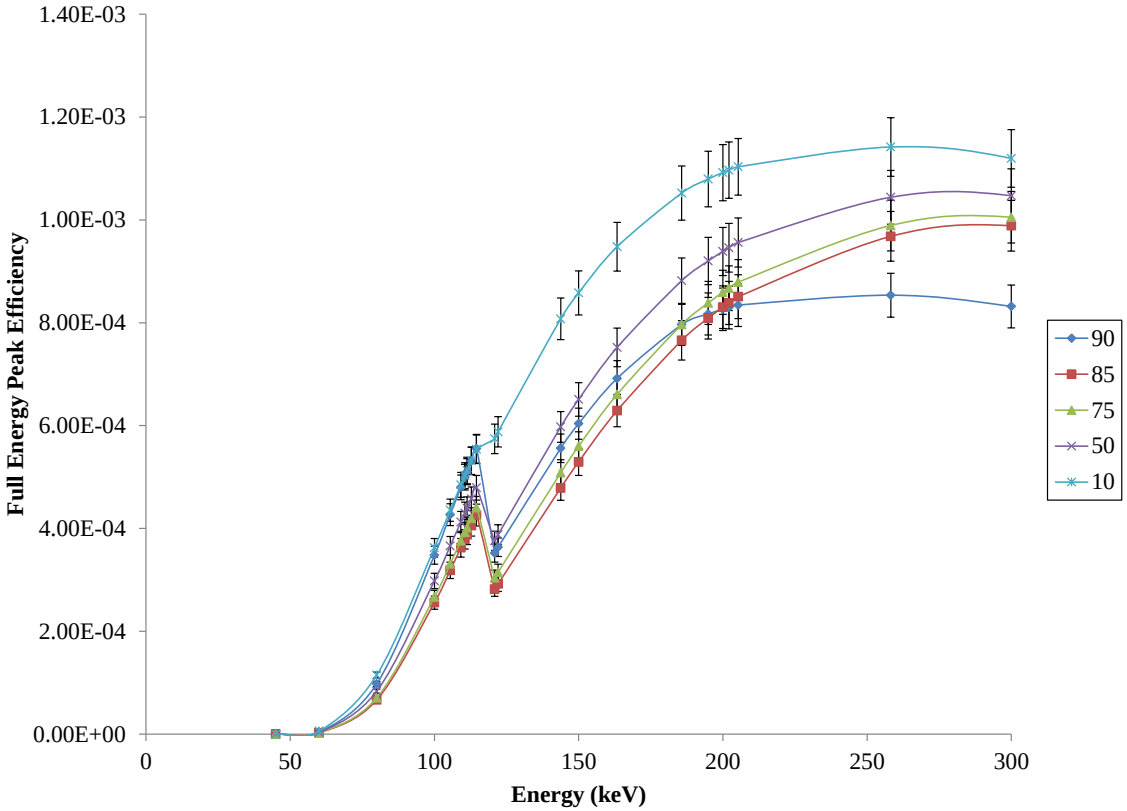

Figure 12-15. ISOCS Calculated Efficiencies for Shielded Osprey Dilution Measurements as a Function of Energy.

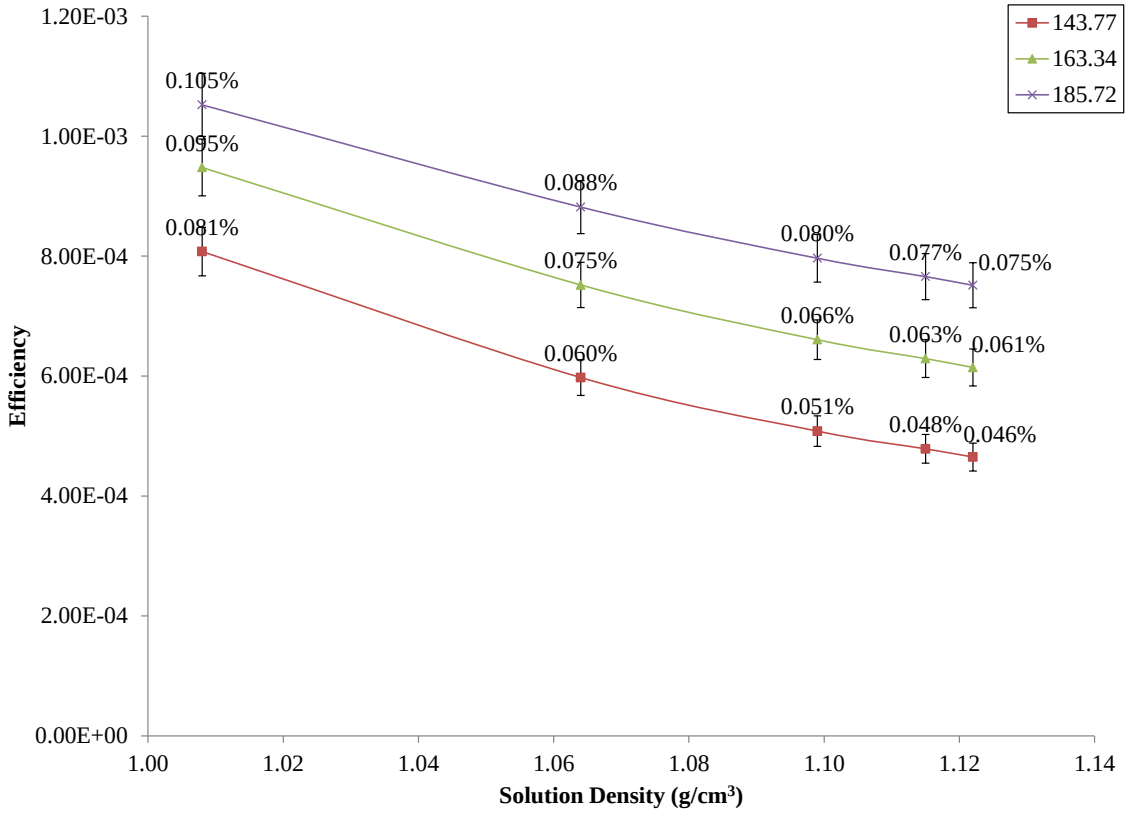

Figure 12-16. ISOCS Efficiency Calculations for Shielded Osprey Dilution Measurements as a Function of UN Solution Density.

A comparison of the Osprey and Falcon efficiencies with shielding/collimation is provided in Figure 12-17.

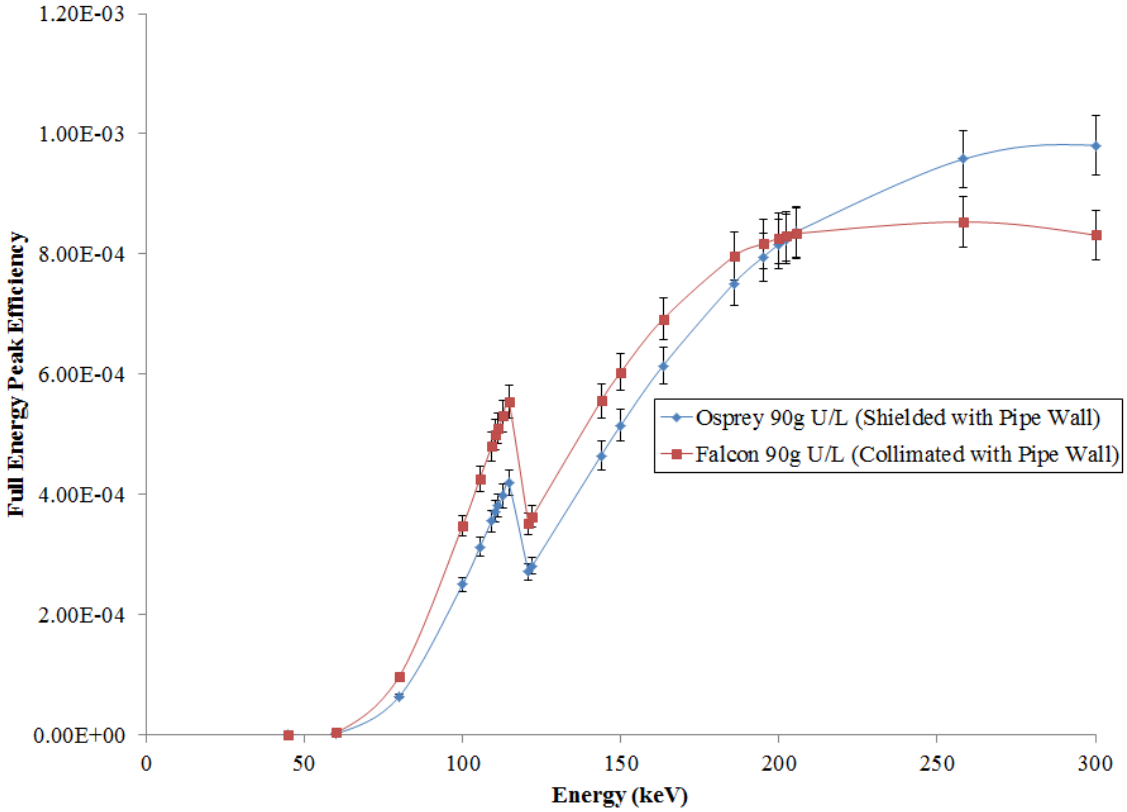

Figure 12-17. Comparison of ISOCS Calculated Efficiencies for Shielded/Collimated Falcon BEGe and Osprey NaI for 90 g U/L in Pipe.

12.4.2 ISOCS Mass and Activity Calculation of UN in Dilution Experiments

Modeling the source-detector setup enables ISOCS to generate the geometry-specific peak efficiencies. These efficiency calibrations were imported into the dilution data taken with Genie [76] for each of the Falcon and Osprey detectors. With ISOCS-

generated peak efficiencies, the mass and subsequent activity of ^{235}U were determined for the dilution setup, and summarized in Table 12-5.[11] Theoretical ^{235}U mass values were calculated using stoichiometric calculations and measured densities for the UN-filled pipe. As the ISOCS system is best optimized for high-resolution detectors, the Falcon ^{235}U mass were in very good agreement with the theoretical values. The ISOCS generated results are less practical for lower-resolution measurements, such as by the Osprey, as shown in Table 12-5. Lower-resolution results are more difficult to unfold and are much more sensitive to continuum effects, which may contribute to the higher mass estimation of ^{235}U for the Osprey. Table 12-6 summarizes the same generated ISOCS efficiency for the 90 g U/L dilution for the UNCLE spectra taken with the Falcon detector. Consistent with the peak area results discussed in Chapter 10, a lower effective mass is seen by the detector due to dynamic flow, as well as any variations in the exact geometry setup from the dilution measurements translated to UNCLE.

11 ISOCS calculates full energy peak efficiencies and should be suitable for HPGe and NaI detectors. However, in real-life applications, NaI detectors have poor energy resolution such that geometry-dependent small-angle scattering stays within the ROI, which itself contains overlapping peaks (143, 186, and 205 keV peaks). Consequently, the interpretation of the full energy peak area is an operational one as much as it is one of physics.

Table 12-5. ISOCS Mass and Activity of UN in Dilution Pipe from Falcon BEGe.

Dilution Concentration (g U/L)	Theoretical Calculation Mass ^{235}U in Pipe (g)	ISOCS Falcon BEGe Mass ^{235}U in Pipe (g)	ISOCS BEGe Specific Activity ^{235}U (photons/ s/g)	ISOCS Osprey Mass ^{235}U in Pipe (g)	ISOCS Osprey Specific Activity ^{235}U (photons/ s/g)
90	1.99	1.85± 0.05	7.84×10^4	6.59±0.33	7.83×10^4
85	1.87	1.79± 0.04	7.83×10^4	5.15±0.21	7.83×10^4
75	1.66	1.62± 0.04	7.86×10^4	5.51±0.22	7.83×10^4
50	1.10	1.09±0.02	7.81×10^4	2.68±0.13	7.84×10^4
10	0.22	0.170±0.005	7.84×10^4	0.54±0.03	7.83×10^4

Table 12-6. ISOCS Mass and Activity of UN in UNCLE from Falcon BEGe.

Dilution Concentration (g U/L)	Mass ^{235}U (g)	ISOCS Falcon Specific Activity ^{235}U (photons/s/g)
Calculation	1.99	8.00×10^4
BEGe Dilution 90g U/L	1.85± 0.05	7.84×10^4
BEGe UNCLE 1070 RPM	1.73± 0.04	7.83×10^4
BEGe UNCLE 500 RPM	1.66± 0.04	7.83×10^4

12.4.3 ISOCS Efficiency Models Due to Absorbers and Self-Shielding

The following ISOCS models build upon characterizing the ε_{full} by determining the effects of removing the collimator/shielding. Since the Falcon is modeled with the W collimator endcap and the Osprey is modeled with the Pb brick arrangement, the uncollimated/unshielded models without 304L piping enable direct comparison of the variables contributing to ε_{full} independent of ε_{absp}.

ISOCS models were constructed without the 304L pipe wall (modeled as dry air). Figure 12-18 shows a comparison of efficiencies calculated by ISOCS for the Falcon with 90 g U/L UN in for various shielding and absorber geometries. These geometries are a variation of calculated efficiencies with and without the 304L pipe wall and/or

collimator. Similarly, Figure 12-19 compares various geometries for the Osprey. Full dilution concentration efficiencies and various shielding configurations are provided in Appendix K. All efficiencies were calculated by ISOCS within 5% uncertainty.

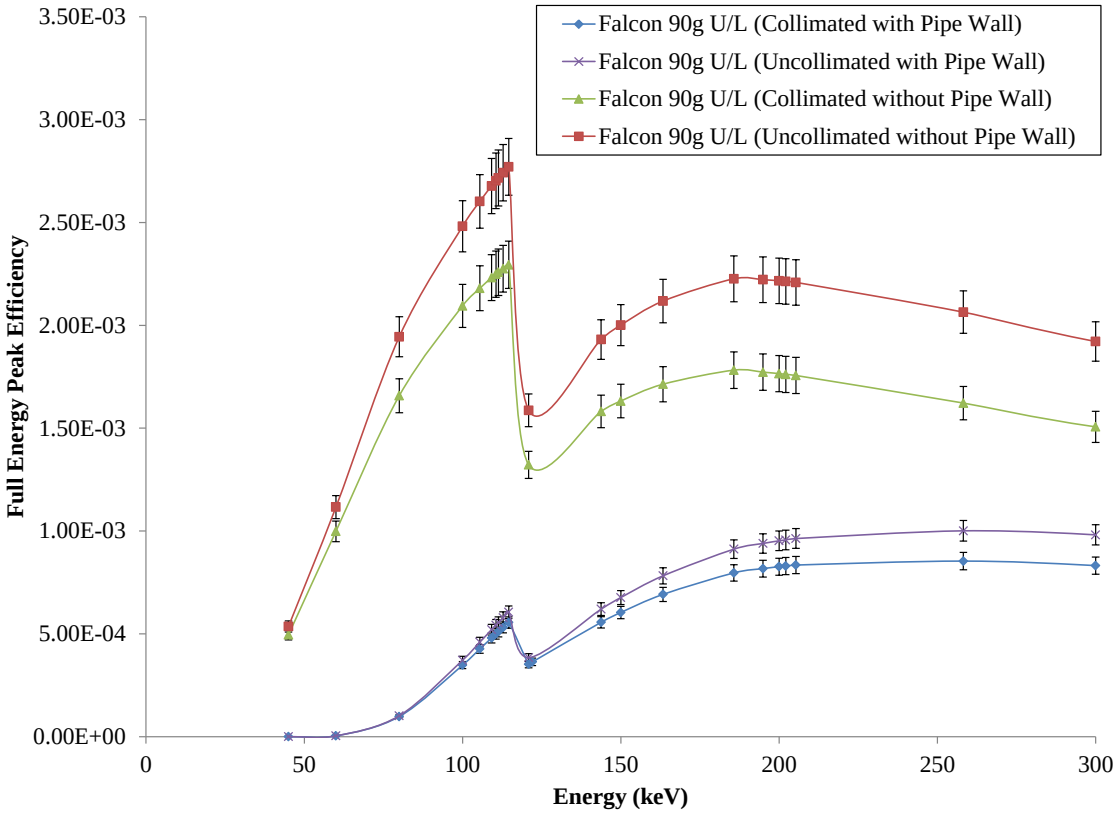

Figure 12-18. Comparison of ISOCS Efficiency Calculations of 90 g U/L UN for Falcon BEGe (i) with Pipe and Collimation; (ii) with Pipe Wall Without Collimation; (iii) with Pipe with Collimation; and (iv) without Pipe or Collimation.

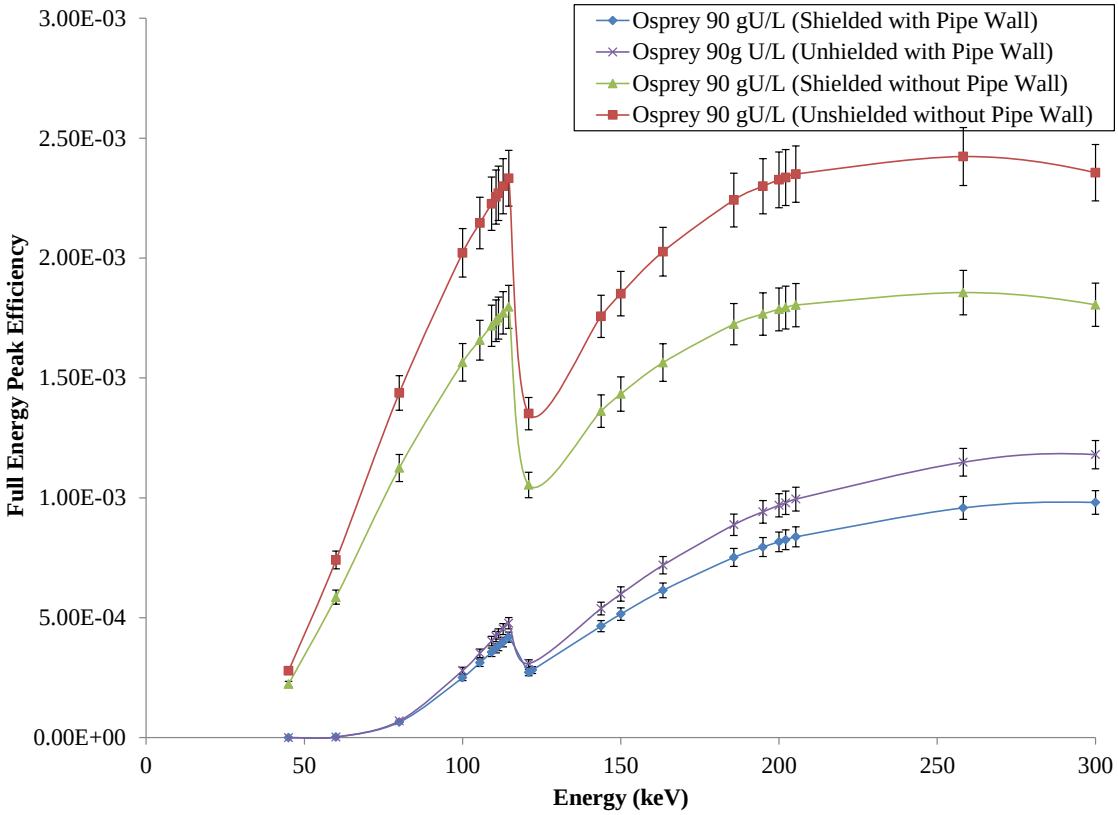

Figure 12-19. Comparison of ISOCS Efficiency Calculations of 90 g U/L UN for Osprey NaI(Tl) (A) with Pipe and Collimation; (B) without Pipe with Collimation; and (C) Pipe or Collimation.

At 185.7 keV, the peak efficiencies generated by ISOCS for these various geometries are summarized in Table 12-7. The notional uncertainty in the ISOCS calculation is ± relative, on the absolute values, based on general guidance from the product literature [63].

Table 12-7. ISOCS 185.7 keV Peak Efficiencies for Various Geometries.

Geometry	Falcon Peak Efficiency	Geometry	Osprey Peak Efficiency
Collimated, Pipe Wall	0.080%	Shielded, Pipe Wall	0.075%
Uncollimated, Pipe Wall	0.091%	Unshielded, Pipe Wall	0.089%
Collimated, No Pipe Wall	0.178%	Shielded, No Pipe Wall	0.172%
Uncollimated, No Pipe Wall	0.223%	Unshielded, No Pipe Wall	0.224%

For the Falcon at 90g U/L, the peak efficiency for a collimated detector with pipe wall is 0.080%. The presence of the pipe wall attenuates the source UN by 59.2%. The ISOCS simulation demonstrates that the presence of the W collimator attenuates 12.1% of the incident 185.7kV photons. As a result, the contribution to ε_{absp} for the Falcon at 90g U/L can be calculated as the quotient of the efficiency with shielding/collimation/piping with the efficiency without these absorbers. The result for the Falcon is a 35.8% contribution to ε_{absp}, of due to pipe wall and collimator effects. Similarly, the pipe wall for the Osprey attenuates 60.3%, where the Pb shielding attenuates 15.7% of the 185.7kV photons. As a result, the contribution to ε_{absp} for the Osprey at 90g U/L is 33.5% due to pipe wall and collimator effects.

12.5 Self-Attenuation Correction Factor

A variety of methods have been employed to determine the peak efficiency of the 185.7 keV emission, including efficiency calculations from MCNPX, measurement data, and ISOCS simulations. Determination of the ε_{sample} provides the *CF(AT)* as outlined by Parker's method in Chapter 7. From the MCNPX F1 tally model conducted in this chapter, the flux over the UN boundary provides ε_{sample} at 40.2±0.2%. The inverse value of this efficiency yields a *CF(AT)* of 2.49±0.02. Using Parker's method in combination with the MCNPX transmission model employed in Chapter 7, *CF(AT)* was plotted as a function of κ. From the calculated ε_{sample}, the κ in Equation 7-2 can be determined from the *CF(AT)* for the Falcon. In addition, using the MCNPX Parker transmission analysis from Chapter 7 with data acquired in Chapters 9 and 10, κ can be experimentally determined. Figure 12-20 shows *CF(AT)* as a function of κ for XCOM, MCNPX (from Parker analysis in Chapter 7), dilution data

(Chapter 9), and UNCLE (Chapter 10). Since *CF(AT)* was determined to be 2.49, the subsequent values for κ (based on dilution data) are provided in Table 12-8, where κ ~0.75–0.76. XCOM is overstated as it theoretically predicts *CF(AT)* for narrow-beam geometry, as explained in Chapter 7 in detail. Variations in reproducible geometry between the dilution and UNCLE measurements explain the difference in κ.

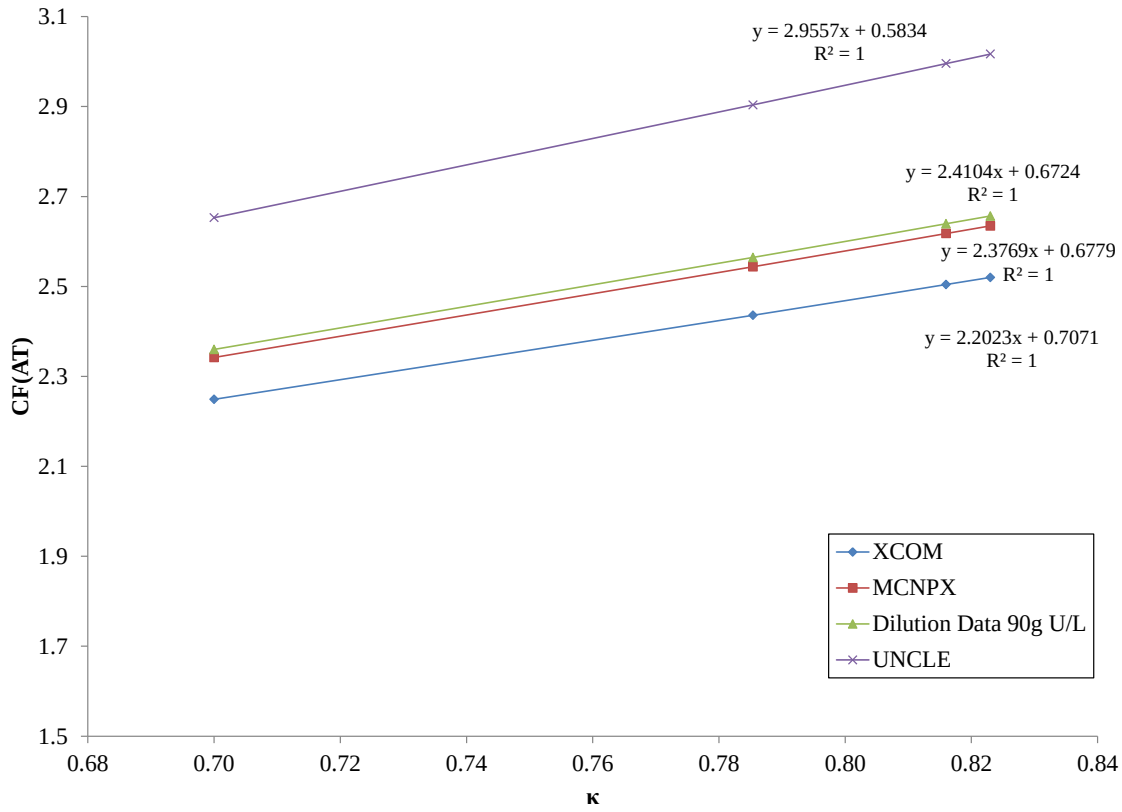

Figure 12-20. Calculation of *CF(AT)* for Various Values of *κ*.

Table 12-8. Calculation of κ Based on Derived Values of *CF(AT)*.

CF(AT)	XCOM	MCNPX	Dilution Data 90 g U/L	UNCLE
2.49	0.81±0.01	0.76±0.01	0.75±0.01	0.65±0.01

12.5.1 Overall Peak Efficiency

Correlating Equations 12-2 and 12-3, the 185.7 keV peak area can be written as a function of source activity and efficiency variables for UN, given in Equation 12-3.

$$185.7keV\ Peak\ Area\ (cps)\ = {}^{235}U\ Activity\ (Bq) \cdot \varepsilon_{peak\ {}^{235}U}\ . \qquad [12\text{-}3]$$

The Falcon measurement data yielded a 185.7 keV peak efficiency ($\varepsilon_{peak}\ of\ {}^{235}U \equiv \varepsilon_{total}$ in Equation 12-1) of (0.073±0.001)%, where the ISOCS yielded (0.080±0.004)%, and MCNPX yielded(0.076±0.009)%. With a branching ratio of 0.572 for 185.7 keV photons per decay [61], and knowing the ^{235}U specific activity of 7.84×10^{4} photons/s/g calculated from ISOCS, peak area can be correlated with ^{235}U mass as shown in Equation 12-4.

$$^{235}U\ Mass = \frac{^{235}U\ Activity\ (Bq)}{^{235}U\ Specific\ Activity\ (photons/s/g)}\ . \qquad [12\text{-}4]$$

The ISOCS and dilution mass values all fall within 5% of the MCNPX simulations. The capabilities and limitations of this confidence level in a process monitoring regime are discussed in Chapter 13 with respect to IAEA safeguards goals.

12.6 Sensitivity Analysis of Detection Efficiency

The use of simulation tools, such as MCNPX and ISOCS, permit testing the sensitivity of detector responses to how variables such as pipe thickness, source-detector geometry, and material properties affect the overall detection efficiency of the assayed ^{235}U signatures.

12.6.1 Spatial – Offset

The effect of detector placement due to spatial offset was evaluated using both experimental measurements, in conjunction with the ISOCS Uncertainty Estimator [63]. As described in Chapter 5, offset measurement data were acquired experimentally for each of the three COTS detectors for a 90 g U/L UN-filled pipe in the dilution experiment setup. Central axis measurements were taken at 1800 s live time, and for 3600 s live time at offset locations. The Falcon measurements were taken with the W collimator/endcap at 0 cm (central axis), 6.5 cm (1/2 collimator diameter) half offset, and 13 cm (full collimator diameter) full offset positions. The Inspector and Osprey measurements were taken with the Canberra 7419 Shield/Collimator with measurements correspondingly taken at 0 cm, 6.5 cm, and 13 cm offset. Spectra for the data are given in Figures 12-21, 12-22, and 12-23 for the Falcon, Osprey, and Inspector detectors, respectively.

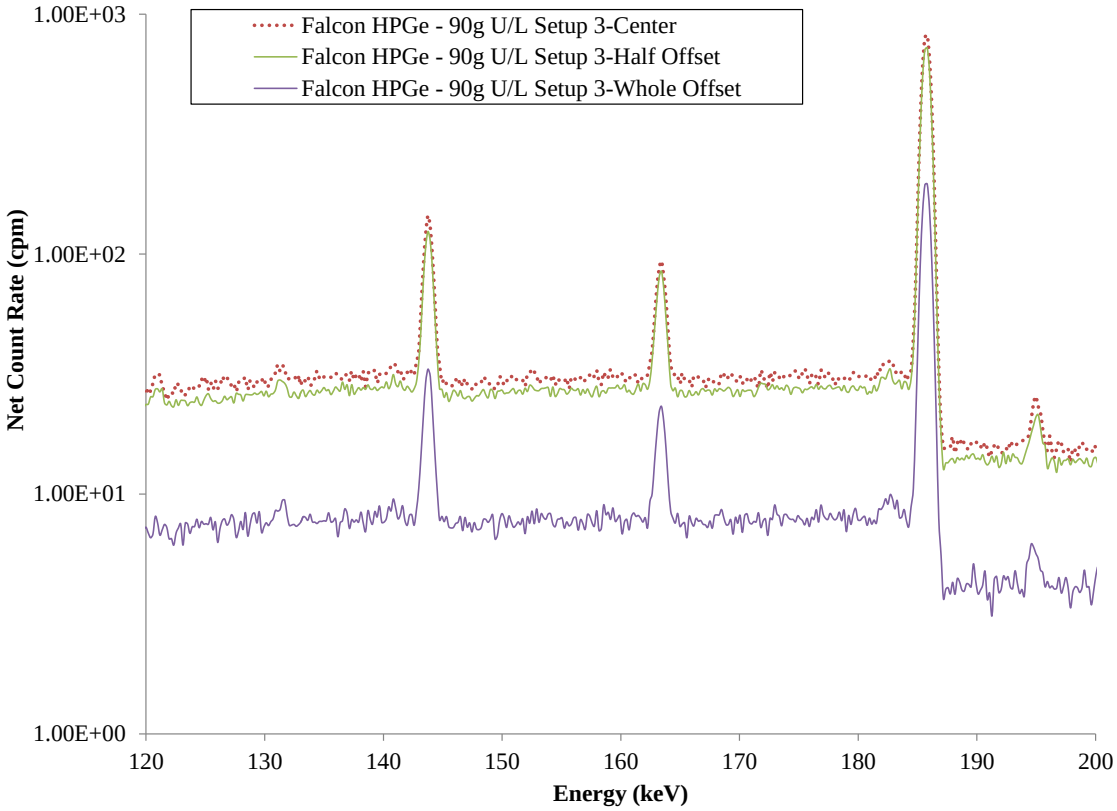

Figure 12-21. Spatial Offset Measurement Values for Falcon BEGe at 90 g U/L.

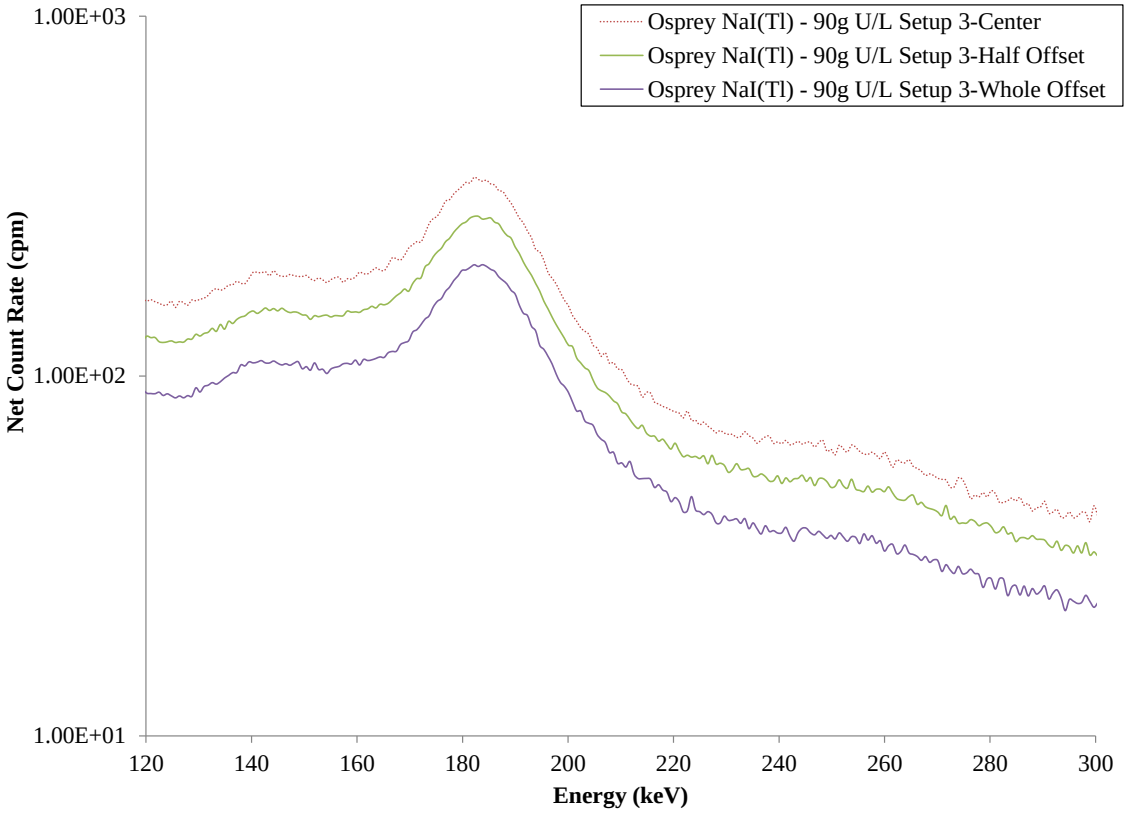

Figure 12-22. Spatial Offset Measurement Values for Osprey NaI(Tl) at 90 g U/L.

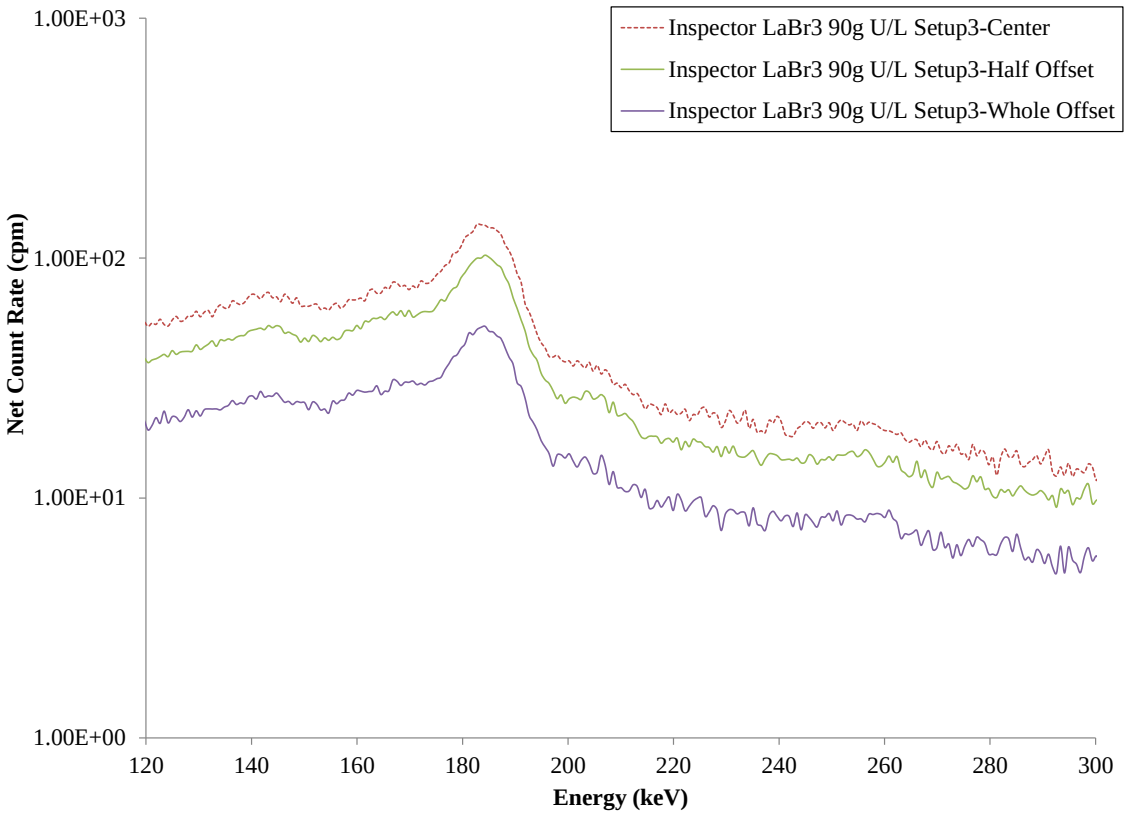

Figure 12-23. Spatial Offset Measurement Values for Inspector 1000 $LaBr_3$ at 90 g U/L.

The ^{235}U 185.7 keV peak area for each detector is plot in Figure 12-24. Although the Osprey has the highest peak area, it shows the lowest offset position sensitivity in relation to the pipe dropping to 62.3% at the half-offset location vis-à-vis the central peak area, and by 53.7% at the whole offset position. The Inspector and Falcon were comparatively more position sensitive. The Inspector peak area dropped to 70.1% at the half offset and by 23.9% at the whole offset position. The peak area sensitivity is less prominent at the half location for the Falcon, which drops 88.5% and by 23.4% at the whole offset position.

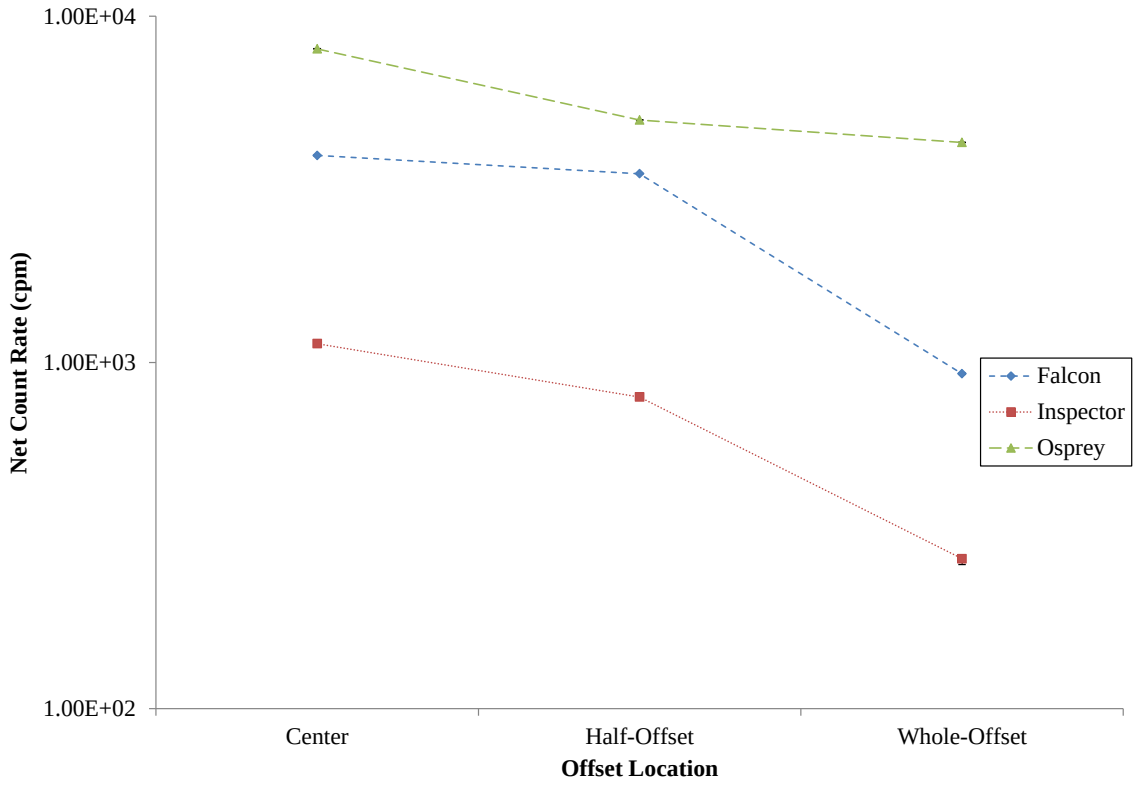

Figure 12-24. 185.7 keV Net Peak Area for Spatial Offset Measurements for All Detectors.

The ISOCS Uncertainty Estimator was employed to calculate the 185.7 keV peak efficiencies at discrete offset locations ranging from 0 to 25 cm. Models created to simulate the Falcon with W collimator and Osprey with Pb shielding, as described in the previous section for the efficiency calculation simulations. Figure 12-25 shows the results of the peak efficiencies from high-intensity ^{235}U signatures from 0 to 25 cm offset values for the Falcon, and Figure 12-26 shows the efficiency results for the Osprey. In both plots, the 185.7 keV emissions were empirically fit to determine the peak efficiencies at 0 cm, 6.5 cm and 13 cm to juxtapose with the measurement offset. These efficiency values are summarized in Table 12-9.

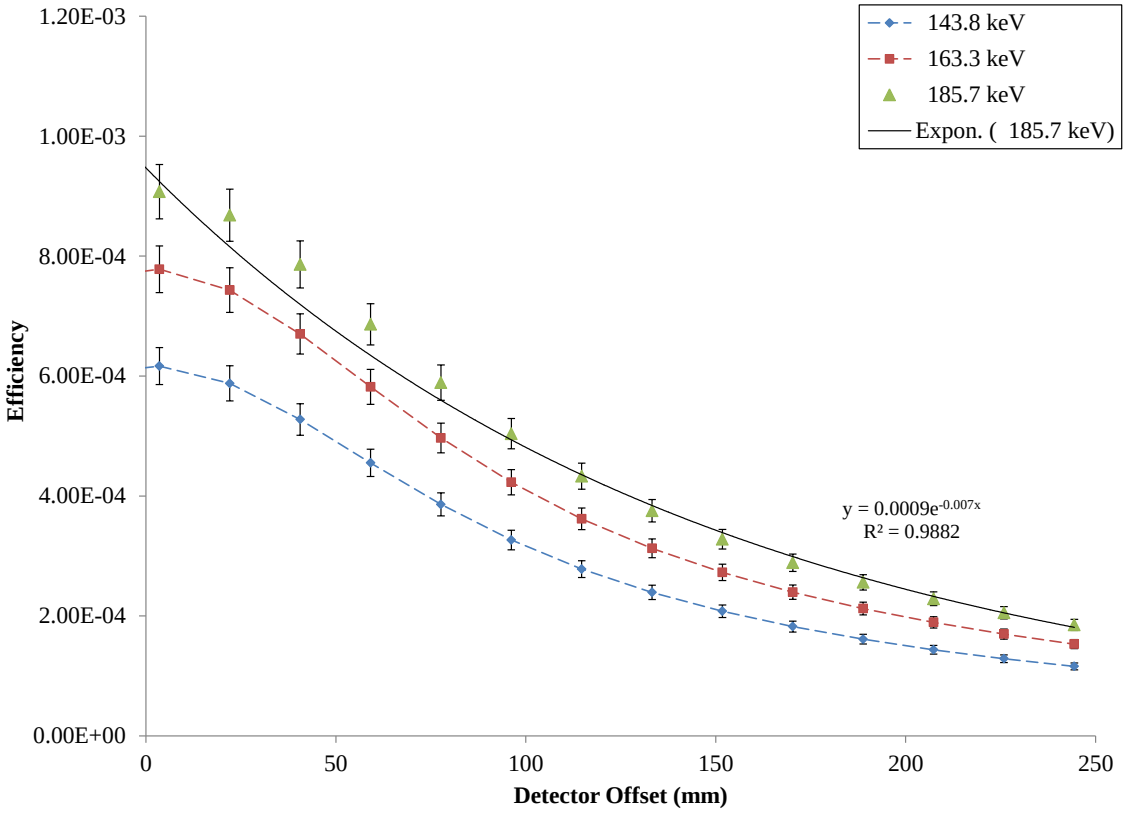

Figure 12-25. ISOCS Uncertainty Estimator Simulations: Efficiency Calculations for Falcon Detector at Various Distances from Source along Central Axis.

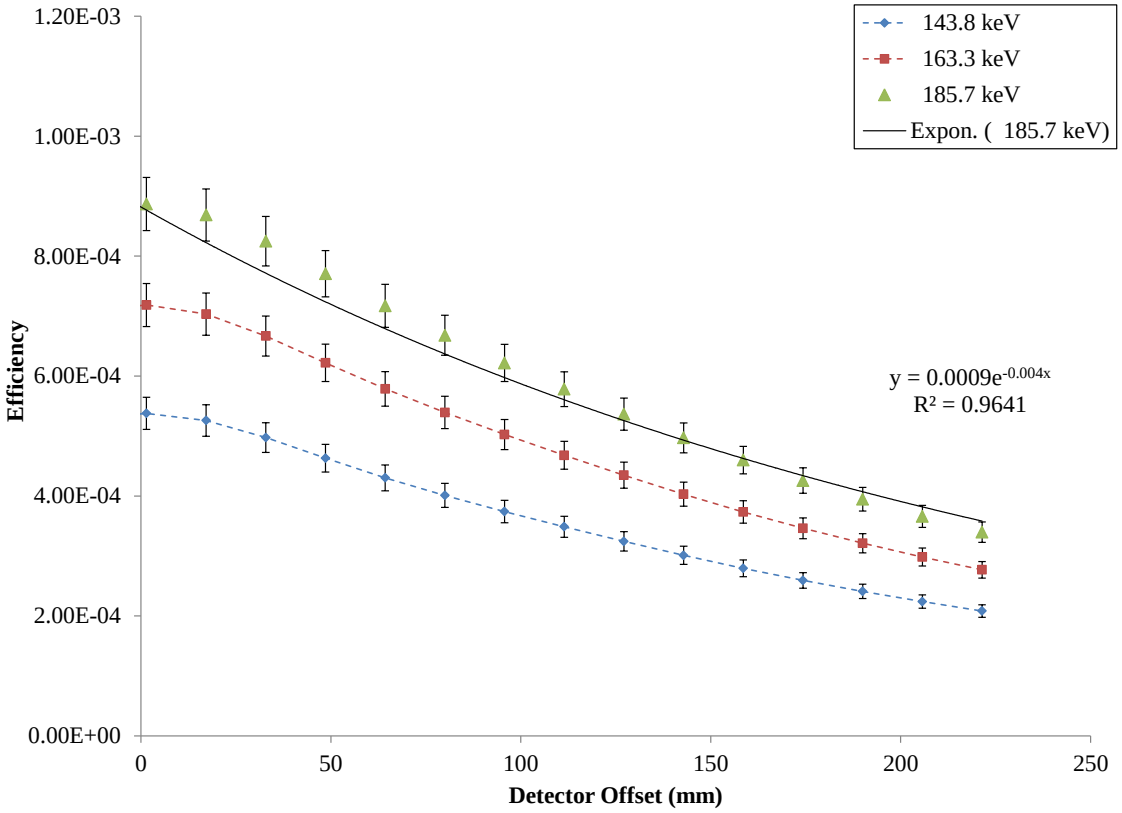

Figure 12-26. ISOCS Uncertainty Estimator Simulations: Efficiency Calculations for Osprey Detector Offset from Central Axis.

For the 185.7 keV peak efficiency to drop to 50% of its initial value, the Falcon must be offset by 9.9 cm, whereas the Osprey must be offset a much greater distance of 17.3 cm, making the Falcon much more position sensitive.

Table 12-9. ISOCS Peak Efficiency Results for Falcon and Osprey Detectors at Measurement Offset Locations.

Offset (cm)	Falcon 185.7 keV Peak Efficiency	Osprey 185.7 keV Peak Efficiency
0	0.090%	0.090%
6.5	0.057%	0.069%
13	0.036%	0.054%

The ISOCS Uncertainty Estimator calculates the efficiency associated with displacing the pipe at set offset distances for the modeled geometry. However, unlike the experimental measurements, ISOCS cannot predict added background effects in an

operational environment that may originate from adjacent pipes and tanks in an NUCP. Background additionally increases the continuum under the peak area. In reality, this can be remedied by an optimized shielding design that encapsulates the pipe and detector to prevent gross displacements between the source and detector, in addition to shielding leakage from background.

12.6.2 Spatial – Source-Detector Distance

Varying the source-detector distance along the central axis was simulated using the Uncertainty Estimator for values up to 120cm. Using Gnuplot [85], an inverse-square function was empirically fit to the efficiency data for the Falcon detector, given in Figure 12-27. The fit parameters are provided in Appendix K.

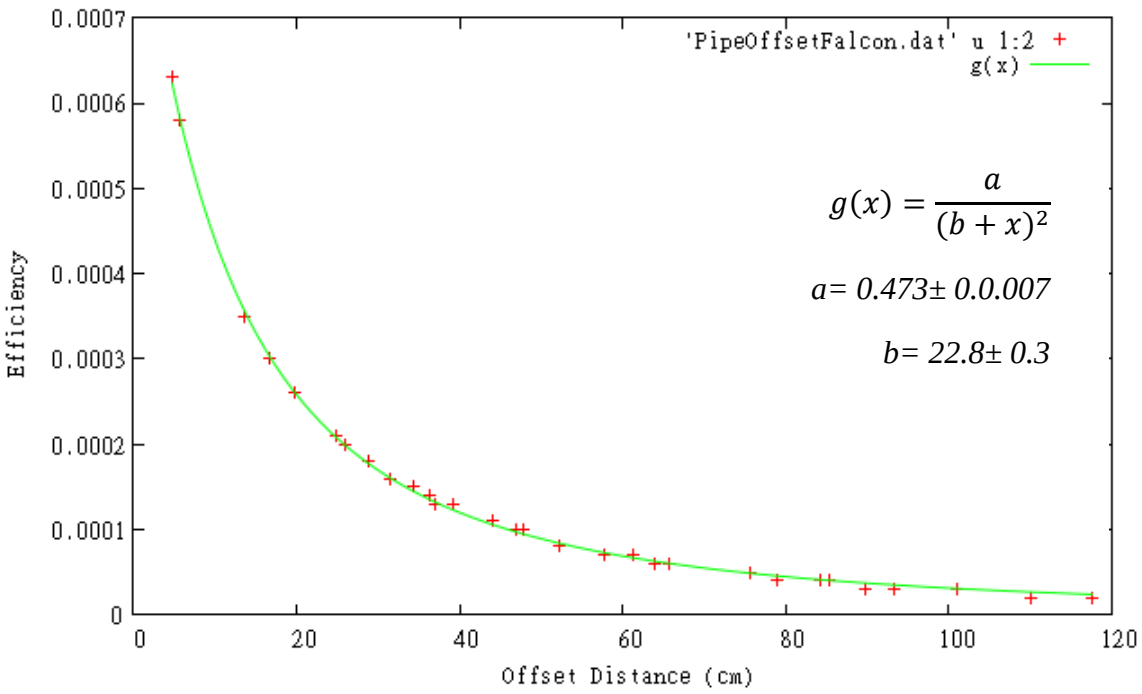

Figure 12-27. ISOCS Uncertainty Estimator Simulations: Efficiency Calculations for Falcon Detector at Various Distances from Source along Central Axis for 185.7 keV Emissions.

As with the offset simulations, Uncertainty Estimator provides an estimate strictly independent of other operational background. Moving the detector further from the pipe would increase the solid angle of the detector over which adjacent radiation sources (and background) reach the detector.

12.6.3 Pipe Thickness

Attenuation due to the pipe wall thickness determines the transmission of the 185.7 keV gamma rays reaching the detector. Correcting for pipe wall thickness also aids in correlating the density, concentration, and enrichment with measured detector data. Values of 304L stainless steel thickness fall within 0.52±0.05 cm. Using the ISOCS Uncertainty Estimator, the 185.7 keV peak efficiency was determined within the range of 0.52±0.05 cm and plotted in Figure 12-28. An efficiency comparison for other ^{235}U high-intensity emissions is provided in Appendix K. Also, Figure 12-28 show the Gnuplot fit for the peak efficiency as a function pipe thickness, with fit parameters provided in Appendix K.

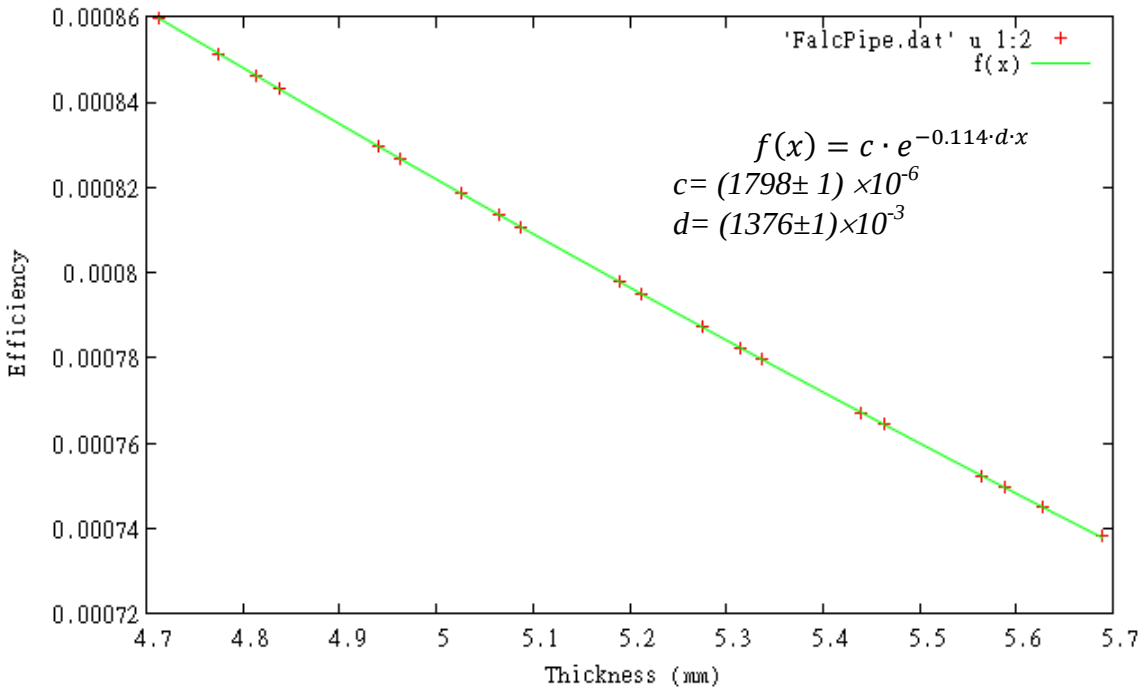

Figure 12-28. ISOCS Uncertainty Estimator Simulations: Efficiency Calculations for Falcon Detector at Various Pipe Thickness Values

As calculated in Chapter 7, the linear attenuation coefficient at 185.7 keV through 304L pipe was calculated to be 1.14 cm^{-1} with a 55.4%. Figure 12-29 shows the relative efficiency compared to a relative thickness from 0.52 cm.

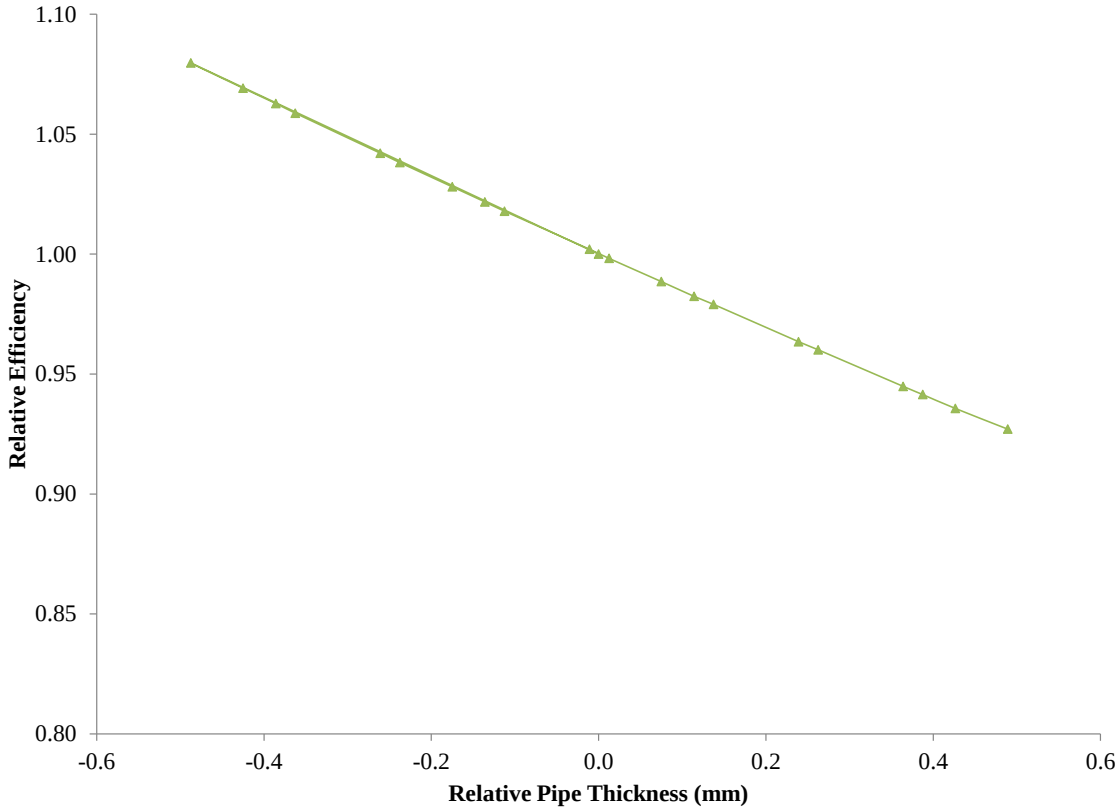

Figure 12-29. Relative Efficiency for Falcon Detector at Various Pipe Thickness Values

At the lower end at 0.47 cm, the efficiency increases by 8%, whereas at the higher end at 0.57 cm, the efficiency drops by 7%. This pipe range represents a sampling of Schedule 40 304L stainless steel pipe available in industrial production [88] [89]. The result of the detection capability for safeguards monitoring becomes pivotal given a potential 0.1–10% variation in throughput (dependent on plant size, mentioned in Chapter 1) as safeguards criteria. In the absence of an empty pipe calibration, even minute variations in pipe thickness become augmented for monitoring low-energy ^{235}U emissions for safeguards process monitoring.

12.7 Enrichment Variables

In the purview of process monitoring, a sensitivity analysis can be conducted to differentiate an increase in concentration vis-à-vis an increase in enrichment content. As described in Chapter 5, traditional verification of uranium content and enrichment is conducted by comparing the 185.7 keV of ^{235}U with the 1001 keV ^{234m}Pa under secular equilibrium conditions. If limited or unverified flowrate data or densitometry measurements are available, enrichment analysis assesses the capabilities and limitations in using passive gamma-ray detectors to characterize UN. As described in Chapter 8, MCNPX simulations were conducted for varying enrichments of UN for the Falcon BEGe. Simulations were conducted at enrichments of 0.76%, 1%, 5%, and 10%.

12.7.1 MCNPX Enrichment Results at 90 g U/L

As described in Chapter 8, MCNPX simulations were conducted for varying enrichments of UN at 90 g U/L for the Falcon BEGe. Simulations were conducted at enrichments of 0.76%, 1%, 5%, and 10%. The resulting spectra are provided in Figure 12-30. Peak area comparisons for high intensity emissions are plot in Figure 12-31.

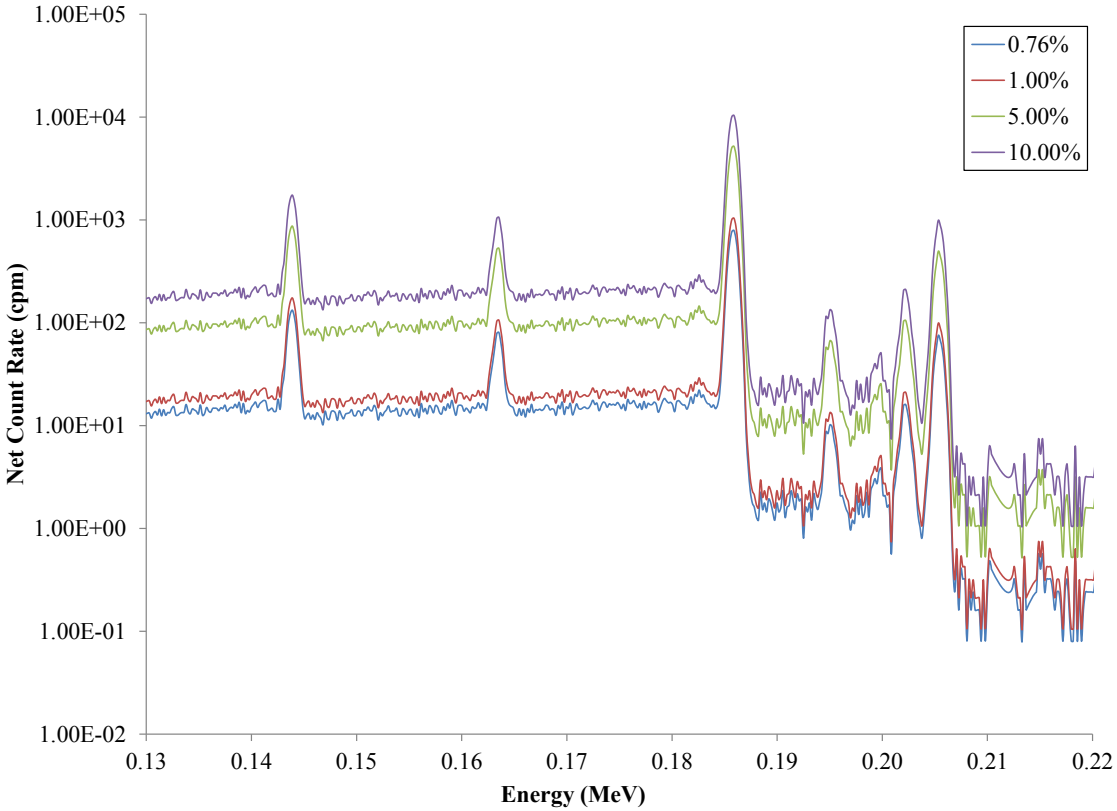

Figure 12-30. MCNPX Spectral Comparison at Various ^{235}U Enrichments for 90 g U/L.

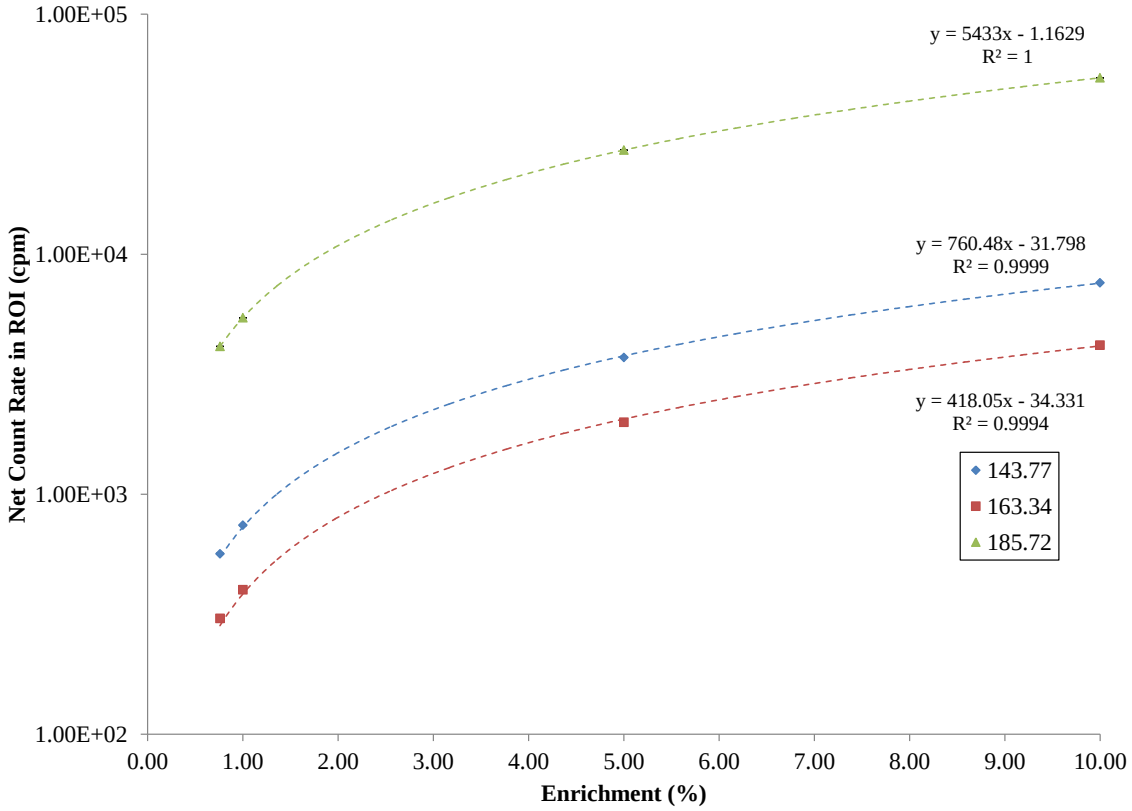

Figure 12-31. MCNPX Peak Area Comparison at Various ^{235}U Enrichments for 90 g U/L.

Note: Error bars plotted for some data points are smaller than the resolution of the graph.

As shown in Figure 12-31, the MCNPX simulations of 90 g U/L show ^{235}U peak area values to linearly correlate with enrichment at high-intensity emission energies. At 185.7 keV, the peak area increases by approximately 5400 cpm per percent enrichment.

12.7.2 MCNPX Enrichment Results at 75 g U/L

For comparison with the concentration data in UNCLE, a mock scenario similar to the previous 90 g U/L enrichment variation was simulated using MCNPX at various enrichments at 75 g U/L for the Falcon. The material composition of the simulated

75 g U/L at various enrichments is given in Table 12-10. The resulting spectra are provided in Figure 12-32. Peak area comparisons for high-intensity emissions are plot in Figure 12-33.

Table 12-10. ^{235}U Activity at Various Enrichments for Fresh UN at 75 g U/L.

Enrichment ^{235}U (wt.%)	Calculated Mass ^{235}U in Pipe	Calculated Activity Fresh ^{235}U (Bq)
0.76	1.49	1.19×10^{5}
1	1.96	1.57×10^{5}
5	9.82	7.86×10^{5}
10	19.65	1.57×10^{6}

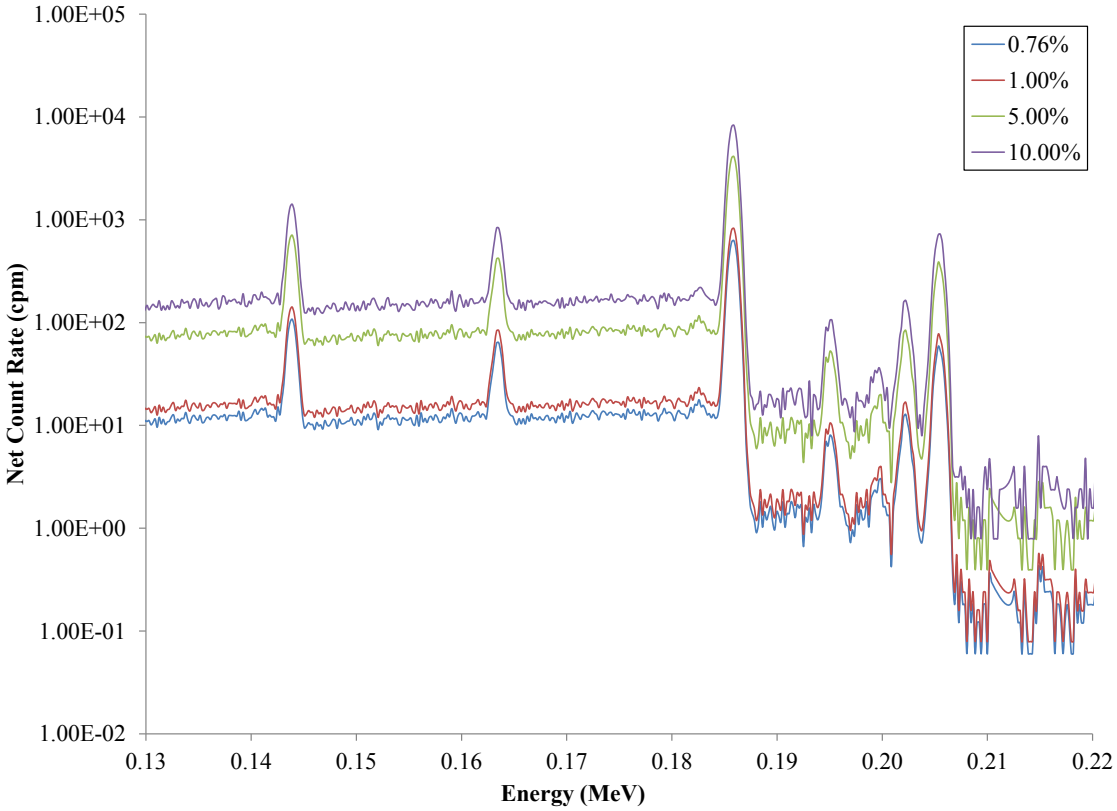

Figure 12-32. MCNPX Spectral Comparison at Various ^{235}U Enrichments for 75 g U/L.

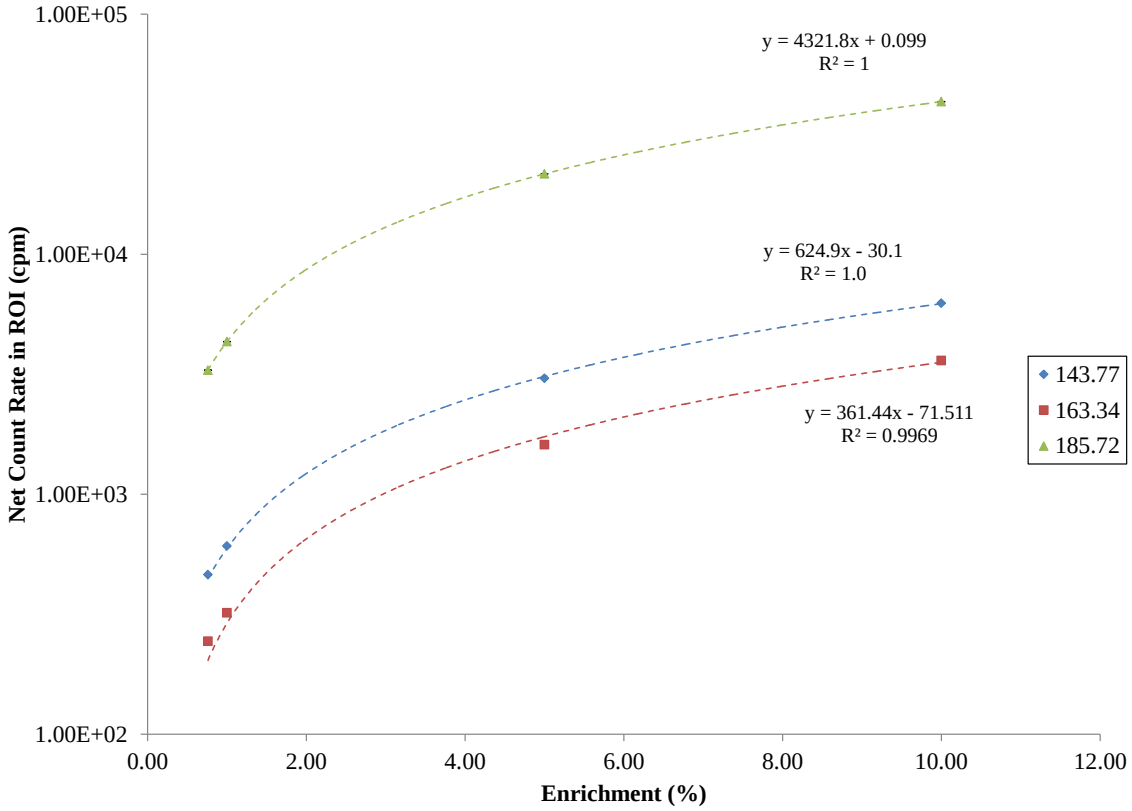

Figure 12-33. MCNPX Peak Area Comparison at Various ^{235}U Enrichments for 75 g U/L.

Note: Error bars plotted for some data points are smaller than the resolution of the graph.

As shown in Figure 12-33, the MCNPX simulations of 75 g U/L show ^{235}U peak area values to linearly correlate, with the 185.7 keV peak area increasing by approximately 4300 cpm per percent enrichment.

12.8 Conclusions

Low- and high-background environment measurements were taken under laboratory and operating conditions, for inclusion into a detailed statistical uncertainty and sensitivity analysis in order to evaluate the robustness of the monitoring signatures.

Peak area uncertainty due to Compton continuum from ^{137}Cs emissions during transmission measurements, as well as from higher-energy ^{238}U in secular equilibrium, increased the continuum, and consequently, the peak area uncertainty for the ^{235}U emissions in the 100–200 keV monitoring range. For laboratory and operational measurements at 90 g U/L, a measurement count time of ~7 s live time was required to maintain a < 5% counting statistics error for the Falcon and the Osprey, where the Inspector required at least 42 s as the detector with the lowest counting efficiency.

Efficiency values for each of the three COTS detectors were calculated for the 185.7 keV peak from a combination of measurement data, ISOCS models, and MCNPX simulations. For the collimated Falcon BEGe, the dilution measurement data yielded a 185.7 keV peak efficiency of 0.073±0.001%, where the ISOCS yielded 0.080±0.004% and MCNPX yielded 0.076%±0.009%. The Osprey 2×2 in. NaI(Tl) yielded a peak efficiency of 0.075% from the ISOCS simulations. In investigating the effects of each of the four variables ($\varepsilon_{geom} \cdot \varepsilon_{absp} \cdot \varepsilon_{sample} \cdot \varepsilon_{int}$), the F1 MCNPX model yielded an ε_{sample} of 40.2±0.2% for the Falcon, resulting in a *CF(AT)* of 2.49, and κ of ~0.75 in Parker's method in determination of self-attenuation effects.

The sensitivity analysis using ISOCS's Uncertainty Estimator provided an indication of how pipe thickness and source-detector distance and offset variables affected the overall efficiency for the modeled Falcon and Osprey detectors. Although the offset measurements varied exponentially as a function of offset distance and source-detector varied as the modified square of inverse of source-detector detector distance, such issues are remedied with effective shielding, sufficiently encasing the detector. The pipe thickness attenuation most affected the 185.7 keV signature peak efficiency by up to 8% for ±0.5 mm changes in Schedule 40 304L stainless steel piping employed in

UNCLE. The result of detection capability for safeguards monitoring becomes pivotal given a potential 0.1–10% variation in throughput as safeguards criteria. Even minute variations in pipe thickness become augmented for monitoring low-energy ^{235}U emissions for process monitoring, which affect the confidence of safeguards conclusions.

If UN concentration is overstated in a declaration and lower concentrations with higher enrichments are processed, this potential "spoofing" avenue could be employed in a scenario where the operator or state was attempting to conduct undeclared activities. This avenue may be possible using partially enriched spent fuel pellets ground into UN, in a similar way to the procedure for preparing the solution employed for UNCLE (which used ~natural enrichment fuel pellets). If independent verification is unavailable for mass flowrate, concentration, or density, then knowledge of potential misuse scenarios is useful in drawing safeguards conclusions. This concept of misuse and spoofing is discussed next in Chapter 13.

CHAPTER 13. DISCUSSION: EVALUATING "SPOOFING"AND DIVERSION SCENARIOS

Using experimental and simulation data from both the dilution and operational measurements, in combination with detailed uncertainty, statistical, and sensitivity analyses, evaluations are made regarding the optimizing gamma-ray NDA instrumentation for process monitoring at this KMP in this chapter. The feasibility of employing passive gamma-ray methods for safeguards monitoring must be evaluated in relation to the IAEA requirement of detecting 1 SQ of material (10 MTU/yr.) in a period of 1 year with a 50% detection probability. Evaluation of potential misuse or spoofing scenarios addresses the robustness of this monitoring system. Although diversion quantities are evaluated vis-à-vis plant throughput, the effects of uncertainties and sensitivities are evaluated.[12]

13.1 NUCP Efficiency Considerations

When estimating uranium losses during conversion in a small-throughput facility, Faulkner *et al.* estimated processing efficiency to be between 94% and 98%, yielding uranium losses that fall between 2 and 6 wt. % per year (~2–6 MTU/yr.) [11]. For medium- and large-scale conversion facilities, efficiency was estimated between 90%

[12] Temporal analysis requiring plant-specific information and cycle lengths are outside the scope of this work. Only the IAEA 1 yr. time frame requirement is considered.

and 98%, yielding waste streams of 20 to 100 MTU/yr. for a medium design plant and as high as 200 to 1000 MTU/yr. for large-scale plants.

In the study of developing a generic model of an NUCP, DOE and the CNEN quantified the material throughput of a Brazilian NUCP with a 500 MTU/yr. throughput *(Table 4-1)* [25]. This was assessed vis-à-vis the aforementioned monitoring points developed at ORNL. From this study, the annual difference between uranium mass entering the facility as yellowcake and exiting the plant as UF_6 was approximately 12 MTU/yr., exceeding the IAEA requirement of 10 MTU/yr.

From the DOE-CNEN study, the largest uranium losses were from insoluble uranium remaining in the filtered solids following dissolution, as well as from uranium aerosols as dust from the dissolver or from uranium powders (AUC, UO_3, UO_2) [25]. As recommended by various independent environmental monitoring studies, these streams could be considered for strategic monitoring points for process monitoring or environmental sampling to verify material balance, facility activities, and compliance [4] [29] [46]. Although these losses could be minimized via recycling, the cost for recapturing these materials is judged often to outweigh the environmental benefit for low-value natural uranium. The DOE-CNEN study concluded that an efficiency of 95% was reasonable for an NUCP [25]; however, this still leaves a 5% inventory difference, which is beyond the 1 SQ proposed by the IAEA.

In a parallel effort between DOE and the Israel Atomic Energy Commission, waste streams were estimated at a loss of 1.7% of the total uranium inventory [32]. By overestimating the waste stream losses, diversion activities could occur undetected. This study also estimated the inventory difference from conversion facilities to be as

high as 2.5%, postulating that MUF at an NUCP should be in the range of 0.1–0.5% with an operating efficiency higher that 99.5% [32]. Considerations in the diversion at an NUCP must be predicated on the quantity of available uranium, the ease of its removal from the conversion process, and the ability to mask this diversion from detection.

13.2 Diversion Stream Modeling

As discussed in Chapter 2, NUCP facilities can be classified according to their throughput (S, M, L). For each of the S, M, and L plants, 1 SQ quantity of 10 MTU represents 10%, 1%, and 0.1% of the yearly inventory that must meet IAEA detection safeguards in the period of 1 year.

Making verification assessments requires converting NDA detector measurement data (185.7 keV peak area count rate) into a mass flow rate.

1. **Solution Concentration** ***(cpm → g U/L)***: The concentration of the UN flowing in the transfer pipes can first be determined by an in-line collimated densitometry source and gamma-ray detector, which will determine UN concentration and density in the detector field of view (pending previous system calibration) from the signature peak area (from Equation 12-3).
2. **Flowrate** ***(RPM→ kg or L UN/hr.)***: A combination of external/inline flowrate meters (Doppler, acoustic, Coriolis) and/or operator declarations provides the flowrate (RPM) and mass flowrate (kg or L UN /hr.) of UN. This conversion was previously discussed in Chapters 5.6 and 10.3.

3. **Mass Flowrate of U *(kg/hr.→ MTU/yr.)***: From Equation 5-10, the concentration and flowrate data can are combined to determine the mass flowrate of U (kg U/hr.). For the 90 g U/L employed in this work, 8.2% of the UN solution. Conversion of kg U/hr. can be converted to NUCP throughput of MTU/yr. for comparison with IAEA requirements. This is discussed in the next section of this chapter.

At a flowrate of 1070 RPM, representative of Springfields' NUCP throughput translates into a mass flow rate of 7963.4 kg UN/hr. At 90 g U/L, this equates to 653 kg U/hr. If UNCLE was run continuously for a whole year, this would correspond to ~5724t U/yr., with 1 SQ representing 0.17% of the annual throughput. This is consistent with the Springfields operating history listed in Appendix A.

Gradually diverting 10 MTU/yr. requires that 1.14 kg U be diverted daily for a 24-hour cycle, or 3.42 kg daily in an 8-hour cycle. These represent 0.17% (24 hr) and 0.52% (8 hr) of throughput for a flowrate of 1070 RPM. At a lower flowrate of 500 RPM, daily diversion values represent 0.39% and 1.18% for the 24- and 8-hour cycles, respectively.

The propagated uncertainty associated with Equation 5-10 is given in Equation 13-1:

$$\frac{\partial C(t)}{C(t)} = \sqrt{(\frac{\partial M(t)}{M(t)})^2 + (\frac{\partial F(t)}{F(t)})^2} \quad , \qquad [13\text{-}1]$$

where
$\delta M(t)$ = uncertainty in mass flowrate of UN (kg/hr),
$\delta C(t)$ = uncertainty in uranium concentration (kg U/L),[13] *and*
$\delta F(t)$ = uncertainty in flowrate (kg or L/h).

Consequently, since 10 MTU represents 0.17% of the potential throughput at UNCLE (and 0.1%, 1% and 10% of L, M, and S NUCP throughput), the overall uncertainty – statistical, "four-factor" gamma-detector efficiency, calibration, and electronic – associated with determining NUCP inventory throughput would be less than 1 SQ.

13.3 Statistical Certainty for Detecting 1 SQ

The required counting times to keep count rate uncertainty under 5% were outlined in Chapter 12. As dilution and operational measurements in UNCLE were taken for 3600 s live time, statistical uncertainty was found to be <1.4% for all flowrates, dilutions, and detectors. At 90 g U/L, operational measurements in UNCLE were taken for 3600 s, with a conservative statistical uncertainty of 0.4% for the Inspector, 0.17% for the Osprey, and 0.22% for the Falcon detector, respectively. These uncertainties are based on the resolution (ROI), where the lower resolution detectors

[13] Both passive and transmission measurements provide the concentration data. Statistical count-rate error associated with the transmission peak and subsequent correlation can be represented as δC, assuming calibration strongly correlates the transmission peak area with the solution U content (mass/density).

encompass multiple ^{235}U emission energies (143, 163, 186 keV) under a single ROI, in addition to being more sensitive to Compton continuum effects. In addition, as concluded in Chapter 10, measurements at UNCLE at two different flowrates of 1070 RPM and 500 RPM yielded no discernible difference with respect to passive gamma-ray measurements. In each case, the assay peak ROI was statistically indistinguishable, due to the fact that the detector is seeing a full pipe of UN, regardless of flowrate. Consequently, the passive gamma-ray measurements employed in the current setup in the scope of this investigation are unable to provide information about flowrate. Inclusion of time-of-flight methods employing a combination of active and passive gamma-ray methods proposed in the final chapter may permit NDA methods to provide this information.

13.3.1 Background Optimization to Detect 1 SQ

Statistical uncertainty always remains inherent in radiation detection measurements. Statistical uncertainty can be most easily minimized by increasing the counting time over which measurements are acquired, as well as having a well-characterized background (or well-shielded detector). To measure 1 SQ in UNCLE, the overall uncertainty of the measurement must be below 0.17%. For S, M, and L NUCPs, detection methods must have a substantially lower measurement uncertainty than 10%, 1%, and 0.1%, respectively. Employing Equation 5-17 to meet these specific criteria, Tables 13-1 and 13-2 show the required counting time for all detectors for the Poisson statistics to fall below 0.10%, 0.17%, 1.0%, and 10%. These values are based on the dilution and 1070 RPM UNCLE measurements, respectively, for the passive 185.7 keV ^{235}U and transmission 661.7 keV ^{137}Cs emissions.

Table 13-1. Optimal Counting Time for Passive and Transmission Dilution Measurements for Predetermined Precision at 90 g U/L.

Detector	Peak Energy (keV)	Counting Time (s)			
		0.10%	**0.17%**	**1.0%**	**10%**
Falcon	185.7	134759.82 (37.43h)	8254.11 (2.29h)	167.65 (2.79m)	1.66
	661.7	-	-	1051.25 (17.52m)	10.06
Inspector	185.7	-	-	1582.75 (26.38s)	10.40
	661.7	-	-	6946.46 (1.93h)	21.24
Osprey	185.7	-	-	167.11 (2.79m)	1.59
	661.7	-	-	1115.47 (18.59m)	8.03

Table 13-2. Optimal Counting Time for Passive and Transmission Dilution Measurements for Predetermined Precision at UNCLE.

Detector	Peak Energy (keV)	Counting Time (s)			
		0.10%	**0.17%**	**1.0%**	**10%**
Falcon	185.7	41500.28 (11.53h)	7999.49 (2.22h)	188.33 (3.14m)	1.87
	661.7	-	-	1408.66 (23.48m)	13.53
Inspector	185.7	-	-	1244.95 (20.75m)	10.29
	661.7			6471.92 (4.49d)	53.02
Osprey	185.7	-	-	216.86 (3.61m)	2.10
	661.7			2861.18 (47.69m)	19.00

As seen with both passive and transmission measurements in Tables 13-1 and 13-2, the penetration of the 661.7 keV ^{137}Cs does not provide sufficient counting statistics to achieve ~1% uncertainty for all detectors.

In practice, the count rate in the peak area ROI, *r* (cpm), in Equation 13-2 is a function of the ^{235}U content (i.e., UN concentration, density) from Equations 5-10 and 13-1, which was demonstrated in the dilution experiment results in Chapter 9. The ROI

count rate, r is not only derived from NDA measurements but can be correlated with solution mass/density, i.e., $r \equiv r[C(\rho)]$ and $\delta r \equiv \delta r[\delta C(\delta \rho)]$.

In addition, statistical uncertainty in Equation 5-16 further contributes to quantifying δr. However, if we consider a period of 1 year of integrated data, the statistical error for an integrated count-rate (under steady-state conditions) is greatly reduced (assuming a well-characterized/shielded background). If the background from adjacent transfer pipes or tanks is poorly shielded for the pipe-detector setup, then (depending on the size/proximity) emissions from adjacent tanks of UN (similar to those of Tanks A and B in UNCLE) artificially increase the peak area underneath the ROI signatures if stray ^{235}U emissions are detected. Optimized shielding and detector placement mitigate the potential of this interference.

Use of the count rate in the ROI to provide information about UN content depends on the assay signature(s) employed in the calculation from either/both of the gross 185.7 keV count rate and the transmission peak area of the densitometry source. The transmission source will determine the density uranium content (insensitive to uranium isotopic composition) and density, where the 185.7 keV will provide a signature indicative of the isotopic content, provided an efficiency calibration or employment of the ISOCS software.

13.3.2 Efficiency Effects on 1 SQ Detection

The product of the peak efficiency and ^{235}U activity from Equation 12-3 yields the ROI signature peak area interrogating the UN sample to provide concentration information. The flowrate and concentration error from Equation 13-1 can

subsequently be transposed into Equation 13-2 to provide the overall uncertainty of the measurement system.

$$\frac{\partial A}{A} = \sqrt{(\frac{\partial \varepsilon}{\varepsilon})^2 + (\frac{\partial r(C)}{r(C)})^2} \quad , \qquad [13\text{-}2]$$

where
δA = uncertainty in ^{235}U activity (Bq),
$\delta \varepsilon$ = uncertainty in ^{235}U 185.7 keV peak efficiency, and
δr = uncertainty in ^{235}U 185.7 keV peak area.

Experimentally, Equation 13-3 governs the uncertainty efficiency as defined in Equation 5-6.

$$\frac{\partial \varepsilon}{\varepsilon} = \sqrt{(\frac{\partial A}{A})^2 + (\frac{\partial r(C))}{r(C)})^2} \, . \qquad [13\text{-}3]$$

From the experimental dilution measurements, at 90 g U/L (and negating δA from the passive or transmission signature emission), the efficiency was explicitly calculated for 185.7 keV emission for the Falcon to be $(729\pm2)\times10^{-4}$%, Inspector $(208\pm1)\times10^{-4}$%, and Osprey $(1481\pm3)\times10^{-4}$%. The peak uncertainty for these detector measurements spans 0.20%–0.55%, and explicitly stems from peak ROI measurements *(r)*. The values of 0.20%–0.55% in UNCLE translate to 11.6–31.4 MTU, which is in excess of the 10 MTU IAEA criterion. Although these data are based on 3600 s of data acquisition, integration over a longer time frame will reduce the statistical error associated with detection measurements.

With the dilution measurements, the activity of the source was known and Equation 13-3 is applicable. For in-field measurements, the efficiency must be determined based explicitly on count-rate data, correlated to ^{235}U mass, uranium concentration, and subsequently material throughput, reverting back to Equation 13-2

for an unknown efficiency. Determination of the system efficiency (and efficiency uncertainty) can be alleviated experimentally through the use of extensive calibration methods or – as conducted in the scope of this work – the use of the COTS software, ISOCS, to simulate the source-detector geometry (based on IAEA DIV and operator declarations) and folded with the acquired spectra to determine the activity (and hence, mass) in the pipe segment in the detector's field of view (see Section 12.4).

As elaborated previously in Chapter 12 in Equation 12-1, the peak efficiency is a combination of factors from the source-detector geometry, source self-absorption, shielding and absorbers, and intrinsic detection efficiency. As a result, these four factors' uncertainty contributes to the overall efficiency of the assay system.

13.3.2.1 Changes in Pipe Thickness

From the data provided in the sensitivity analysis of Chapter 12, the pipe thickness was the most prominent variable. With a change of 0.5 mm in pipe thickness, the detection efficiency decreases by up to 8% in the case of the Falcon and Osprey at 90 g U/L, as calculated by ISOCS. The addition of 0.5 mm of stainless steel thickness decreases the 185.7 keV peak efficiency of the Falcon from 0.080% to 0.074%. Consequently, 8% of the UNCLE annual throughput is ~458 MTU, which is much greater than the IAEA requirement of 10 MTU. Even changing the pipe thickness by ~0.1mm decreases the aforementioned peak efficiency to 0.078%. This 2.5% decrease in efficiency equates a difference of 143.1 MTU/yr., still in ample excess of the IAEA. Consequently, the utmost smallest modification in pipe specification is enough to spoof detected NDA signatures to produce enough variation to divert a much greater quantity than 1 SQ. All defined detector locations and shielding arrangements must be maintained tamper-proof.

13.3.2.2 Changes in Concentration

As concentration values change, the mass, density, and self-attenuation of UN also vary accordingly. However, we must delineate in mass as a function of concentration with changes in attenuation as a function of concentration. As the concentration of UN increases, so does the uranium mass, thereby increasing the ^{235}U transmission. However, with an increase in concentration comes an increase in density, as well as self-attenuation, thereby decreasing the ^{235}U transmission. In order to interpret stand-alone NDA peak area measurements, we must attempt to distinguish between these two scenarios. Figure 13-1 summarizes the mass (g), self-attenuation correction factor for 185.7 keV photons, density (g/cm^3), and linear attenuation (cm^{-1}) of UN as a function of solution concentration (g U/L). All parameters linearly correlate with the concentration of UN. As a function of concentration, the mass is most sensitive to changes in concentration as ~2.6 g U per g U/L increase in UN solution, and the density varies 0.0013 g/cm^3 per g U/L UN. The self-attenuation of the 185.7 keV ^{235}U photons varies as 0.0074 per g U/L change in UN, where the linear attenuation varies as 0.0015 cm^{-1} per g U/L. Changes in mass are much more pronounced as a function of concentration, whereas changes in attenuation are less sensitive. Exploitation of these physical properties enables a would-be rogue diverter to conduct undeclared activities undetected.

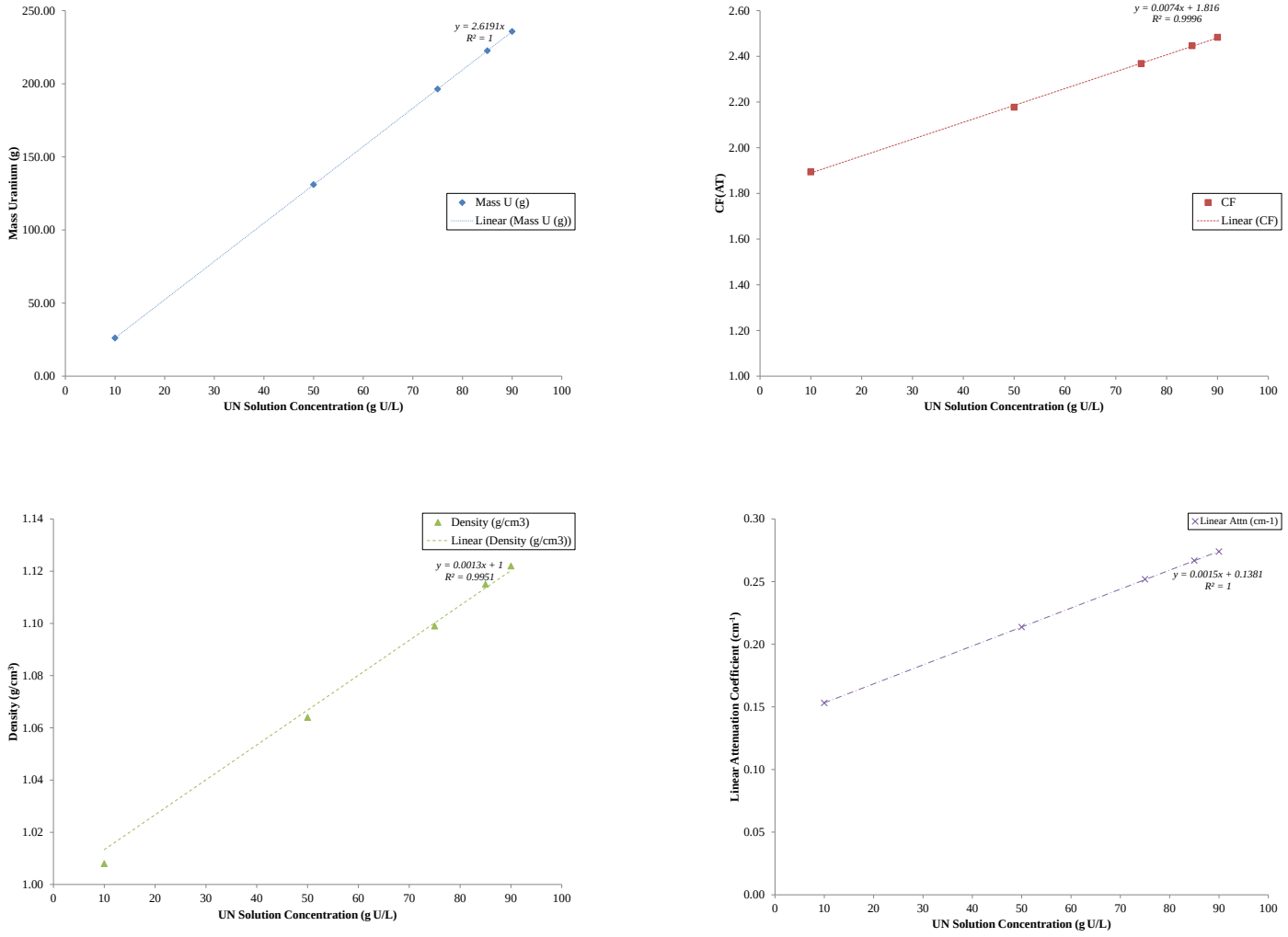

Figure 13-1. Comparison of Mass, Self-Attenuation Correction, Density, and Linear Attenuation as Functions of UN Concentration.

Based on the dilution experiments of Chapter 9, it is statistically indiscernible to differentiate a change of ~5 g U/L, especially in the case of low-resolution measurements, in the presence of high Compton continuum contributions, or the use of insensitive transmission sources such as ^{137}Cs. As seen in the dilution experiments in Chapter 9, the area of the 185.7 keV peak decreases from 3963.2 cpm at 90 g U/L to 3910.1 cpm at 85g U/L – a difference of ~53 cpm, or 1.34%

If such a substitution were made in UNCLE at 1070 RPM, this quantity equates to 318 MTU/yr. Even at the lower flowrate tested at 500 RPM, a change of 5 g U/L equates to 141 MTU/yr. Consequently, a change of < 0.5g U/L would produce on the order of ~10 MTU/yr. Based on the NDA measurements presented in Chapters 9 and 10, a 0.5 g U/L change could not be confidently discriminated, relying solely NDA measurements, most notably in the case of low-resolution measurements.

13.3.2.3 Changes in Enrichment

Any variation in enrichment will remain undifferentiated by a transmission densitometry source, the density can remain unchanged, and these sources are elementally sensitive only to the uranium content. However, the combination of both the passive 185.7 keV and transmission peak further aid in determining the nuclide content of ^{235}U in UN. From 0.76% to 1%, the 185.7 keV peak area increases by 31.5% from 4129 cpm to 5433 cpm, as calculated by the MCNPX enrichment simulations in Chapter 12.

The UN measured in this work (originating from UNCLE) employed 0.76 wt.% enriched ^{235}U. At higher enrichments, the concentration of uranium in UN remains the same, but criticality safety becomes more prevalent at much higher enrichments.

Noticeable modifications to plant configurations and equipment to accommodate for criticality safety would provide an obvious indicator of processing of much higher enrichments. However, for a would-be rogue diverter, processing a subtle change in enrichment, such as from 0.76% to 1% presented in the simulations of Chapter 11, would be a potential avenue for producing more undeclared ^{235}U. For a concentration of 90 g U/L at an NUCP of UNCLE's throughput, increasing from 0.76% to 1% ^{235}U enrichment (i.e., 0.061 wt.% in UN to 0.0802 wt.%) keeps the annual throughput the same, in terms of MTU/yr., but increases the ^{235}U throughput from 42.6 MT/yr. to 55.9 MT/yr. – an excess of 1 SQ which could be diverted to undeclared UF_6. Even with sophisticated inline flowrate meters, although the mass throughput can be determined, the absence of NDA sampling would not verify this increase.

To determine how common 185.7 keV peak area signals correlate with UN concentration and/or enrichment, the dilution concentrations (10–90 g U/L at 0.76% enrichment) in Figure 13-2 (from Chapter 11 simulations) and the 75 g U/L and 90 g U/L (0.76–10% enrichments) were compared in Figure 13-3 with respect to ^{235}U mass in the pipe segment.

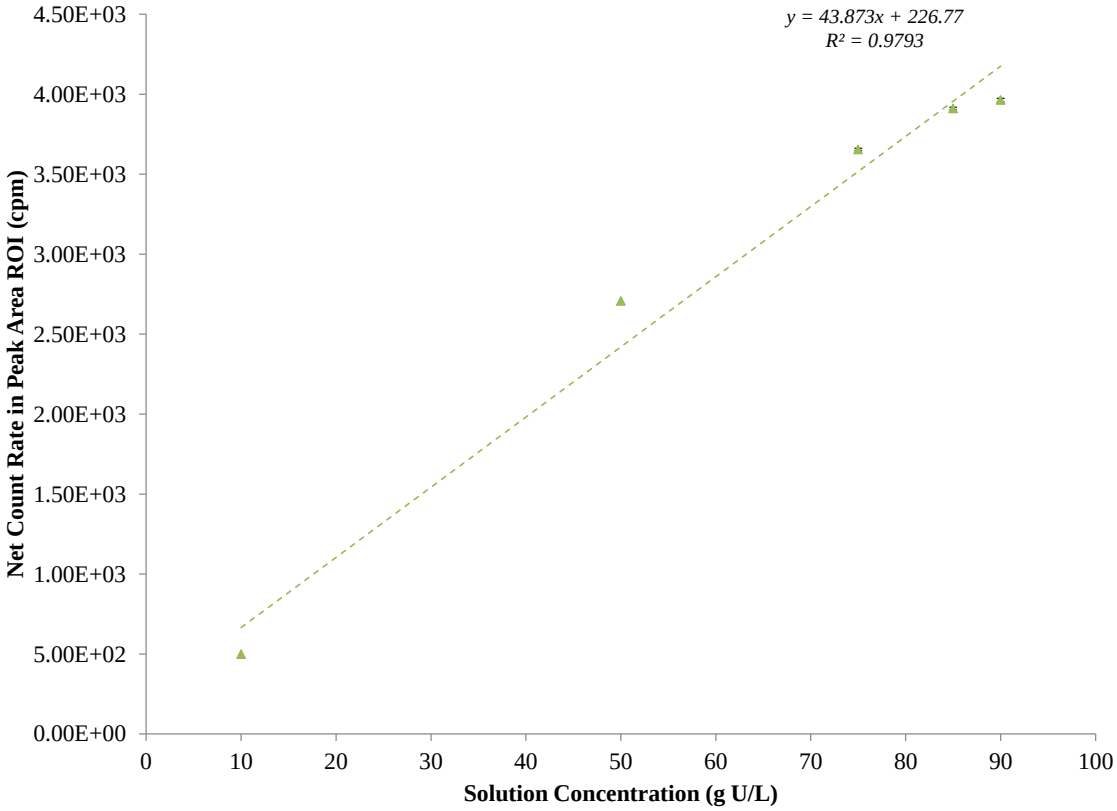

Figure 13-2. MCNPX Net Peak Area for ^{235}U 185.7 keV Emission as a Function of Dilution Concentration at 0.76% Enrichment (UNCLE).

Note: Error bars plotted for some data points are smaller than the resolution of the graph.

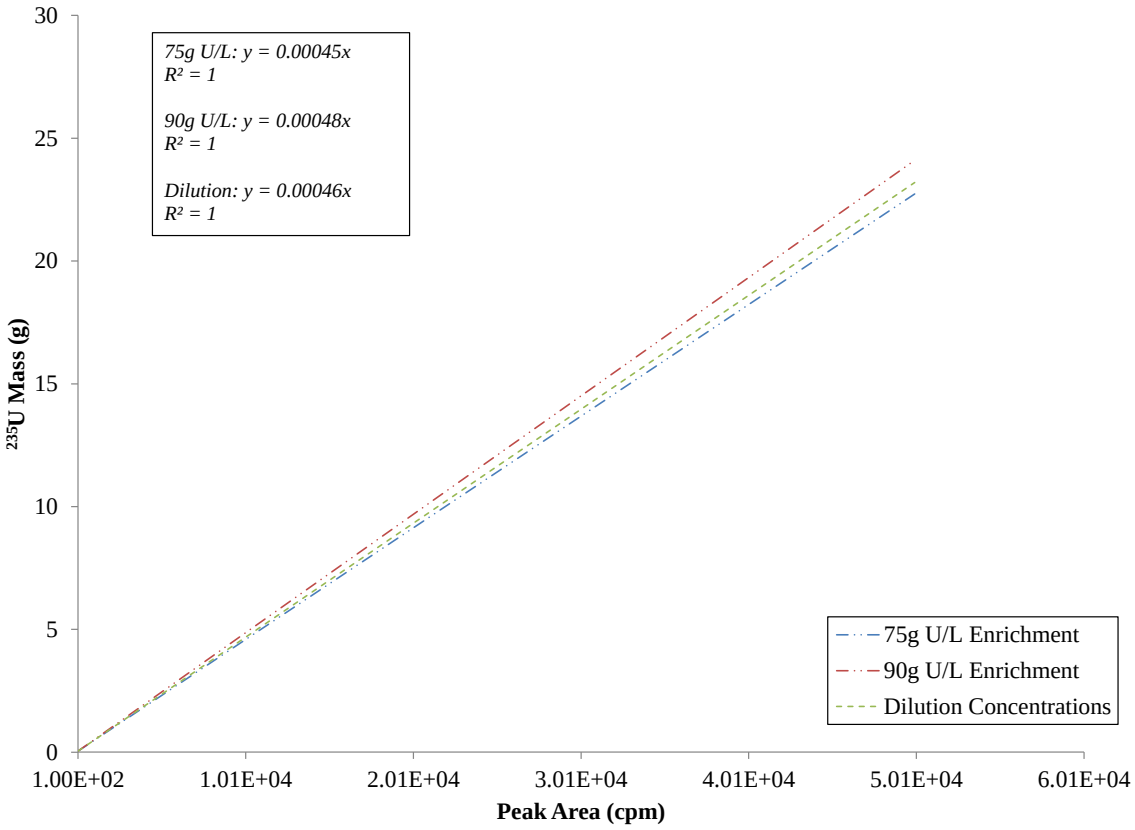

Figure 13-3. ^{235}U Mass in Pipe Segment as a Function of MCNPX Net Peak Area for 185.7 keV Emissions for 75 g U/L and 90 g U/L Simulated Enrichments and Dilution Concentrations.

Note: Error bars plotted for some data points are smaller than the resolution of the graph.

Although operator declarations are meant to be verified with this process monitoring system, a combination of data (densitometry, mass flowrate) is required to verify UN content. As shown in Figure 13-3, in the absence of mass flowrate, densitometry data, or ^{238}U signatures assuredly in secular equilibrium, passive gamma-ray count rates can be interpreted according to Figure 13-3 (summarized in Table 13-3).

Table 13-3. ^{235}U Mass (g) in Pipe Segment as a Function of 185.7 keV Net Peak Area.

185.7 keV Peak Area (cpm)	1000	2000	3000	4000	5000	6000
75g U/L Enrichment (g)	0.45	0.91	1.36	1.82	2.27	2.73
90g U/L Enrichment (g)	0.48	0.96	1.45	1.93	2.41	2.89
Dilution Concentrations (g)	0.46	0.93	1.39	1.86	2.32	2.78

Figure 13-3 and Table 13-3 show the corresponding ^{235}U content in the pipe segment as a function of 185.7 keV peak area emissions derived from MCNPX simulation. Based on these values, for a peak area of 4000 cpm this corresponds to either 75 g U/L at 0.93% enrichment or 86.1 g U/L dilution concentration at 0.76%. As a result, a potential rogue diverter could exploit this property for unverified and uncorroborated NDA measurements.

13.3.3 Material Substitution

One of the major concerns outlined in Chapter 4 is the potential for material substitution to alter the throughput values. In the absence of independent verification, or sole reliance flowrate meters, the UN solution can be substituted with dummy materials. Material substitution occurs under two key modes: (1) direct substitution to spoof the inline flowrate meter while a subset of actual content is produced and diverted through undeclared activities and (2) partial substitution to spoof the inline flowrate meter while processing higher-than-declared ^{235}U enrichments. To provide a quantitative estimate of these activities, a set of MNCPX simulations was conducted where 90 g U/L (0.76 wt.%) UN was partially substituted with lead (II) nitrate, $Pb(NO_3)_2$, dissolved in water. Lead (II) nitrate, occurs as a colorless crystal with a density of 4.53 g/cm^3. Unlike other lead salts, it is water soluble with a solubility of 52 g/100 mL at 293K [90]. These simulations were set up as outlined in Chapter 8 using the Falcon BEGe model, with the appropriate material substitutions (provided in

Appendix L). The equivalent UN solution mass of 5 g U/L, 10 g U/L and 20 g U/L was replaced with $Pb(NO_3)_2$ dissolved in water and maintained at the original solution density of 1.122 g/cm^3 In principle, maintaining this mass during material substitution would spoof a simple flowrate meter measuring throughput in kg/hr.

In order to potentially spoof NDA instrumentation, the remaining UN was varied in enrichment from 0.76 wt.%–10 wt.% ^{235}U to determine if the 185.7 keV peak area could be approximated to the original declaration of 90 g U/L at 0.76 wt.%. From the original 0.76% enriched solution at 90 g U/L, a substitution of 5, 10, and 20 g U/L UN solution equivalent represents a decrease of 5.6%, 11.2%, and 22.3% ^{235}U content, respectively. By comparison, the dilution in UN concentrations (as conducted in Chapter 9) represents a ^{235}U decrease of 6.0% to 89.0% ranging from 85 g U/L down to 10 g U/L.

Substituting the equivalent of 5 g U/L with $Pb(NO_3)_2$ decreases the uranium mass in the simulated pipe segment of the 90 g U/L solution from 1.99 g by ~0.1 g U, where at 10 g and 20 g substitutions, the uranium content decreases by 0.22 g and 0.44 g in the pipe segment, respectively. Table 13-4 translates these simulated mass substitutions made for the pipe segment into NUCP throughput for 1070 RPM (5724 MTU/yr.) and 500 RPM (2537 MTU/yr.) mass flowrates, previously tested in UNCLE. For each of the mass substitutions, the density of the $Pb(NO_3)_2$ was maintained at the same density as the UN solution (1.122 g/cm^3). Since the density is maintained, it is clear that flowrate monitoring alone cannot determine the content in the NUCP transfer pipes.

Table 13-4. Annual ^{235}U Throughput (MTU/yr.) in UNCLE for 1070 and 500 RPM Flowrates.

1070RPM	0.76%	1.00%	5.00%	10.00%
	MT ^{235}U/yr.			
90g U/L	43.5	57.2	286.2	572.4
5g U/L Pb Substitution	40.2	52.9	264.4	528.8
10g Pb Substitution	37.8	49.8	248.8	497.6
20g Pb Substitution	33.1	43.5	217.7	435.4

500RPM	0.76%	1.00%	5.00%	10.00%
	MT ^{235}U/yr.			
90g U/L	19.3	25.4	126.8	253.7
5g Pb Substitution	17.8	23.4	117.2	234.3
10g Pb Substitution	16.8	22.1	110.3	220.5
20g Pb Substitution	14.7	19.3	96.5	193.0

As shown in Table 13-4, it is possible to replicate the equivalent mass flowrate by maintaining the solution density and making the material substitutions given in Appendix L. The use of passive and transmission densitometry gamma-ray monitoring techniques provides an additional obstacle for rogue entities to spoof. Analysis of the ^{235}U 185.6 keV peak provides further information regarding the uranium content in the flowing UN. Table 13.5 provides the ROI peak areas for this emission for the aforementioned Pb material substitutions and enrichment variations.

Table 13-5. Comparison of ROI Peak Area (cpm) for (A) Dilution and (B) Pb Substituted Solution at Various Enrichments.

Values are graphically plot in Appendix L.

(A)

Dilution Concentration (g U/L)	Peak Area in 185.7 keV ROI (cpm)
90	4131±23
85	3929±22
75	3651±21
50	2687±16
10	639±6

(B)

Material Substitution Enrichment (%)	Peak Area in 185.7 keV ROI (cpm)			
	90g U/L	**5g U/L Pb Substitution**	**10g U/L Pb Substitution**	**20g U/L Pb Substitution**
0.76	4129±8	3954±8	3766±8	3392±8
1	5433±10	5205±9	4956±9	4463±9
5	27161±21	26021±21	24773±20	22311±19
20	54330±30	52054±29	49558±29	44623±27

In the absence of densitometry using a uranium-sensitive transmission source, determination of ^{235}U throughput is easily defeated through flowrate measurements alone. In addition, Table 13-5 demonstrates that, although densities are maintained, Pb substitutions and enrichment alterations can be made to replicate declared baseline mass throughput and ^{235}U throughput. As such, a baseline of 90 g U/L at 0.76% enrichment provides the same mass throughput and a statistically comparable 185.7 keV peak area count rate as 1% enriched material with 20 g U/L equivalent substituted with the Pb solution. For a rogue diverter, diverting 20 g U/L equivalent volume of UN while replacing it further downstream with Pb solution is a potential spoofing avenue (among many possible perturbations) that could be exercised.

13.3.4 Peak Area Interpretation

Experimental measurements and simulation have established performance criteria and allowed calculation tools to be benchmarked and validated. In particular, the experiments may be considered to provide the basis for concentration/density calibration. Correlation of the UN solution density, concentration, transmission, ^{235}U mass, and 185.7 keV peak areas and solution concentrations is given in Figures 13-4 and 13-5. Each of these relationships is a simple transform. Consequently, we can propose a model for which NDA data can determine information about the original solution density, concentration, and enrichment to reflect the algorithms presented in Chapter 5-8.

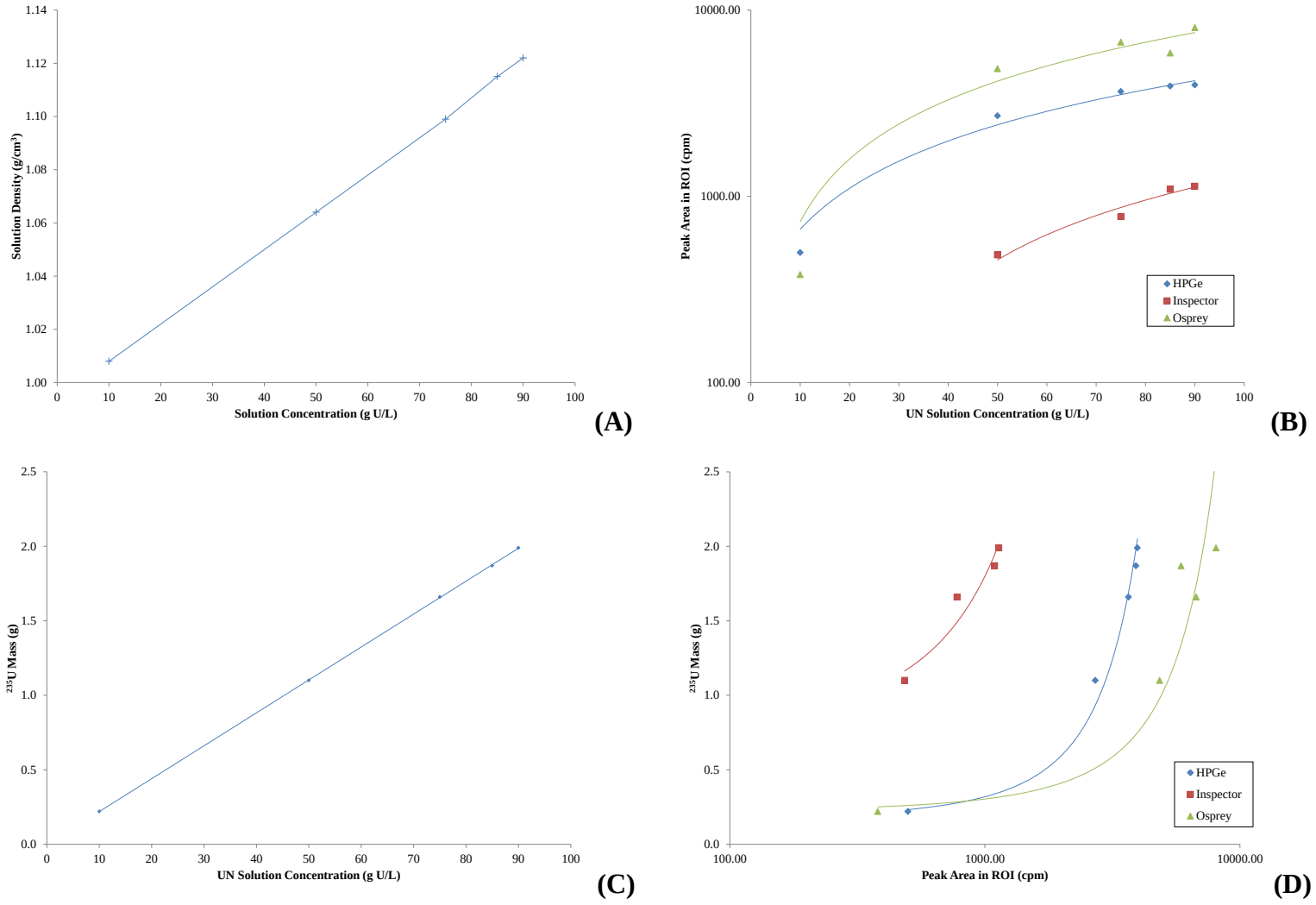

Figure 13-4. Correlating UN Solution Density, ^{235}U Mass, ^{235}U 185.7 keV Peak Area, and Solution Concentration.

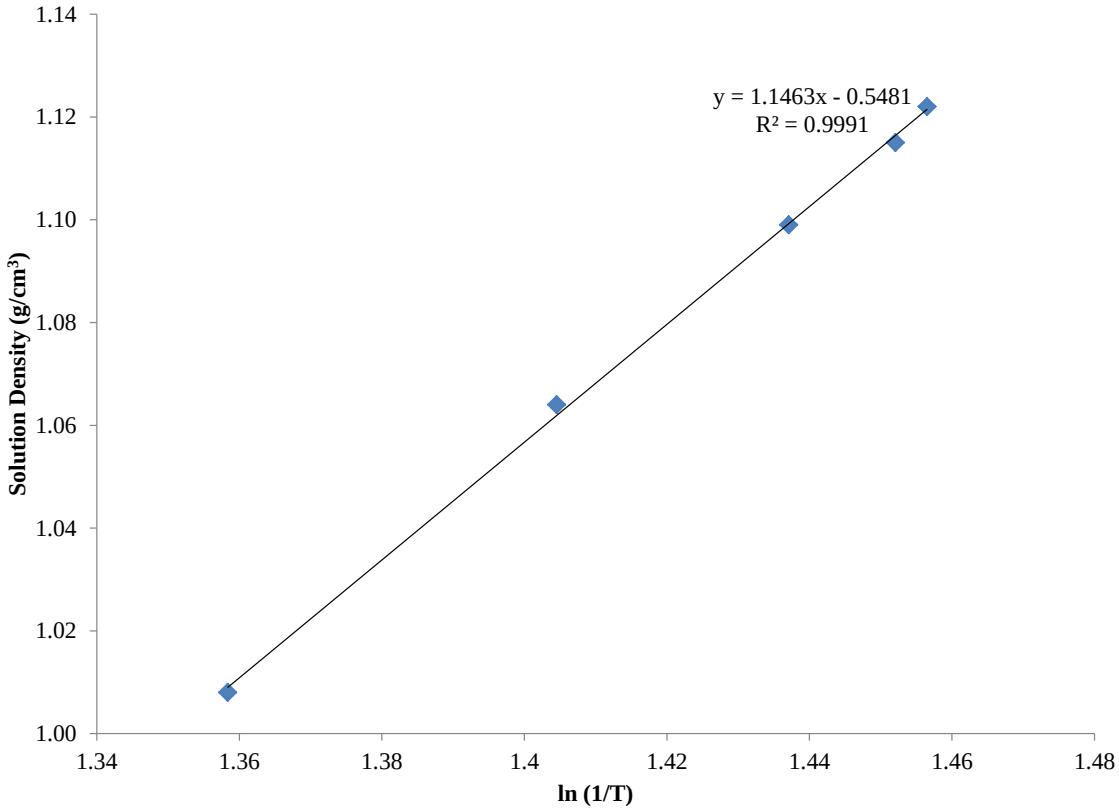

Figure 13-5. UN Solution Density Calibration Data as a Function of ^{137}Cs Transmission.

Independent verification of these variables is essential in determining safeguards compliance and verifying undeclared activities are not occurring. Individually, flowrate, passive, and densitometry measurements are unable to provide fully sufficient information to verify compliance and detect misuse. However, the combination of operator declarations and traditional IAEA methods/technology (DIV, PIV, flowrate, MC&A) with calibrated in-line NDA instrumentation (density, enrichment, concentration) provides a more comprehensive, independent means of verifying NUCP activities. These methods are summarized in Table 13-6.

Table 13-6. Capabilities of Installed Instrumentation for NUCP Safeguards Monitoring.

Measurement Technique	Solution Density	Uranium Concentration	^{235}U Enrichment
Flowrate meter	X		
Gamma-ray 185.7 keV Peak		(X)	X
Gamma-Ray Transmission Densitometry	X	(X)	

(X) = In combination

13.4 Conclusions

Variation in uranium content – either concentration or enrichment – remains a challenge using stand-alone NDA methods. Without verifiable declarations or further data – i.e., density/densitometry, mass flowrate data, or ^{238}U signatures in secular equilibrium – interpretation of the 185.7 keV peak area alone is incomplete, as was shown in the example juxtaposing enrichment variations between 0.76%–10% for 75 and 90 g U/L with the dilution data for concentrations from 10–90g U/L at 0.76%. Although an increase in concentration and/or enrichment would yield higher peak area count rates, the effect of increased self-shielding due to an increase in density would be indicative of an increased uranium concentration. Simple material substitutions using $Pb(NO_3)_2$ demonstrate that flowrate meters can be easily spoofed. With a slight adjustment of enrichment, 185.7 keV emission monitoring can be spoofed to look like natural uranium at a declared 90 g U/L, demonstrating that a combination of passive and transmission measurements must be employed to ensure such misuse does not occur.

Completely independent, stand-alone passive gamma ray techniques cannot immediately detect diversion and misuse at the IAEA limit of 10 MTU/yr. without sufficient efficiency calibration of the detection system and knowledge of the UN-pipe

configuration. However, in conjunction with IAEA safeguards verification practices under INFCIRC 153 and INFCIRC 540 (such as DIV, inspection and MC&A), enhanced combined passive and active/transmission gamma-ray techniques can provide a PM tool for independently verifying declarations.

CHAPTER 14. CONCLUSIONS AND FUTURE WORK

In the context of recent IAEA policy recommendations for monitoring purified compounds in uranium conversion facilities, the scope of this project addressed instrumentation testing in dilution measurements and at ORNL's UNCLE facility. The objective of this work was to determine the capabilities of passive gamma-ray systems for PM in NUCPs and whether it was possible to meet the IAEA safeguards criteria of detecting 1 SQ (10 MTU) in a time frame of 1 year with a 50% probability of detection. The KMP interpreted as first satisfying INFCIRC/153 Para. 34(C) materials occurred following solvent extraction, producing UN during the conversion process. Based on in-depth experimental measurements, simulations, and uncertainty/sensitivity quantification, the abilities of COTS gamma-ray detectors were evaluated to determine their role in an overall safeguards system to determine if IAEA safeguards criteria could be met. Based on the capabilities of NDA methods using passive gamma-ray methods, further work and recommendations are provided in order for the IAEA to meet its safeguards PM goals under PP18.

14.1 Conclusions

14.1.1 Experiment Conclusions

Gamma-ray signatures for UN originating from the UNCLE facility were identified and detector instrumentation was evaluated as part of a broader study addressing safeguards applications. Since secular equilibrium cannot be ensured for the source UN, assay signatures were confined to high-intensity direct emissions from ^{235}U.

Experimental measurements were conducted using the Canberra 2×2-in. NAIS with the Osprey digital tube base, the Canberra Inspector 1000 with 1.5×1.5-in. $LaBr_3$

Probe, and the Canberra Falcon BEGe detectors for dilution concentrations of 10–90 g U/L of UN (0.76 wt.% enrichment), as well as in an operational environment in UNCLE at 90 g U/L at 1070 RPM and 500 RPM pump speeds (7963.4 kg/h and 3528.9 kg/h, respectively). Both passive and transmission (^{137}Cs) measurements were conducted to correlate the signature peak areas with the UN solution concentration, density, and mass. In the dilution measurements, a pipe segment was fabricated based on the UNCLE specifications, where the detector response sensitivity was determined for assaying 185.7 keV emissions from ^{235}U, as well as the sensitivity of the 661.7 keV emission from ^{137}Cs as a transmission densitometry source. For all detectors, the 185.7 keV peak correlated with the UN concentration, whereas the 661.7 keV transmission source was very insensitive to changes in uranium concentration and solution density. Similarly, in the operational measurements in UNCLE at 90 g U/L, in varying pump flowrate speed from 1070 RPM to 500 RPM, each of the detectors was insensitive to flowrate. At each flowrate, the response was essentially unchanged, due to the detector seeing a full pipe of UN in its source-detector geometry, independent of pump speed.

From the experimental dilution measurements at 90 g U/L, the peak uncertainty for the detector measurements spans 0.20%–0.55%. In UNCLE, this uncertainty range translates to 11.6–31.4 MTU, which is in excess of the 10 MTU IAEA criterion. In addition, the dilution experiments demonstrated that it is statistically indiscernible to differentiate a concentration change of ~5 g U/L, especially in the case of low-resolution measurements, in the presence of high Compton continuum contributions, or the use of insensitive transmission sources such as ^{137}Cs. As the concentration changes from 90 g U/L to 85g U/L, the 185.7 keV peak area decreases only by 1.34%

At 90 g U/L, operational measurements in UNCLE were taken for 3600 s, with a conservative statistical uncertainty of 0.4% for the Inspector, 0.17% for the Osprey, and 0.22% for the Falcon detector, respectively. To measure 1 SQ in UNCLE, the overall uncertainty of the measurement must be below 0.17%. Consequently, optimized background shielding and increased counting time will enhance statistical confidence in gamma-ray spectroscopic data.

14.1.2 Simulation Conclusions

The relative insensitivity of ^{137}Cs to uranium content is supported by the convergence of the MAC at higher energies for UN. Lower energy densitometry sources, for instance ^{57}Co (122 keV) and ^{133}Ba (356 keV), were theorized to be better able to discriminate uranium content. In the absence of available ^{133}Ba and ^{57}Co sources, Monte Carlo models for the Falcon BEGe were constructed to determine the detector sensitivity to these transmission sources. Although ^{57}Co was most sensitive to uranium content at dilution concentrations, it may perhaps be too sensitive because of Compton continuum contributions from ^{235}U emissions between 140–205 keV, contributing higher peak area uncertainty in the 122 keV signature. In addition, from a practical standpoint, due to the short half-life of ^{57}Co and the low penetrability of 122 keV photons, a high intensity ^{57}Co source would be required and would need to be replaced often in an operational monitoring setting. Transmission densitometry employing ^{133}Ba 356 keV emissions were viable for discriminating among UN dilution concentrations, but were not as sensitive as ^{57}Co. Also, ^{133}Ba densitometry measurements using the 356 keV peak would prove problematic with low-resolution detectors, as ^{133}Ba has multiple lines that would interfere with the 185.7 keV signal unless high-resolution gamma spectroscopy was used.

Conversion activities occur in outdoor industrial-scale chemical plants with multiple transfer pipes and chemical storage tanks. The effect of these adjacent tanks and background measurements affects the peak area uncertainty, and hence the confidence of the assay peak area signatures. Sufficient shielding helps mitigate these background effects and must be considered in the installation of any radiation monitoring system in such facilities. In addition, peak area uncertainty due to Compton continuum from ^{137}Cs emissions during transmission measurements, as well as from higher-energy ^{238}U in secular equilibrium, increased the continuum, and consequently, the peak area uncertainty for the ^{235}U emissions in the 100–200 keV monitoring range. A dual detector option – a thin (planar) detector for the 185.7 keV and a large volume (coaxial) detector for the transmission measurement – could be possible, but would add to the cost and complexity for a field setting.

14.1.3 Sensitivity Analysis Conclusions

Efficiency values for each of the three COTS detectors were calculated for the 185.7 keV peak from a combination of measurement data, ISOCS models, and MCNPX simulations, all of which were in good agreement. Efficiency calibration is essential in determining the mass throughput of the UN based on gamma-ray detection. Characterization of each of the four variables ($\varepsilon_{geom} \cdot \varepsilon_{absp} \cdot \varepsilon_{sample} \cdot \varepsilon_{int}$) was conducted via a sensitivity analysis to determine the effect on the overall detection efficiency. The sensitivity analysis using ISOCS's Uncertainty Estimator provided an indication of how pipe thickness and source-detector distance and offset variables affected the overall efficiency for the modeled Falcon and Osprey detectors. The pipe thickness attenuation most affected the 185.7 keV signature peak efficiency by up to 8% for ±0.5 mm changes in Schedule 40 304L stainless steel piping employed in UNCLE. As a result, characterization of an empty pipe in the efficiency

calibration will provide essential information regarding control of this variable. In addition, empty pipe characterization provides one component to the calculation of the *CF(AT)* using Parker's method, to determine how the ε_{sample} affects the overall detection efficiency. Using Parker's method and a combination of experimental and Monte Carlo simulated data using the Falcon BEGe, a *CF(AT)* of 2.49 (ε_{sample} of 40.2±0.2%) and κ of ~0.75 was determined for self-attenuation effects.

14.1.4 Overall Detector Performance

In assessing overall performance, the three COTS detectors employed in this work are each potentially viable instruments for monitoring UN in NUCPs. Pending resolution and efficiency trade-offs, in addition to Compton continuum sensitivities, the COTs detectors are commercially available, economically competitive, and field portable. These detectors are also part of standard instrumentation employed by IAEA. Although the Falcon BEGe demonstrated best performance due to its superior resolution and portability (using a mechanically cooled system), the cost-effectiveness becomes prohibitive in the purview of budgetary considerations. Well-characterized lower resolution detectors, such as the Osprey and Inspector, may prove suitable. Recent advancements in software peak unfolding and attribution codes, such as those explored by the Advanced Synthetically Enhanced Detector Resolution Algorithm (ASEDRA) [91] and GAmma Detector Response and Analysis Software (GADRAS) [92] codes, show promise in robustly extracting signature information from low-resolution measurements. It is thus recommended that these options be explored in subsequent activities.

14.2 Conclusions Regarding IAEA Safeguards Requirements

In principle, NDA principles using passive gamma-ray detection are viable for process monitoring at NUCPs. Passive gamma-ray methods are difficult to spoof, inexpensive to employ using COTS instrumentation, and already exist as part of the IAEA standard complement of measurement techniques. Unlike precursor work, employing neutron detection does not meet performance specifications due to ^{3}He shortages in addition to the inability to distinguish (α,n) interactions in nitrogen and oxygen in the UN solution, and cosmic-ray induced spallation neutrons in an outdoor operational environment. The use of flowrate meters alone are also limited to determining mass balance, with little independent verification about the material content (concentration, enrichment) of the uranium in the NUCP. In addition, flowrate meters are also high in error, which would not meet the 1 SQ requirement for medium-to-large facilities > 100 MTU. The use of inline flowrate meters is politically not viable, as these have been construed by target nation states as invasive, unnecessary, and interruptive of NUCP operations for installation. Use of flowmeters and online uranium concentration monitors using gamma-ray detection, in tandem, has been explored where the combination of the two have successfully been developed for enrichment monitoring [93] [94]. These principles are directly applicable to NUCP monitoring.

Variation in uranium content – either concentration or enrichment – remains a challenge using stand-alone NDA methods. Without verifiable declarations or further data – i.e., density/densitometry, mass flowrate data, or ^{238}U signatures in secular equilibrium – interpretation of the 185.7 keV peak area alone is incomplete. However, the introduction of a transmission densitometry source does provide information regarding solution concentration, and analysis of the 185.7 keV ^{235}U high intensity emission provides information regarding uranium enrichment. Together, these two signatures provide invaluable information regarding the UN content, where stand-

alone neutron methods and independent flowrate analysis were unable to meet these performance specifications [6, 33, 34, 36-40, 42-45].

Although the IAEA requirement of 1 SQ (10 MTU) in a period of 1 year cannot be detected using stand-alone NDA measurements, consideration must be given to estimations of how 5 MTU is all that is required to produce 1 SQ of centrifuge material [32]. For NUCPs classified as S (~100 MTU/yr.), 1 SQ represents ~ 10% of the plant throughput. At these levels, it is possible to detect misuse. In current real-world facilities, NDA methods would be applicable to NUCPs such as those in Brazil and Argentina. However, considering the implementation of this criterion in such facilities as those in Canada – with throughput higher by levels of magnitude – diversion of 1 SQ becomes essentially undetectable given the systematic uncertainty. Given that the UNCLE facility is capable of circulating UN at the level of a large throughput facility, and given its extremely modest size, consideration must be given to how easily operational design (such as a diversion stream) can easily produce undeclared UN.

14.3 Future Work

Based on the technical and instrumentation conclusions of this study, further work is required in order for the IAEA to consider implementing the recommendations of PP18 and its anticipated successor Policy Paper 21. Employing NDA as part of a comprehensive safeguards approach for monitoring 34(C) materials in an NUCP is essential. Based on the instrumentation and methods employed in the scope of this work, the following approaches – both policy and technical – are proposed for continued development of a safeguards system for monitoring 34(C) materials in NUCPs.

14.3.1 Proposed Instrumentation Enhancements for NDA-Based Safeguards

The experimental design employed in the scope of this project was developed as a proof of principle to test the capabilities of passive gamma-ray detection. Translating this instrumentation into a full-scale field setting would benefit from instrumentation optimization.

- **In-field Efficiency Calibration:** Development of an in-field efficiency calibration either using ISOCS or calibration standards with an empty transfer pipe would provide essential information in translating detected counts to mass throughput of UN in NUCP transfer pipes. This can be employed using Parker's method (empirically calibrated), calibration standards, and/or commercially available software, such as ISOCS, to provide incremental correction factors for interpolation.

- **Transmission Source Collimation:** Due to limitations in source availability in the scope of this project, as well as limitations geometry optimization due to the contamination incident, employing a collimator with the transmission source would provide a uniform photon beam, bringing the source-detector geometry closer to a "good"/narrow-beam setup. In addition, testing ^{57}Co and/or ^{133}Ba would provide experimental validation of the simulation results regarding source sensitivity to uranium concentration. The source strength requires optimization, whereas the current experiment was limited by sources on hand.

- **Shielding Optimization:** Reduction of background – whether from environmental or adjacent pipes/tanks – is essential in providing an accurate measurement of UN. Although the detector shielding in the scope of this work was limited, and given the low-background environment for the dilution experiments, field tests of encased shielding would solve the twofold problem of background shielding, in addition to maintaining source-detector geometry placement to avoid detector displacement vis-à-vis the monitored pipe.

- **Flowrate Determination:** The use of inline flowmeters has been viewed as politically unfavorable, due to the invasiveness of installation in operational facilities. In addition, inline flowmeters also lack the ability to accurately determine the uranium content in the monitored UN. The use of a combination of active and passive gamma-ray methods could alleviate the reliance on external flowrate meters and provide information regarding flowrate. Use of two inline gamma-ray detectors using time-of-flight techniques could potentially provide information regarding flowrate. The first detector could employ a pulsed transmission source, such as a neutron-generating source, inducing neutron

activation. This first detector would both determine the UN concentration using transmission densitometry as well as activate nuclei in the UN to emit signature photons downstream. The second detector could detect the 185.7 keV signature peak, as well as the activated photons via prompt or delayed (n,γ) gamma rays. Neutron activation in nitric acid solvent or raffinate from nitrogen or oxygen signatures is also a potential avenue of activation analysis.

14.3.2 Future Work – IAEA-Level Strategic Approaches

Gamma-ray monitoring alone cannot provide a full safeguards solution, but is one component of a tiered approach. In conjunction with current IAEA practices, such as DIV, inspection, CS, and MC&A, the combined passive and active/transmission gamma-ray techniques can provide a PM tool for independently verifying operator declarations. Installation of such a system also acts as a deterrent, increasing the risk for potentially rogue states engaging in undeclared NUCP processing activities. Declarations and flowrate data further enhance the ability to draw safeguards conclusions regarding NUCP activities, where passive gamma-ray systems ensure material substitution or falsification of records is not occurring.

A 3D laser system from Zoller+Frolich (Z+F) Imager 5006i [95] has been preliminarily tested at the UNCLE facility to identify physical alterations (valve handles, equipment movement – depicted in Appendix C) and shows promise as a potential DIV tool for IAEA use in NUCPs as part of a comprehensive safeguards system [43]. In addition, environmental sampling and monitoring techniques have been proposed by Yoshida *et al.* for soil sampling outside conversion facilities [96] and by R. S. Kemp for monitoring aerosols produced by UF_6 released by NUCPs [97].

As the IAEA is preparing a policy paper to succeed PP18, entitled Policy Paper 21, "Determination of Materials Meeting the Conditions of Paragraph 34(c) of INFCIRC/153 (Corrected)" (not published), the following instrumentation and policy research directly links proposed work on the results of this dissertation with IAEA monitoring goals.

14.3.2.1 Strategic and Technical Implementation Challenges of Advancing Front-End IAEA Safeguards under Policy Paper 21

Technical and strategic implementation challenges, case studies, and state responses to these changes will be examined. This analysis extends into a comprehensive assessment of the motivations, impacts, and effectiveness of such safeguards efforts on the overall NPT regime.

Safeguarding nuclear material in the front end of the fuel cycle has only been implemented at the stage at which UF_6 was declared as feedstock for enrichment plants. Recent IAEA circulars and policy papers have sought to implement safeguards when any purified aqueous uranium solution or uranium oxides suitable for isotopic enrichment or fuel fabrication exist. Under Policy Paper 21 and its precursor – Policy Paper 18 – the IAEA suggests that these purified uranium compounds satisfy the criteria for safeguards under INFCIRC/153 Paragraph 34(c), and should be subject to safeguards procedures no later than the first point in the conversion process.

Consequently, Policy Paper 21 presents a plurality of strategic challenges in its technical, legal, and policy implementation. The proposed work will address how the evolution of technology (i.e., laser enrichment) redefines products meeting Paragraph 34(c) criteria, thus necessitating safeguards implementation prior to enrichment. As such, international safeguards agreements remain a highly negotiated political and legal dialogue between the IAEA and nation states, where the nuances of the implementation of Policy Paper 21 among states with and without the Additional Protocol (AP) in effect remain entirely unexplored. Introduction of new technology, such as discussed in this thesis, will likely require a joint development effort to ensure full transparency and acceptance.

The core policy questions in Policy Paper 21 must be addressed: With the evolution of new nuclear fuel cycle technology, what is the requirement for the Non-Proliferation Treaty (NPT) as a binding legal and policy agreement to evolve with these technology changes? How must the technology-policy nexus be bridged in the preview of technological progress? Finally, how must NGSI cohesively leverage its resources for technology, policy, and human capital development required of Policy Paper 21?

Technical and strategic implementation challenges, case studies, and state responses to Policy Paper 21 must be examined. This analysis extends into a comprehensive assessment of the motivations, impacts, and effectiveness of such safeguards efforts on the overall NPT regime. The recommendations made under Policy Paper 21 must further be extrapolated for states with Comprehensive Safeguards Agreements (CSA) in effect under INFCIRC/153, versus states with the AP in effect under INFCIRC/540. Furthermore, the *IAEA Regional Seminar on Good Practices in the Processing and Control of Uranium Ore Concentrate* in April 2012 highlighted the need to address

the role on export control verification in front-end activities, as no indication was given regarding any strategic approach to Policy Paper 21.

This approach to Policy Paper 21 will address technical, policy, and strategic implementation challenges associated with all stakeholders – IAEA, national authorities, and operators.

Resources have not yet been allocated for addressing the interplaying nexus of strategic issues regarding Policy Paper 21 from technical, policy, and legal perspectives, as they apply to operators, nation states, and the IAEA. Furthermore, despite previous periodic work, DOE must determine how to leverage its resources addressing the aforementioned challenges/stakeholders by producing a cohesive policy roadmap for these parallel activities. A cohesive strategy regarding the technology-policy nexus should be proposed as it pertains to all stakeholders under Policy Paper 21.

14.3.2.2 Development of a Statistical IAEA Safeguards Tool for Correlating Unique Front-End Process History Signatures Using Chemical Impurity and Isotopic Analysis

Process monitoring, verification, and ensuring the continuity of knowledge (CoK) of front-end fuel cycle activities for uranium ore concentrates (UOCs) in mining/milling and purified uranium compounds at NUCPs are a high priority for the IAEA but remain undeveloped in safeguards technology development and integration. From

priorities outlined in the *IAEA Department of Safeguards Long-Term R&D Plan 2012-2023* [98], front-end technologies, tools, and methods are needed to support such safeguards activities as Complementary Access under INFCIRC/540 (Corrected), [16] Policy Paper 21, and the Illicit Trafficking Database. Policy 21 suggests implementing safeguards when any purified aqueous uranium solution or uranium oxides exist, which are suitable for isotopic enrichment or fuel fabrication. Conversion facilities produce purified uranium solutions that should satisfy the criteria for safeguards, but are not yet monitored. With the discussion of advancing the starting point of safeguards earlier in the fuel cycle, as dictated in INFCIRC/153-34(c) [15], the IAEA has expressed a need to develop technologies and tools to address this safeguards challenge in Policy Paper 21.

Further investigation via this proposed follow-on project will do the following.

- 1. Determine unique radiological and chemical impurity signatures from samples spanning front-end fuel cycle products to statistically correlate identified signatures with material history and origin.
- 2. Produce an IAEA end-user tool that statistically correlates signatures from laboratory and in-field measurements to draw conclusions regarding material origin for verification and process monitoring.

The proposed work is aimed at delivering frontline safeguards relevance by ensuring CoK is maintained for verification of purified uranium compounds. To address this safeguards challenge, material signatures for uranium compounds must be identified in order to determine the unique isotopic and chemical impurity fingerprints that dictate the front-end production history (mining, milling, conversion). Isotopic and chemical impurity analysis of products (uranium ore, yellowcake, uranyl nitrate, conversion

precipitates, uranium oxides, UF_4, and UF_6) spanning front-end processes will provide benchmark data for statistical algorithm development. This follow-on work will produce an IAEA software tool based on (principal component) statistical analysis. This tool will be validated with samples of known origin and tested. This tool will enable the IAEA to populate a database of material signatures and draw decisive safeguards conclusions regarding material origin.

APPENDIX A. GLOBAL INFRASTRUCTURE INVENTORY OF CONVERSION FACILITIES

Table A-1. Status, Classification and Design Capacity of World Uranium Conversion Facilities.

Country	Facility Name	Fuel Type	Facility Status	Facility Type	Design Capacity (t HM/ yr.)
Argentina	Cordoba Conversion Facility	Conversion to UO_2	In Operation (1982)	Commercial	175
Argentina	Pilcaniyeu Conversion Facility	Conversion to UF_6	In Operation (1984)	Commercial	62
Brazil	BRW Conversion	Conversion to UF_6	Under Construction	Pilot plant	40
Brazil	IPEN – Conversion Unit	Conversion to UF_6	Shutdown	Pilot plant	90
Brazil	IPEN – U Reduction Unit	Conversion to U Metal	Shutdown	Pilot plant	30
Canada	Cameco – Blind River (UO_3)	Conversion to UO_3	In Operation	Commercial	18000
Canada	Cameco – Port Hope (U)	Conversion to U Metal	In Operation (1985)	Commercial	2000
Canada	Cameco – Port Hope (UF_6)	Conversion to UF_6	In Operation (1984)	Commercial	12500
Canada	Cameco – Port Hope (UO_2)	Conversion to UO_2	In Operation (1980)	Commercial	2800
China	Lanzhou	Conversion to UF_6	In Operation (1980)	Commercial	3000
Democratic People's Republic of Korea*	Nuclear Fuel Fabrication Plant	Conversion to U metal	Standby	-	-
France	Areva NC W Plant	Re-Conversion to U_3O_8 (Dep. U)	In operation	Commercial	14000
France	Comurhex II – Malvesi (UF_4)	Conversion to UF_4	Under Construction	Commercial	15000
France	Comurhex II – Pierrelatte (UF_6)	Conversion to UF_6	Under Construction	Commercial	15000
France	Comurhex Malvesi (UF_4)	Conversion to UF_4	In Operation (1959)	Commercial	14000

Country	Facility Name	Fuel Type	Facility Status	Facility Type	Design Capacity (t HM/ yr.)
France	Comurhex Pierrelatte (Rep. U)	Conversion to UF_6	Shutdown		350
France	Comurhex Pierrelatte (UF_6)	Conversion to UF_6	In Operation (1961)		14000
France	Ore Treatment Plant Geugnon	Conversion to U Metal	Decommissioned		450
France	Ore Treatment Plant Le Bouchet	Conversion to U Metal	Decommissioned		100
France	TU2 Cogema	Conversion to UO_2	Shutdown		350
France	URT II _ Pierrelatte (Rep. U)	Conversion to UF_6	Under Study Assessment	Commercial	1500
France	W Defluorinat (Depl. UF_6)	Conversion to U_3O_8 (Dep. U)	In Operation (1984)	Commercial	14000
India(*)	NFC (UOP) – Block A	Conversion to UO_2	In Operation (1972)	Commercial	450
Indonesia	Serpong Conversion Facility	Conversion to UO_2	Shutdown	Pilot plant	0.1
Iran(*,**)	Esfahan Uranium Conversion Facility	Conversion to UF_6	Pilot plant	-	200
Japan	Ningyo – Toge Ref. Conv. Plant (Dry Process)	Conversion to UF_6	Shutdown	Pilot plant	200
Japan	Ningyo – Toge Ref. Conv. Plant (Wet Process)	Conversion to UF_6	Shutdown	Pilot plant	0
Korea, Republic of	Uranium Conversion Facility	Conversion to UO_2	Decommissioning	Pilot plant	200

Country	Facility Name	Fuel Type	Facility Status	Facility Type	Design Capacity (t HM/ yr.)
Mexico	Uranium Concentrate Conversion to Refining Pilot Plant (PPRCU)	Conversion to UO_2	Decommissioned	Commercial	2.25
Pakistan	Islamabad	Conversion to UO_2	In Operation (1986)	Commercial	0
Russia	Angarsk	Conversion to UF_6	In Operation (1954)	Commercial	20000
Russia	Chepetski Machine Plant – Conversion	Conversion to UF_4	In Operation	Commercial	2000
Russia	Ekaterinburg (Sverdlovsk - 44)	Conversion to UF_6	In Operation (1949)	Commercial	4000
Russia	Tomsk – Siberian Chemical Combine (Seversk)	Conversion to UF_6	Shutdown	Commercial	10000
South Africa	Valindaba (UF_6)	Conversion to UF_6	Shutdown	Commercial	1400
Turkey	CNRC Nuclear Fuel Pilot Plant – Conversion	Conversion to UO_2	In Operation	Pilot plant	0.1
United Kingdom	NDA Conversion Plant	Conversion to U Metal	Standby	Commercial	4
United Kingdom	Springfields Enr. U. Residue Recovery Plant	Conversion to UO_2	In Operation (1985)	Commercial	65
United Kingdom	Springfields IDR Plant	Conversion to UO_2	Decommissioning	Commercial	500
United Kingdom	Springfields Line 2 Hex Plant	Conversion to UF_6	Decommissioned	Commercial	5500
United Kingdom	Springfields Line 3 Hex Plant	Conversion to UF_6	Decommissioned	Commercial	1200
United Kingdom	Springfields Line 4 Hex Plant	Conversion to UF_6	In Operation (1994)	Commercial	6000
United Kingdom	Springfields Main Line Chemical Plant	Conversion to UF_4	In Operation (1960)	Commercial	10000

Country	Facility Name	Fuel Type	Facility Status	Facility Type	Design Capacity (t HM/ yr.)
United Kingdom	Springfields OFC IDR UO_2 Line	Conversion to UO_2	In Operation (1995)	Commercial	550
United Kingdom	Springfields U Metal Plant	Conversion to U Metal	In Operation (1960)	Commercial	2000
USA	Gore	Conversion to UF_6	Decommissioning	Commercial	9090
USA	Hanford	Conversion to UO_3	Shutdown	Laboratory	0
USA	Metropolis Converdyn	Conversion to UF_6	In Operation (1959)	Commercial	17600
USA	Plant 7 (Hex Reduction Plant)	Conversion to UF_4	Decommissioned	Commercial	0
USA	Weldon Spring Site	Conversion to UO_2	Decommissioned	Commercial	0

KEY:

Non-Nuclear Weapons States (Non-AP Signatory)	Non-Nuclear Weapons State (AP Signatory)	Nuclear Weapons States (AP Signatory)	Nuclear Weapons States without Comprehensive Safeguards Agreements (Non-NPT Signatory)	States in Violation of INFCIRC/153

Data obtained from [3].

**AP signed, but not in force.*

***Updates to the NFCIS since 2012 no longer list these States.*

APPENDIX B. IAEA STANDING ADVISORY GROUP ON SAFEGUARDS IMPLEMENTATION ANALYSIS OF 34(C) IN THE FUEL CYCLE

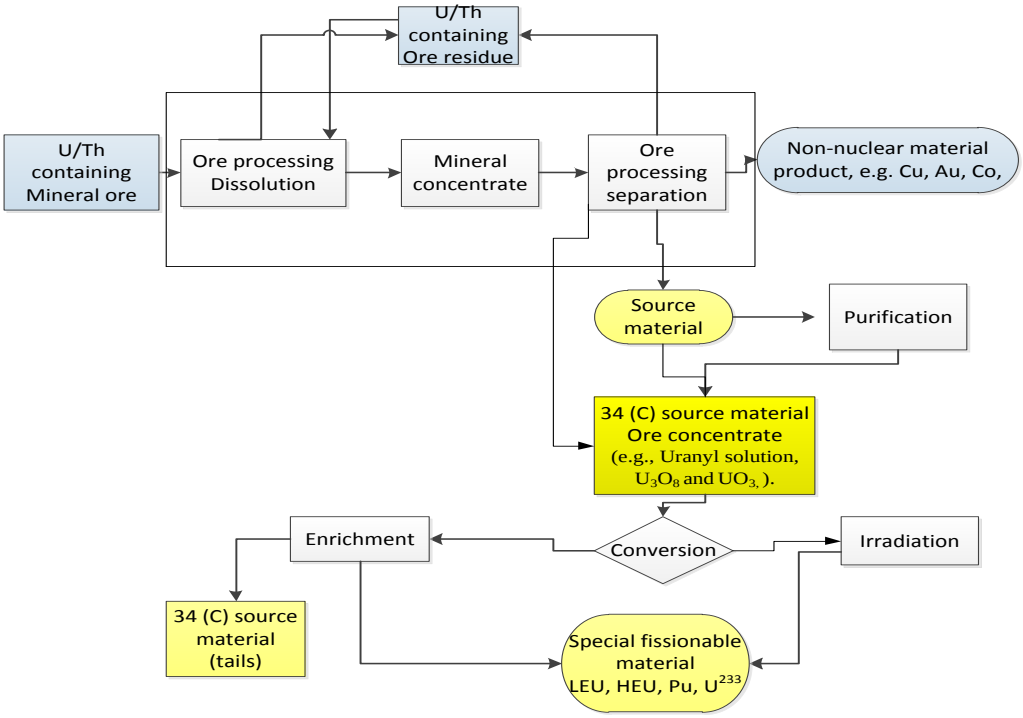

Figure B-1. SAGSI Assessment of Fuel Cycle Materials Meeting 34(C) Criteria.

Reproduced from [21].

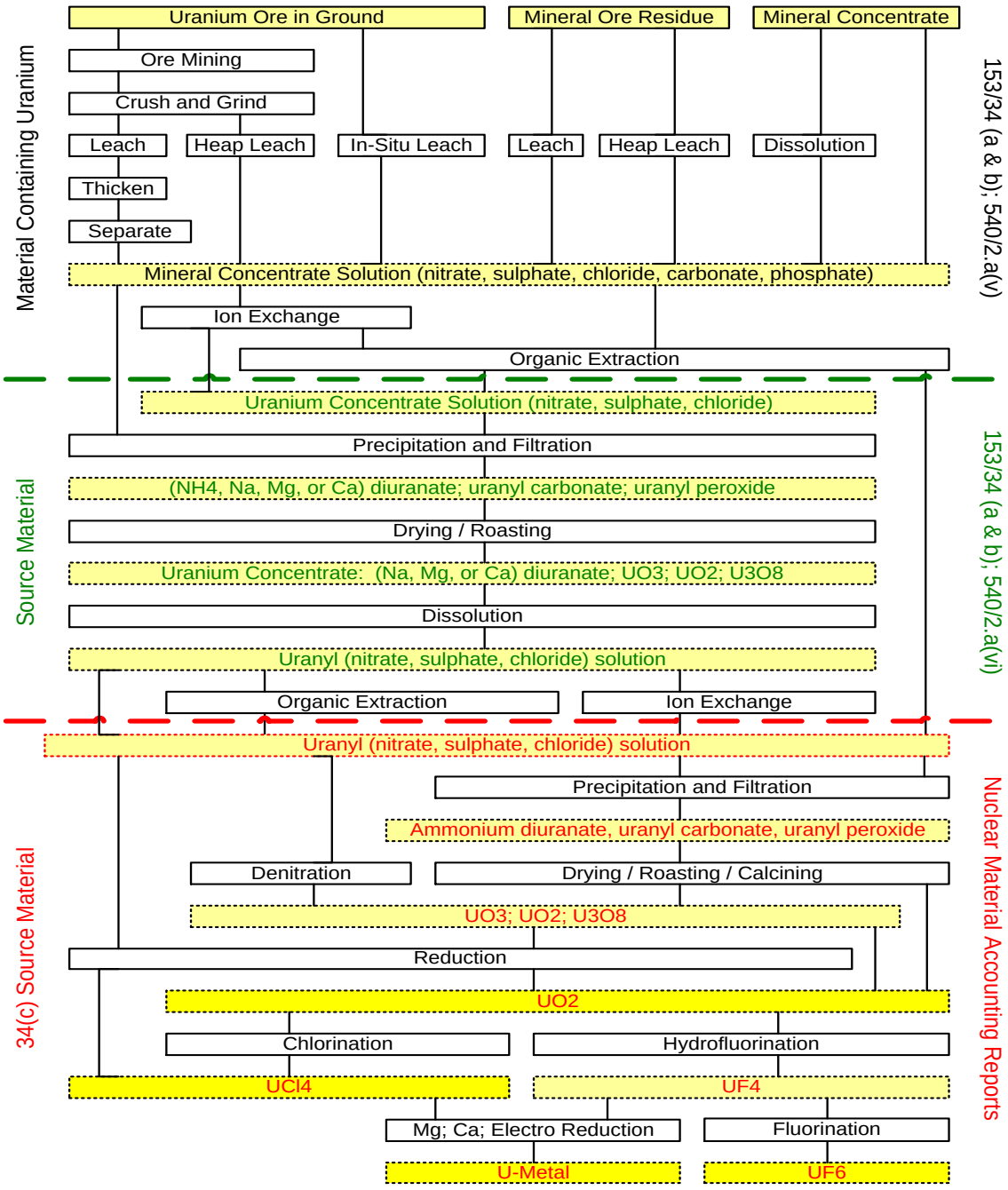

Figure B-2. SAGSI Assessment of 34(c) Materials in the Conversion Process.

Reproduced from [21].

APPENDIX C: UNCLE FACILITY AT ORNL

The Uranyl Nitrate Calibration Loop Equipment (UNCLE) facility was designed to provide a state-of-the-art test facility evaluating and testing safeguards instruments for application in a NUCP.

UNCLE consists of two 100-gal stainless steel tanks, with thermocouples and pressure transducers located at key points throughout the loop (pump inlet, pump outlet, and within the calibration area). UNCLE utilizes three computers: (1) standard PC for data acquisition of the temperatures and pressures; (2) standard PC for neutron detector data; and (3) MIL-SPEC computer running IAEA-standard Multi-Instrument Collect (MIC) software for the flowmeter providing mass and volumetric flow rates.

The piping in the main flow loop in the UNCLE facility consists of nominal 3-in. schedule 40 stainless steel pipe. One tank currently has approximately 90 gal of natural uranyl nitrate solution with a concentration of 90g U/L. The second tank is currently empty but has been used in the past for leak checking with water.

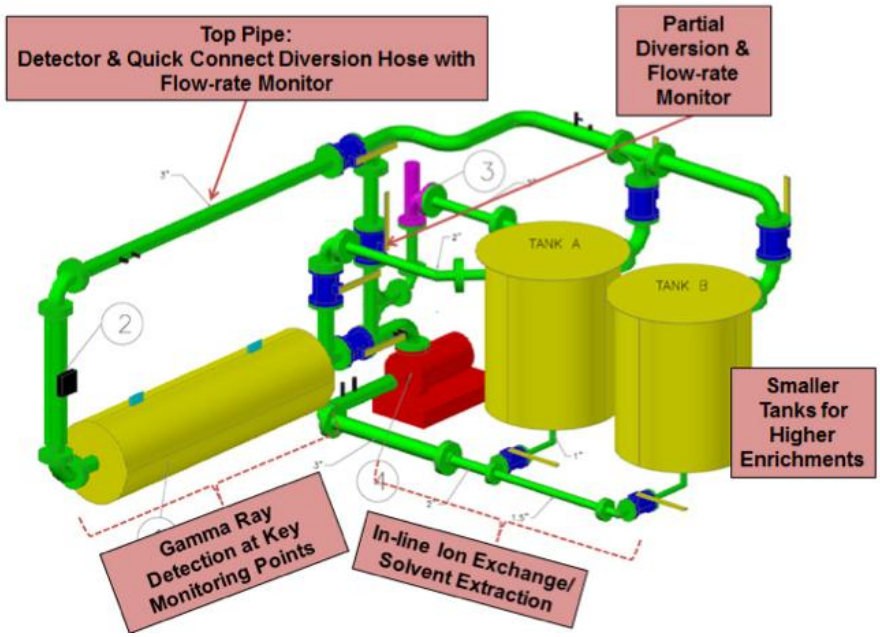

Figure C-1. UNCLE Facility Schematic at ORNL.

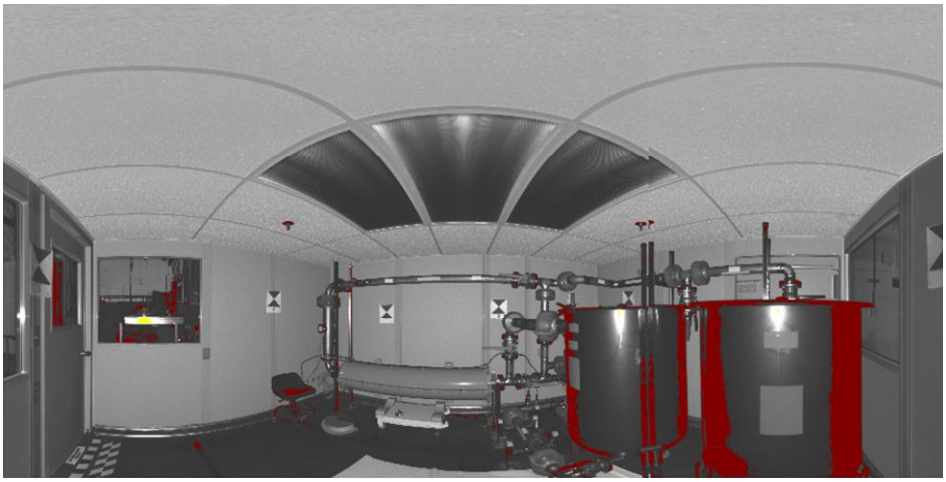

Figure C-2. Two-Dimensional Image of UNCLE Facility.

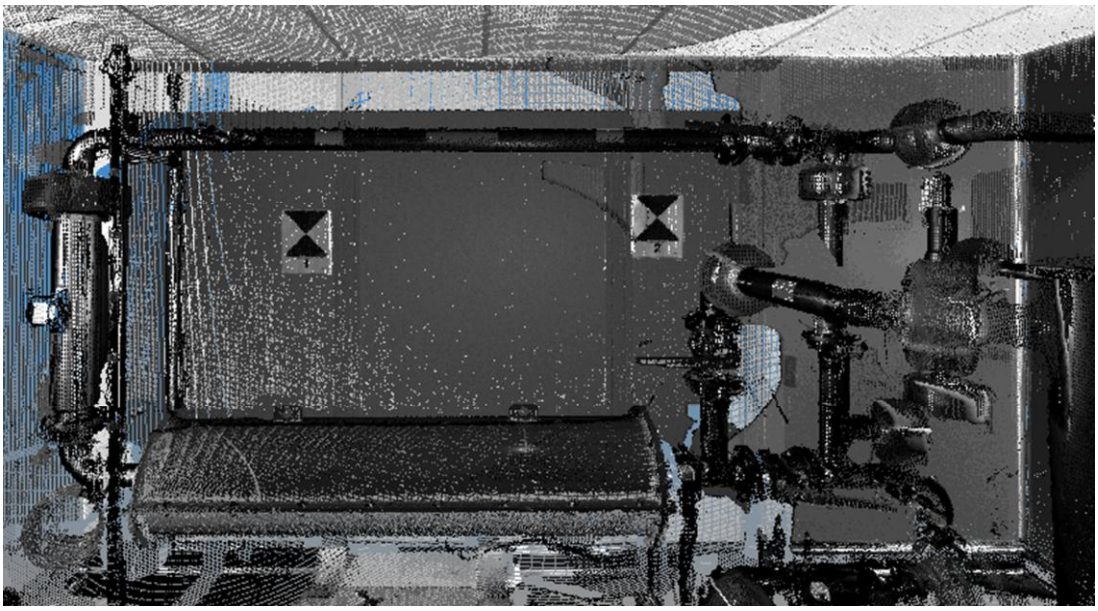

Figure C-3. 3-D Image Taken with Overview of the Z+F Imager 5006i.

APPENDIX D: MASS ATTENUATION COEFFICIENT GRAPHS

Table D-1. Infinite Thickness Values for External Transmission Source Gamma -Ray Emissions at Dilution Concentrations of UN.

	Infinite Thickness (cm)					
Energy (keV)	**90g U/L**	**85g U/L**	**75g U/L**	**50(g U/L**	**10g U/L**	**0g U/L**
122.1	13.20	13.75	14.99	19.25	35.45	44.64
356.0	48.55	49.16	50.55	54.33	61.51	63.23
661.7	70.78	71.32	72.54	75.52	80.80	81.75

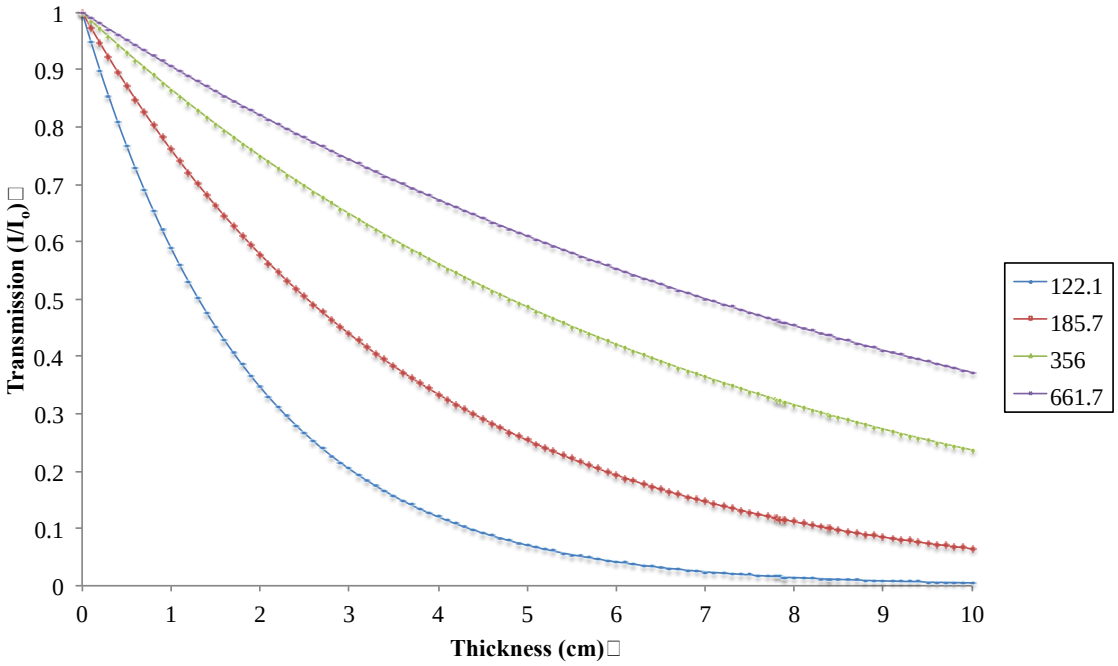

Figure D-1. Gamma-Ray Transmission through Uranyl Nitrate Solution at 90 g U/L at Various Energies.

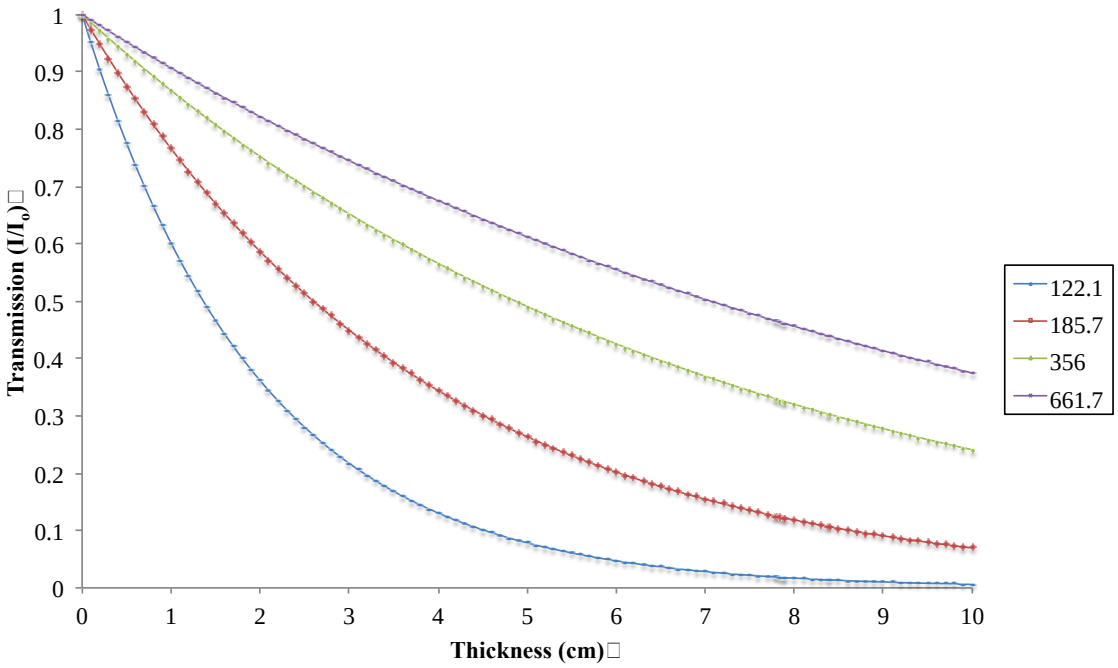

Figure D-2. Gamma Ray Transmission through Uranyl Nitrate Solution at 85 g U/L at Various Energies.

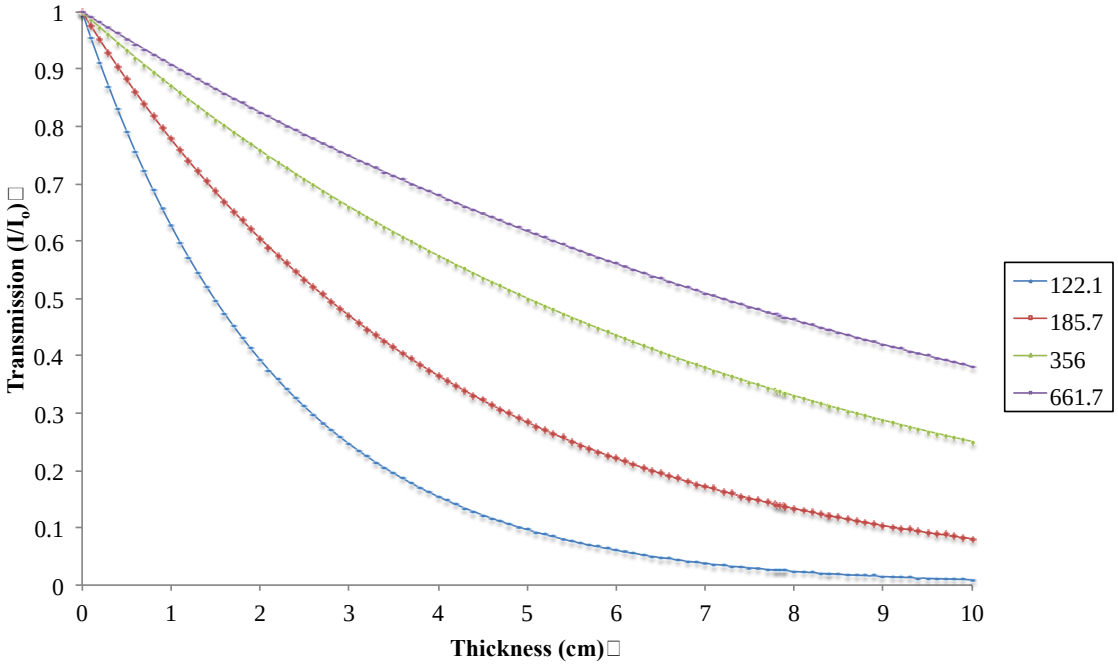

Figure D-3. Gamma Ray Transmission through Uranyl Nitrate Solution at 75 g U/L at Various Energies.

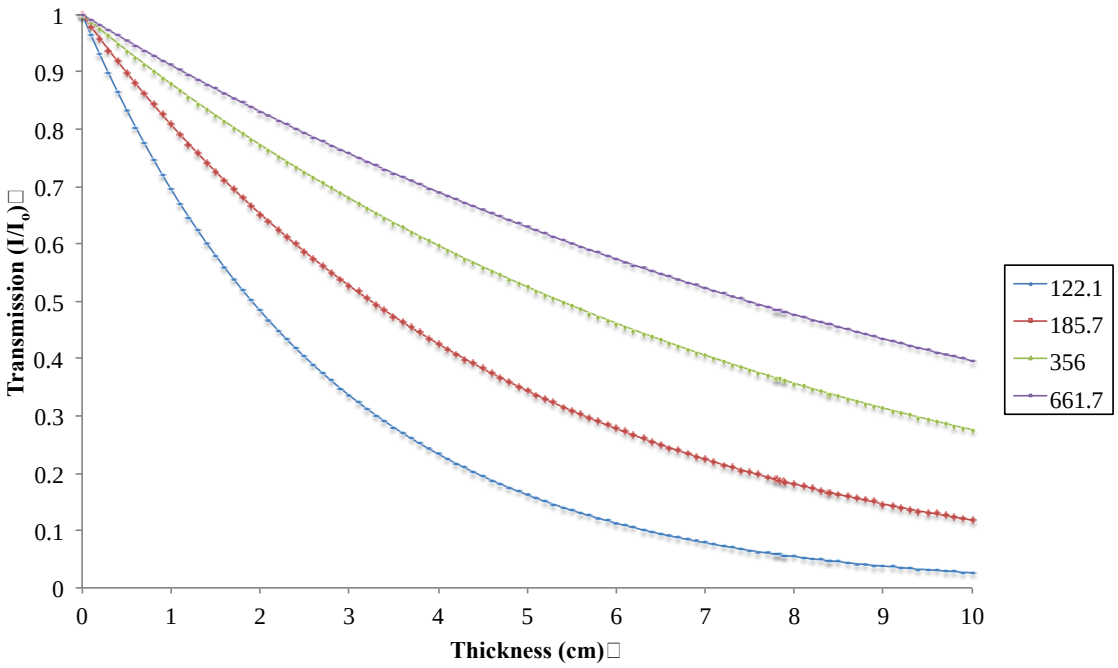

Figure D-4. Gamma-Ray Transmission through Uranyl Nitrate Solution at 50 g U/L at Various Energies.

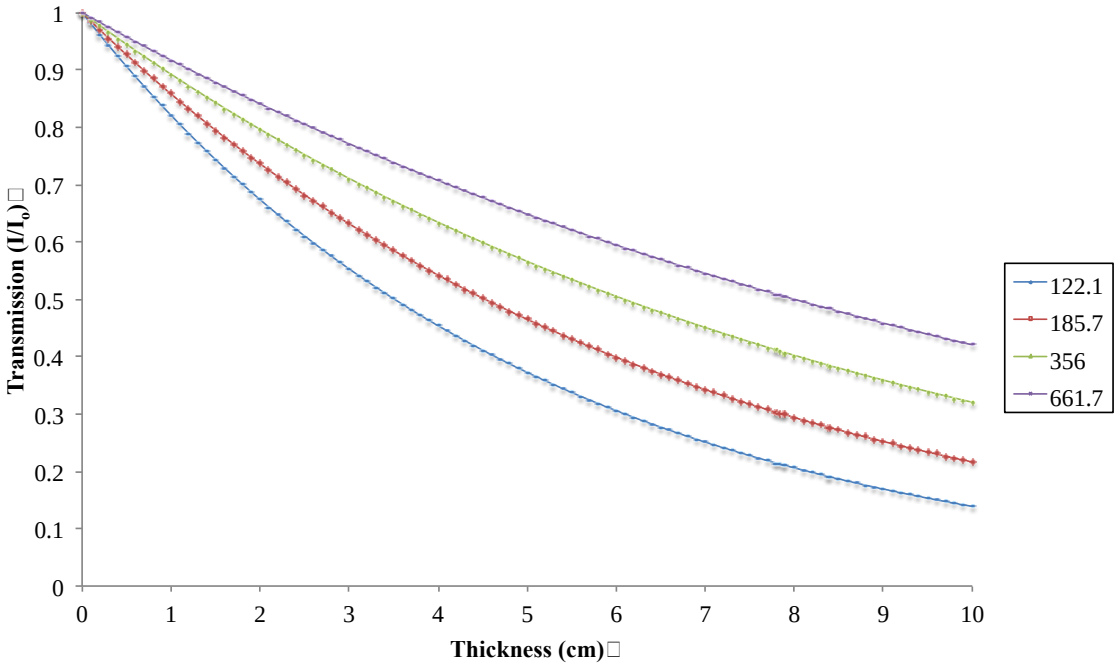

Figure D-5. Gamma-Ray Transmission through Uranyl Nitrate Solution at 10 g U/L at Various Energies.

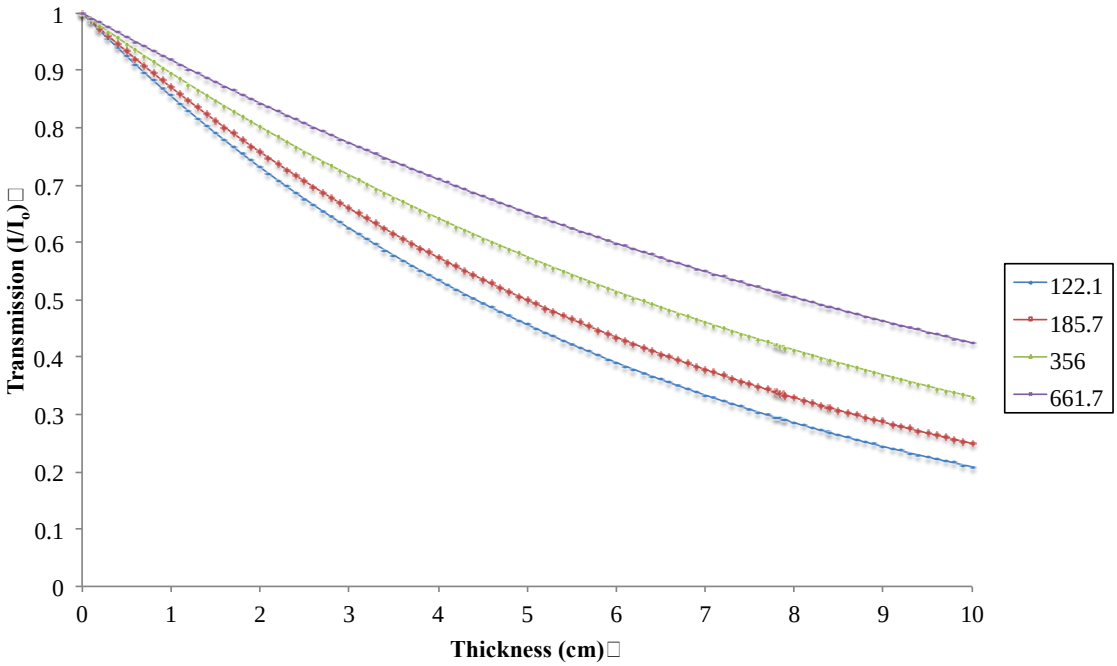

Figure D-6. Gamma-Ray Transmission through Uranyl Nitrate Solution at 0 g U/L (pure NO_3 + H_2O) at Various Energies.

APPENDIX E: MCNP INPUT FILES

MCNP Sample Input – Passive at 90g U/L

```
C NUCP MCNPX Models  (UNCLE system)
c 90g/L  - F8 Tally
c            Shaheen Dewji
c
c
c
c  Cells
c
c  101     3 -0.001293 -101 102    imp:p=1 $ Tally Surface
102     1  -7.92    -102 103        imp:p=1 $ SS Tube
103     2  -1.122   -103           imp:p=1 $ U Nitrate
104     6 -1.03 -107               imp:p=1 $Epoxy Lid
106     3  -0.001293  -108 104  imp:p=1 $ Air btn col detector
105     9 -2.7 -104 134          imp:p=1 $ Detector Al Endcap
107     5  -11.0  104 108 -135 imp:p=1 $ Cu col detector
108    5  -11.0  135 -125  imp:p=1 $ Tin col detector
109     5 -11.0  125 -105       imp:p=1 $ W Collimator
111     0 -134 124   imp:p=1 $ Detector Vacuum
110    10 -5.3234 -124 imp:p=1 $ Ge Crystal
112     4 -11.34  -106       imp:p=1 $ Pb Shield Bottom Brick
113     4 -11.34  -109       imp:p=1 $ Pb Shield Top Brick
114     4 -11.34  -110       imp:p=1 $ Pb Shield Right Brick
115     4 -11.34  -111       imp:p=1 $ Pb Shield Left Brick
116     4 -11.34  -113       imp:p=1 $ Pb Backshield
c 900     0  -999 102 105 106 107 109  110 111 113 imp:p=1 $ Environment Shell
900     3 -0.001293  -999 102 105 107 106 109 110 111 113 imp:p=1 $ Environment Shell
999     0             999          imp:p=0 $ Void
c
c

c
c   Surface
c 101  1 rcc 0    0   -0.635    0   0   63.6524    4.51325 $ Tally Box
102   1 rcc  0    0   -0.635    0   0   63.6524    4.44 $ SS Tube
103   1 rcc  0    0    0        0   0   60.2742    3.92   $ UN
124   1 rcc -8.275 0    31.8262 -2.0 0   0          2.985 $ Ge crystal
134   1 rcc -6.905 0    31.8262 -4.1 0   0          3.95 $ vacuum
104   1 rcc -6.785 0    31.8262 -4.3 0   0   4.1 $ Detector Endcap .12cm thick
108   1 rcc -5.235 0    31.8262 -5.85 0  0   5.7     $ Air around detector
105   1 rcc -5.235 0    31.8262 -15  0   0   6.5    $ W Collimator
125   1 rcc  -5.235 0    31.8262 -15  0  0  6.0    $ Sn Collimator
135   1 rcc  -5.235 0    31.8262 -15  0  0  5.9    $ Cu Collimator
107   1 rcc -5.075 0    31.8262 -0.16  0 0 6.5    $ Epoxy Front Lid
106   1 rpp -15.075 -5.075 -10.15 10.15 16.6762 21.6762    $ Pb Shield Bottom Brick
109   1 rpp -10.075 -5.075 -10.15 10.15 41.9762 51.9762 $ Pb Shield Top Brick
110   1 rpp -10.075 -5.075 6.51 16.51 21.6763 41.9761 $ Pb Shield Right Brick
111   1 rpp -10.075 -5.075 -16.51 -6.51 21.6763 41.9761 $ Pb Shield Left Brick
113   1 rpp 4.7002 9.7002 -10.15 10.15  26.8262 36.8262 $Backshield
999   1 rcc  0    0   -75       0   0   200        50      $ Void Cylinder
c

c
c
c   ***  MATERIAL CARDS  ***
c   ------------------------
```

```
c
c     Material 1, Stainless Steel 304L      (-7.92)
m1    26000.          0.05936  $MAT4
      24000.          0.01743 28000.          0.00772 25055.          0.00174
c
c     Material 2,  Uranium nitrate solution.  Mostly water.
c     From UNCLE description
c     90 grams Uranium / 1000 mL H2O  (-1.122)
m2    92238. -0.0796   $MAT8
      92235. -0.00061
      92234. -0.000005
      8000. -0.815185
      1000. -0.097521
      7000. -0.007080
c
c     Material 3, Air
m3    8016.           -0.2314
     7014.           -0.7558 18000.          -0.0128
c
c     Material 4, Pb
m4 82000. -1
c     Material 5, Collimator (density 11g/cc)
m5 74000. -0.98 6000 -0.0171 1000 -0.0029
c
c     Material 6, Epoxy (density 1.07g/cc)
m6 1000 -0.06 6000 -0.721 8000 -0.219
c     Material 7, Copper
m7 29000 -1
c     Material 8, Tin
m8 50000 -1
c     Material 9, Al
m9 13000 -1
c     Material 10, HPGe
m10   32000.04p 1 $HPGe
c
c Data Cards
c
c
c   ***  TRANSFORMATION  ***
c   ------------------------
tr1  0 0 0
c
c
c   ***  SOURCE DEF  ***
c   --------------------
c     Cell source of Uranium dissolved in water,
c     spontaneous fission spectrum, U-238
c     cylindrical source centered in solution pipe
sdef PAR=2  POS=0 0 0   AXS=0 0 1  RAD=d1   EXT=d2  ERG=d3 CEL=103
si1    3.92
sp1  -21  1                    $Radial sampling
si2   60.2742
sp2  -21  0                    $Vertical cylinder sampling
C RadSource Run: Tue May 15 13:33:13 2012
C
C Input Isotopes
C U-234  0.01%
C U-235  0.76%
C U-238  99.23%
C
C Total: 100%
```

```
C
C Age: 0 s, 0 yrs
C ========================================================
C  1    DISCRETE GAMMA LINE energies (MeV)
SI3 L 0.0316 0.0347 0.0414 0.04195 0.05122 0.0541 0.05425 0.06437 0.0727 &
0.07372 0.0748 0.09609 0.10916 0.11545 0.12035 0.13655 0.14076 0.1424 &
0.143764 0.15093 0.163358 0.1733 0.18252 0.185712 0.19494 0.198928 &
0.1996 0.202111 0.205309 0.21528 0.221399 0.228785 0.233469 0.240875 &
0.24684 0.2515 0.26645 0.275129 0.275428 0.2795 0.281441 0.28292 0.28956 &
0.29165 0.2943 0.301741 0.31069 0.317062 0.3258 0.3435 0.3454 0.3459 &
0.35603 0.3685 0.3718 0.38782 0.3903 0.41029 0.433 0.4484 0.4551 &
0.5172 0.7425 0.7947
C
C  1    ASSOCIATED photon intensities :
SP3 D 0.00016 0.00037 0.0003 0.0006 0.0002 0.0003 0.0003 0.0001 &
0.0011 0.0001 0.0006 0.00086 0.0154 0.0007 0.00026 0.00012 0.0022 &
0.00005 0.1096 0.00076 0.0508 0.0001 0.0034 0.572 0.0063 0.00042 &
0.001 0.0108 0.0501 0.00027 0.0012 0.00008 0.00029 0.00075 0.00053 &
0.0004 0.00006 0.00042 0.00007 0.0027 0.00006 0.00005 0.00007 0.00038 &
0.00033 0.00005 0.00004 0.00001 0.000004 0.00003 0.0007 0.00038 0.00005 &
0.0007 0.0007 0.00038 0.0004 0.00003 0.00004 0.00001 0.00008 0.000004 &
0.000004 0.000006
c   ---------------------
c   ***  TALLY CARDS  ***
c   ---------------------
C Summed Tally
C
F8:P 110
FC8 Tally No GEB
C
C
F18:P 110
FC18 Tally With GEB
FT18 GEB 0.000594701 0.000763331 0.85487
C
C Energy Bins
C
E0 0 1e-8 .0000194 8190i 1.5925365 $8192 bins
PHYS:P 4J 1
MODE P
print
nps 1e8
```

MCNP Sample Input – ^{137}Cs Transmission at 85g U/L
Note: ^{57}Co and ^{133}Ba SDEF are provided as comments

```
C NUCP MCNPX Models  (UNCLE system)
c 85g/L 137Cs Transmission
c            Shaheen Dewji, MARCH 2013
c
c
c
c  Cells
c
c  101     3 -0.001293 -101 102    imp:p=1 $ Tally Surface
102     1  -7.92    -102 103        imp:p=1 $ SS Tube
103     2 -1.115    -103           imp:p=1 $ U Nitrate
104     6 -1.03 -107               imp:p=1 $Epoxy Lid
106     3  -0.001293  -108 104  imp:p=1 $ Air btn col detector
105     9 -2.7 -104 134          imp:p=1 $ Detector Al Endcap
107     5  -11.0  104 108 -135 imp:p=1 $ Cu col detector
108    5  -11.0  135 -125  imp:p=1 $ Tin col detector
109     5 -11.0  125 -105      imp:p=1 $ W Collimator
111     0 -134 124   imp:p=1 $ Detector Vacuum
110    10 -5.3234 -124 imp:p=1 $ Ge Crystal
112     4 -11.34  -106       imp:p=1 $ Pb Shield Bottom Brick
113     4 -11.34  -109       imp:p=1 $ Pb Shield Top Brick
114     4 -11.34  -110       imp:p=1 $ Pb Shield Right Brick
115     4 -11.34  -111       imp:p=1 $ Pb Shield Left Brick
116     4 -11.34  -113       imp:p=1 $ Pb Backshield
122     7 -1.00 -152 imp:p=1 $ Source
c 900     0  -999 102 105 106 107 109  110 111 113 152 imp:p=1 $ Environment Shell
900     3 -0.001293  -999 102 105 107 106 109 110 111 113 152 imp:p=1 $ Environment Shell
999     0             999          imp:p=0 $ Void
c
c

c
c   Surface
c 101  1 rcc 0    0   -0.635    0   0   63.6524    4.51325 $ Tally Box
102   1 rcc  0    0   -0.635    0   0   63.6524    4.44 $ SS Tube
103   1 rcc  0    0    0        0   0   60.2742    3.92   $ UN
124   1 rcc -8.275 0    31.8262 -2.0 0   0          2.985 $ Ge crystal
134   1 rcc -6.905 0    31.8262 -4.1 0   0          3.95 $ vacuum
104   1 rcc -6.785 0    31.8262 -4.3 0   0   4.1 $ Detector Endcap .12cm thick
108   1 rcc -5.235 0    31.8262 -5.85 0  0   5.7     $ Air around detector
105   1 rcc -5.235 0    31.8262 -15  0   0   6.5    $ W Collimator
125   1 rcc  -5.235 0    31.8262 -15  0  0  6.0    $ Sn Collimator
135   1 rcc  -5.235 0    31.8262 -15  0  0  5.9    $ Cu Collimator
107   1 rcc -5.075 0    31.8262 -0.16  0 0 6.5    $ Epoxy Front Lid
106   1 rpp -15.075 -5.075 -10.15 10.15 16.6762 21.6762    $ Pb Shield Bottom Brick
109   1 rpp -10.075 -5.075 -10.15 10.15 41.9762 51.9762 $ Pb Shield Top Brick
110   1 rpp -10.075 -5.075 6.51 16.51 21.6763 41.9761 $ Pb Shield Right Brick
111   1 rpp -10.075 -5.075 -16.51 -6.51 21.6763 41.9761 $ Pb Shield Left Brick
113   1 rpp 4.7002 9.7002 -10.15 10.15  26.8262 36.8262 $Backshield
152   1 rcc 4.5001 0 31.8262 0.2 0 0 1 $Source
999   1 rcc  0    0   -75       0   0   200        50      $ Void Cylinder
c

c
c
c   ***  MATERIAL CARDS  ***
c   ------------------------
c
```

```
c     Material 1, Stainless Steel 304L      (-7.92)
m1    26000.          0.05936  $MAT4
      24000.          0.01743 28000.          0.00772 25055.          0.00174
c
c     Material 2,  Uranium nitrate solution 85gU/L.  Mostly water.
c     From UNCLE description
c     85 grams Uranium / 1000 mL H2O  (-1.115)
m2    92238. -0.0795649   $MAT8
      92235. -0.000579
      92234. -0.000004
      8000. -0.818842
      1000. -0.098196
      7000. -0.006729
c
c     Material 3, Air
m3    8016.           -0.2314
     7014.           -0.7558 18000.          -0.0128
c
c     Material 4, Pb
m4 82000. -1
c     Material 5, Collimator (density 11g/cc)
m5 74000. -0.98 6000 -0.0171 1000 -0.0029
c
c     Material 6, Epoxy (density 1.07g/cc)
m6 1000 -0.06 6000 -0.721 8000 -0.219
c
c     Material 7, Polyester for Source (density 1.0g/cc)
m7 6000 0.333 1000 0.533 8000 0.133
c     Material 8, Tin
m8 50000 -1
c     Material 9, Al
m9 13000 -1
c     Material 10, HPGe
m10   32000.04p 1 $HPGe
c
c Data Cards
c
c
c   ***  TRANSFORMATION  ***
c   ------------------------
tr1  0 0 0
c
c
c   ***  SOURCE DEF  ***
c   --------------------
c     Cell source of Uranium dissolved in water,
c     spontaneous fission spectrum, U-238
c     cylindrical source centered in solution pipe
sdef PAR=2 CEL=d1 POS=FCEL d2 RAD=FCEL d5 AXS=FCEL d8 EXT=FCEL d11 ERG=FCEL d20
c
SI1 L 103 122 $ Cells to sample from S1 - UN and S2
SP1 D 1 1 $ 50% from each
c
c set POS for each source
c
DS2 L 0 0 0  4.5001 0 31.8262
C SP3 1
C SP4 1
c
c set RAD for each source
c
```

```
DS5 S 6 7
SI6 3.92
SP6 -21 1
SI7 1.0
SP7 -21 0
c
c set AXS for each source
c
DS8 L 0 0 1  1 0 0
c
c set EXT for each source
c
DS11 s 12 13
SI12  0 60.2742
SP12  -21  0                    $Vertical cylinder sampling
SI13 0 0.2
SP13 -21 0
c
c set ERG for each source
c
DS20 S 21 22
SI21    L 0.0316 0.0347 0.0414 0.04195 0.05122 0.0541 0.05425 0.06437 0.0727 &
0.07372 0.0748 0.09609 0.10916 0.11545 0.12035 0.13655 0.14076 0.1424 &
0.143764 0.15093 0.163358 0.1733 0.18252 0.185712 0.19494 0.198928 &
0.1996 0.202111 0.205309 0.21528 0.221399 0.228785 0.233469 0.240875 &
0.24684 0.2515 0.26645 0.275129 0.275428 0.2795 0.281441 0.28292 0.28956 &
0.29165 0.2943 0.301741 0.31069 0.317062 0.3258 0.3435 0.3454 0.3459 &
0.35603 0.3685 0.3718 0.38782 0.3903 0.41029 0.433 0.4484 0.4551 &
0.5172 0.7425 0.7947
C
C  1    ASSOCIATED photon intensities
SP21    D 0.00016 0.00037 0.0003 0.0006 0.0002 0.0003 0.0003 0.0001 &
0.0011 0.0001 0.0006 0.00086 0.0154 0.0007 0.00026 0.00012 0.0022 &
0.00005 0.1096 0.00076 0.0508 0.0001 0.0034 0.572 0.0063 0.00042 &
0.001 0.0108 0.0501 0.00027 0.0012 0.00008 0.00029 0.00075 0.00053 &
0.0004 0.00006 0.00042 0.00007 0.0027 0.00006 0.00005 0.00007 0.00038 &
0.00033 0.00005 0.00004 0.00001 0.000004 0.00003 0.0007 0.00038 0.00005 &
0.0007 0.0007 0.00038 0.0004 0.00003 0.00004 0.00001 0.00008 0.000004 &
0.000004 0.000006
C Cs137 Source
SI22 L 0.6617
SP22 D 0.851
C Co57 Source
C SI22 L 0.0144 0.122 0.1364743
C SP22 D 0.0916 0.856 0.1068
C Ba133 Source
C SI22 L 0.0306252 0.0309727 0.034987 0.0809969 0.276397 0.302851 &
C       0.356005 0.383851
C SP22 D  0.341219 0.63072 0.121729 0.337528 0.070851 0.183964 &
C      0.6215 0.0891231
c   ----------------------
c   ***  TALLY CARDS  ***
c   ----------------------
C Summed Tally
C
F8:P 110
FC8 Tally No GEB
C
C
F18:P 110
FC18 Tally With GEB
```

```
FT18 SCD GEB 0.000594701 0.000763331 0.85487
FU18 21 22
C
C Energy Bins
C
E0 0 1e-8 .0000194 8190i 1.5925365 $8192 bins
PHYS:P 4J 1
MODE P
print
nps 1e8
```

MCNP Sample Input – Enrichment at 90g U/L / 5% ^{235}U Enrichment

```
C NUCP MCNPX Models  (UNCLE system)
c 90g/L  - F8 Tally      5% Enrichment
c             Shaheen Dewji, MARCH 2012
c
c
c
c  Cells
c
c  101     3 -0.001293 -101 102    imp:p=1 $ Tally Surface
102     1  -7.92    -102 103        imp:p=1 $ SS Tube
103     2  -1.122   -103           imp:p=1 $ U Nitrate
104     6 -1.03 -107              imp:p=1 $Epoxy Lid
106     3  -0.001293  -108 104  imp:p=1 $ Air btn col detector
105     9 -2.7 -104 134          imp:p=1 $ Detector Al Endcap
107     5  -11.0  104 108 -135 imp:p=1 $ Cu col detector
108    5  -11.0  135 -125  imp:p=1 $ Tin col detector
109     5 -11.0  125 -105      imp:p=1 $ W Collimator
111     0 -134 124   imp:p=1 $ Detector Vacuum
110    10 -5.3234 -124 imp:p=1 $ Ge Crystal
112     4 -11.34  -106       imp:p=1 $ Pb Shield Bottom Brick
113     4 -11.34  -109       imp:p=1 $ Pb Shield Top Brick
114     4 -11.34  -110       imp:p=1 $ Pb Shield Right Brick
115     4 -11.34  -111       imp:p=1 $ Pb Shield Left Brick
116     4 -11.34  -113       imp:p=1 $ Pb Backshield
c 900     0  -999 102 105 106 107 109  110 111 113 imp:p=1 $ Environment Shell
900     3 -0.001293  -999 102 105 107 106 109 110 111 113 imp:p=1 $ Environment Shell
999     0             999          imp:p=0 $ Void
c
c

c
c   Surface
c 101  1 rcc 0    0   -0.635    0   0   63.6524    4.51325 $ Tally Box
102   1 rcc  0    0   -0.635    0   0   63.6524    4.44 $ SS Tube
103   1 rcc  0    0    0        0   0   60.2742    3.92   $ UN
124   1 rcc -8.275 0    31.8262 -2.0 0   0          2.985 $ Ge crystal
134   1 rcc -6.905 0    31.8262 -4.1 0   0          3.95 $ vacuum
104   1 rcc -6.785 0    31.8262 -4.3 0   0   4.1 $ Detector Endcap .12cm thick
108   1 rcc -5.235 0    31.8262 -5.85 0  0   5.7     $ Air around detector
105   1 rcc -5.235 0    31.8262 -15  0   0   6.5    $ W Collimator
125   1 rcc  -5.235 0    31.8262 -15  0  0  6.0    $ Sn Collimator
135   1 rcc  -5.235 0    31.8262 -15  0  0  5.9    $ Cu Collimator
107   1 rcc -5.075 0    31.8262 -0.16  0 0 6.5    $ Epoxy Front Lid
106   1 rpp -15.075 -5.075 -10.15 10.15 16.6762 21.6762    $ Pb Shield Bottom Brick
109   1 rpp -10.075 -5.075 -10.15 10.15 41.9762 51.9762 $ Pb Shield Top Brick
110   1 rpp -10.075 -5.075 6.51 16.51 21.6763 41.9761 $ Pb Shield Right Brick
111   1 rpp -10.075 -5.075 -16.51 -6.51 21.6763 41.9761 $ Pb Shield Left Brick
113   1 rpp 4.7002 9.7002 -10.15 10.15  26.8262 36.8262 $Backshield
999   1 rcc  0    0   -75       0   0   200        50      $ Void Cylinder
c

c
c
c   ***  MATERIAL CARDS  ***
c   ------------------------
c
c     Material 1, Stainless Steel 304L      (-7.92)
m1    26000.          0.05936  $MAT4
      24000.          0.01743 28000.          0.00772 25055.          0.00174
```

```
c
c     Material 2,  Uranium nitrate solution.  Mostly water.
c     From UNCLE description        5% Enriched
c     90 grams Uranium / 1000 mL H2O  (-1.122)
m2    92238. -0.076199   $MAT8
      92235. -0.004011
      92234. -0.000005
      8000. -0.815185
      1000. -0.097521
      7000. -0.007080
c
c     Material 3, Air
m3    8016.          -0.2314
     7014.          -0.7558 18000.          -0.0128
c
c     Material 4, Pb
m4 82000. -1
c     Material 5, Collimator (density 11g/cc)
m5 74000. -0.98 6000 -0.0171 1000 -0.0029
c
c     Material 6, Epoxy (density 1.07g/cc)
m6 1000 -0.06 6000 -0.721 8000 -0.219
c     Material 7, Copper
m7 29000 -1
c     Material 8, Tin
m8 50000 -1
c     Material 9, Al
m9 13000 -1
c     Material 10, HPGe
m10   32000.04p 1 $HPGe
c
c Data Cards
c
c
c   ***  TRANSFORMATION  ***
c   -------------------------
tr1  0 0 0
c
c
c   ***  SOURCE DEF  ***
c   --------------------
c     Cell source of Uranium dissolved in water,
c     spontaneous fission spectrum, U-238
c     cylindrical source centered in solution pipe
sdef PAR=2  POS=0 0 0   AXS=0 0 1  RAD=d1   EXT=d2  ERG=d3 CEL=103
si1    3.92
sp1  -21  1                    $Radial sampling
si2   60.2742
sp2  -21  0                    $Vertical cylinder sampling
C ========================================================
C  1    DISCRETE GAMMA LINE energies (MeV)
SI3 L 0.0316 0.0347 0.0414 0.04195 0.05122 0.0541 0.05425 0.06437 0.0727 &
0.07372 0.0748 0.09609 0.10916 0.11545 0.12035 0.13655 0.14076 0.1424 &
0.143764 0.15093 0.163358 0.1733 0.18252 0.185712 0.19494 0.198928 &
0.1996 0.202111 0.205309 0.21528 0.221399 0.228785 0.233469 0.240875 &
0.24684 0.2515 0.26645 0.275129 0.275428 0.2795 0.281441 0.28292 0.28956 &
0.29165 0.2943 0.301741 0.31069 0.317062 0.3258 0.3435 0.3454 0.3459 &
0.35603 0.3685 0.3718 0.38782 0.3903 0.41029 0.433 0.4484 0.4551 &
0.5172 0.7425 0.7947
C
C  1    ASSOCIATED photon intensities :
```

```
SP3 D 0.00016 0.00037 0.0003 0.0006 0.0002 0.0003 0.0003 0.0001 &
0.0011 0.0001 0.0006 0.00086 0.0154 0.0007 0.00026 0.00012 0.0022 &
0.00005 0.1096 0.00076 0.0508 0.0001 0.0034 0.572 0.0063 0.00042 &
0.001 0.0108 0.0501 0.00027 0.0012 0.00008 0.00029 0.00075 0.00053 &
0.0004 0.00006 0.00042 0.00007 0.0027 0.00006 0.00005 0.00007 0.00038 &
0.00033 0.00005 0.00004 0.00001 0.000004 0.00003 0.0007 0.00038 0.00005 &
0.0007 0.0007 0.00038 0.0004 0.00003 0.00004 0.00001 0.00008 0.000004 &
0.000004 0.000006
c   ---------------------
c   ***  TALLY CARDS  ***
c   ---------------------
C Summed Tally
C
F8:P 110
FC8 Tally No GEB
C
C
F18:P 110
FC18 Tally With GEB
FT18 GEB 0.000594701 0.000763331 0.85487
C
C Energy Bins
C
E0 0 1e-8 .0000194 8190i 1.5925365 $8192 bins
PHYS:P 4J 1
MODE P
print
nps 1e8
```

APPENDIX F: SIMULATION OUTPUT

F.1 Source Definition Comparison of Simulations

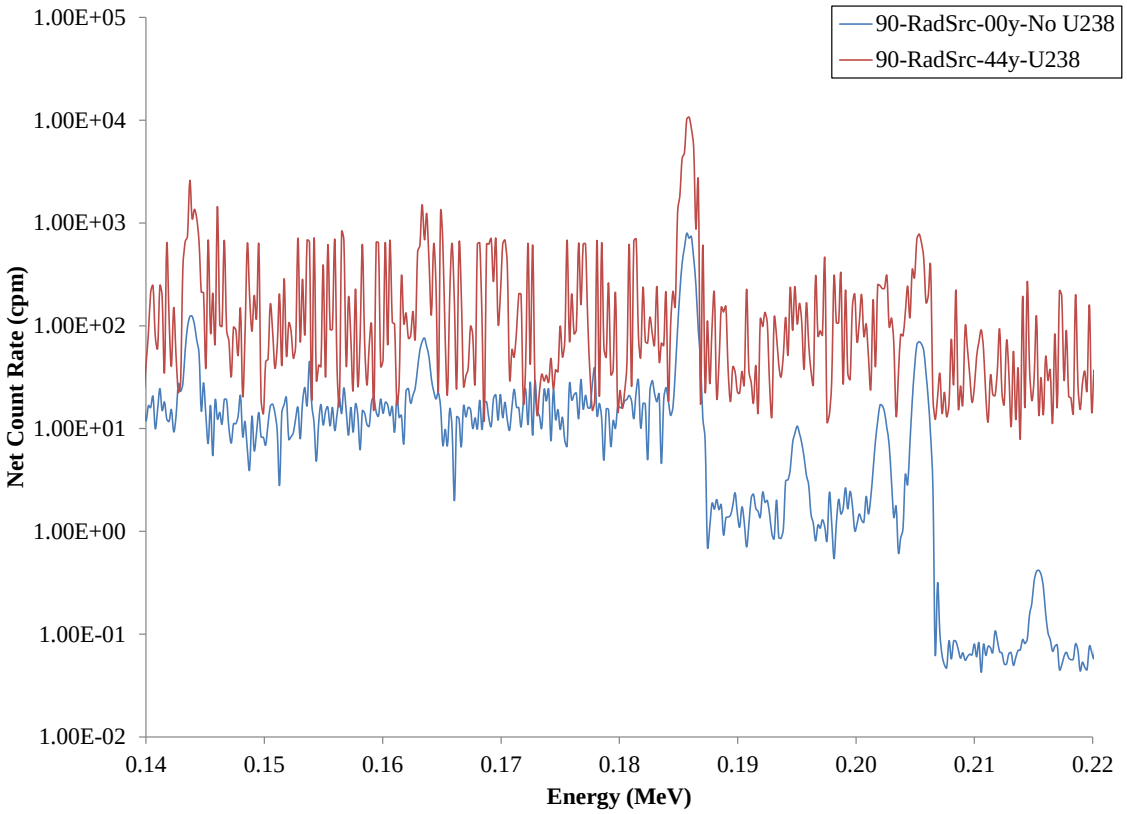

Figure F-1. Comparison of MCNPX Simulation for ^{235}U Source Definition with and without ^{238}U Source Definition.

Table F-1. Peak Area and Continuum Comparison of MCNPX 185.7 keV Emission with and without ^{238}U Source Definition.

Source	Peak Area ROI (keV)	Integral (cpm)	Continuum (cpm) *[% of Integral]*	Net Peak Area (cpm) *[% of Integral]*
^{235}U (without ^{238}U)	(184.5, 187.8)	$(4.4\pm0.1)\times10^{3}$	$(1.6\pm0.1)\times10^{2}$ *(3.7%)*	$(4.3\pm0.1)\times10^{2}$ *(96.3%)*
^{235}U (with ^{238}U)	(184.5, 187.8)	$(5.2\pm0.5)\times10^{4}$	$(2.81\pm0.05)\times10^{4}$ *(5.5%)*	$(4.9\pm0.5)\times10^{4}$ *(94.5%)*

F.2 Simulation Output for Passive and Transmission Simulations

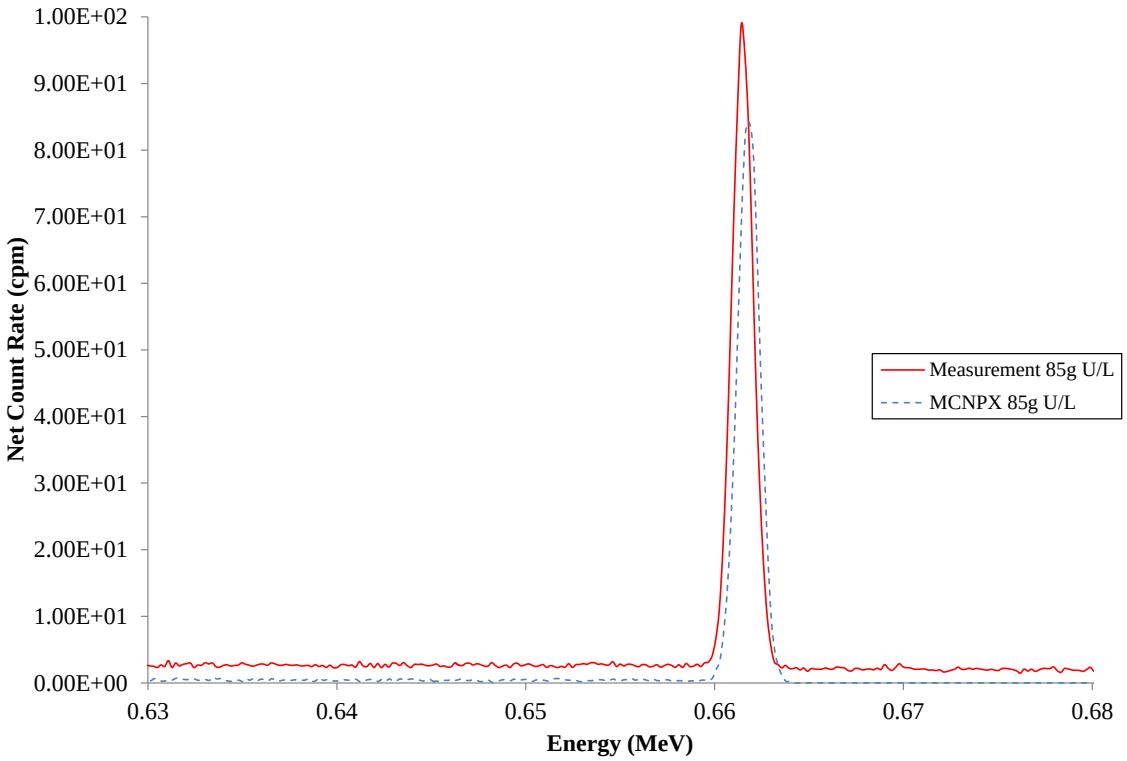

Figure F-2. 85 g U/L Comparison of ^{137}Cs Transmission Measurement Data with MCNPX Simulation.

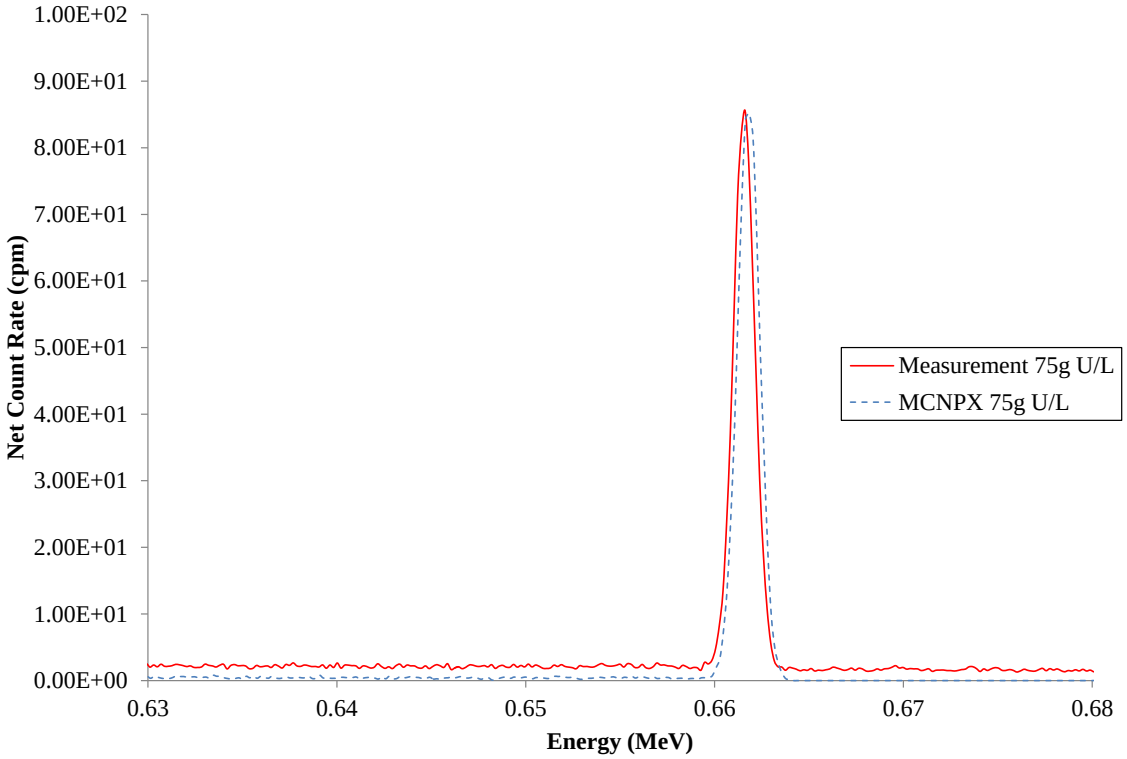

Figure F-3. 75 g U/L Comparison of ^{137}Cs Transmission Measurement Data with MCNPX Simulation.

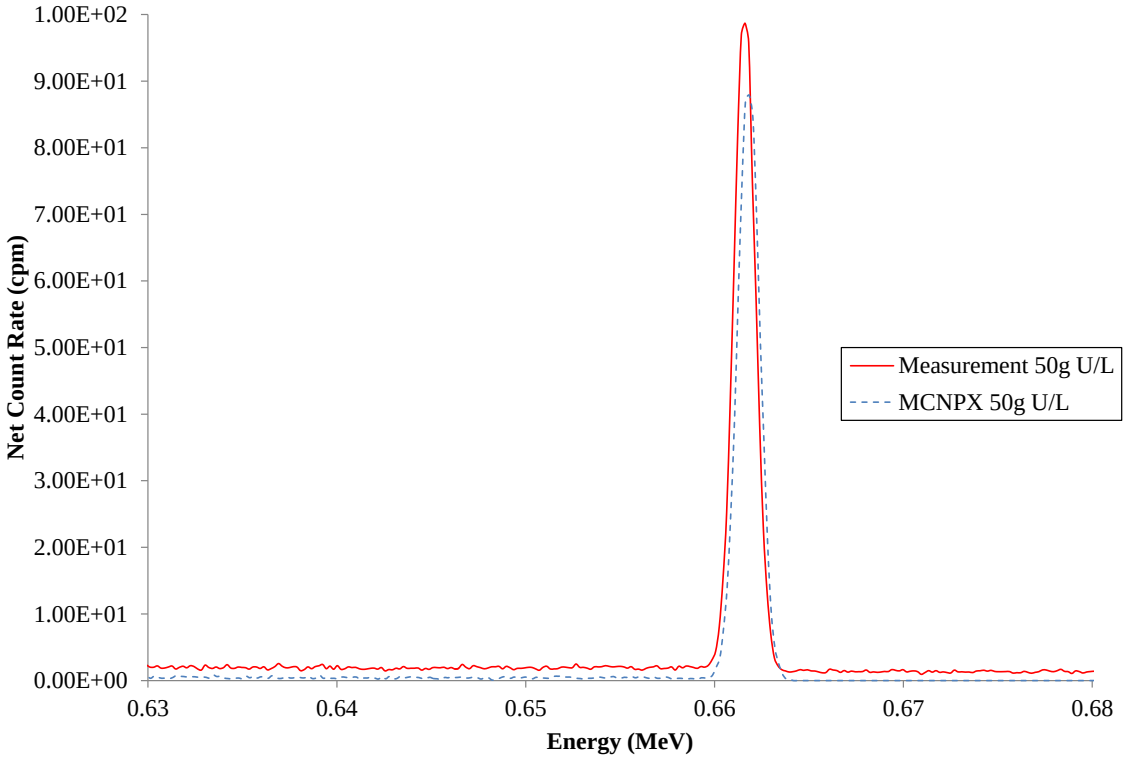

Figure F-4. 50 g U/L Comparison of ^{137}Cs Transmission Measurement Data with MCNPX Simulation.

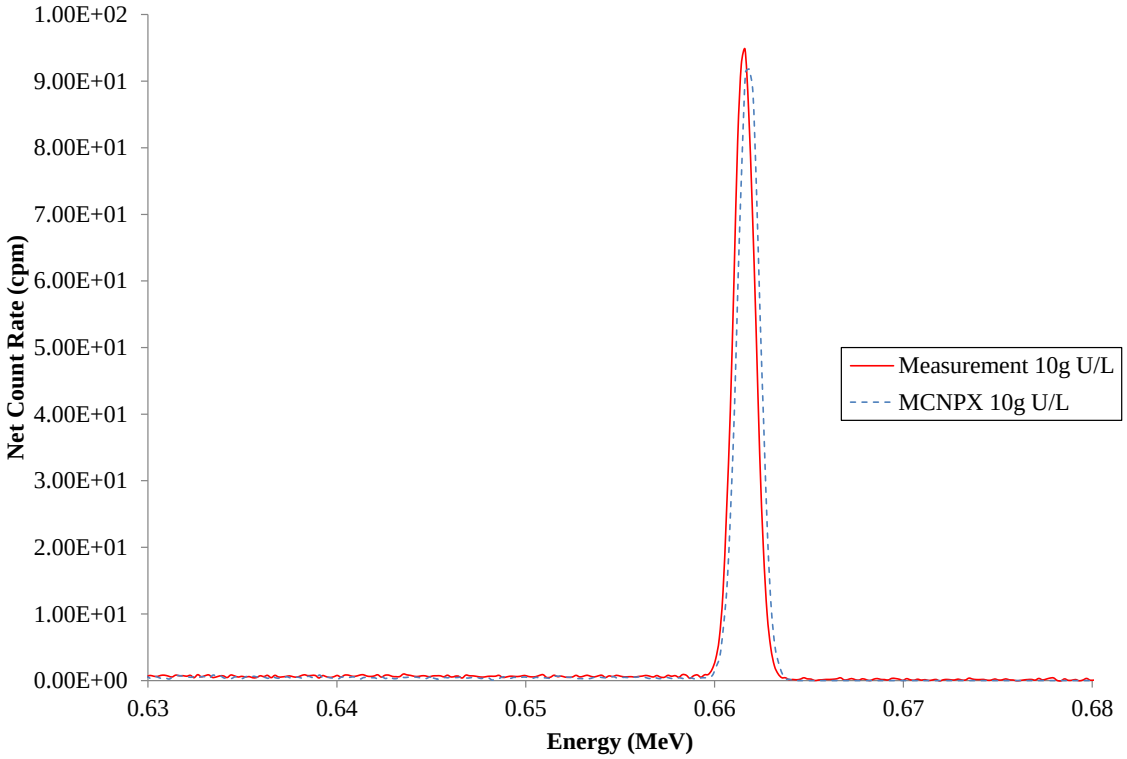

Figure F-5. 10 g U/L Comparison of ^{137}Cs Transmission Measurement Data with MCNPX Simulation.

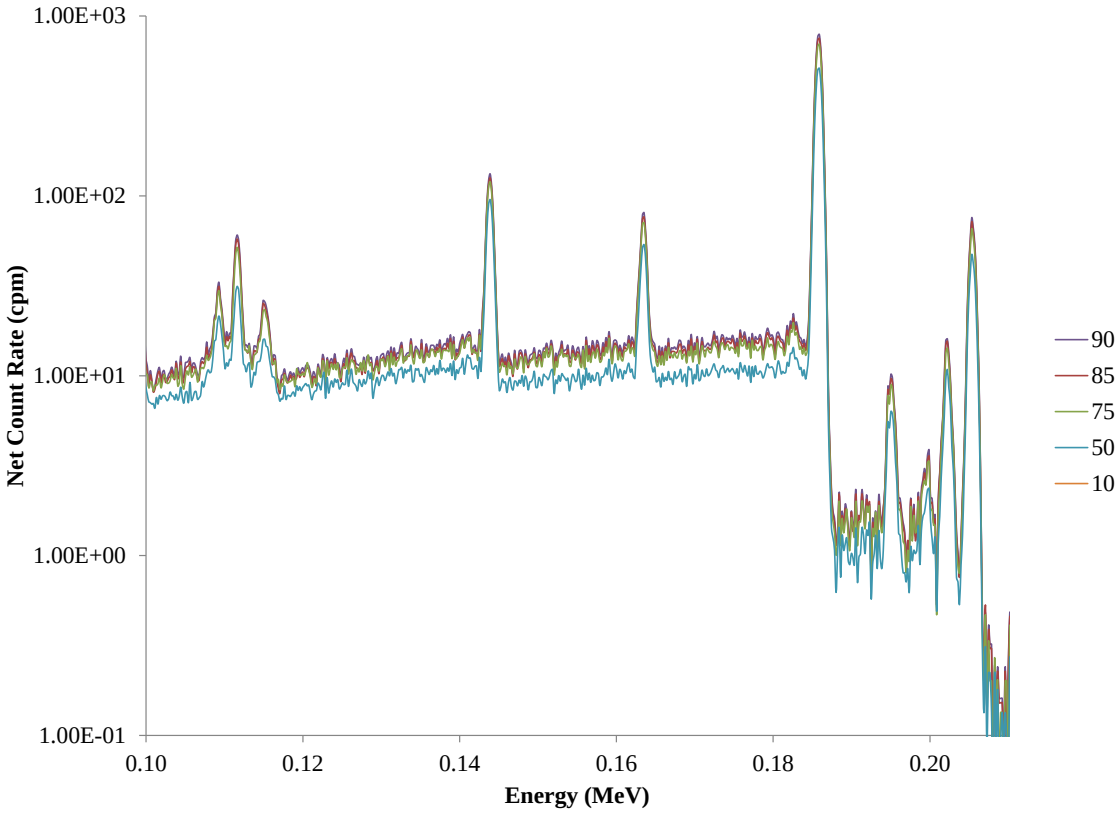

Figure F-6. MCNPX Simulation for Passive Dilution Measurements.

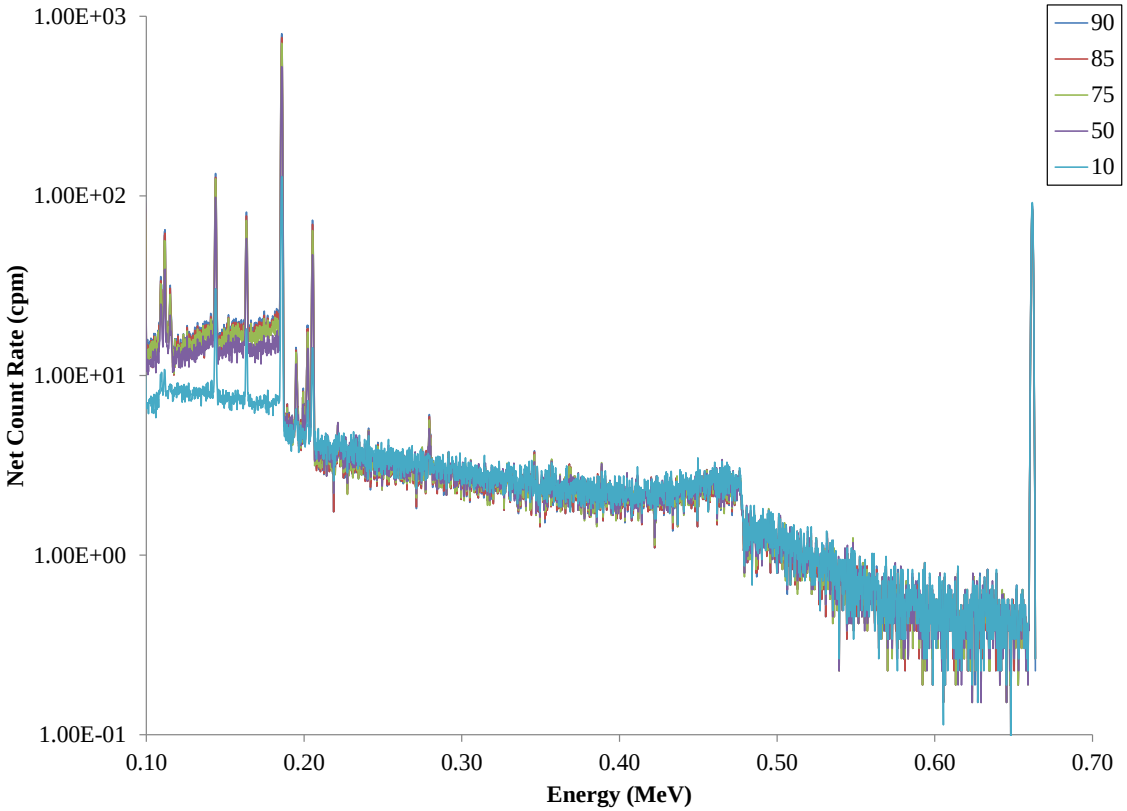

Figure F-7. ^{137}Cs Transmission MCNPX Simulation Data Spectra at Dilution Concentrations.

APPENDIX G: DILUTION MEASUREMENT FULL SPECTRA

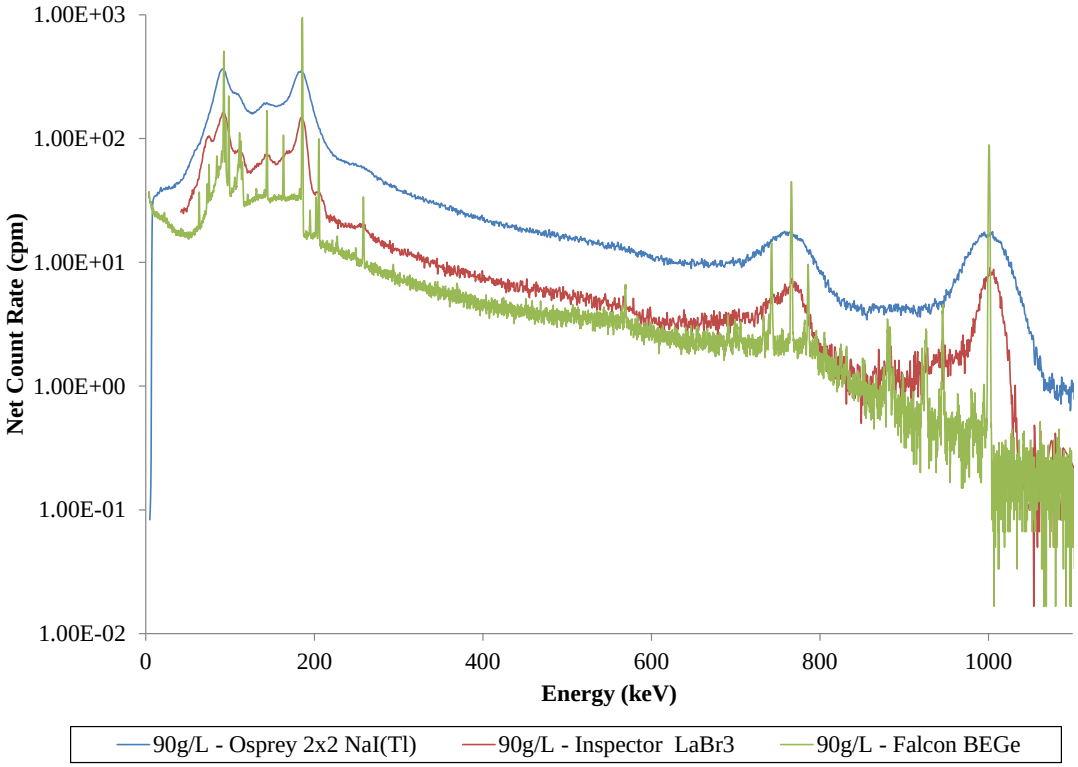

Figure G-1. 90 g U/L Dilution Measurement Data for All Detectors.

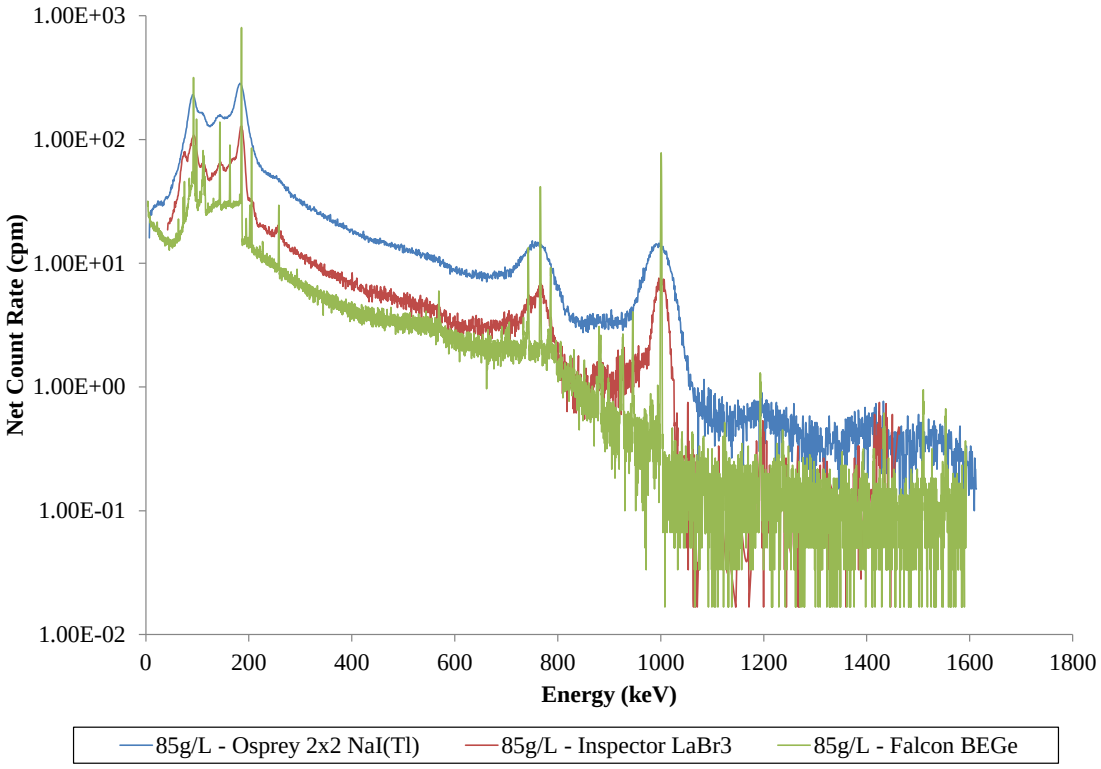

Figure G-2. 85 g U/L Dilution Measurement Data for All Detectors.

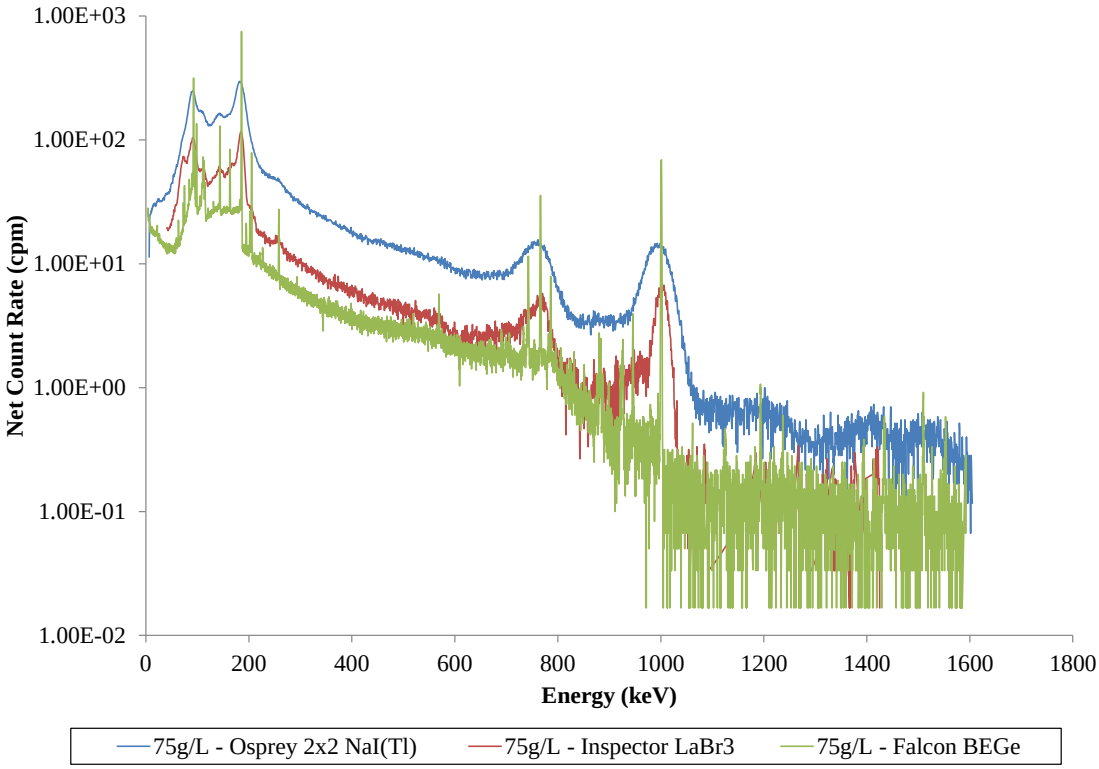

Figure G-3. 75 g U/L Dilution Measurement Data for All Detectors.

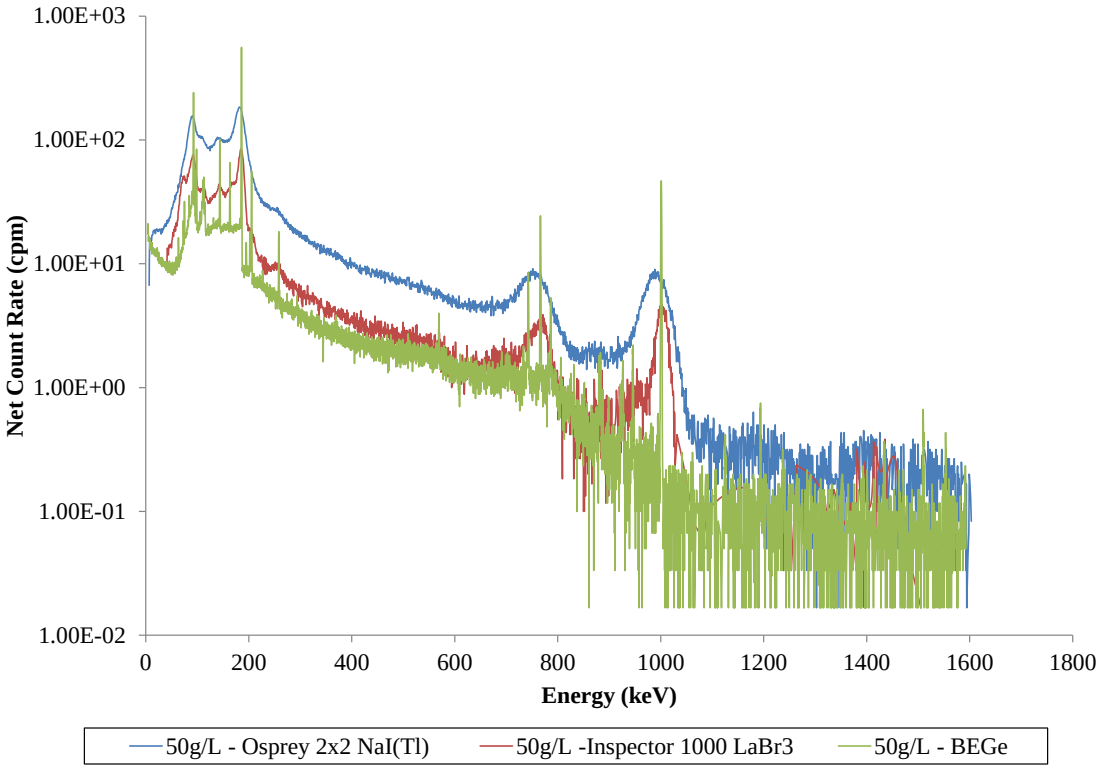

Figure G-4. 50 g U/L Dilution Measurement Data for All Detectors.

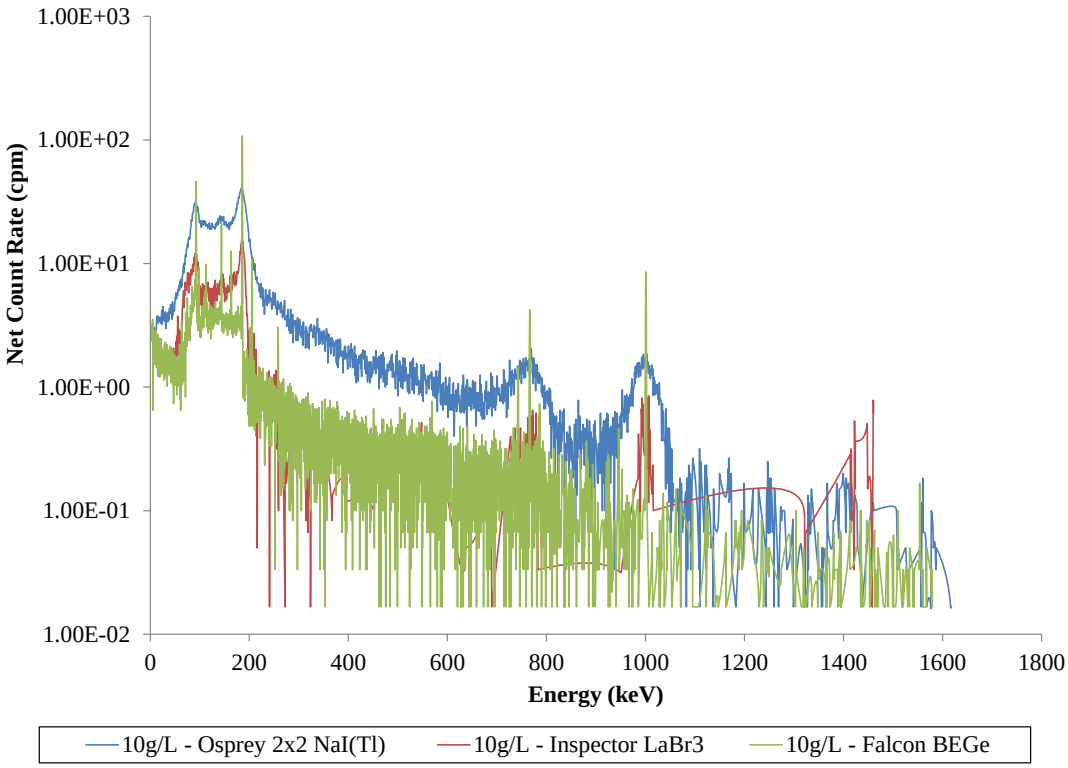

Figure G-5. 10 g U/L Dilution Measurement Data for All Detectors.

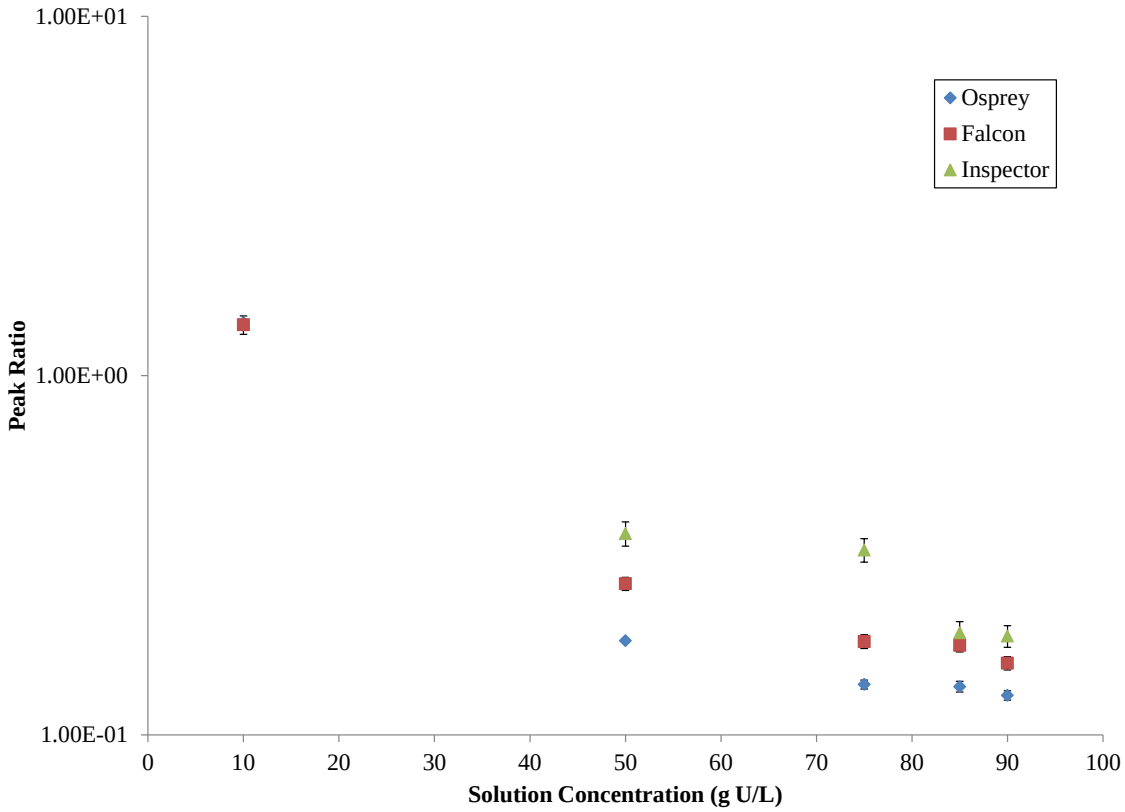

Figure G-6. Peak Area Ratios of ^{137}Cs Emissions of 661.7 keV to 185.7 keV for Transmission Measurement Data as a Function of Solution Concentration.

Note: Error bars plotted for some data points are smaller than the resolution of the graph.

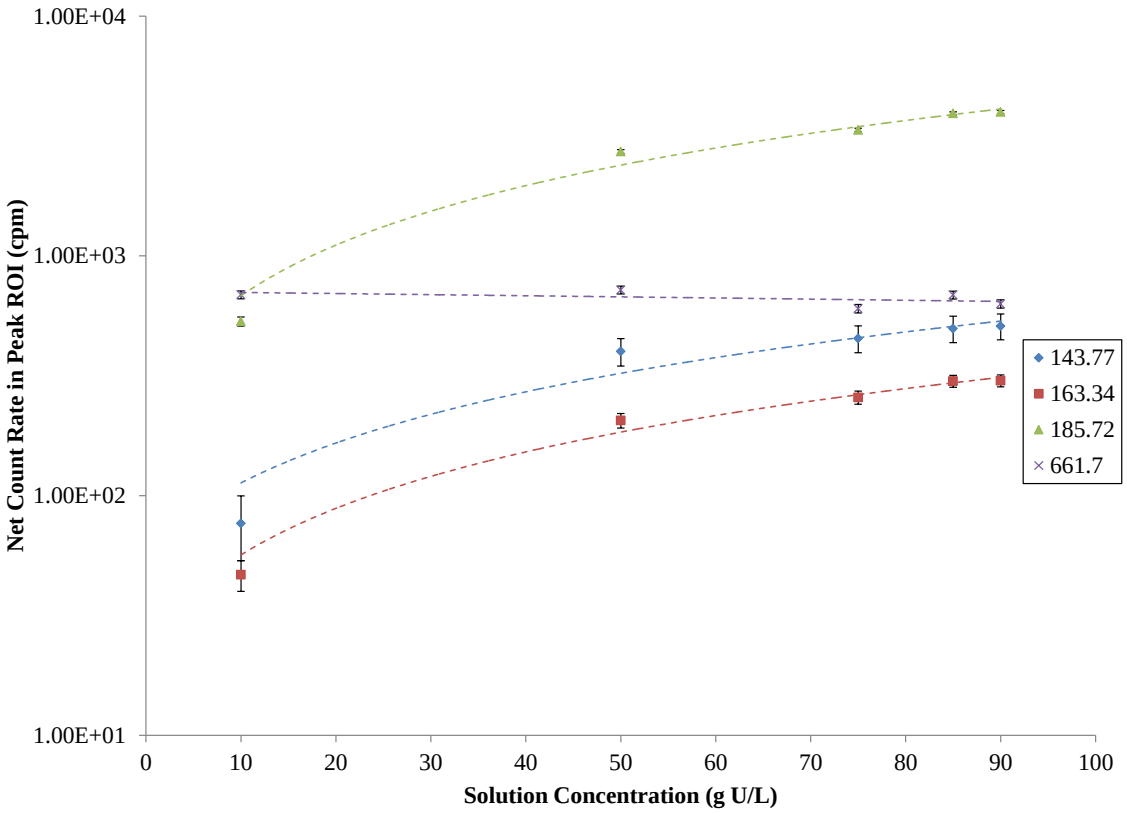

Figure G-7. Peak Area Values as a Function of Solution Concentration for ^{137}Cs Transmission Measurements for Falcon BEGe.

Note: Error bars plotted for some data points are smaller than the resolution of the graph.

APPENDIX H: DILUTION MEASUREMENT FULL SPECTRA

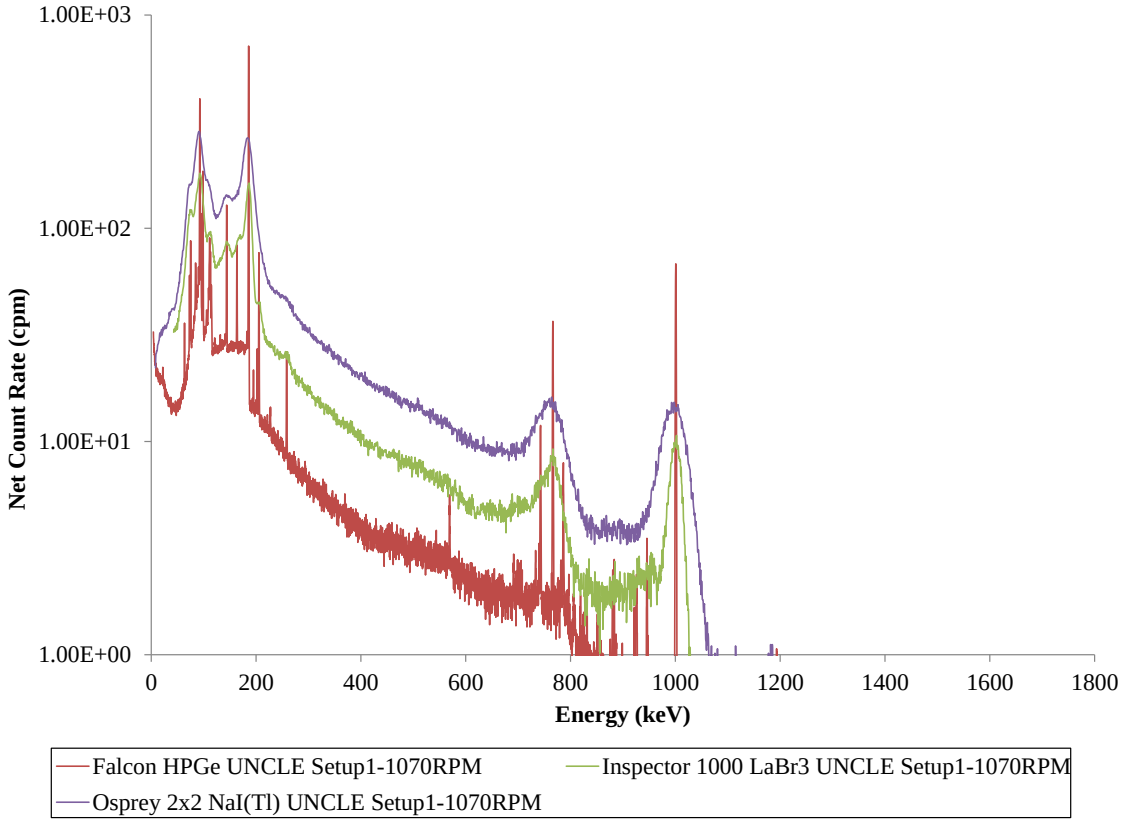

Figure H-1. Full Spectrum Detector Comparison of UNCLE Flowrate Measurements at 1070 RPM.

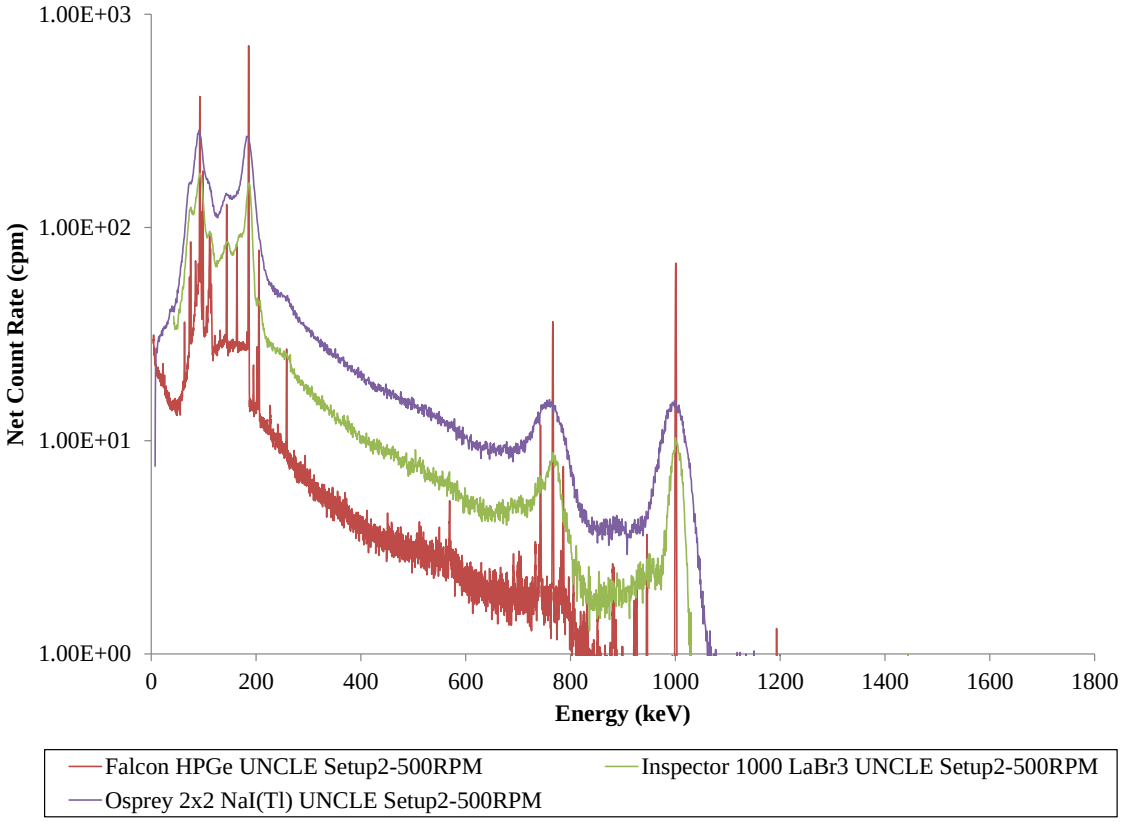

Figure H-2. Full Spectrum Detector Comparison of Backshield at 500 RPM Flowrate at UNCLE.

Table H-1. Peak Area Statistics Comparing Static (Dilution) and Dynamic (UNCLE) Measurements.

Inspector $LaBr_3$				
Dilution Concentration (g U/L)	**90**	**85**	**75**	**50**
185.7 keV Peak Area (cpm)	1133.00	1011.78	777.33	484.40
UNCLE Flowrate (RPM)	1070	500	-	-
185.7 keV Peak Area (cpm)	1314.62	1443.12	-	-

Falcon BEGe				
Dilution Concentration (g U/L)	**90**	**85**	**75**	**50**
185.7 keV Peak Area (cpm)	4381.77	4370.07	4052.8	2964.27
UNCLE Flowrate (RPM)	1070	500	-	-
185.7 keV Peak Area (cpm)	3547.40	3556.97	-	-

Osprey 2x2 NaI(Tl)				
Dilution Concentration (g U/L)	**90**	**85**	**75**	**50**
185.7 keV Peak Area (cpm)	8052.77	5879.7	6733.33	4842.72
UNCLE Flowrate (RPM)	1070	500	-	-
185.7 keV Peak Area (cpm)	6045.7	6466.25	-	-

APPENDIX I: BACKGROUND MEASUREMENTS

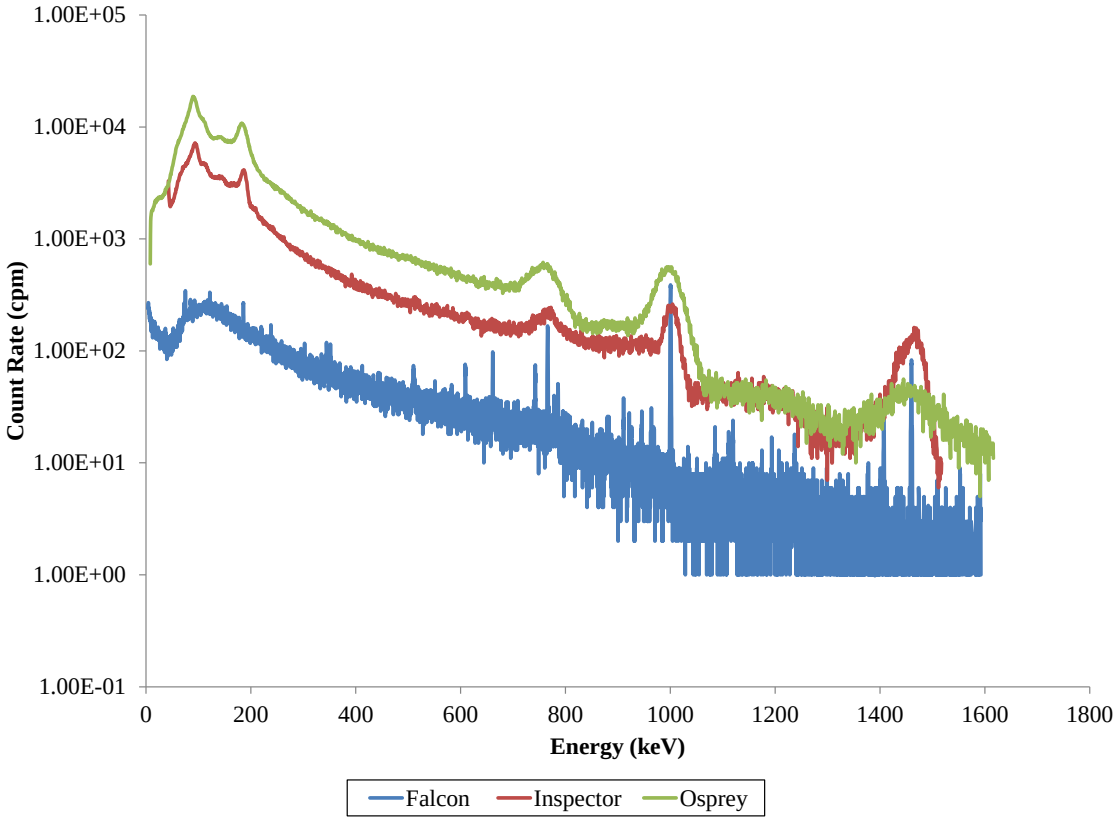

Figure I-1. Operational Background Taken from UNCLE at Standoff.

APPENDIX J: MCNPX EFFICIENCY MODELS

```
C NUCP MCNPX Models  (UNCLE system)
c 90g/L  - F1 Tally
c
c  Cells
c
c  101    3 -0.001293 -101 102    imp:p=1 $ Tally Surface
  102    1   -7.92 -102 103  $ SS Tube
  103    2  -1.122 -103  $ U Nitrate
  104    6   -1.03 -107  $Epoxy Lid
  106    3 -0.001293 -108 104  $ Air btn col detector
  105    9    -2.7 -104 134  $ Detector Al Endcap
  107    5     -11 104 108 -135  $ Cu col detector
  108    5     -11 135 -125  $ Tin col detector
  109    5     -11 125 -105  $ W Collimator
  111    0         -134 124  $ Detector Vacuum
  110   10 -5.3234 -124  $ Ge Crystal
  112    4  -11.34 -106  $ Pb Shield Bottom Brick
  113    4  -11.34 -109  $ Pb Shield Top Brick
  114    4  -11.34 -110  $ Pb Shield Right Brick
  115    4  -11.34 -111  $ Pb Shield Left Brick
  116    4  -11.34 -113  $ Pb Backshield
c 900    0  -999 102 105 106 107 109  110 111 113 imp:p=1 $ Environment Shell
  900    3 -0.001293 -999 102 105 107 106 109 110 111 113  $ Environment S
  999    0         999  $ Void

c
c   Surface
c 101  1 rcc 0    0   -0.635    0   0   63.6524    4.51325 $ Tally Box
  102    1 rcc 0 0 -0.635 0 0 63.6524 4.44  $ SS Tube
  103    1 rcc 0 0 0 0 0 60.2742 3.92  $ UN
  124    1 rcc -8.275 0 31.8262 -2 0 0 2.985  $ Ge crystal
  134    1 rcc -6.905 0 31.8262 -4.1 0 0 3.95  $ vacuum
  104    1 rcc -6.785 0 31.8262 -4.3 0 0 4.1  $ Detector Endcap .12cm thick
  108    1 rcc -5.235 0 31.8262 -5.85 0 0 5.7  $ Air around detector
  105    1 rcc -5.235 0 31.8262 -15 0 0 6.5  $ W Collimator
  125    1 rcc -5.235 0 31.8262 -15 0 0 6  $ Sn Collimator
  135    1 rcc -5.235 0 31.8262 -15 0 0 5.9  $ Cu Collimator
  107    1 rcc -5.075 0 31.8262 -0.16 0 0 6.5  $ Epoxy Front Lid
  106    1 rpp -15.075 -5.075 -10.15 10.15 16.6762 $ Pb Shield Bottom Br
           21.6762
  109    1 rpp -10.075 -5.075 -10.15 10.15 41.9762 $ Pb Shield Top Brick
           51.9762
  110    1 rpp -10.075 -5.075 6.51 16.51 21.6763 $ Pb Shield Right Brick
           41.9761
  111    1 rpp -10.075 -5.075 -16.51 -6.51 21.6763 $ Pb Shield Left Brick
           41.9761
  113    1 rpp 4.7002 9.7002 -10.15 10.15 26.8262 36.8262  $Backshield
  999    1 rcc 0 0 -75 0 0 200 50  $ Void Cylinder
c

c
c Data Cards
c
c
c   ***  TRANSFORMATION  ***
c   ------------------------
tr1  0 0 0
```

```
mode  p
c
c
c   ***  MATERIAL CARDS  ***
c   ------------------------
c
c     Material 1, Stainless Steel 304L      (-7.92)
m1    26000.          0.05936  $MAT4
      24000.          0.01743 28000.          0.00772 25055.          0.00174
c
c     Material 2,  Uranium nitrate solution.  Mostly water.
c     From UNCLE description
c     90 grams Uranium / 1000 mL H2O  (-1.122)
m2    92238.          -0.0796  $MAT8
      92235.          -0.00061 92234.          -5e-006 8000.          -0.815185
      1000.          -0.097521 7000.          -0.00708
c
c     Material 3, Air
m3    8016.           -0.2314  $MAT
      7014.           -0.7558 18000.          -0.0128
c
c     Material 4, Pb
m4    82000.              -1  $MAT
c     Material 5, Collimator (density 11g/cc)
m5    74000.            -0.98  $MAT
      6000.           -0.0171 1000.           -0.0029
c
c     Material 6, Epoxy (density 1.07g/cc)
m6    1000.             -0.06  $MAT
      6000.            -0.721 8000.            -0.219
c     Material 7, Copper
m7    29000.              -1  $MAT
c     Material 8, Tin
m8    50000.              -1  $MAT
c     Material 9, Al
m9    13000.              -1  $MAT
c     Material 10, HPGe
m10   32000.04p             1  $HPGe
imp:p             1 15r                   0  $ 102, 999
c
c
c   ***  SOURCE DEF  ***
c   --------------------
c     Cell source of Uranium dissolved in water,
c     spontaneous fission spectrum, U-238
c     cylindrical source centered in solution pipe
sdef PAR=2  POS=0 0 0   AXS=0 0 1  RAD=d1   EXT=d2  ERG=d3 CEL=103
si1    3.92
sp1  -21  1                     $Radial sampling
si2   60.2742
sp2  -21  0                     $Vertical cylinder sampling
c RadSource Run: Tue May 15 13:33:13 2012
c
c Input Isotopes
c U-234  0.01%
c U-235  0.76%
c U-238  99.23%
c
c Total: 100%
c
c Age: 0 s, 0 yrs
```

```
c ======================================================
c  1    DISCRETE GAMMA LINE energies (MeV)
si3 L 0.0316 0.0347 0.0414 0.04195 0.05122 0.0541 0.05425 0.06437 0.0727 &
0.07372 0.0748 0.09609 0.10916 0.11545 0.12035 0.13655 0.14076 0.1424 &
0.143764 0.15093 0.163358 0.1733 0.18252 0.185712 0.19494 0.198928 &
0.1996 0.202111 0.205309 0.21528 0.221399 0.228785 0.233469 0.240875 &
0.24684 0.2515 0.26645 0.275129 0.275428 0.2795 0.281441 0.28292 0.28956 &
0.29165 0.2943 0.301741 0.31069 0.317062 0.3258 0.3435 0.3454 0.3459 &
0.35603 0.3685 0.3718 0.38782 0.3903 0.41029 0.433 0.4484 0.4551 &
0.5172 0.7425 0.7947
c
c  1    ASSOCIATED photon intensities :
sp3 D 0.00016 0.00037 0.0003 0.0006 0.0002 0.0003 0.0003 0.0001 &
0.0011 0.0001 0.0006 0.00086 0.0154 0.0007 0.00026 0.00012 0.0022 &
0.00005 0.1096 0.00076 0.0508 0.0001 0.0034 0.572 0.0063 0.00042 &
0.001 0.0108 0.0501 0.00027 0.0012 0.00008 0.00029 0.00075 0.00053 &
0.0004 0.00006 0.00042 0.00007 0.0027 0.00006 0.00005 0.00007 0.00038 &
0.00033 0.00005 0.00004 0.00001 0.000004 0.00003 0.0007 0.00038 0.00005 &
0.0007 0.0007 0.00038 0.0004 0.00003 0.00004 0.00001 0.00008 0.000004 &
0.000004 0.000006
c   ---------------------
c   ***  TALLY CARDS  ***
c   ---------------------
c F1 Tally Over Axial length of UN for CF
f1:p 103.1 103.2 103.3 T
fc1 UN Energy Bin F1 Tally
c
c F1 Tally Over Axial length of Pipe for CF
f11:p 102.1 102.2 102.3 T
fc11 Pipe Energy Bin F1 Tally
c
c F1 Tally Over Axial length of Coll Front for CF
f21:p 105.1 108.3 T
fc21 Collimator Energy Bin F1 Tally
c
c F1 Tally Over Detector Housing
f31:p 104.1 104.2 104.3 T
fc31 Housing Energy Bin F1 Tally
c
c F1 Tally Over Crystal for CF
f41:p 124.1 124.2 124.3 T
fc41 Crystal Energy Bin F1 Tally
c
c Energy Bins
e0 0 1e-8 .0000194 8190i 1.5925365 $8192 bins
phys:p 4J 1
print
nps 1e8
```

APPENDIX K: ISOCS SIMULATIONS

K.1 ISOCS Models for Falcon and Osprey Detectors

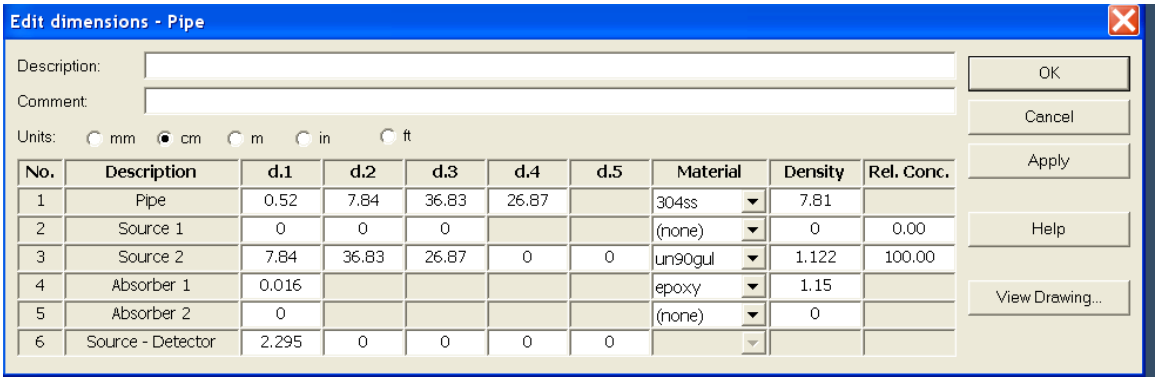

(A)

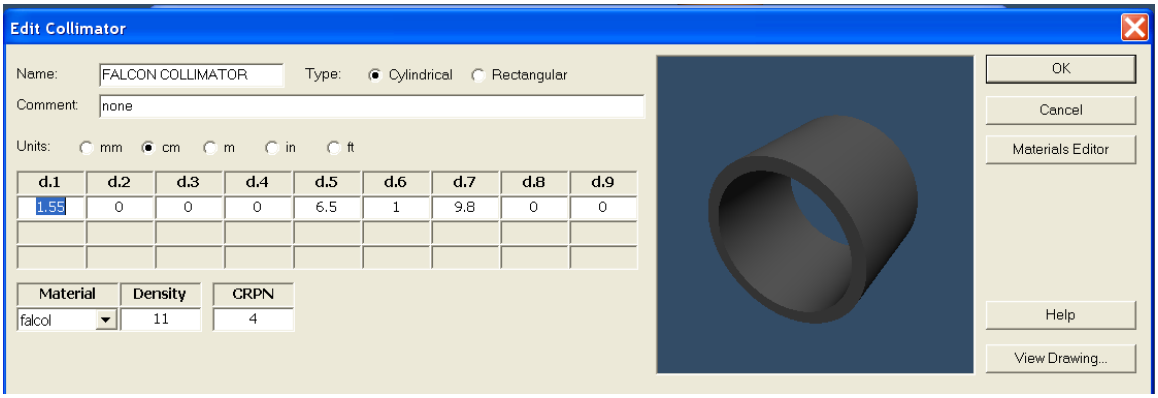

(B)

Figure K-1. ISOCS Software Interface and Input Parameters for (A) Falcon BEGE Detector and (B) Tungsten Collimator.

(A) UN-Filled Pipe Parameters:
1.1 = Pipe thickness
1.2 = Pipe inner diameter
1.3 = Pipe height (+ axis)
1.4 = Pipe height (- axis)
3.1= UN inner diameter
3.2 = UN height (+ axis)
3.3 = UN height (- axis)
4.1 = Epoxy face on Falcon tungsten detector

(B) Falcon Tungsten Parameters:
1.1 = Distance in front of detector face
1.5 = Outer diameter
1.6 = Collimator thickness
1.7 = Collimator length

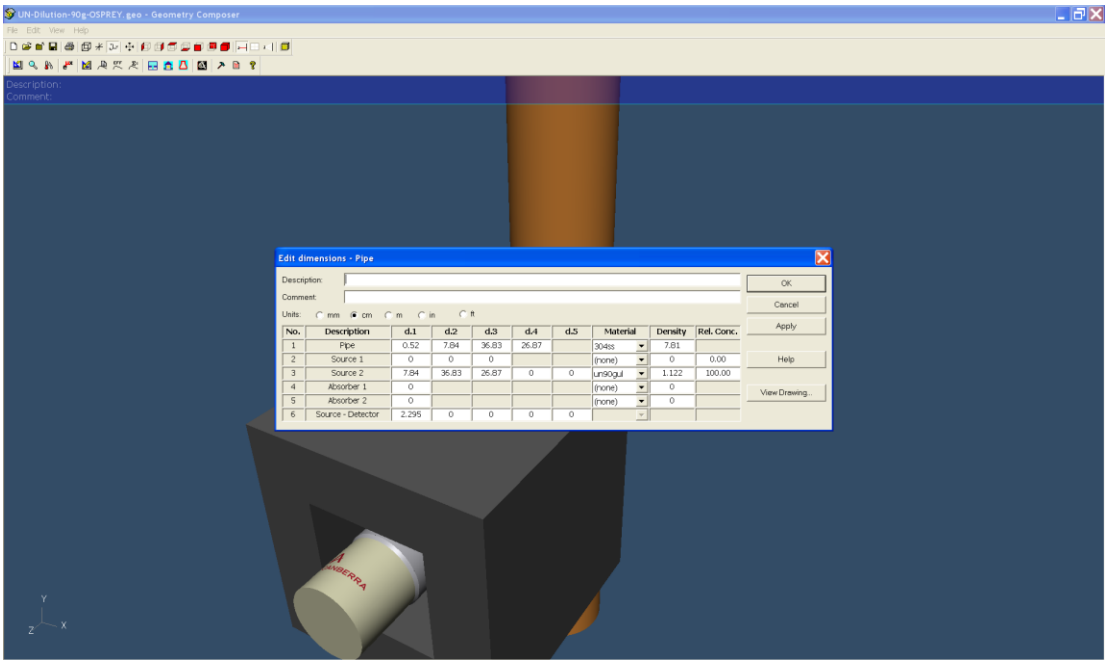

(A)

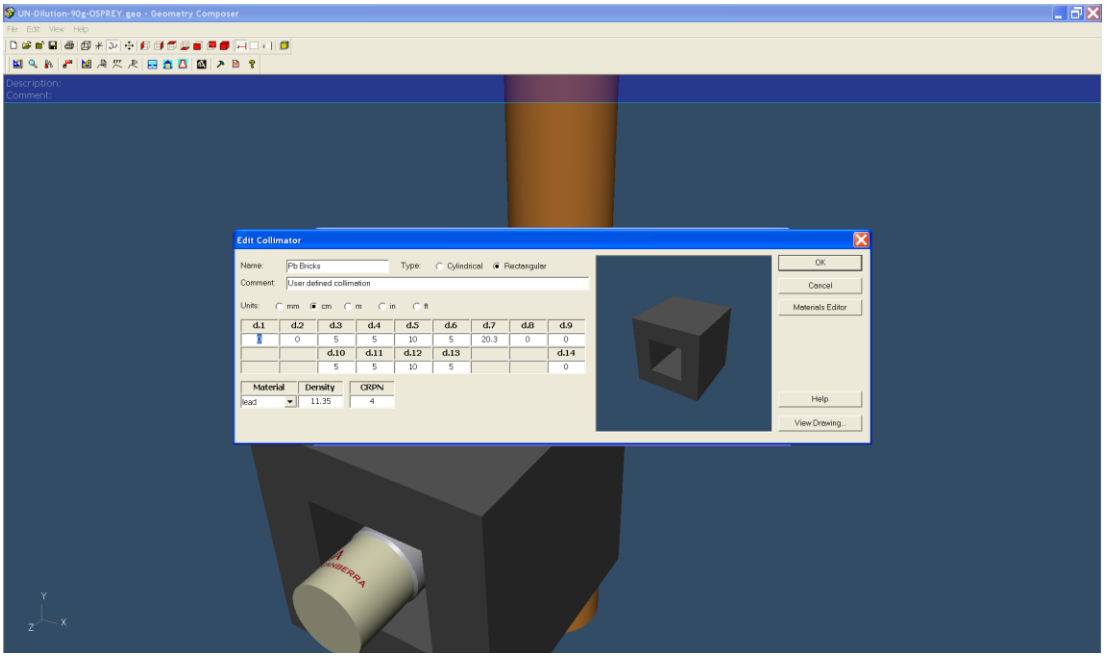

(B)

Figure K-2. ISOCS Software Interface and Input Parameters for (A) Osprey 2x2-NaI(Tl) Detector and (B) Pb Shielding.

K.2 ISOCS Efficiency Values at for Collimated/Shielded Detectors without Pipe Wall at Dilution Concentrations

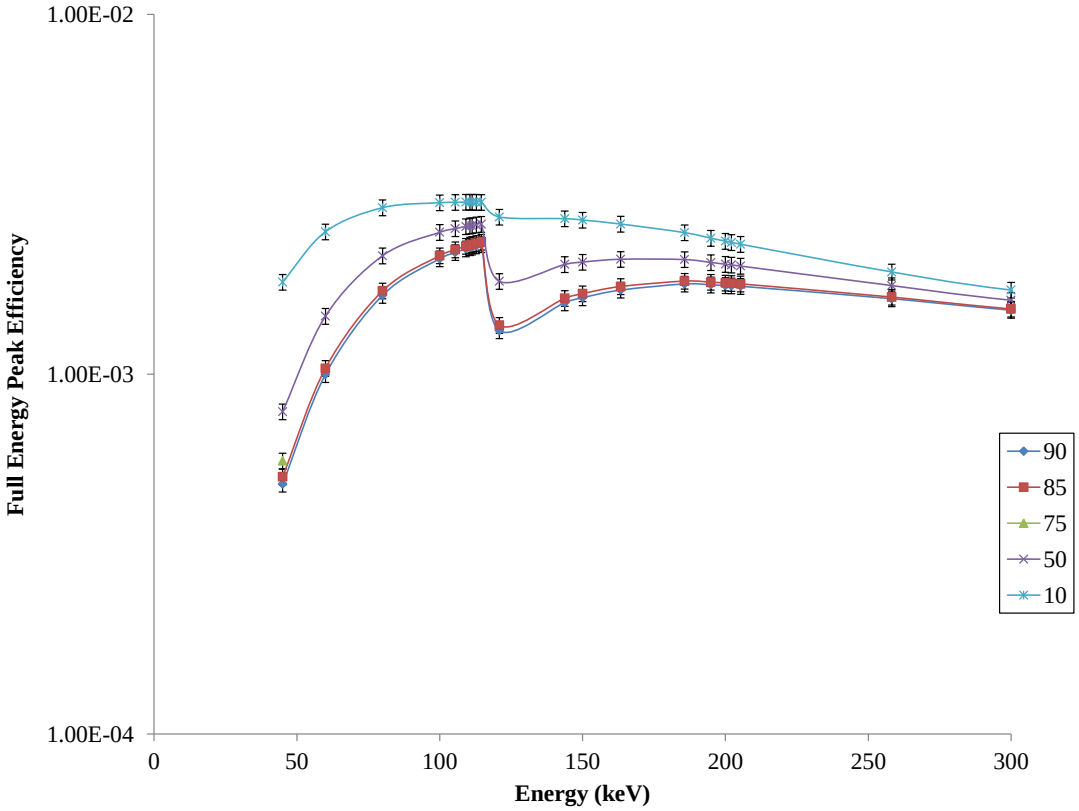

Figure K-3. ISOCS Efficiency Calculations of UN for Collimated Falcon without Pipe Wall.

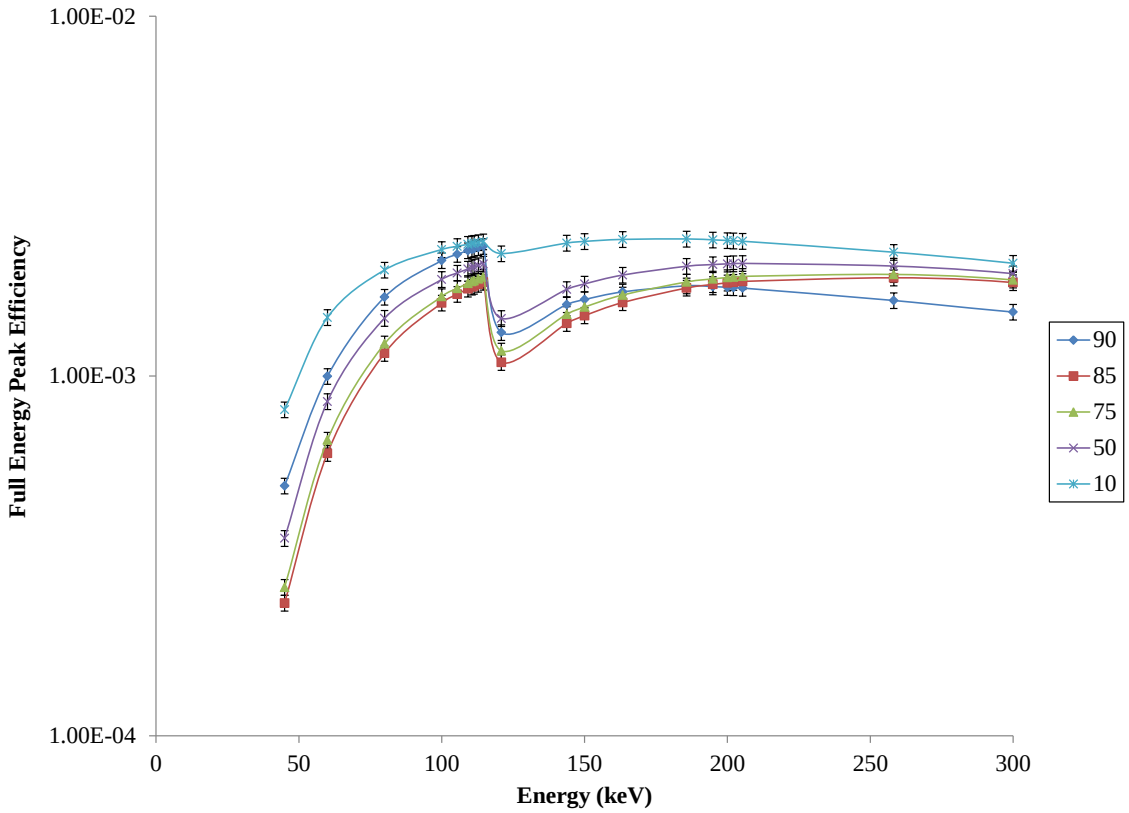

Figure K-4. ISOCS Efficiency Calculations of UN for Shielded Osprey without Pipe Wall.

K.3 ISOCS Efficiency Values at for Uncollimated/Unshielded Detectors without Pipe Wall at Dilution Concentrations

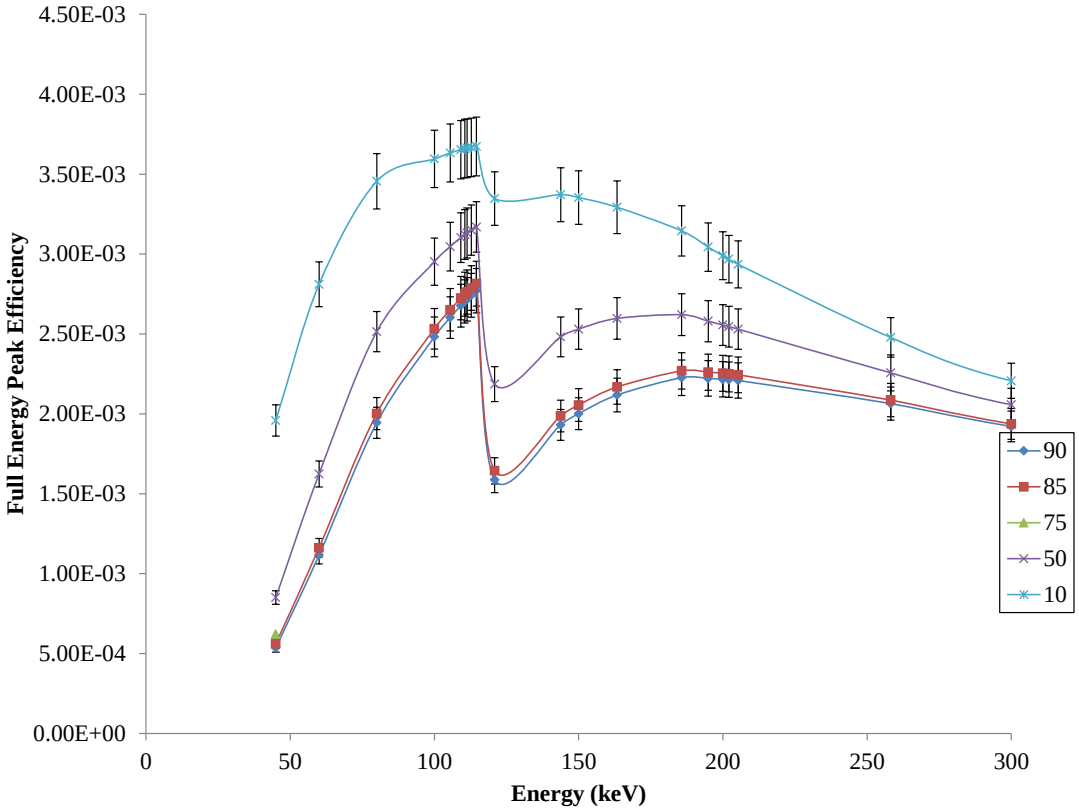

Figure K-5. ISOCS Efficiency Calculations of UN for Uncollimated Falcon without Pipe Wall.

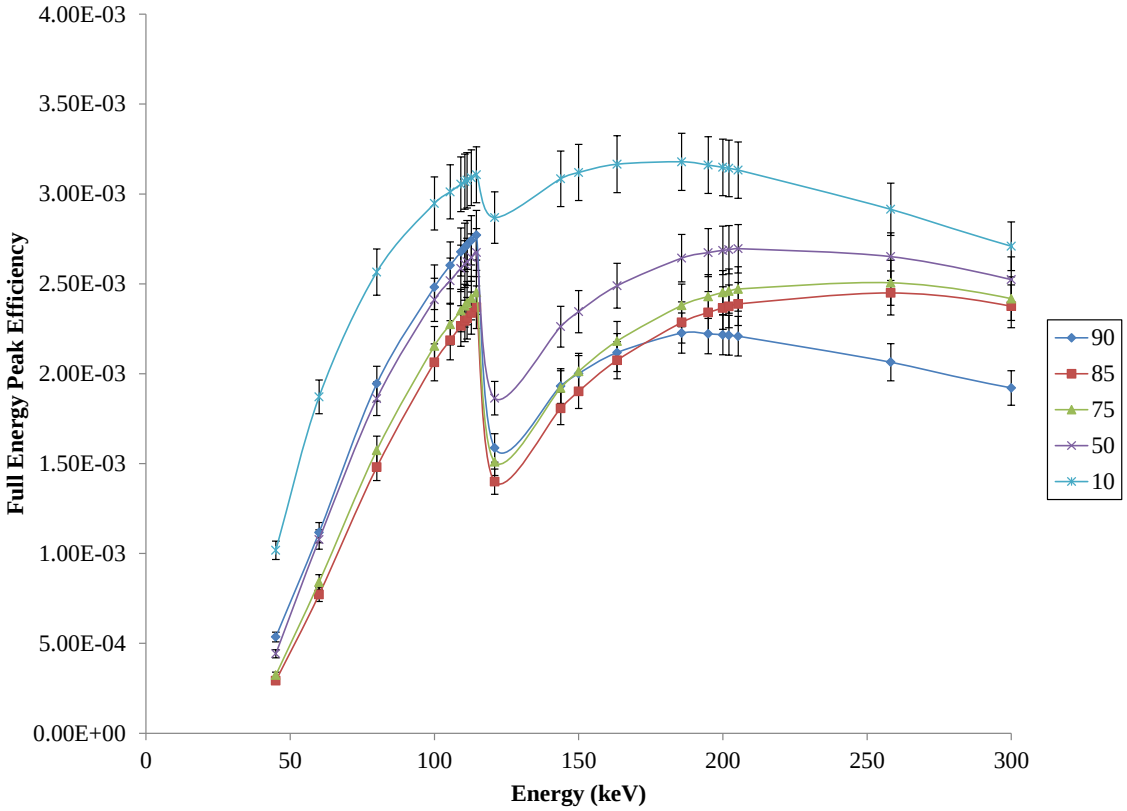

Figure K-6. ISOCS Efficiency Calculations of UN for Unshielded Osprey without Pipe Wall.

K.4 ISOCS Efficiency Comparison for Falcon and Osprey without Pipe Wall

At 90 g U/L (without pipe wall), Figure K-7 shows a comparison of the efficiency of the Pb-shielded Osprey with the W collimated Falcon. At 90 g U/L, Figure K-8 shows a comparison of the efficiencies of the unshielded/uncollimated detectors without the pipe wall.

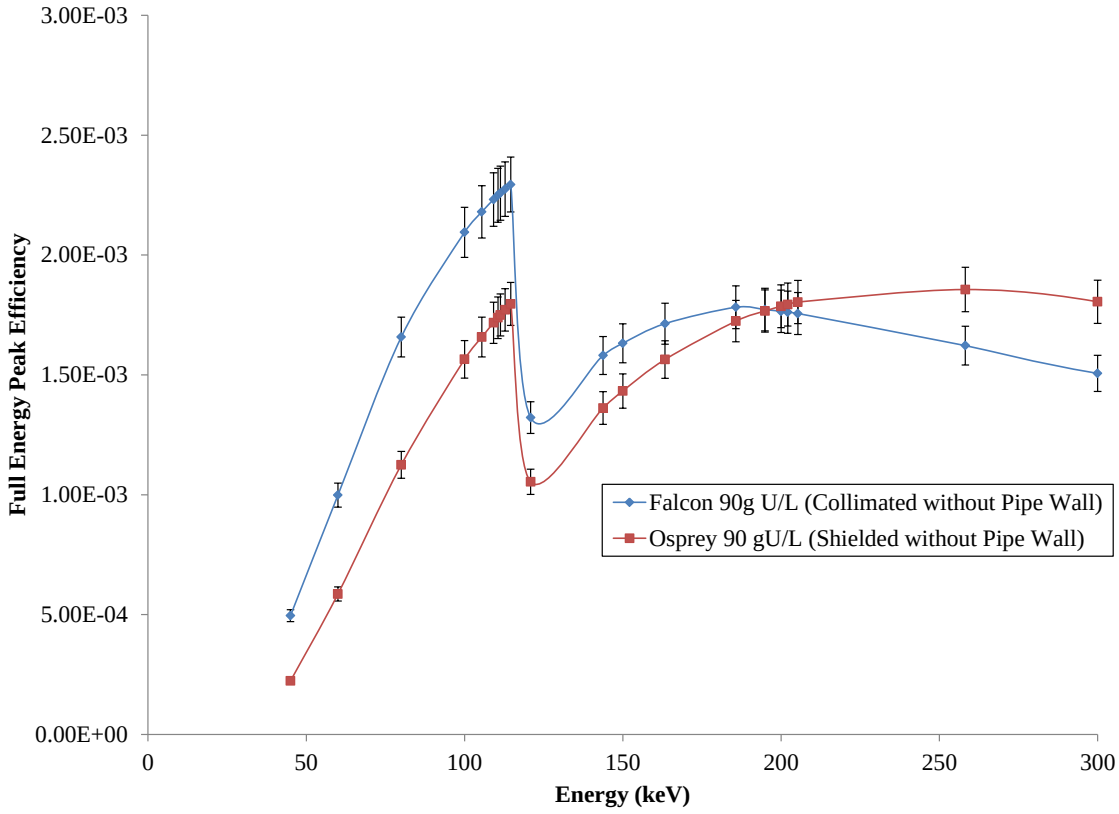

Figure K-7. Comparison of ISOCS Calculated Efficiencies for Shielded/Collimated Falcon BEGe and Osprey NaI for 90g U/L with Pipe Wall.

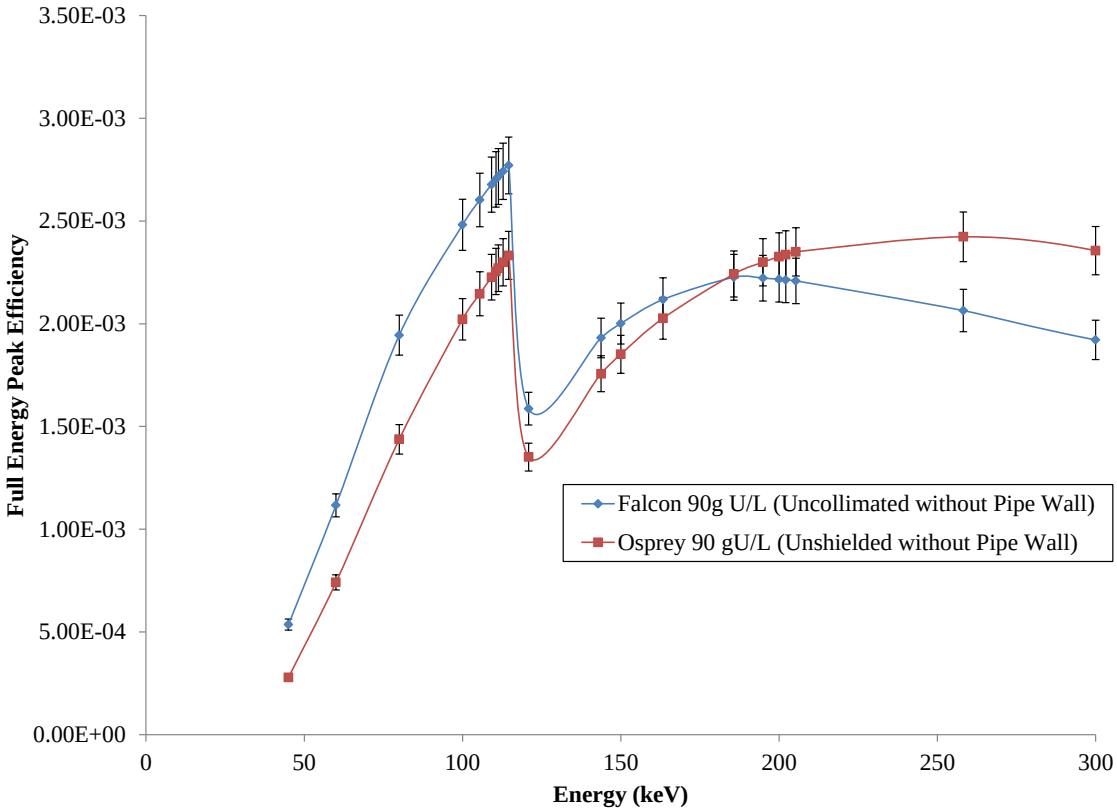

Figure K-8. Comparison of ISOCS Calculated Efficiencies for Unshielded/Uncollimated Falcon BEGe and Osprey NaI for 90 g U/L without Pipe Wall.

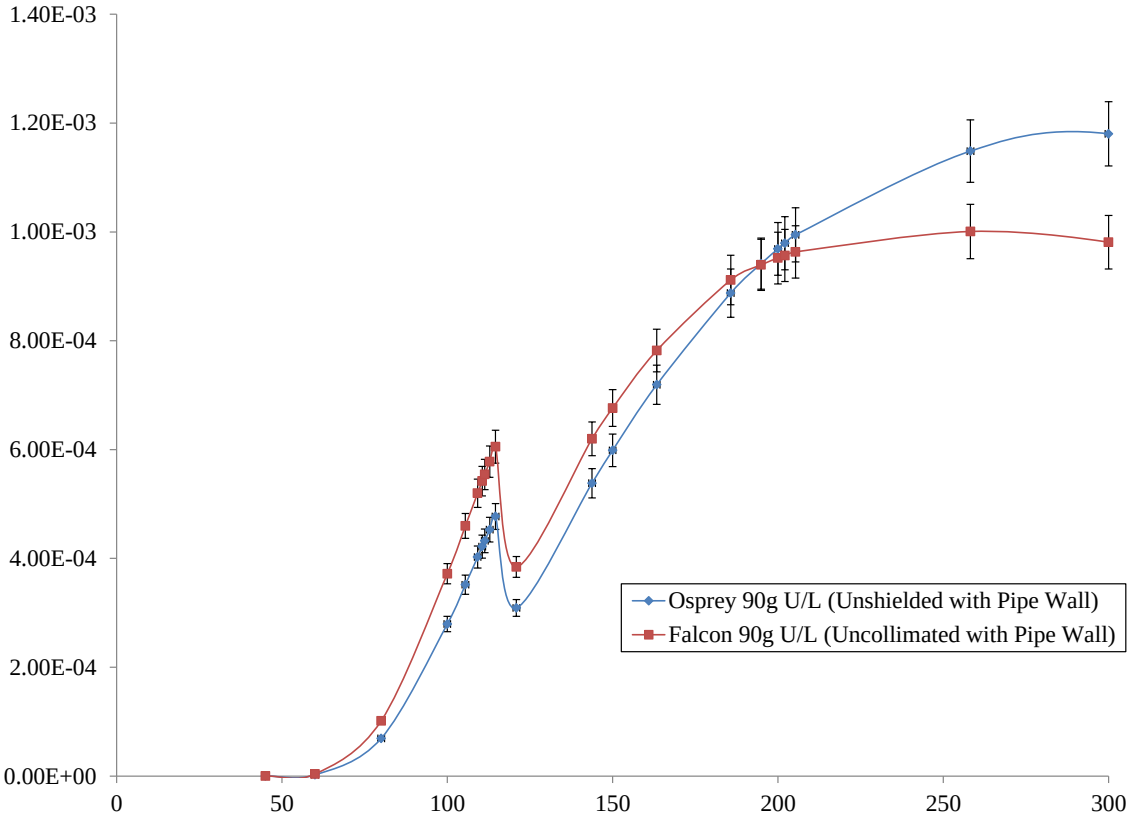

Figure K-9. Comparison of ISOCS Calculated Efficiencies for Unshielded/Uncollimated Falcon BEGe and Osprey NaI for 90 g U/L with Pipe Wall.

K.5 ISOCS Uncertainty Estimator Results

K.5.1 Source-Detector Distance Variation

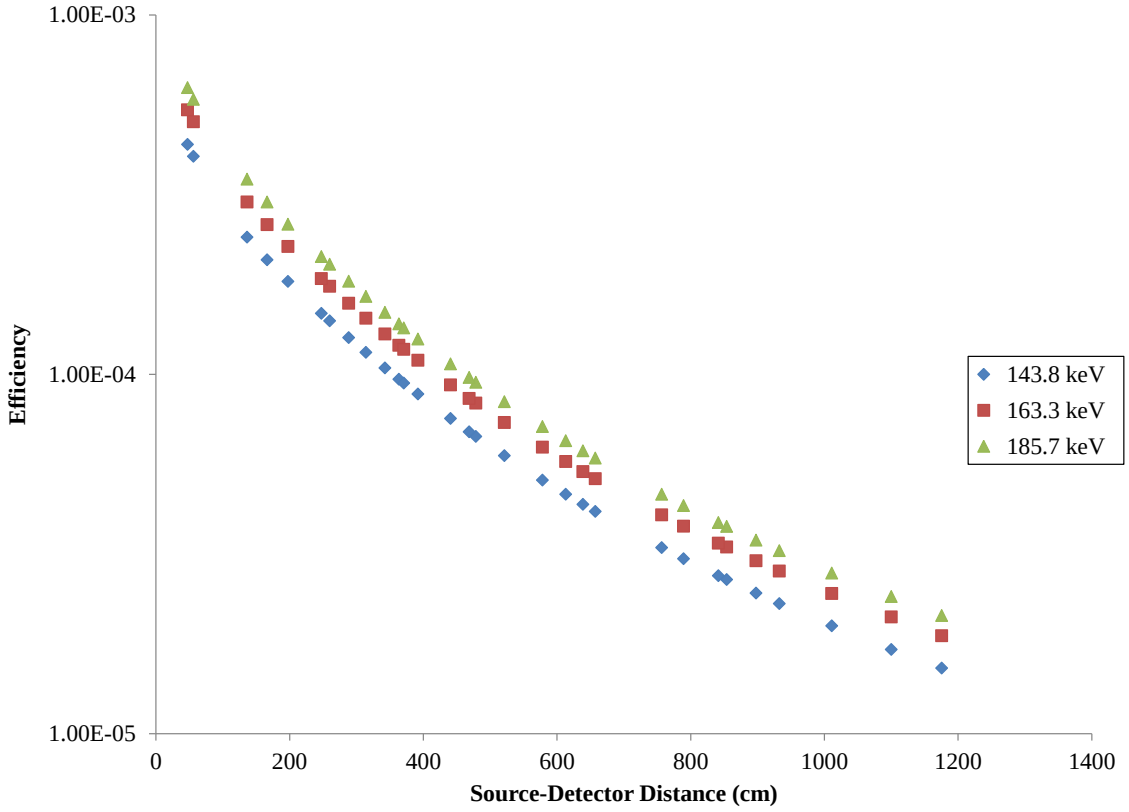

Figure K-10. ISOCS Uncertainty Estimator Simulations: Efficiency Calculations for Falcon Detector at Various Distances from Source Along Central Axis.

Gnuplot Fit for 185.7 keV Efficiency Effect on Source-Detector Distance

$$g(x) = \frac{a}{(b+x)^2} \qquad \text{[K-1]}$$

After 132 iterations the fit converged.
final sum of squares of residuals : 5.03138e-010
rel. change during last iteration : -1.89784e-012

degrees of freedom (FIT_NDF) : 28
rms of residuals (FIT_STDFIT) = sqrt(WSSR/ndf) : 4.23901e-006
variance of residuals (reduced chisquare) = WSSR/ndf : 1.79692e-011

Final set of parameters		Asymptotic Standard Error	
a	= 0.473218	+/- 0.007003	(1.48%)
b	= 22.8315	+/- 0.242	(1.06%)

correlation matrix of the fit parameters:

	a	b
a	1.000	
b	0.968	1.000

K.5.2 Pipe Thickness Variation

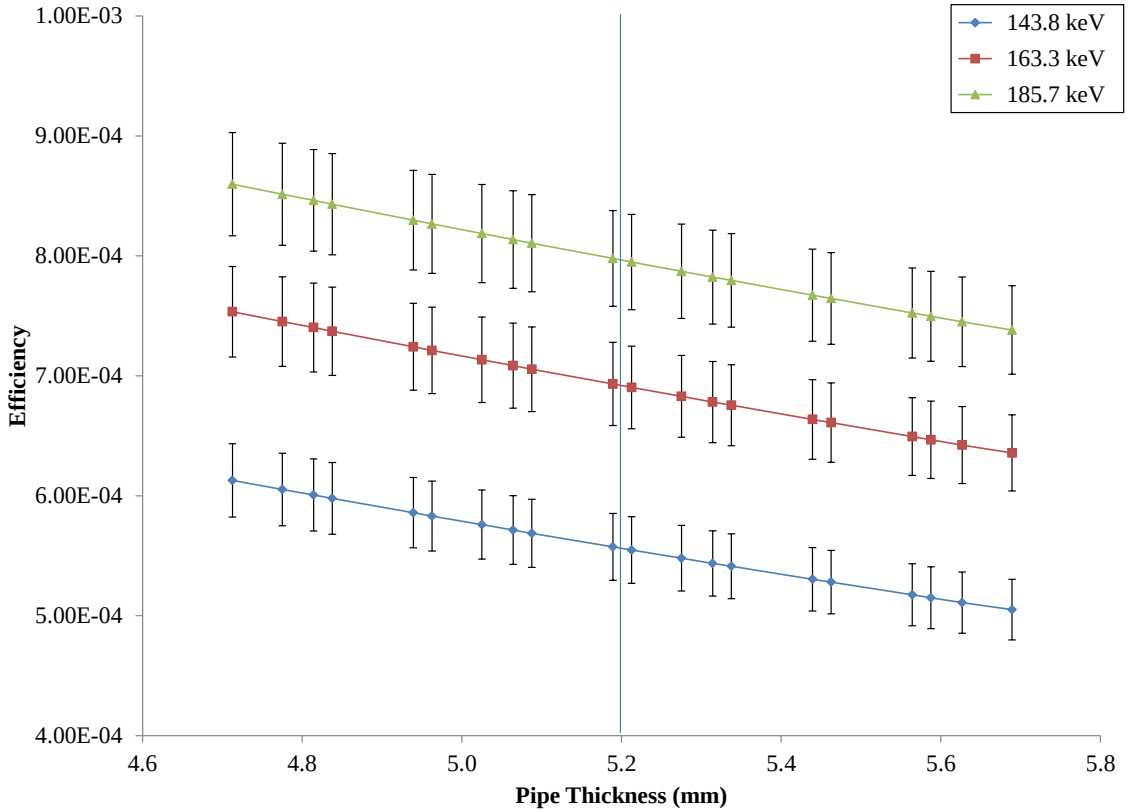

Figure K-11. ISOCS Uncertainty Estimator Simulations: Efficiency Calculations for Falcon Detector at Various Pipe Thickness Values.

APPENDIX L: MATERIAL SUBSTITUTION ANALYSIS USING MCNPX

Table L-1. Equivalent 90 g U/L UN Solution Mass Replacement for $Pb(NO_3)_2$.

Concentration U (g U/L)	Equivalent Mass UN Solution (g UN/L)
5	62.3
10	124.7
20	249.33

Table L-2. Mass Fraction of UN-$Pb(NO_3)_2$ Solution Employed in MCNPX Simulations for Various Enrichments.

L-2 (A). 5g U/L Substitution

Enrichment	0.76%	1.00%	5.00%	10.00%
^{238}U	7.57%	7.57%	7.57%	7.57%
^{235}U	0.00058%	0.00076%	0.00379%	0.00757%
N	0.69%	0.69%	0.69%	0.69%
H	9.80%	9.80%	9.80%	9.80%
O	81.81%	81.81%	81.81%	81.81%
Pb	0.12%	0.12%	0.12%	0.12%

L-2 (B). 10g U/L Substitution

Enrichment	0.76%	1.00%	5.00%	10.00%
^{238}U	7.07%	7.06%	6.77%	6.42%
^{235}U	0.05%	0.07%	0.36%	0.71%
N	0.66%	0.66%	0.66%	0.66%
H	9.86%	9.86%	9.86%	9.86%
O	82.11%	82.11%	82.11%	82.11%
Pb	0.24%	0.24%	0.24%	0.24%

L-2 (C). 20g U/L Substitution.

Enrichment	0.76%	1.00%	5.00%	10.00%
^{238}U	6.19%	6.18%	5.93%	5.61%
^{235}U	0.05%	0.06%	0.31%	0.62%
N	0.62%	0.62%	0.62%	0.62%
H	9.97%	9.97%	9.97%	9.97%
O	82.70%	82.70%	82.70%	82.70%
Pb	0.48%	0.48%	0.48%	0.48%

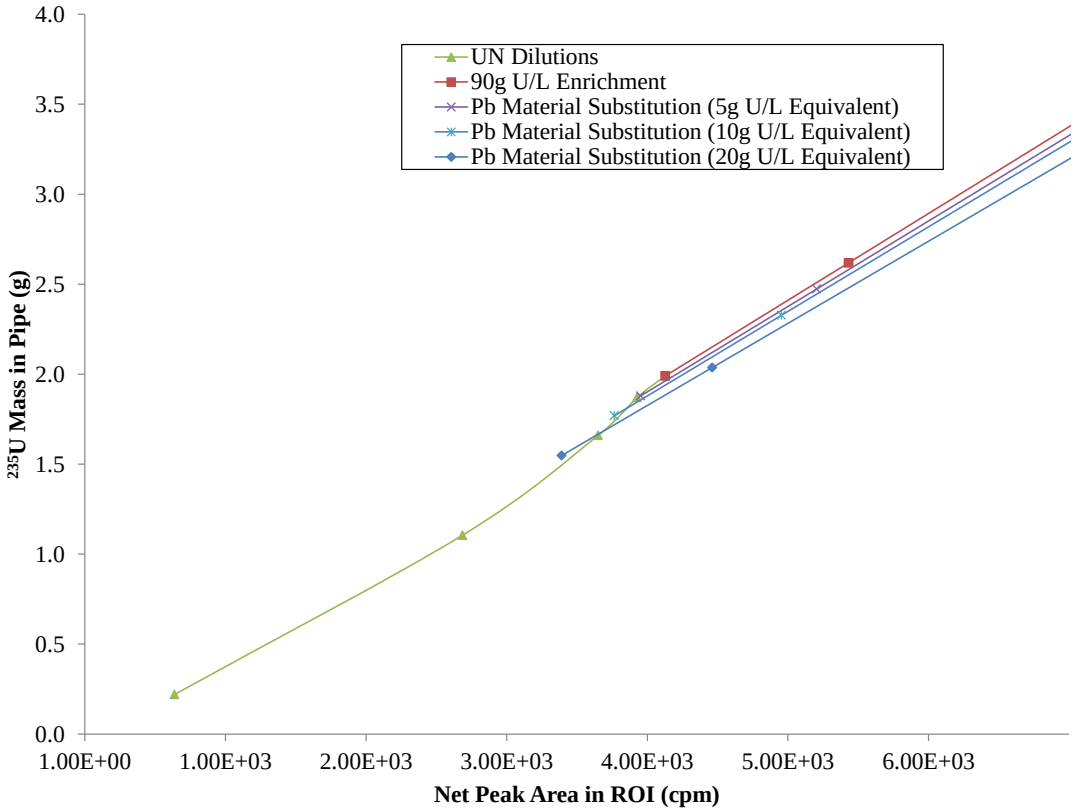

Figure L-1. Peak Area (cpm) in 185.7 keV ROI for ^{235}U as a Function of ^{235}U Mass in MCNPX Simulated Pipe Segment.

WORKS CITED

[1] International Atomic Energy Agency, "Safeguards Measures Applicable in Conversion Plants Processing Natural Uranium (Policy Paper 18)," 2009, July 28 2009.

[2] B. D. Boyer, *et al.*, "International Safeguards Approach for Uranium Ore Concentrates to Uranium Hexafluoride Conversion Plants," in *45th Annual Meeting of the Institute of Nuclear Materials Management (INMM)*, Orlando, FL, 2004.

[3] International Atomic Energy Agency. Integrated Nuclear Fuel Cycle Information Systems [Online]. Available: http://infcis.iaea.org/

[4] WISE Uranium Project. (2013, 12 February). *Uranium Hexafluoride Conversion Facilities*. Available: http://www.wise-uranium.org/efac.html#CONV

[5] World Nuclear Association. (2011, Oct. 25). *Uranium Enrichment*. Available: http://world-nuclear.org/info/inf28.html

[6] J. L. Ladd-Lively, "Uranyl Nitrate Flow Loop," Oak Ridge National Laboratory, Oak Ridge, TN ORNL/TM-2008/048, October 2008.

[7] A. A. Moghissi, *et al.*, *Radioactive Waste Technology*. New York: American Society of Mechanical Engineers, 1986.

[8] Lawrence Livermore National Laboratory. (2007). *Identifying the Source of Stolen Nuclear Materials*. Available: https://www.llnl.gov/str/JanFeb07/Smith.html

[9] S. M. Francis, "Safeguards by Design for Uranium Conversion Facilities," in *50th Annual Meeting of the Institute of Nuclear Materials Management* Tucson, AZ, 2009.

[10] M. Benedict and T. H. Pigford, *Nuclear Chemical Engineering*. New York: McGraw-Hill Book Company Inc., 1957.

[11] R. L. Faulkner, *et al.*, "Oak Ridge Efforts to Enhance Conversion Plant Safeguards," in *45th Annual Meeting of the Institute of Nuclear Materials Management (INMM)*, Orlando, FL, 2004.

[12] Argonne National Laboratory. (2013). *Properties of Uranium Hexafluoride (UF6)*. Available: http://web.ead.anl.gov/uranium/guide/uf6/propertiesuf6/

[13] M. H. Schwartz and J. Steyn. (2010) New Capacity Needed. *Nuclear Engineering International*. 23-24. Available: http://www.neimagazine.com/story.asp?storyCode=2057706

[14] J. Doo, *et al.*, "Safeguards Approach for Natural Uranium Conversion Plants," in *44th Annual Meeting of the Institute of Nuclear Materials Management (INMM)*, Phoenix, AZ, 2003.

[15] International Atomic Energy Agency, "The Structure and Content of Agreements between the Agency and States Required in Connection with the Treaty on the Non-Proliferation of Nuclear Weapons," in *INFCIRC 153 (corrected)*, International Atomic Energy Agency, Ed., ed, 1972.

[16] International Atomic Energy Agency, "Model Protocol Additional to the Agreement(s) between state(s) and the International Atomic Energy Agency for the Application of Safeguards," in *INFCIRC 540 (corrected)*, International Atomic Energy Agency, Ed., ed, 1997.

[17] O. J. M. Peixoto and H. E. Vicens, "Alternative Techniques When Applying Safeguards to Natural Uranium Conversion Plants," in *48th Annual Meeting of the Institute of Nuclear Materials Management* Tuscon, AZ, 2007.

[18] A. C. Raffo-Caiado, *et al.*, "Safeguards Options for Natural Uranium Conversion Facilities— A Collaborative Effort between the U.S. Department of Energy and the

National Nuclear Energy Commission of Brazil," in *49th Annual Meeting of the Institute of Nuclear Materials Management*, Nashville, TN, 2008.

[19] American Society for Testing and Materials, "ASTM C788 - 03(2009) Standard Specification for Nuclear-Grade Uranyl Nitrate Solution or Crystals," ed. West Conshohocken: ASTM International, 2013.

[20] American Society for Testing and Materials, "ASTM C753 - 04(2009) Standard Specification for Nuclear-Grade, Sinterable Uranium Dioxide Powder," ed. West Conshohocken: ASTM International, 2013.

[21] B. Moran, "Recommendations on Safeguards for Uranium Concentrates Meeting 34(c) Criteria," International Atomic Energy Agency, Presented to SAGSI Working Group Meeting 2011 April 05. 2011.

[22] International Atomic Energy Agency. (2013). *Conclusion of Additional Protocols: Status as of 9 April 2013*. Available: http://www.iaea.org/safeguards/documents/AP_status_list.pdf

[23] K. E. Owen, "Implementation of IAEA Policy Paper 18 in Canada," in *Symposium on International Safeguards: Addressing Verification Challenges*, Vienna, Austria, 2006.

[24] P. Burton, "Canadian Perspective on Safeguards at the Front End of the Fuel Cycle," presented at the 9th International Conference on Facility Operations- Safeguards Interface, Savannah, GA, 2012.

[25] M. Manning, *et al.*, "Investigating Safeguards Options for Natural Uranium Conversion Facilities: A Collaborative Effort between the U.S. Department of Energy (DOE) and the National Nuclear Energy Commission of Brazil (CNEN)," in *46th Annual Meeting of the Institute of Nuclear Materials Management (INMM)*, Phoenix, AZ, 2005.

[26] International Atomic Energy Agency, "Facility Design and Plant Operation Features that Facilitate the Implementation of IAEA Safeguards," Vienna 2009.

[27] O. J. M. Peixoto and H. E. Vicens, "Alternative Techniques When Applying Safeguards to Natural Uranium Conversion Plants," in *48th Annual Meeting of the Institute of Nuclear Materials Management (INMM)*, Tucson, AZ, 2007.

[28] L. G. Loden and J. M. Begovich, "Implementing Safeguards-by-Design at Natural Uranium Conversion Plants," Oak Ridge National Laboratory, Oak Ridge, TN ORNL/TM-2011/, 2011.

[29] L. Loden and J. Begovich, "Implementing Safeguards-by-design at Natural Uranium Conversion Plants," NGSI-SBD-002, 2012.

[30] H. A. Elayat, *et al.*, "Systems Analysis of Safeguards Effectiveness in a Uranium Conversion Facility," in *45th Annual Meeting of the Institute of Nuclear Materials Management (INMM)*, Orlando, FL, 2004.

[31] T. Burr, *et al.*, "Meta-Analysis Options for Inconsistent Nuclear Measurements," *Nuclear Science and Engineering*, vol. 173, pp. 15-27, 2013.

[32] D. Nusbaum, *et al.*, "Strengthening Safeguards in the Nuclear Fuel Cycle: 1. Diversion Scenarios in the Nuclear Fuel Cycle," in *8th International Conference on Facility Operations – Safeguards Interface*, Portland, OR, 2008.

[33] A. C. Raffo Caiado, *et al.*, "Model of a Generic Natural Uranium Conversion Plant - Suggested Measures to Strengthen International Safeguards," Oak Ridge National Laboratory, Oak Ridge, TN ORNL/TM-2008/195, 2009.

[34] M. M. Pickrell, *et al.*, "Measurement of Uranium Throughput for Accountability in a Natural Uranium Conversion Plant," in *47th Annual Meeting of the Institute of Nuclear Materials Management (INMM)*, Nashville, TN, 2006.

[35] J. L. Ladd-Lively, "Safeguards Application of Flowmeters in Natural Uranium Conversion Plants," in *47th Annual Meeting of the Institute of Nuclear Materials Management (INMM)*, Nashville, TN, 2006.

[36] J. L. Ladd-Lively, "Uranyl Nitrate Calibration Loop Equipment (UNCLE) at ORNL," in *48th Annual Meeting of the Institute of Nuclear Materials Management (INMM)*, Tucson, AZ, 2007.

[37] J. L. Ladd-Lively, "Status Update: Uranyl Nitrate Calibration Loop Equipment (UNCLE) at ORNL," in *49th Annual Meeting of the Institute of Nuclear Materials Management (INMM)*, Nashville, TN, 2008.

[38] J. L. Ladd-Lively, "Status Update: Uranyl Nitrate Calibration Loop Equipment (UNCLE) at ORNL," in *50th Annual Meeting of the Institute of Nuclear Materials Management (INMM)*, Tucson, AZ, 2009.

[39] J. L. Ladd-Lively, *et al.*, "Calibration of Safeguards Monitors Using the Uranyl Nitrate Calibration Loop Equipment (UNCLE) at ORNL," in *51st Annual Meeting of the Institute of Nuclear Materials Management (INMM)*, Baltimore, MD, 2010.

[40] M. M. Pickrell, *et al.*, "Development of Instrumentation for the Measurement and Safeguarding of Uranium in a Natural Uranium Conversion Plant," in *48th Annual Meeting of the Institute of Nuclear Materials Management (INMM)*, Phoenix, AZ, 2005.

[41] M. C. Miller, *et al.*, "Source Term Analysis in Support of Safeguards Approaches for Uranium Conversion Facilities," in *45th Annual Meeting of the Institute of Nuclear Materials Management (INMM)*, Orlando, FL, 2004.

[42] E. B. Rauch, *et al.*, "Optimization of a Uranyl Nitrate Passive Neutron Counter," in *51st Annual Meeting of the Institute of Nuclear Materials Management (INMM)*, Baltimore, MD, 2010.

[43] D. Lee, *et al.*, "Status Update: Calibration of Safeguards Monitors Using the Uranyl Nitrate Calibration Loop Equipment (UNCLE) at ORNL," in *52nd Annual Meeting of the Institute of Nuclear Materials Management (INMM)*, Palm Desert, CA, 2011.

[44] D. Lee, *et al.*, "Uranyl Nitrate Calibration Loop Equipment (UNCLE) 2011 Annual Report," Oak Ridge National Laboratory, Oak Ridge, TN ORNL/TM-2011/498, 2011.

[45] J. L. Ladd-Lively, "Dissertation Proposal: Development of a Monitoring Framework for the Detection of Diversion of Intermediate Products in a Generic Natural Uranium Conversion Plant," Chemical & Biomolecular Engineering, University of Tennessee, Knoxville, 2008.

[46] International Atomic Energy Agency. (2011). *Safeguards Techniques and Equipment: 2011 Edition*. Available: http://www-pub.iaea.org/books/iaeabooks/8695/Safeguards-Techniques-and-Equipment-2011-Edition

[47] S. LaMont, *et al.*, "Use of Chemical and Isotopic Tracers as Part of an Improved Safeguards Approach in Uranium Conversion Facilities," in *8th International Conference on Facility Operations – Safeguards Interface*, Portland, OR, 2008.

[48] S. A. Dewji, *et al.*, "Use of the UNCLE Facility to Assess Integrated Online Monitoring Systems for Detection of Diversion at Uranium Conversion Facilities," in *52nd Annual Meeting of the Institute of Nuclear Materials Management (INMM)*, Palm Desert, CA, 2011.

[49] S. A. Dewji, *et al.*, "Development of Integrated Online Monitoring Systems for Detection of Diversion at Natural Uranium Conversion Facilities," in *54th Annual Meeting of the Institute of Nuclear Materials Management (INMM)*, Palm Desert, CA, 2013.

[50] S. A. Dewji, *et al.*, "Detector Validation and Source Term Analysis of Uranyl Nitrate to Detect Diversion at Natural Uranium Conversion Facilities," in *53rd Annual*

Meeting of the Institute of Nuclear Materials Management (INMM), Orlando, FL, 2012.

[51] L. Hiller, *et al.*, "RadSrc Library and Application Manual," Lawrence Livermore National Laboratory, Livermore, CA UCRL-TM-229498, 16 February 2007.

[52] W. B. Wilson, *et al.*, "SOURCES 4C: A Code for Calculating (alpha,n), Spontaneous Fission, and Delayed Neutron Sources and Spectra," in *American Nuclear Society/Radiation Protection and Shielding Division 12th Biennial Topical Meeting*, Santa Fe, NM, 2002.

[53] L. Yaffe, "SOLUBILITY OF URANYL NITRATE HEXAHYDRATE AND THORIUM NITRATE TETRAHYDRATE IN ORGANIC SOLVENTS AT 20 °C," *Canadian Journal of Research,* vol. 27b, pp. 638-645, 1949/07/01 1949.

[54] R. Hunt, "Personal Communication," S. A. Dewji, Ed., E-mail Communication ed. Oak Ridge, 2012.

[55] R. L. Heath, *et al.*, "Gamma Ray Spectrum Catalogue, 4th Edition," Idaho National Laboratory1999.

[56] H. Bateman, "Solution of a system of differential equations occurring in the theory of radioactive transformation," *Proc. Cambridge Phil. Soc.*, vol. 15, pp. 423-427, 1910.

[57] J. S. Bogard. Health Physics Society Public Information: Ask the Experts [Online]. Available: http://hps.org/publicinformation/ate/q2770.pdf

[58] M. J. Berger, *et al.* (2011, December 3). *XCOM: Photon Cross Sections Database*. Available: http://www.nist.gov/pml/data/xcom/

[59] D. Reilly, "Origin of Gamma-Rays," in *Passive Nondestructive Assay of Nuclear Materials*, Los Alamos National Laboratory, Ed., ed: U.S. Nuclear Regulatory Commission Office of Nuclear Regulatory Research, 1991.

[60] F. H. Attix, "Gamma- and X-Ray Interactions in Matter," in *Introduction to Radiological Physics and Radiation Dosimetry*, ed: Wiley-VCH Verlag GmbH, 1986, pp. 124-159.

[61] S. Y. F. Chu, *et al.* The Lund/LBNL Nuclear Data Search [Online]. Available: http://nucleardata.nuclear.lu.se/toi/

[62] G. Knoll, *Radiation Detection and Measurement*. New York: John Wiley & Sons, 2000.

[63] Canberra Industries Inc. (2008). *In Situ Gamma Spectroscopy with ISOCS, an In Situ Object Counting System*. Available: http://www.canberra.com/pdf/Literature/M2352-InSitu-ISOCS-AN.pdf

[64] S. K. Smith and M. Lucas, "Gamma-Ray Detectors," in *Passive Nondestructive Assay of Nuclear Materials*, D. Reilly, *et al.*, Eds., ed Washington: Los Alamos National Laboratory/U.S. Nuclear Regulatory Commission, 1991.

[65] J. L. Parker, "Use of Calibration Standards and the Correction for Sample Self-Attenuation in Gamma-Ray Nondestructive Assay," Los Alamos National Laboratory, Los Alamos LA-10045, 1984.

[66] K. E. Morris, *et al.*, "Segmented Gamma Scanner for Small Containers of Uranium Processing Waste- 12295," presented at the Waste Management 2012 Phoenix, AZ, 2012.

[67] S. A. Philips and S. Croft, "In-line Monitoring of Radium Slurry by Gamma-Ray Spectrometry," presented at the 10th International Conference on Environmental Remediation and Radioactive Waste Management, Glasgow, Scotland, 2005.

[68] G. V. Walford, *et al.*, "Evaluation of Gamma Ray Detector Performances for Differing Special Nuclear Material (SNM) Geometries," in *52nd Annual Meeting of the Institute of Nuclear Materials Management (INMM)*, Palm Desert, CA, 2011.

[69] Canberra Industries Inc. (2011, InSpector™ 1000 Digital HandHeld Multichannel Analyzer. Available: http://www.canberra.com/pdf/Products/In1K-SS-C38987.pdf
[70] Canberra Industries Inc. (2010, Broad Energy Germanium Detectors (BEGe). Available: http://www.canberra.com/products/detectors/pdf/BEGe-SS-C40013.pdf
[71] Canberra Industries Inc. (2011). *NAIS-2x2-NaI(Tl) LED Stabilized Scintillation Detector*. Available: http://www.canberra.com/prodcuts/detectors/pdf/NAIS-2x2-SS-C38656.pdf
[72] Canberra Industries Inc. (2011, Osprey™ – Universal Digital MCA Tube Base for Scintillation Spectrometry. Available: http://www.canberra.com/products/radiochemistry_lab/pdf/Osprey-SS-C38659.pdf
[73] Canberra Industries Inc. (2011, Falcon 5000® Portable HPGe-Based Radionuclide Identifier. Available: http://www.canberra.com/products/hp_radioprotection/pdf/Falcon-SS-C38597.pdf
[74] D. Scargill, "The Application of High-Resolution Gamma Spectrometry to the In-Line Determination of Uranium and Plutonium Concentrations in Solution.," ed. Oxfordshire: United Kingdom Atomic Energy Authority,, 1981.
[75] U. Sundar, *et al.*, "Rapid measurements of concentrations of natural uranium in process stream samples via gamma spectrometry at an extraction facility.," *Talanta*, vol. 73, pp. 476-482, 2007.
[76] Canberra Industries, "Genie 2000 Gamma Analysis Software," 3.0 ed: Canberra Industries, 2004.
[77] A. C. Raffo Caiado, *et al.*, "Safeguards Options for Natural Uranium Conversion Facilities— A Collaborative Effort between the U.S. Department of Energy and the National Nuclear Energy Commission of Brazil," in *49th Annual Meeting of the Institute of Nuclear Materials Management (INMM)*, Nashville, TN, 2008.
[78] Los Alamos National Laboratory, "MCNPX User's Manual - Version 2.6.0," Los Alamos National Laboratory, Los Alamos, NM LA-CP-07-1473, 2008.
[79] D. Reilly, *et al.*, *Passive Nondestructive Assay of Nuclear Materials*. Washington: Los Alamos National Laboratory/U.S. Nuclear Regulatory Commission, 1991.
[80] N. Tsoulfanidis, *Measurement and detection of radiation*, 3rd ed. New York: McGraw-Hill, 2010.
[81] R. Venkataraman, "E-mail Personal Communication: Falcon and ISOCS," S. A. Dewji, Ed., ed, 2013.
[82] J. L. Botts, *et al.*, "Density, actidity, and conductivity measurements of uranyl nitrate/nitric acid solutions," ed. Oak Ridge: Oak Ridge National Laboratory, 1978.
[83] H. A. Smith and P. A. Russo, *Passive Nondestructive Assay of Nuclear Materials*: U.S. Nuclear Regulatory Commission Office of Nuclear Regulatory Research, 1991.
[84] National Institute of Standards and Technology. NIST Standard Reference Materials [Online]. Available: http://content.yudu.com/Library/A1tssu/NISTStandardReferenc/resources/120.htm
[85] T. Williams and C. Kelley, "Gnuplot 4.4.3: An Interactive Plotting Program.," ed, 2011.
[86] Canberra Industries Inc. (2012, NaI Detector Accessories. Available: http://www.canberra.com/products/detectors/pdf/NaI-Det-Access-SS-M1184.pdf
[87] J. L. Parker, "Attenuation Correction Procedures," in *Passive Nondestructive Assay of Nuclear Materials: Attenuation Correction Procedures*, Los Alamos National Laboratory, Ed., ed: U.S. Nuclear Regulatory Commission Office of Nuclear Regulatory Research, 1991.

[88] Onlinemetals.com. (2013). *Schedule 40 Stainless Steel Pipe T-304/304L*. Available: http://www.onlinemetals.com/merchant.cfm?id=58&showunits=mm&step=2&sortby=od&top_cat=1

[89] Ace Stainless Supply. (2013). *Schedule 40 - 304L - Pipe*. Available: http://www.acestainless.com/pipe/schedule-40

[90] H. L. Clever and F. J. Johnston, "The solubility of some sparingly soluble lead salts: An evaluation of the solubility in water and aqueous electrolyte solution," *Journal of Physical and Chemical Reference Data,* vol. 9, pp. 751-784, 1980.

[91] G. Sjoden, *et al.*, "Recent advances in the use of ASEDRA in post processing scintillator spectra for resolution enhancement," *Journal of Radioanalytical and Nuclear Chemistry,* pp. 365-371, 2012.

[92] D. R. Waymire and D. J. Mitchell, "GADRAS User Manual," Sandia National Laboratory 2009.

[93] T. Uckan, *et al.*, "Fissile Mass Flow Monitor Gamma Ray Detector System Designed for Large-Size Process Pipes," Oak Ridge National Laboratory, Ed., ed. Oak Ridge, 2004.

[94] J. March-Leuba, *et al.*, "Benchmark Gamma Spectroscopy Measurements of UF6 in an Aluminum Pipe with a NaI Detector ", Oak Ridge National Laboratory, Ed., ed. Oak Ridge, 2009.

[95] Zoller+Frohlich GmbH. (2011). *Z+F IMAGER® 5006i - Z+F USA, Inc.* Available: http://www.zf-usa.com/wp-content/uploads/2011/10/IMAGER_5006EX.pdf

[96] S. Yoshida, *et al.*, "Concentrations of uranium and 235U/238U ratios in soil and plant samples collected around the uranium conversion building in the JCO campus," *Journal of Environmental Radioactivity,* vol. 50, pp. 161-172, 2000.

[97] R. S. Kemp, "Initial Analysis of the Detectability of UO2F2 Aerosols Produced by UF6 Released from Uranium Conversion Plants," *Science & Global Security,* vol. 16, pp. 115-125, 2008/12/11 2008.

[98] International Atomic Energy Agency, "IAEA Department of Safeguards Long-Term R&D Plan, 2012-2023," International Atomic Energy Agency, Ed., ed. Vienna: International Atomic Energy Agency, , 2013.